Dielectric Resonator Bandstop Filters

Richard Kayip Chan

Submitted in accordance with the requirements for the degree of Doctor of Philosophy

The University of Leeds

School of Electronic and Electrical Engineering

April 2011

The candidate confirms that the work submitted is his own and that appropriate credit has been given where reference has been made to the work of others.

This copy has been supplied on the understanding that it is copyright material and that no quotation from the thesis may be published without proper acknowledgement

Abstract

Dielectric resonators have been widely employed in wireless and satellite communication systems due to their inherently large Q allowing them to fashion low loss and narrow bandwidth filters. Recent progress has adopted these resonators in applications requiring low volume and mass for demanding specifications. The technology at present consists of an assortment of bandpass filters using dielectric resonators but there is little published material on bandstop filters employing such resonators. Bandstop filters are desirable to suppress frequencies at the front end of wireless communication systems. To meet future demands, it is imperative to reduce the costs of these filters in both volume and weight using dielectric resonators.

This thesis presents compact mono-mode and dual-mode bandstop dielectric resonator structures. The former consists of a dielectric-loaded waveguide cavity filter that offers a miniaturised version to typical cavity dielectric resonator filters requiring high unloaded Qs. The mono-mode filter described is ideal for relaxed specifications requiring a lower Q resonator to replace common coaxial resonator filters. For applications requiring high bandwidth, this resonator is improved by coupling a dielectric ring resonator to a coaxial transmission line. A novel dual-mode bandstop resonator is developed taking advantage of the geometry of a cylindrical puck within a single shielded cavity to create two degenerate modes with equal resonant frequency, effectively replacing two mono-mode cavities. Miniaturisation is achieved by sitting the dielectric puck at the base of the cavity and correct phase separation between the orthogonal modes is produced from a curved uniform transmission line.

The mode behaviour is observed in the physical realisations using a 3D FEM solver. Advanced filtering functions using prescribed reflection zeros is demonstrated with the simulation of a dual-cavity, dual-mode bandstop resonator where inter- and intra- cavity couplings are controlled. The miniaturisation techniques discussed in this thesis will provide cost-reduction for microwave communication systems requiring high-Q bandstop filters.

Contents

Acknowledgments

Firstly I would like to thank Ian Hunter for his invaluable supervision and guidance throughout this work. Thanks also to Filtronic for funding this work.

Many thanks to Terry Mosely and Nick Banting for the amount of time spent discussing the construction of the filters. I would also like to thank Richard Cameron for his comments in this thesis.

A big thank you to my Mother and Father for making all this possible.

List of Figures

List of Tables

Chapter 1

Introduction

With current trends in communication systems calling for lower manufacturing costs and higher performance, resonating elements with high quality factors, Qs, become a neccessity. These elements play a fundamental role in the design of microwave filters as the resonator quality factor is proportional to volume and becomes an important limiting factor. Typically, waveguide structures have been used for their high Q and high temperature stability allowing very narrow bandwidths in a large frequency domain, 900 MHz to 100 GHz. The disadvantage is bulky and cumbersome filters are required that are expensive to produce and excessively heavy. Microstrip and stripline technology have been the main constituents in removing these bulky waveguides in the majority of microwave systems and are used in the high frequency domain, 100 MHz to 30 GHz, to realise high bandwidth filters due to their low Q. Their small dimensions and ease of integration with microwave circuits are of great interest but their disadvantage is their low losses are usually compensated by active devices or superconducting technology.

A miniaturisation technique providing a low-loss solution employs dielectric resonators, DRs, as they allow a reduction in size inversely proportional to the square root of the permittivity of the dielectric material used. In addition, the loss in a dielectric-loaded cavity with metallic shielding is dominated by the loss tangent owing to the dielectric material and minimally dependent on the outer

conductor loss. An advantage with this is that dielectric losses are improving constantly due to more advanced materials being produced, whereas metallic losses have remained fairly constant with no signs of improvement, with the exception of superconductors. As a result, these resonators have the ability to function as waveguide filters but are much better in terms of minimisation, stability and weight. This advantage can be seen in satellite communication systems where inherently high-loss microstrip and stripline technology are disregarded for a DR equivalent application. In recent years, these low-loss DRs have led to the realisation of small, reliable, lightweight and stable microwave systems.

In microwave filter technology, DRs have been preferred for their superior high Q, low loss and miniaturisation attributes. In recent years, motivation for more compact and ease of bulk manufacture at low cost have increased demand for these types of filters. For example, in wireless communications, a more cost-effective solution that can replace coaxial air-filled resonators with smaller, low-cost DR filters is a necessity. Further size-reduction techniques have been developed in the form of higher-order mode filters, [1]. These higher-order mode filters are more complex in design and often rely on measured data to implement the required resonator frequencies and coupling coefficients that satisfy the equivalent circuit model. With improved computer speeds, full-wave electromagnetic field simulation software becomes increasingly useful in simulating these 3D structures reducing practical test times and enabling the filter designer to observe modal-field behaviour for different parameters.

Although much work has been presented using DRs with bandpass filters, only a limited number of publications on bandstop filters employing DRs have been published and very little is known about dual-mode dielectric bandstop filters. Filters with DRs coupled to microstrip line have been presented but require housing that increase their volume, [2] and [3]. A triple mode hybrid reflection filter was also presented using two cubic dielectric resonators coupled together through a 3 dB quadrature hybrid, [4]. The design requires complex tuning for each mode and is limited as it caters for filters of degree six and above. More conventionally,

mono-mode DRs have been coupled to waveguide transmission lines for attenuation behaviour but each DR requires a cavity which also increases volume, [5]. It is the aim of this thesis to design bandstop filters using DRs making full use of their high Q and low loss to achieve miniaturisation techniques suitable for wireless systems where the emphasis is on cost and not highly demanding low-loss performance. The first objective is to provide a solution for a mono-mode dielectric resonator bandstop filter providing a low-cost alternative to coaxial bandstop resonators. The second objective is to incorporate the hybrid dual-mode property of dielectric resonators allowing the reduction in cavity number compared to mono-mode resonators. The final objective is to propose an improvement for each resonator type to address shortcomings and demonstrate realisability of advanced filtering functions. This thesis provides an introduction to size reduction for bandstop filters employing dielectric resonators that have potential for further filtering techniques and, therefore, only provides possibilities for the use of this structure to implement fullly advanced filter functions.

1.1 Applications of Microwave Filters

Microwave filters are used to define wanted and unwanted frequency bands. They play an important role in terrestial, radio and satellite communications along with radar systems. As communication systems improve at a tremendous rate, the difficulty to meet filter specifications becomes more challenging. In a cellular base station, they perform important roles at different stages of the radio frequency, RF, front-end unit, figure 1.1. Typically, low loss is required in the passband with a high rejection of signals at the passband edges to give greater selectivity. This prevents a high level of cross-channel interference between the number of subscribers that share the spectrum available to them.

A broad stopband and highly symmetrical frequency response is usually preferred for bandpass filters, although asymmetrical designs can sometimes be more advantageous when distinguishing between two adjacent bands in the spectrum.

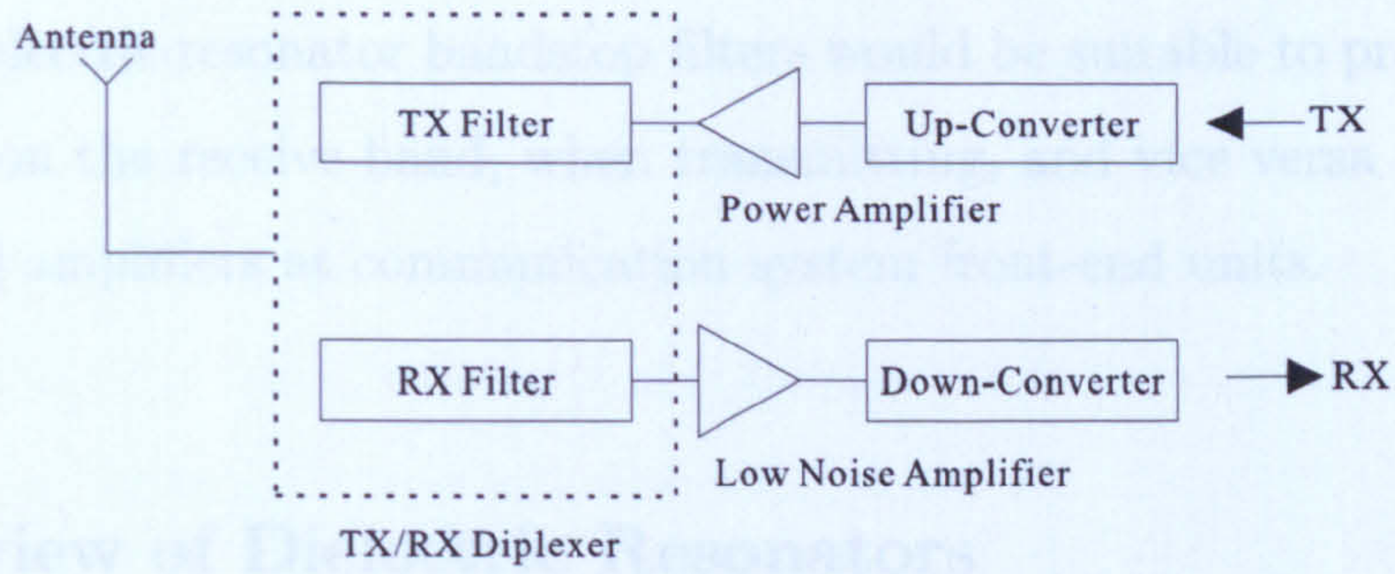

Figure 1.1: RF front-end of a cellular radio base-station

This is the case for diplexers where a highly asymmetrical attenuation specification is needed as more rejection is required from each filter over the passband of the other filter, figure 1.2.

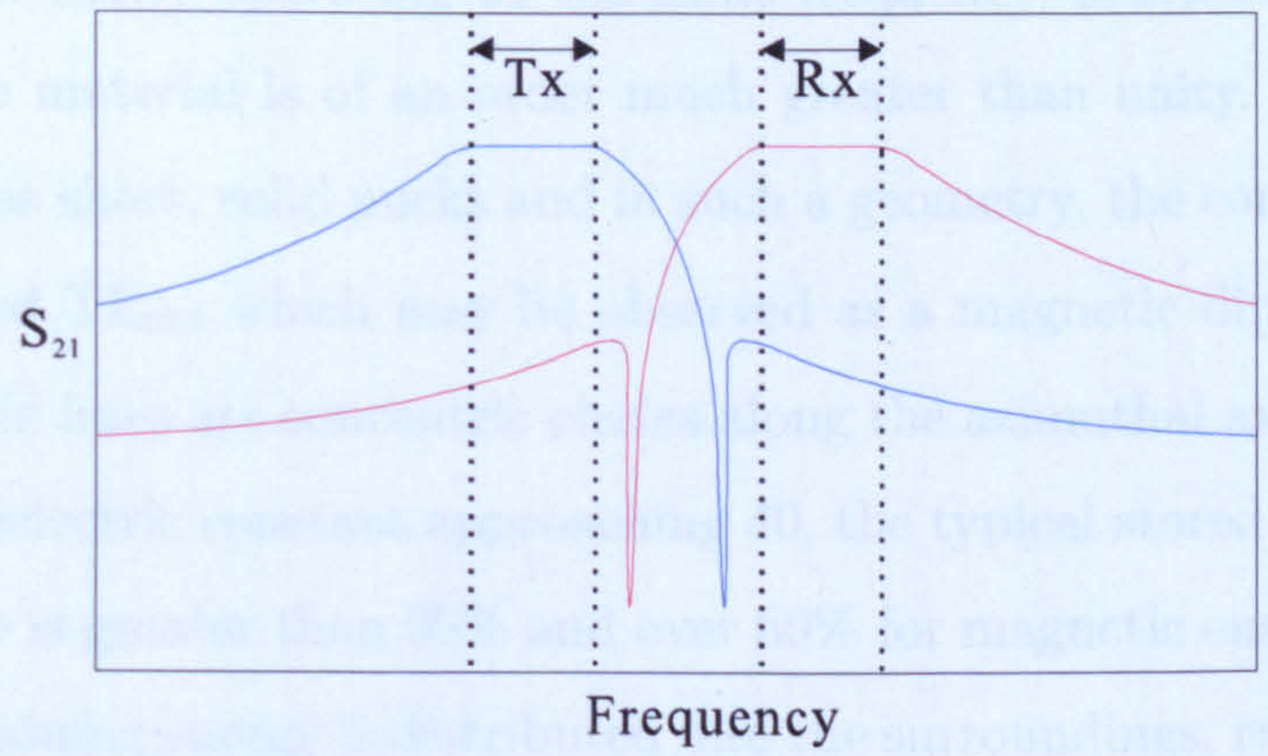

Figure 1.2: Typical diplexer response

Bandstop filters have been widely used in many microwave circuits and systems [6], [7]. In particular, narrowband reject, or notch, filters have become more important in most microwave communications and radar systems as there are more unwanted signals and interferences at air interfaces. Systems that utilise the spectrum with interleaving spectra require notch filters to avoid interference between two operators if they are too close. For example, in the Advanced Mobile Phone System/Global System for Mobile communications AMPS/GSM, these extremely narrowband filters often require resonators with unloaded Q factors in excess of 25 000. To realise such filters, cavity structures measuring 9 x 9 x 9 cm, at 2 GHz, are usually required per resonator leading to physically large devices. Microwave filters with both a compact size and high Q are desired. The

proposed dielectric resonator bandstop filters would be suitable to provide a level of rejection on the receive band, when transmitting, and vice versa between the diplexer and amplifiers at communication system front-end units.

1.2 Review of Dielectric Resonators

Low-loss DRs or superconductor filters are capable of high Qs and although the latter may produce Qs in the order of 100 000, DRs do have the potential to attain Qs exceeding 20 000. They are considerably smaller than the size of a hollow resonant cavity operating at the same frequency, provided the dielectric constant of the material is of an order much greater than unity. DRs are commonly shaped as short, solid pucks and in such a geometry, the common resonant mode is denoted $TE_{01\delta}$ which may be observed as a magnetic dipole, figure 1.3. The electric field lines are concentric circles along the azimuthal axis and for DRs with relative dielectric constant approaching 40, the typical stored electric energy for $TE_{01\delta}$ mode is greater than 95% and over 60% for magnetic energy within the puck. The remaining energy is distributed into the surroundings, rapidly decaying away from the resonator surface. Ceramics used in constructing DR filters typically have dielectric constants in the range 20 to 90, thus, DR filters gain a huge size advantage compared to similar waveguide or coaxial filters when operating. In addition, although planar filters are more convenient to fabricate and, consequently, can replace bulky waveguides in the majority of microwave systems, their low Q, only up to 500, limits them to moderate performance and cannot be used in demanding communication system applications. DR filters are then useful to fill the gap between waveguide and stripline technologies accomodating the high Qs needed and also a system integrability approaching that of planar resonators. Furthermore, they offer versatility and are adaptable to various microwave structures and coupling configurations. Unfortunately, the disadvantage of DRs is although their geometrical forms may be simple, an exact solution for Maxwell equations become more difficult to obtain than for hollow metal cavities. This is

even more so for DRs shielded in metal cavities, in which, the uniform fields from isolated resonators become distorted due to the presence of metal boundaries, figure 1.4. However, boundary approximations are possible and simple resonant frequency equations may be derived. For example, the resonant frequency for an isolated $TE_{01\delta}$ mode dielectric cylindrical resonator is

$$f_0 = \frac{34(\frac{a}{l} + 3.45)}{a\sqrt{\epsilon_r}} \tag{1.1}$$

where a is the radius in mm, l the height in mm and ϵ_r is the dielectric constant of the resonator. This formula has an accuracy of 2% for $0.5 < a/l < 2$ and $30 < \epsilon_r < 50$. For a resonator with radius 18.5 mm and height 23 mm, its resonant frequency in free space is 1.18 GHz. When the dielectric is placed in the centre of a shielded cavity with square sides 60 mm and height 50 mm, the resonant frequency increases to 1.3 GHz.

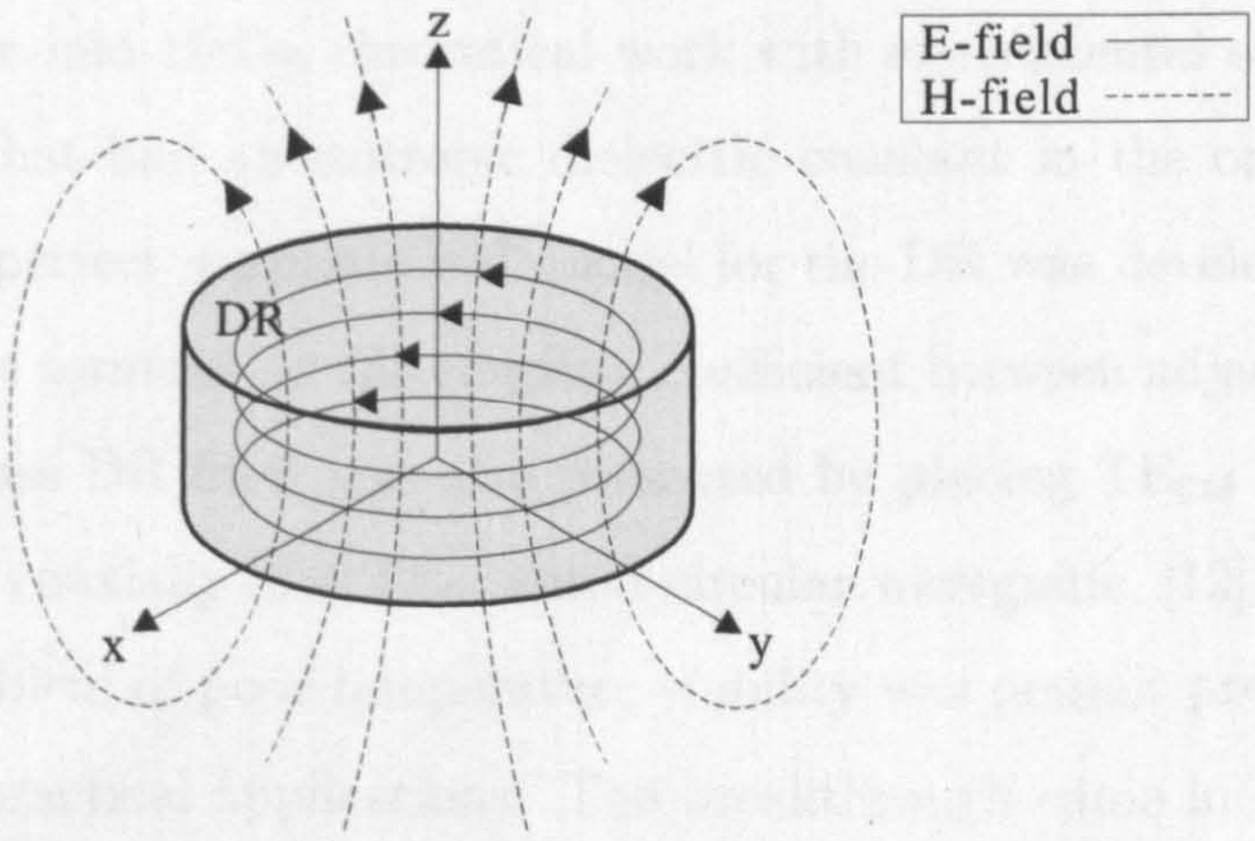

Figure 1.3: $TE_{01\delta}$ resonant mode dielectric resonator

1.2.1 Background

The propagation of guided electromagnetic waves in dielectric media was first studied in the early days of microwaves leading to the prominence of the DR where unmetalised dielectric objects functioned as microwave resonators, [8]. The term

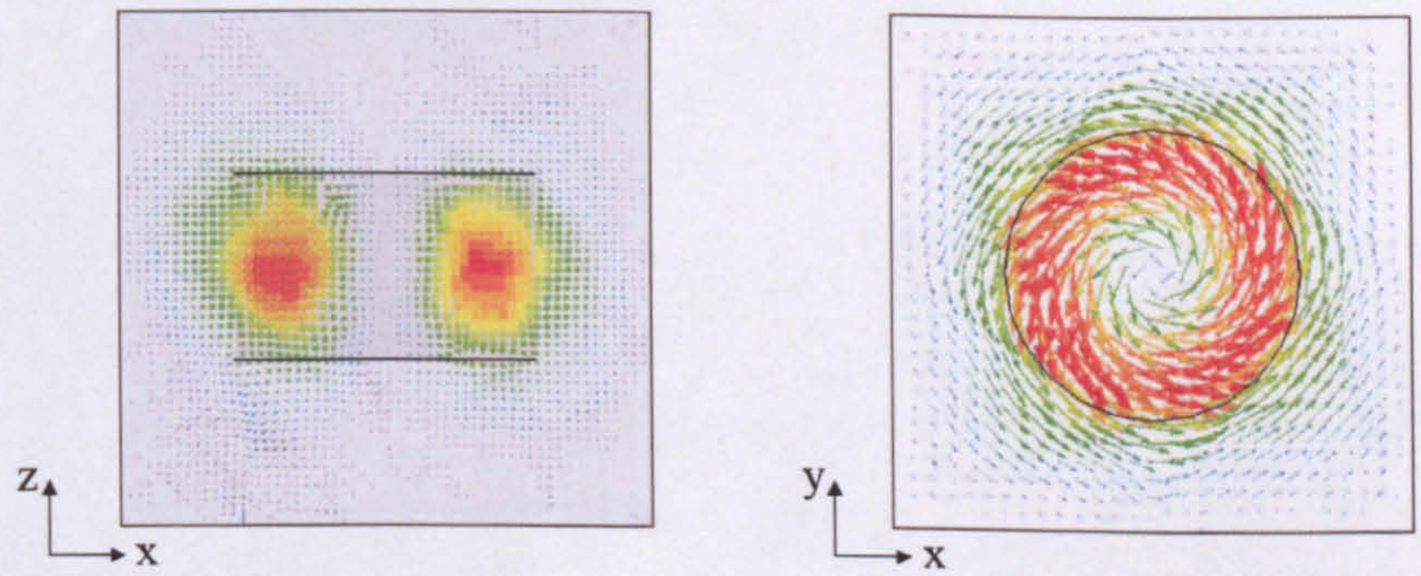

Figure 1.4: E-field plots of shielded $TE_{01\delta}$ mode dielectric resonator

dielectric resonator was coined in 1939 but the theoretical work reported failed to generate significant interest until the early 1960s. DRs were rediscovered and first analysed in terms of mode and resonator designs, [9], [10]. Unfortunately, high-dielectric constant materials at the time had poor temperature stability causing unwanted frequency shifts in microwave systems. As a consequence, in spite of their high-Q factor and small size, DRs were not considered suitable for microwave systems. In the mid-1960s, theoretical work with experimental evaluation of rutile ceramics that had an isotropic dielectric constant in the order of 100 was studied and a perfect magnetic wall model for the DR was developed along with an approximate formula for the coupling coefficient between adjacent resonators, [11]. A bandpass DR filter was also presented by placing $TE_{01\delta}$ mode dielectric rod resonators coaxially in a TE_{01} cutoff circular waveguide, [12]. As before, the continuing problem of poor temperature stability was present preventing the development of practical applications. The breakthrough came in the 1970s when the first temperature-stable and low-loss barium tetratitanate ceramics were developed by Raytheon, [13]. Bell laboratories reported a modified material to the afore-mentioned one leading to improved performance, [14]. These results led to the first realisations of DRs as microwave components but these materials were in short supply and were not marketable for commercial purposes. Murata Manufacturing Company provided the first commercial DRs using $(Zr,Sa)TiO_4$ ceramics that offered adjustable compositions allowing temperature coefficients to vary between +10 and -12 ppm/°C, [15]. This allowed the desired small control-

lable temperature coefficients over the useful operational temperature range. It was from this point onwards that the DR developed rapidly in microwave filters, [16, 17, 18, 19]. Furthermore, new filter technologies, such as dual-mode filters and elliptic function response filters were developed, [20], along with techniques to improve the spurious response, [21, 22, 23]. To accomodate these improvements, rigorous models involving full-wave modeling and analytical methods were implemented, [24, 25, 26].

1.2.2 Dielectric Resonator Filters

DR filters play an important role in mobile and satellite communications. A typical DR filter consists of a number of dielectric resonators, mounted inside cavities machined in a metallic enclosure or an evanescent-mode waveguide. Probes are used to couple the input and output electromagnetic energy and irises are typically used for inter-cavity resonator coupling. DR filters used in microwave systems can be divided into two configurations: individual DRs that are loaded coaxially in a metallic enclosure or individual resonators mounted in a planar configuration. The first practical DR filter was reported in 1975 and a schematic of the 6.9 GHz filter is shown in figure 1.5, [15].

The mono-mode filter with all resonators operating in the $TE_{01\delta}$ mode provides low loss and small volume. A planar layout offers many advantages over an in-line configuration although they are larger in size. These advantages include a flexible layout structure, simple DR supports and easier tuning mechanisms for mass production, therefore, these are widely used in base stations for mobile communication systems, [27]. A major problem with DR filters is the proximity of spurious modes. For instance, in a filter operating under $TE_{01\delta}$ mode, the ratio of this fundamental resonant frequency to the first spurious $HE_{11\delta}$ mode resonance is 1.3:1, although this may be improved to 1.5:1 by inserting a hole in the centre of the DR. Inter-resonator coupling is magnetic and controlled through irises since a greater proportion of magnetic than electric energy leaks from DRs. A typical

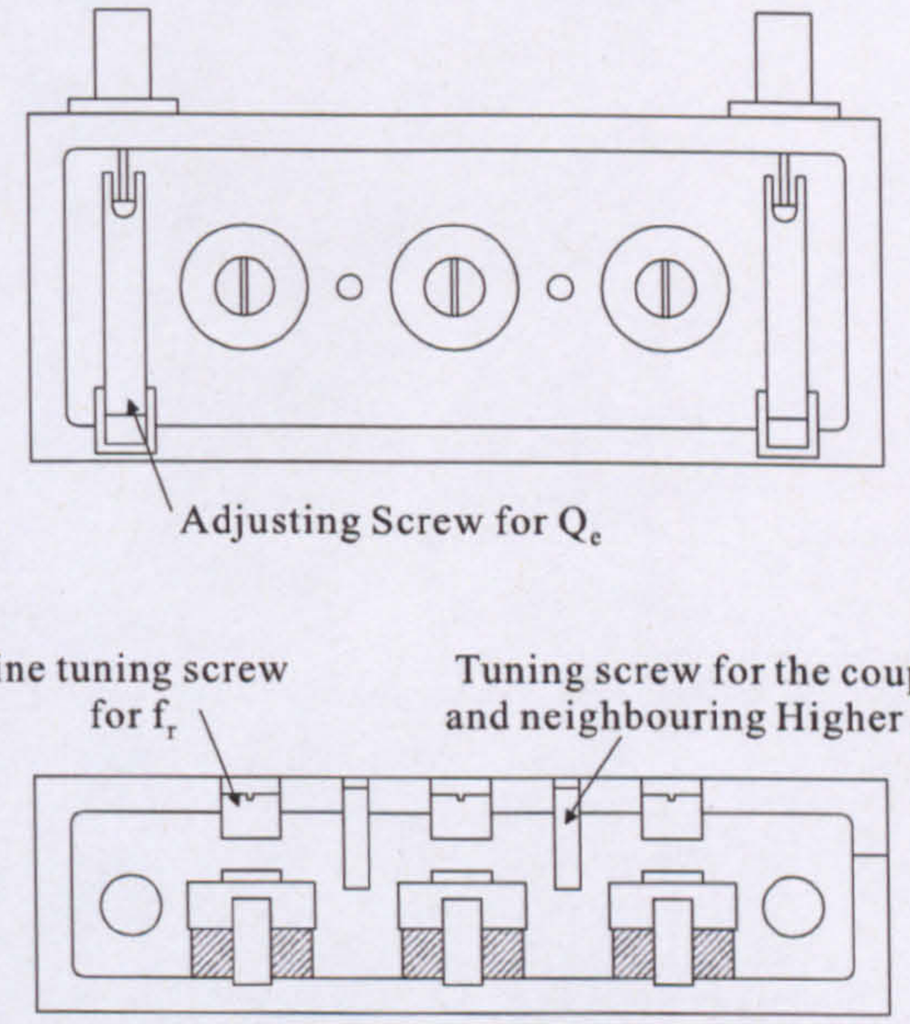

Figure 1.5: Structure of 6.9 GHz DR filter, [15]

$TE_{01\delta}$ DR filter for cellular base station applications is pictured in figure 1.6. In this configuration, non-adjacent couplings can be used to realise more advanced filter features, such as elliptic function or asymmetrical responses. Quadruplet and triplet sections can be regarded as basic building blocks to generate symmetric or asymmetric transmission zeros for TE mode cavities.

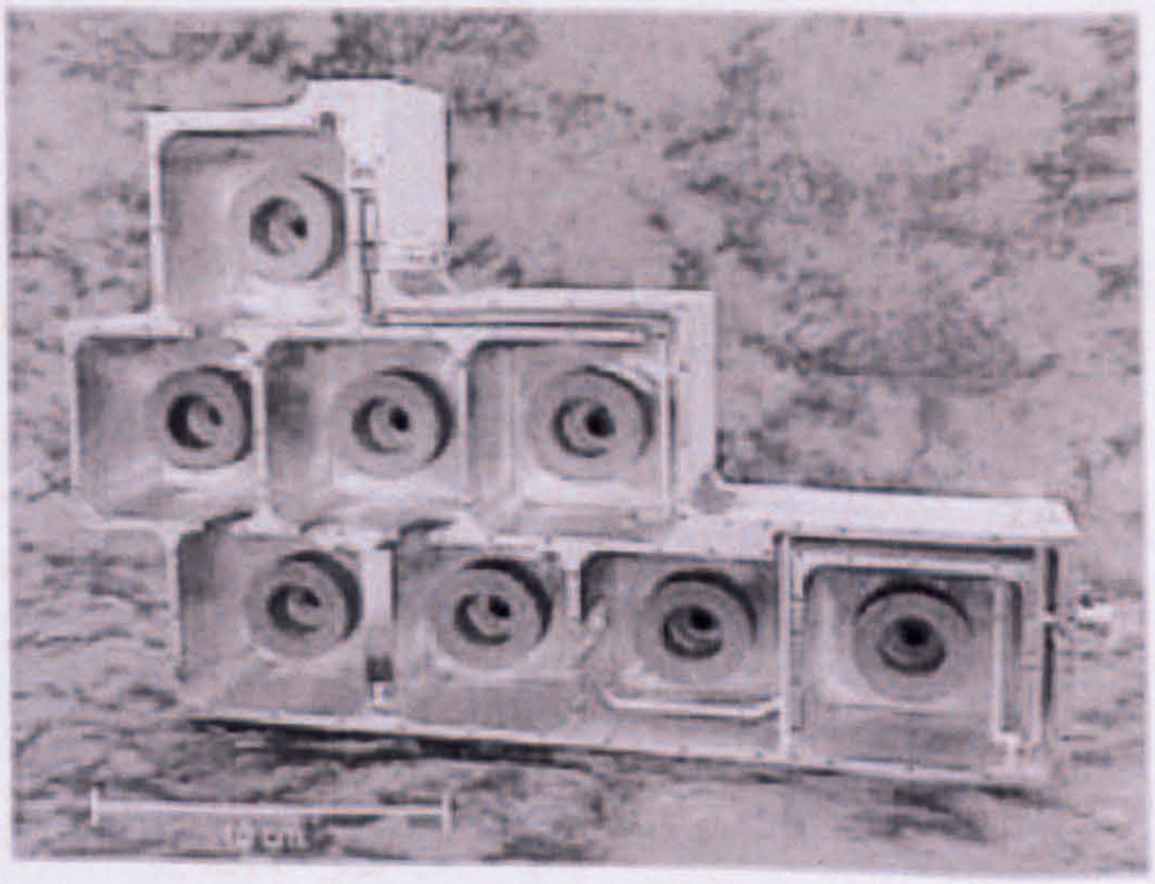

Figure 1.6: $TE_{01\delta}$ DR filter for cellular base-station application, [28]

An alternative structure consists of grounded dielectric rods operating in the single $TM_{01\delta}$ mode. This filter has a simpler structure compared to the previous

structure since no irises are needed as the dielectric rods are coupled to each other electrically. A compact DR filter may be constructed by placing these high-Q dielectric rods coaxially in a $TM_{01\delta}$ circular cutoff waveguide as shown in figure 1.7.

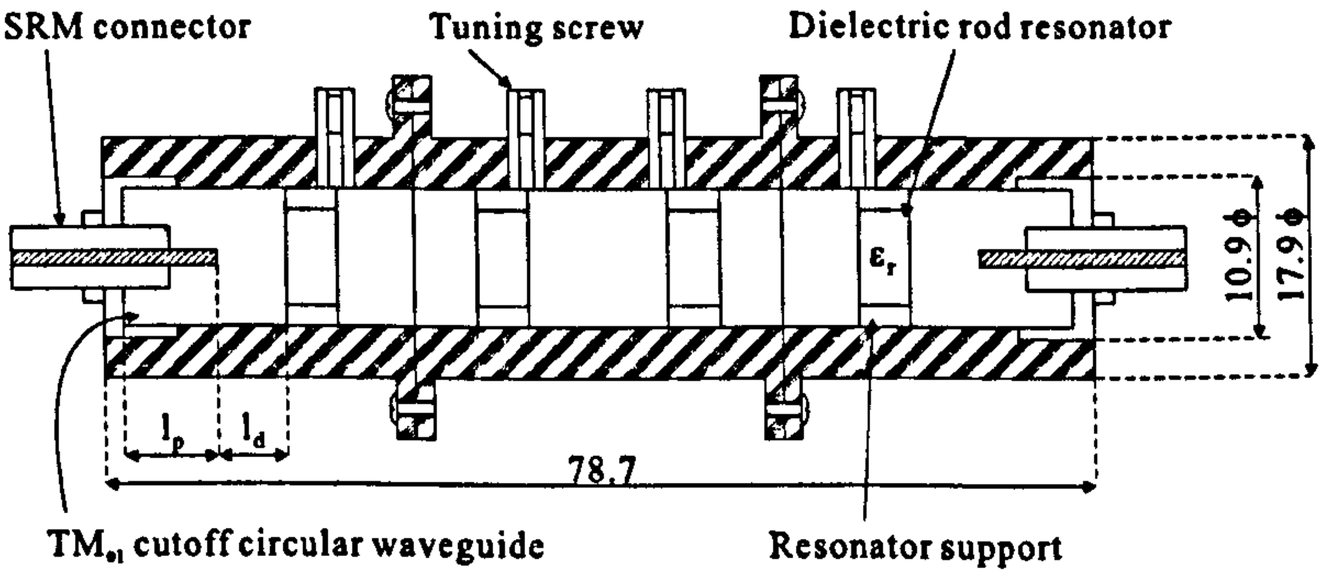

Figure 1.7: Configuration of a $TM_{01\delta}$ mode DR filter, [29]

Even with a dielectric constant of 45, a typical 900 MHz resonator occupies a cavity size of 8 x 8 x 5 cm which is still relatively large. As a consequence, size-reduction techniques become a major factor. Higher-order modes are usually considered as spurious modes, however, certain modes have the property to generate multiple modes for a given structure. The $HE_{11\delta}$ mode is such a mode allowing dual-mode operation and for certain diameter-length, D/L, ratios of a cylindrical puck its resonant frequency falls below that of the $TE_{01\delta}$ mode. The dual $HE_{11\delta}$ dual-degenerate mode in cylindrical DRs was first reported by Fiedziusko in 1982, [30], as shown in figure 1.8. In this configuration, only half the number of physical cavities is needed, offering smaller volume and DRs are mounted axially in the centre of each circular cavity in evanescence. Low-loss, stable mounting is required to assure good electrical and thermal performance. Coupling between modes within a single cavity is achieved via a mode-coupling screw with an angular location of 45° with respect to orthogonal tuning screws. Intercavity coupling is provided by coupling slots in the form of cruciform irises situated throughout the filter such that both resonances are able to couple to each other in adjacent cavities. Elliptic function responses can also be produced by cross couplings between non-adjacent cavitites and the signs of these couplings are determined by the orientations of the tuning screws relative to each other.

The theory used for an empty cavity dual-mode filter based on a coupling screw design can also be applied here to determine the required couplings as shown in figure 1.9, [31].

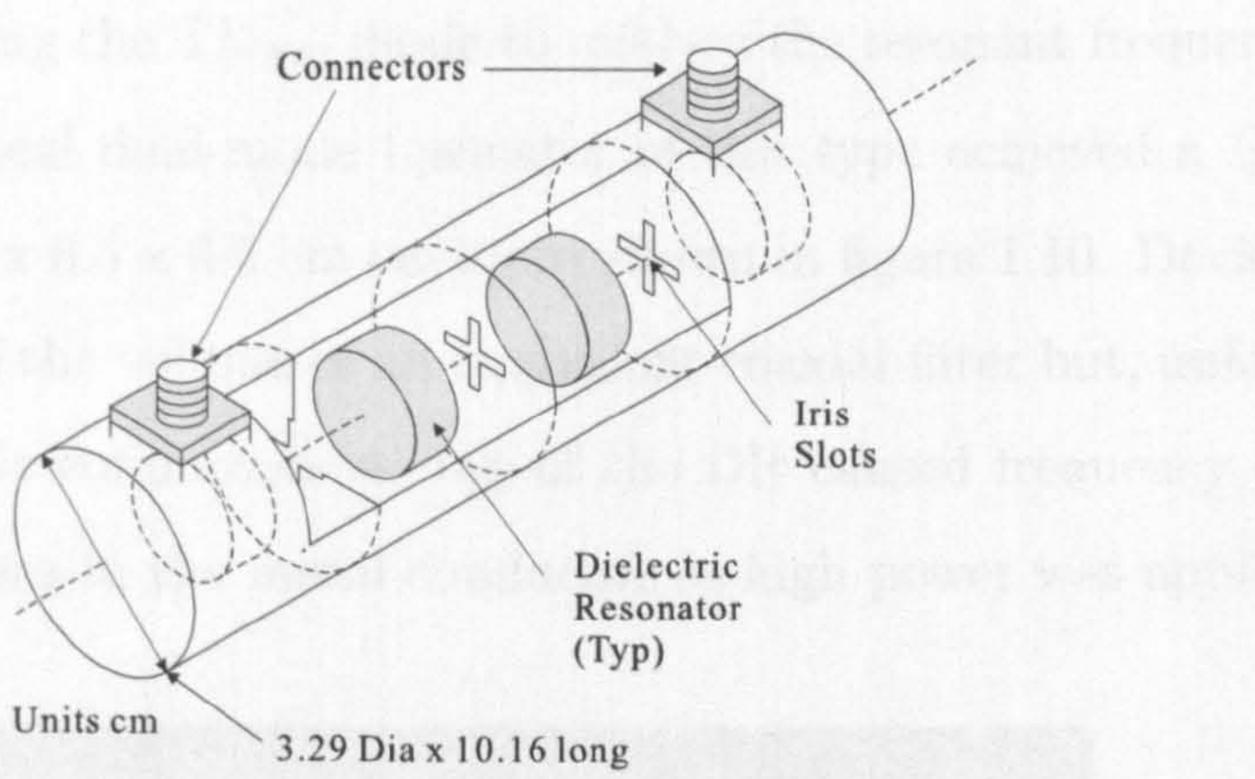

Figure 1.8: Dual-mode configuration of a DR filter, [30]

Although good size-reduction is achieved, unfortunately the $HE_{11\delta}$ mode is not the fundamental mode for this cylindrical resonator and a straight 2:1 reduction in size is not possible for the same Q. These bandpass filter devices are commonly used in mobile and satellite communications applications due to their low loss and small size compared to single-mode realisations. Subsequently, this work has since been improved upon by Zaki, [18], Kobayashi, [32], and Gendraud, [33].

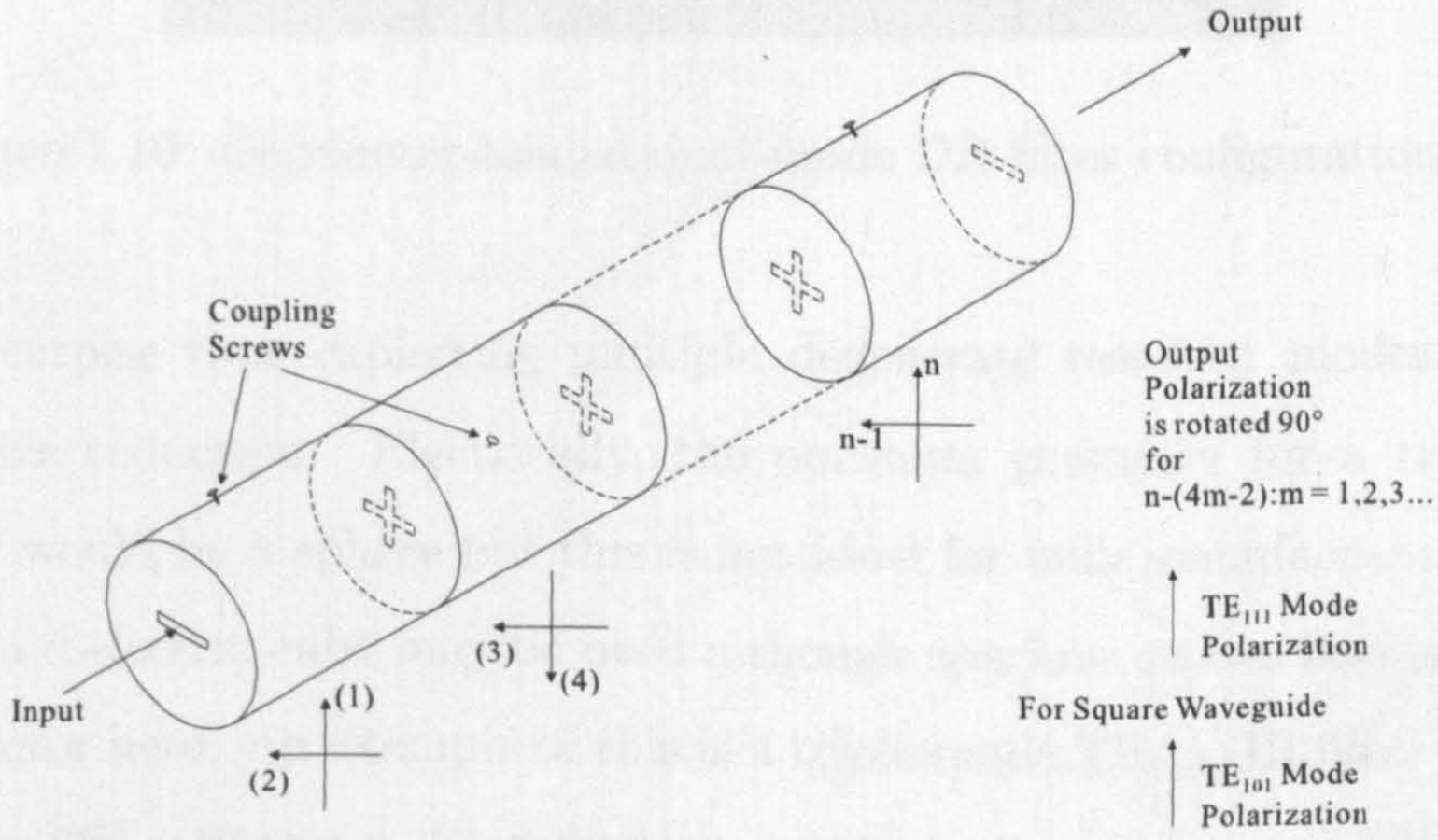

Figure 1.9: Tuning screw orientations for cross couplings in an elliptic function DR dual-mode filter, [31]

A planar modification was reported by positioning the DR on the base of the

cavity with conducting discs placed on top of each resonator, [34]. By loading the DR with conductors at both ends, tangential electric, E fields are diminished at both the top and bottom of the DR. This allowed a simple model to be used for this structure using the TM_{110} mode to analyse the resonant frequency and Q theoretically. A typical dual-mode resonator of this type achieved a Q_u of 6300 at 900 MHz in a 6.5 x 6.5 x 6.5 cm cavity as shown in figure 1.10. Devices of this type can occupy half the volume of an equivalent coaxial filter but, unfortunately placing these metallic conductors on top of the DR caused frequency drifts due to frequency variations in the metal conductor as high power was applied.

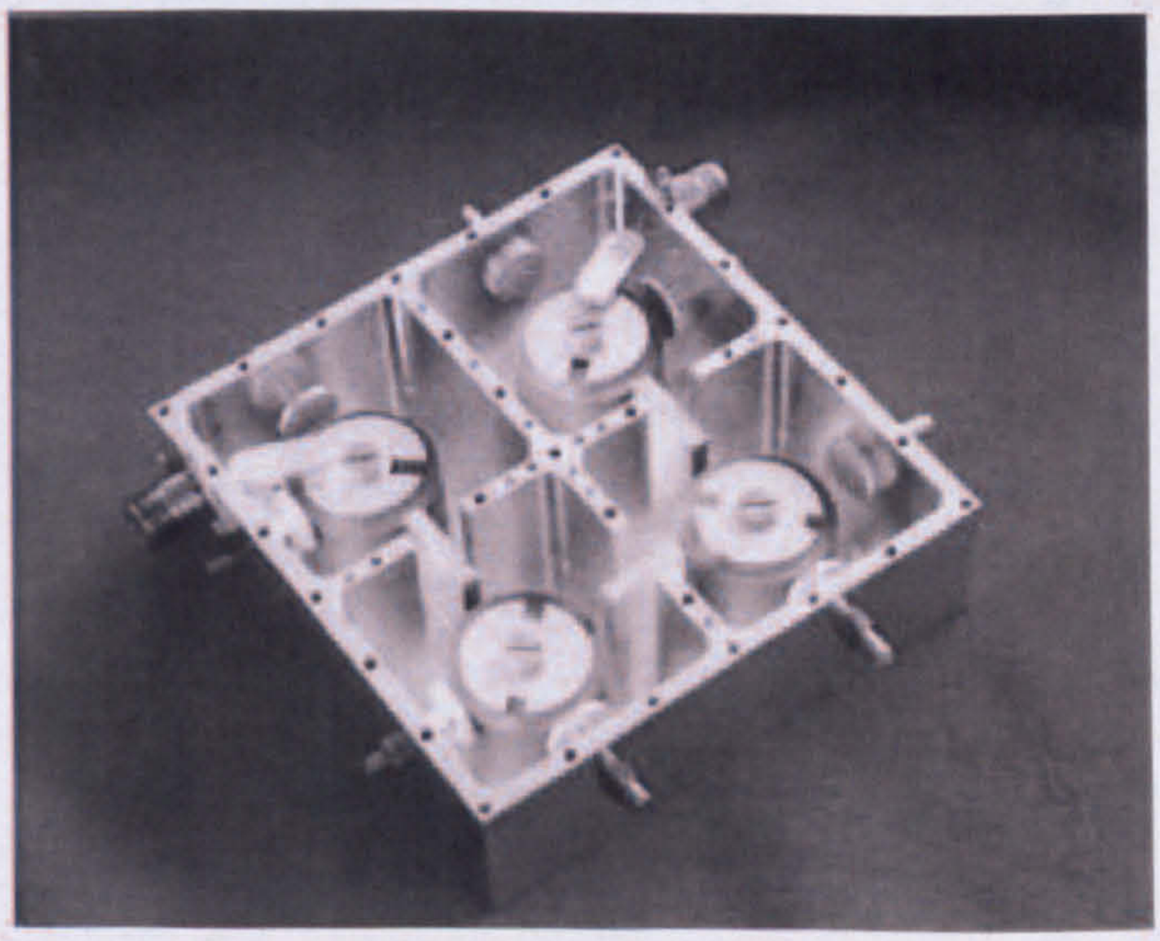

Figure 1.10: Conductor-loaded dual-mode DR filter configuration, [34]

It is no surpise that exploiting multiple degenerate resonant modes will give greater size reduction. Electrically, the optimum geometry for a triple-mode resonator would be a sphere but this is not ideal for bulk manufacture. To compromise, a dielectric cube may be used although spurious modes become a detrimental factor here. An example of this is a triple-mode $TE_{01\delta}$ DR filter operating at 2 GHz, [35], offering a 2:1 reduction in size over conventional $TE_{01\delta}$ filters. A quadruple-mode DR filter has also been realised and a 2 GHz compact filter suitable for WCDMA communication systems has been reported as shown in figure 1.11, [36].

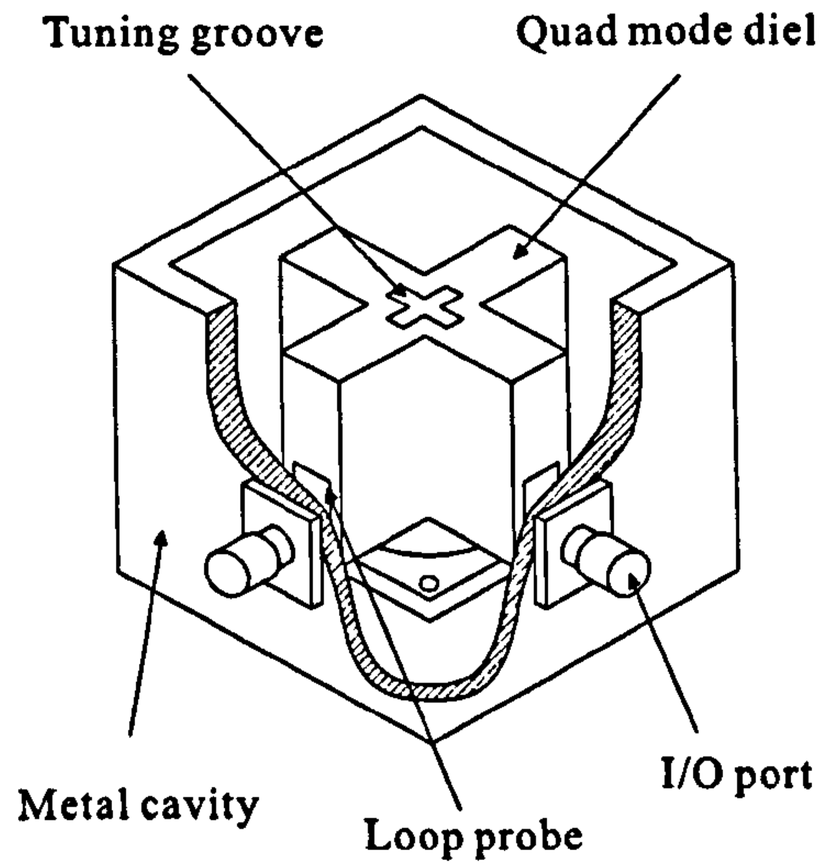

Figure 1.11: Quadruple-mode DR filter configuration, [36]

Although multimode DR filters have many advantages, they also have a major drawback in having inferior out-of-band spurious characteristics. Usually, an additional lowpass filter is needed to eliminate the unwanted modes but this increases the size, insertion loss, complexity and cost of the filter. Significant efforts has been put into improving the spurious response of DR filters, especially dual-mode filters. For example, both the $TE_{01\delta}$ mode and $HE_{11\delta}$ mode filters have very limited spurious free performance but by combining them into a mixed-mode DR filter, spurious performance can be improved. An example uses $TE_{01\delta}$ mono-mode and $HE_{11\delta}$ dual-mode DRs to produce an elliptic function filter as shown in figure 1.12, [22]. A lateral offset between the axes of the $TE_{01\delta}$ and $HE_{11\delta}$ mode cavities provides greater coupling because the magnetic field at the cavity centre is maximum for $HE_{11\delta}$ mode and minimum for $TE_{11\delta}$ mode respectively.

Unfortunately, an in-line configuration is seen as too cumbersome due to the lateral dispositions between the two cavitites accomodating the single and dual-mode resonators. A planar configuration is, therefore, much simpler to implement as shown in figure 1.13, [23]. The spurious frequencies of the two types of resonators are offset to produce a 500 MHz spurious free window, however, since the filter essentially operates under single-mode operation, the dual degenerate modes are split such that only one of the dual-modes is used adding further complexity.

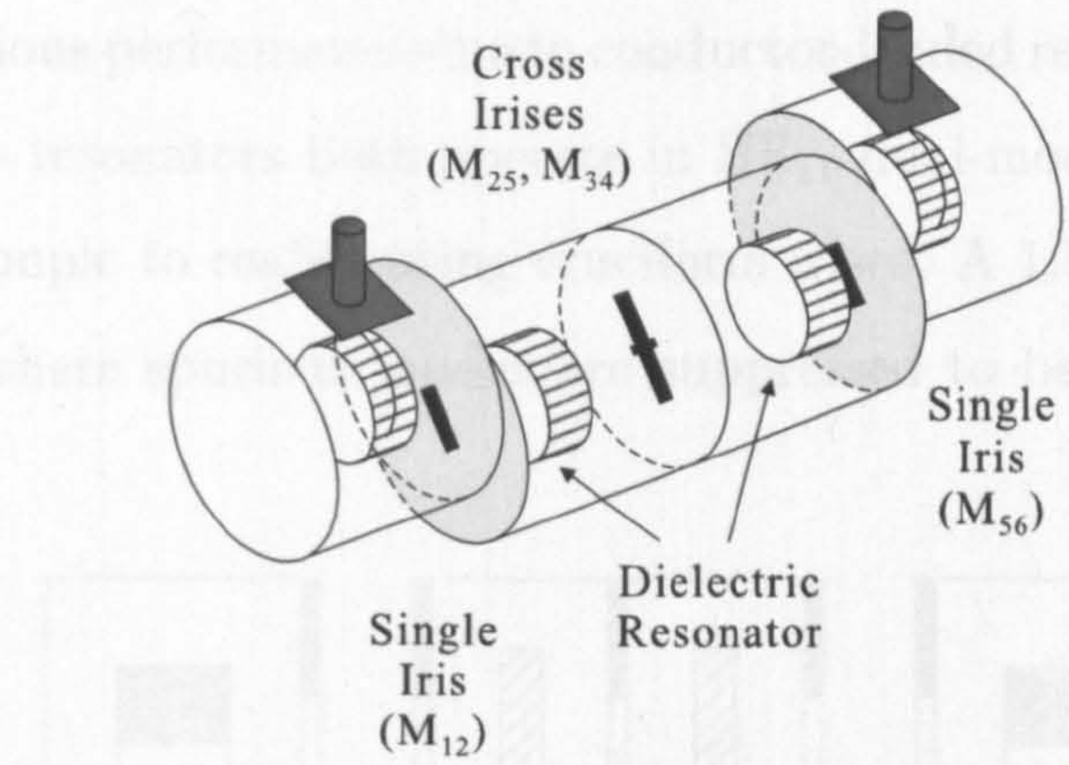

Figure 1.12: Configuration of a 6^{th} degree mixed-mode elliptic function DR filter, [22]

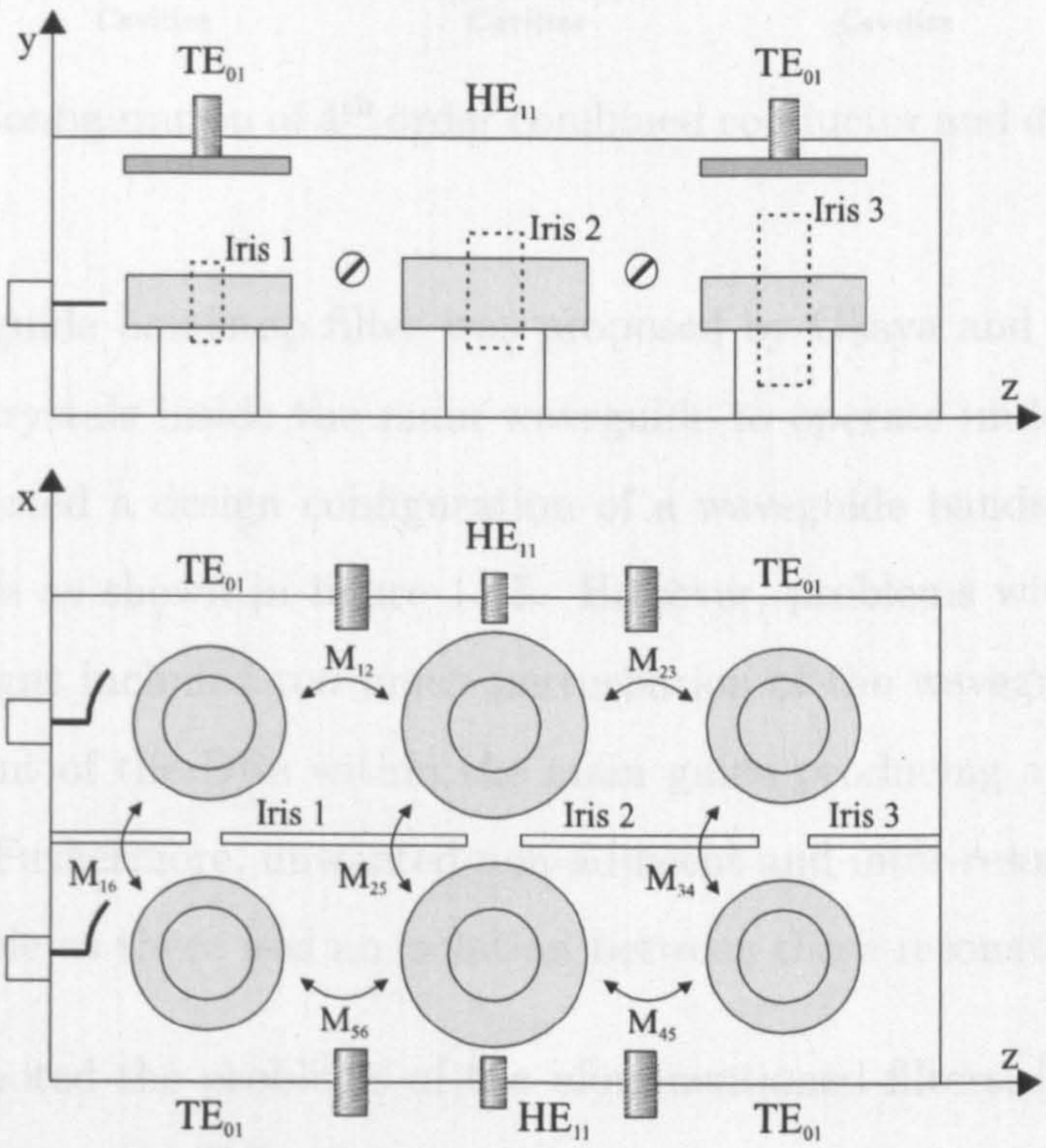

Figure 1.13: Structure of 6^{th} degree mixed-mode DR filter, [23]

Another technique to improve spurious performance is to combine different types of resonators together. One such resonator is produced on the basis that if the DR in a dual-mode filter is replaced by a perfect electric conductor, significant miniaturisation can be achieved, since the relative dielectric constant of the resonator now approaches infinity. The dielectric-loaded resonators have higher Q than conductor-loaded resonators, therefore, low loss is also achievable along with

impressive spurious performance due to conductor-loaded resonators. Another advantage is these resonators both operate in HE_{11} dual-mode so that inter-cavity couplings are simple to realise using cruciform irises. A 1.55 GHz filter is shown in figure 1.14 where spurious modes are suppressed to below -40 dB up to 2.8 GHz, [37].

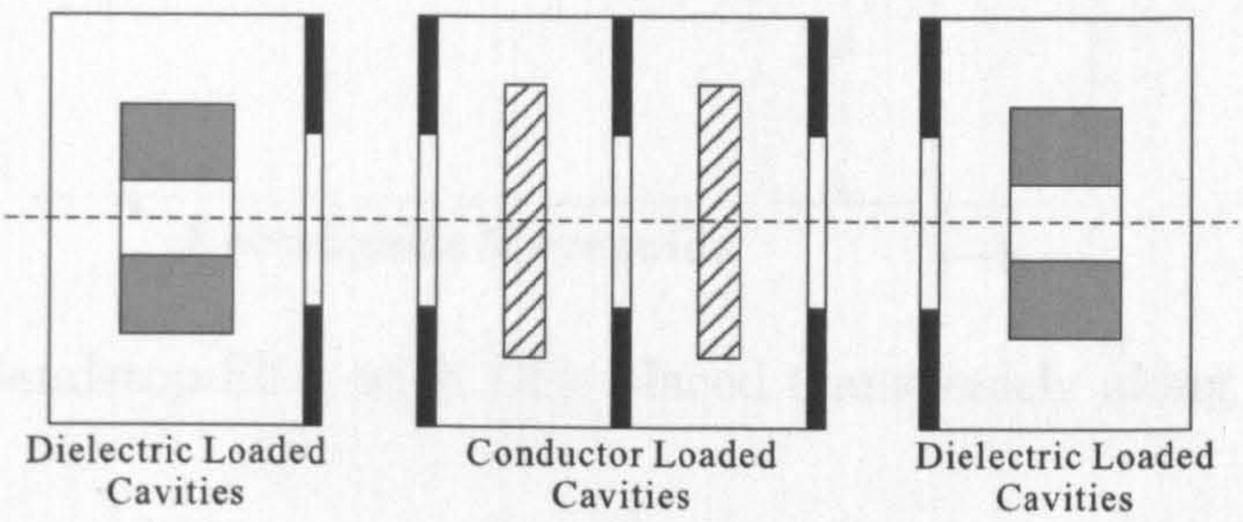

Figure 1.14: Configuration of 4^{th} order combined conductor and dielectric-loaded filter, [37]

The first waveguide bandstop filter was proposed by Okaya and Barash, [9], by placing rutile crystals inside the main waveguide to operate under $TE_{01\delta}$ mode. Cohn also reported a design configuration of a waveguide bandstop filter using TiO_2 resonators as shown in figure 1.15. However, problems with these earlier waveguide designs included too much perturbation of the waveguide modes due to the placement of the DRs within the main guide producing a poor match in the passband. Futhermore, unwanted non-adjacent and inter-resonator couplings were unavoidable as there was no isolation between these resonators.

Chung-li Ren noted the problems of the aforementioned filters, [38], and solved them by positioning the DRs outside the main waveguide. In this configuration the resonators were isolated in their own metal enclosure coupled to the main waveguide through small apertures on the waveguide walls as shown in figure 1.16. The couplings between the waveguide and resonators could now be controlled via apertures and there was now scope for independent tuning for each DR.

In all the above configurations, the placement of the resonators is seen to be cumbersome especially in providing supports for each cylindrical puck. Also, as waveguides are used as the propagation medium, a 3/4 wavelength separation is

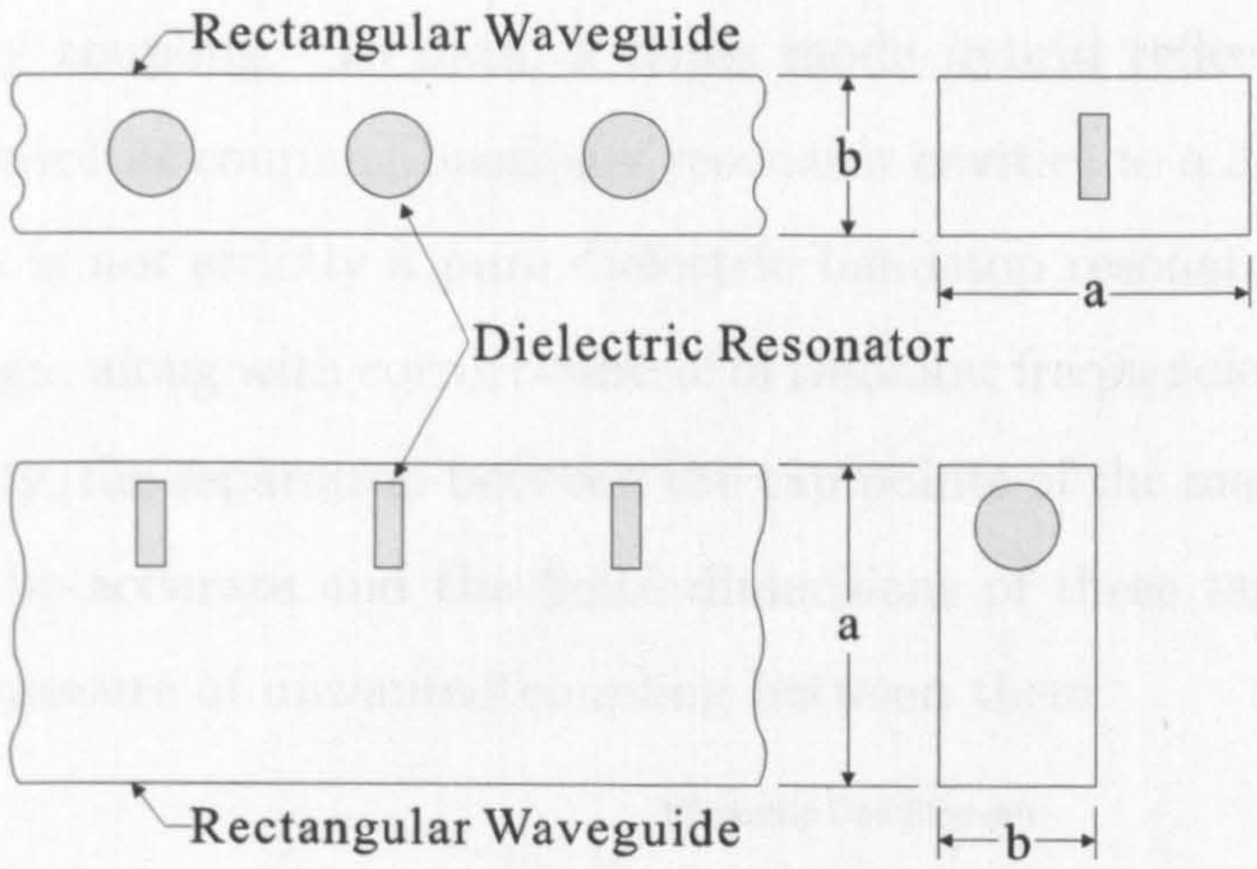

Figure 1.15: Bandstop filter with DRs placed transversely along waveguide, [38]

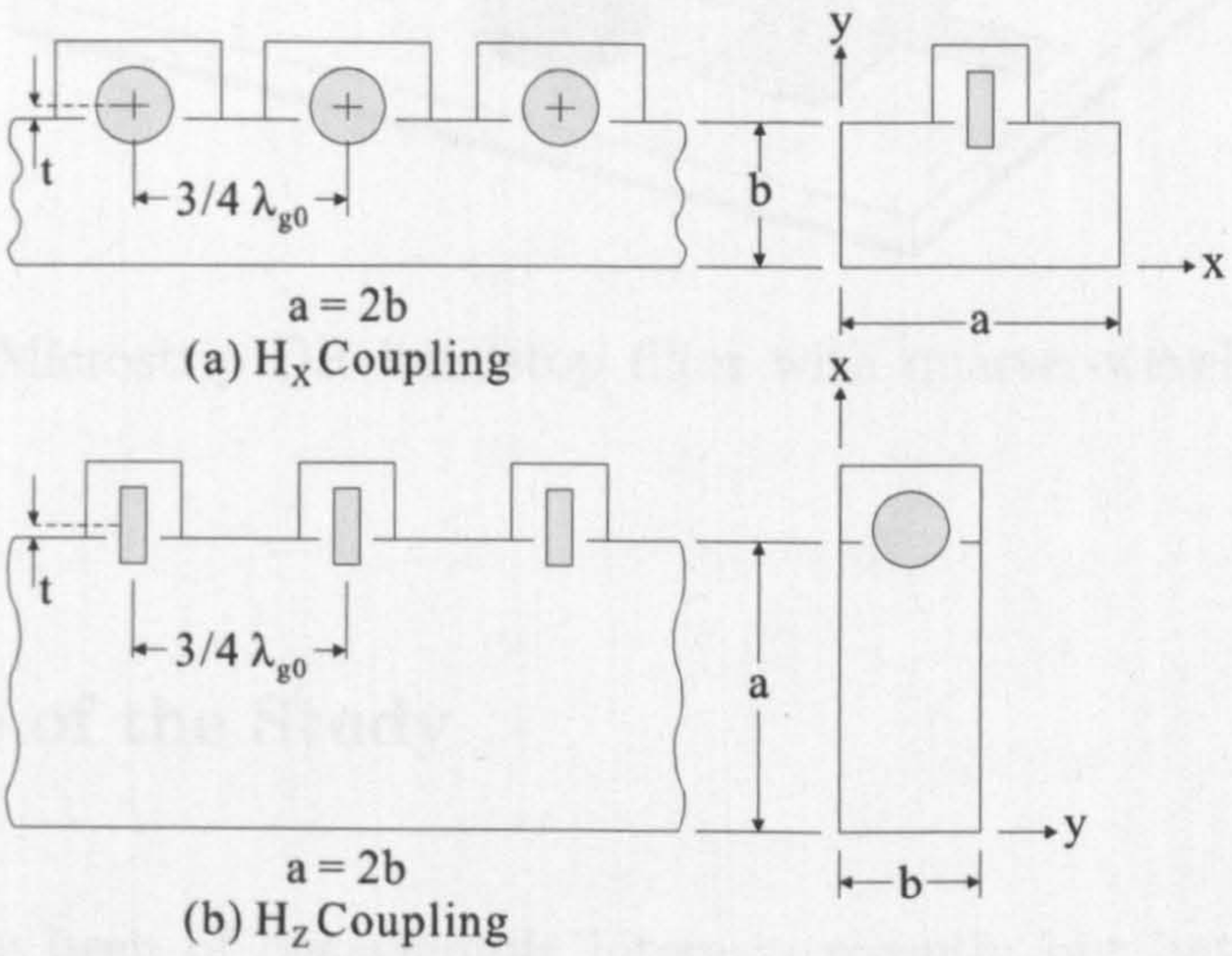

Figure 1.16: Bandstop filter with DRs placed outside waveguide, [38]

needed between each resonator to avoid excessive fringing field coupling between resonators leading to a degradation in the response in the above topologies. For TEM lines, such as coaxial or microstrip, only 1/4 wavelength separations are needed producing more compact structures shown in figure 1.17, [26]. These designs have shown how cumbersome the fabrication process can be to provide the correct resonant frequency, coupling and phase separation between each resonator. It is, therefore, not surprising that there has been very few bandstop filter designs involving higher order modes where the coupling scheme involves a large number of tuning elements for independent control of each degenerate modes, intra-cavity

and inter-cavity coupling. To date, a triple mode hybrid reflection mode was described but involves coupling bandpass resonator cavities to a 3 dB quadrature hybrid, thus, it is not strictly a pure dielectric bandstop resonator. To realise a dual-mode design, along with correct control of resonant frequencies and couplings within the cavity, the separation between the tap points of the main transmission line must also be accurate and the finite dimensions of these tap elements will provide some measure of unwanted coupling between them.

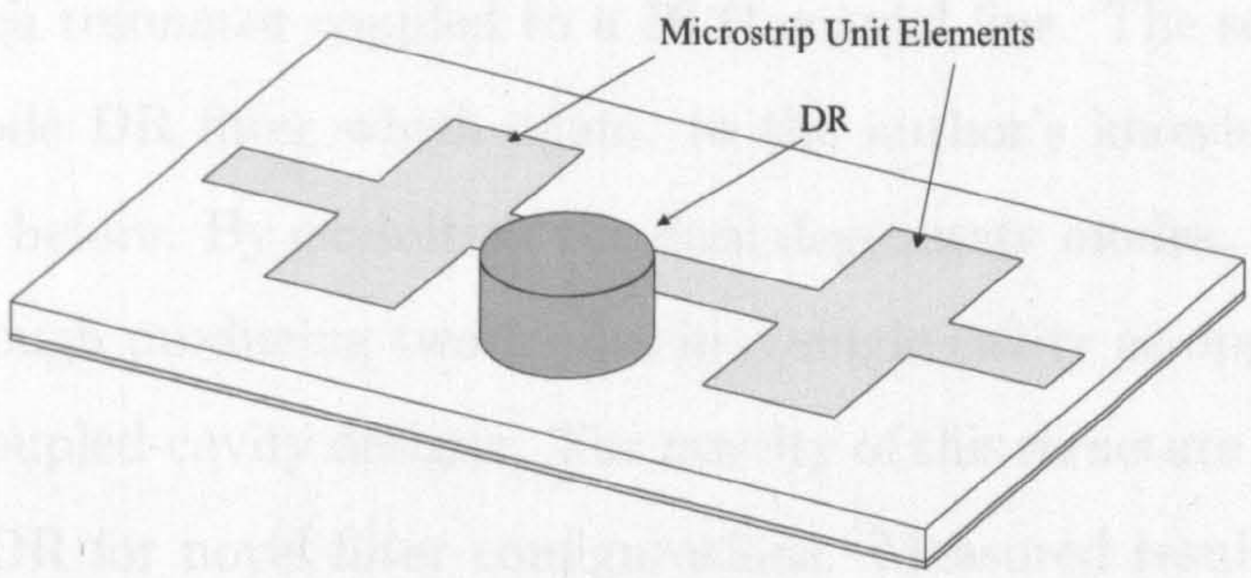

Figure 1.17: Microstrip DR bandstop filter with quarter-wavelength unit elements

1.3 Scope of the Study

DR filters have been of considerable interests recently but have only evolved around bandpass filters. There is little published material on DR bandstop filters, thus, the proposal for this work was to develop and realise practical bandstop filters using high permittivity dielectric materials to miniaturise conventional air-cavity resonators in microwave bandstop filters. Note that the development of novel filter prototypes is out of the scope of this thesis, therefore, classical Chebyshev, inverse Chebyshev approximations and direct-coupled configurations were used for the design process. The majority of the research work centred around the factors in the physical realisations using 3D HFSS simulations. Firstly, a mono-mode design has been incorporated using dielectric-loaded rectangular waveguides. To the author's knowledge, previously only cylindrical pucks have been coupled to transmission lines forming a bandstop filter. In using the properties

of a dielectric-loaded waveguide resonator, an advantage is seen in the spurious performance as compared to an isolated dielectric resonator. Using rectangular DRs also provide ease of manufacturing compared to cylindrical resonators providing lower costs for mass manufacturing. The design is much simpler as these waveguide resonators are grounded against cavity walls, leaving only a coupling face to the transmission line and an open face for tuning. The result is no complex design is required for the dimensions of the cavity. A Chebyshev filter was designed with each resonator coupled to a 50 Ω coaxial line. The second structure uses a dual-mode DR filter which again, to the author's knowledge, has never been published before. By exploiting the dual degenerate modes, miniaturisation is achieved through producing two modes in a single cavity as opposed to monomodes in two coupled-cavity designs. The novelty of this structure is its versatility as a practical DR for novel filter configurations. Measured results produced an inverse Chebyshev response. To achieve coupling into both modes, a right-angle coaxial line was designed and the resonators were magnetically coupled through fixing small coaxial probes to metal posts in the base of the cavity. A number of HFSS simulations were performed in the design of both filters including use of the eigenmode solver and parametric analysis to achieve the required dimensions for fabrication. The final section leverages the dual-mode bandstop resonator in novel direct-coupled configurations, including a cul-de-sac form, with EM simulations demonstrating only a quarter wavelength transmission line is required to directly couple the source and load resonators to create miniaturised dielectric resonator bandstop filters.

1.4 Organisation of Thesis

Firstly, this chapter has identified the benefits of DRs and how, only in recent times, they have become popular in the microwave industry due to the availability of temperature-stable materials. Advantages over bulky waveguide and coaxial structures have been discussed. The benefits in using higher-order modes includ-

ing recent DR filter designs has also been described and this allows a substantial reduction in volumes of cavity filters.

In Chapter 2, a review is presented of filter designs stating the stages from the initial prototype to the transformed circuit model. Also included is an advanced synthesis technique using a coupling matrix to generate generalised Chebyshev polynomials to design direct-coupled bandstop filters. Note that physical realisations are not discussed here.

Chapter 3 reviews the properties of DRs and how they are designed using a variety of methods from simple models to more rigorous numerical models. Couplings between these DRs and different transmission lines is also discussed.

Chapter 4 covers the design of a $TE_{10\delta}$ mode compact DR bandstop filter. First, a rectangular waveguide is analysed before the concept of dielectric-loading is introduced and the effects on its Q factor are considered. A bandstop filter is designed based on the Chebyshev characteristic. Simulated and measured results for a 4^{th} degree bandstop filter are shown with shortcomings in the fabrication discussed. At the end of this chapter a novel wideband dielectric-loaded coaxial resonator is introduced.

In Chapter 5, a novel HEE_{11} dual-mode dielectric bandstop resonator is analysed and an experimental cavity is developed with discussions on problems faced in the design process. A dual-cavity 4^{th} degree bandstop filter is designed and measured. The direct-coupled bandstop resonator is discussed showing how the dual-mode bandstop resonator compliments the synthesised coupling matrices for the original and cul-de-sac forms.

Lastly, Chapter 6 summarises the fundamental aspects of this thesis, along with advantages and shortcomings for both filters. Improvements are also discussed.

Chapter 2

Filter Design

2.1 Introduction

Microwave filters are important to extract the desired frequency spectrum from a wide variety of electrical signals. This chapter describes basic concepts and theories of microwave and RF filters and their design considerations, [39]. Generally, an ideal filter has a brick-wall transfer response with instantaneous transition bands and constant group delay in the passband but this is impractical due to finite-order limitations of lossy practical filters. To realise the filter function required, the transfer and reflection polynomials for a lowpass prototype must be established. It is seen later that a lowpass prototype can be translated to a highpass, bandpass or bandstop response as required and the synthesis of a prototype circuit will lead to the eventual physical implementation in transmission line, waveguide, printed circuit or other media filters. The design procedure follows from the required specifications outlining the required transfer function, return loss, degree of filter and location, if required, of transmission zeros to form the ideal characteristics of the filter polynomials. The recursive technique was first introduced to calculate these polynomials for symmetrical and asymmetrical performance, [40]. The polynomials may then be translated into a prototype network either through the circuit synthesis, [41], or the direct coupling matrix approach, [42]. An advantage of the latter is the coupling matrix may be trans-

formed to suit the physical couplings required in the physical implementation, [43] and [44]. This is the case for dual-mode designs where the matrix can be arranged to form the necessary coupling paths. The prototype network may then be realised by a physical resonator using 3D electromagnetic, EM, simulations as a guide to achieve the correct dimensions for the entire filter. Tuning methods are also implemented to compensate for any discrepencies between the simulated and fabricated designs taking into account manufacturing errors. The theory behind much of these techniques is out of the scope of this thesis but may be found in [45].

2.2 Types of Filters

Filters can be classified as one of lowpass, highpass, bandpass or bandstop, [46]. The first is a filter permitting low frequencies and rejecting frequencies higher than the rated cutoff frequency and the highpass performs the opposite function. Bandpass and bandstop combine lowpass and highpass filters to select interested bandwidths and reject others. The lowpass prototype is defined as a two-port lumped-element operating in a 1 Ω system with angular cutoff frequency of 1 rad/s, $\omega = 1$. In addition, it is passive and reciprocal. These responses can be analysed by the synthesis of ladder networks, of which the simplest is Cauer's form consisting of series inductors and shunt capacitors as shown in figure 2.1.

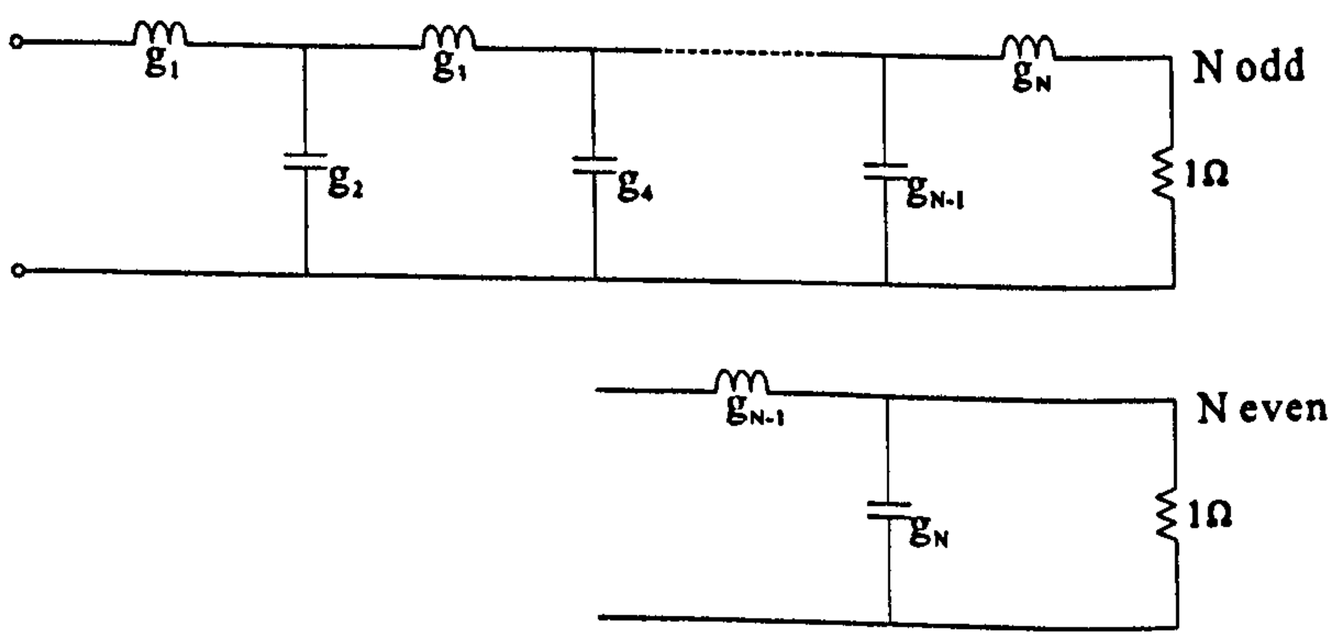

Figure 2.1: Lowpass prototype ladder filter networks

An alternative transformation technique, [47], compliments inverters with reactive

elements in a lowpass ladder network where the inverters are coupled with series inductors or shunt capacitors, figure 2.3. This process provides a good approximation for narrow bandwidths upto 20% depending on the physical realisation. An inverter, shown in figure 2.2, is a frequency independent two-port network where the relationship between the input impedance, Z_{in} and load impedance, Z_L, is defined by

$$Z_{in} = \frac{K^2}{Z_L} \tag{2.1}$$

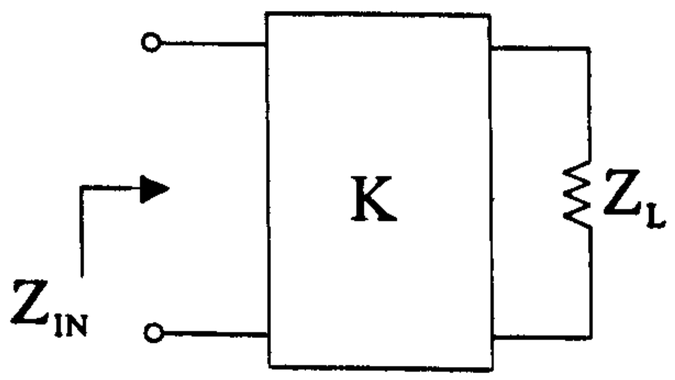

Figure 2.2: Impedance inverter terminated in a load

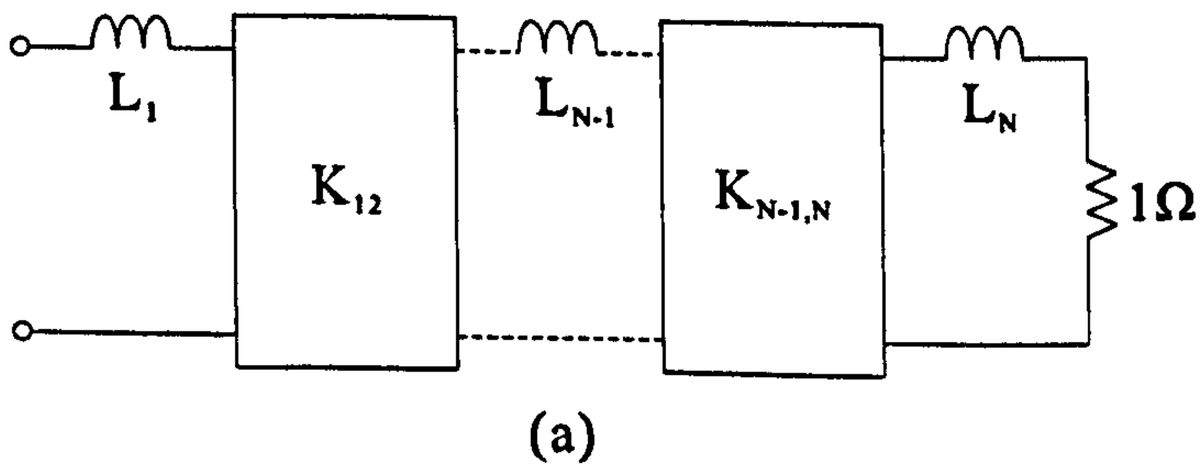

Figure 2.3: General N^{th} degree inverter coupled lowpass prototype with (a) inductors (b) capacitors

2.3 Impedance Transformations

For impedance transformation, the 1 Ω impedance of the prototype is converted to an impedance level of Z_0 by scaling all the reactive elements in the filter by Z_0 using the following transformations

$$\begin{aligned} L &\rightarrow Z_0 L \\ C &\rightarrow \frac{C}{Z_0} \\ K &\rightarrow Z_0 K \end{aligned} \tag{2.2}$$

2.4 Lowpass to Bandstop Transformation

Bandstop configuration allows power to pass through the resonator at frequencies outside resonance but power is absorbed from the coupled line at resonance increasing the effective impedance of the resonator leading to more reflections. The transformation from the lowpass prototype to a bandstop filter with arbitrary centre frequency and bandwidth can be performed where the transmission zeros at infinity for the lowpass prototype is mapped to ω_0. The response is shown in figure 2.4 and the transformation is set out below.

$$\omega \rightarrow \frac{-1}{\alpha\left(\frac{\omega}{\omega_0} - \frac{\omega_0}{\omega}\right)} \tag{2.3}$$

where,

$$\omega_0 = (\omega_1 \omega_2)^{1/2} \tag{2.4}$$

and the bandwidth scaling factor, α is given by,

$$\alpha = \frac{\omega_0}{\omega_2 - \omega_1} = \frac{\omega_0}{\Delta\omega} \tag{2.5}$$

when ω_1 and ω_2 are the band edge frequencies.

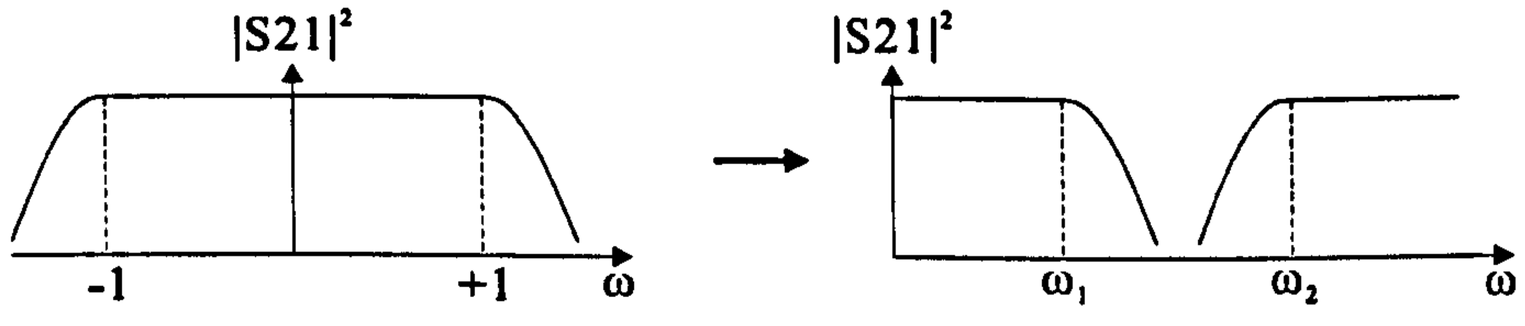

Figure 2.4: Lowpass to bandstop transformation

Applying this transformation leads to the transformation of elements as shown in figure 2.5.

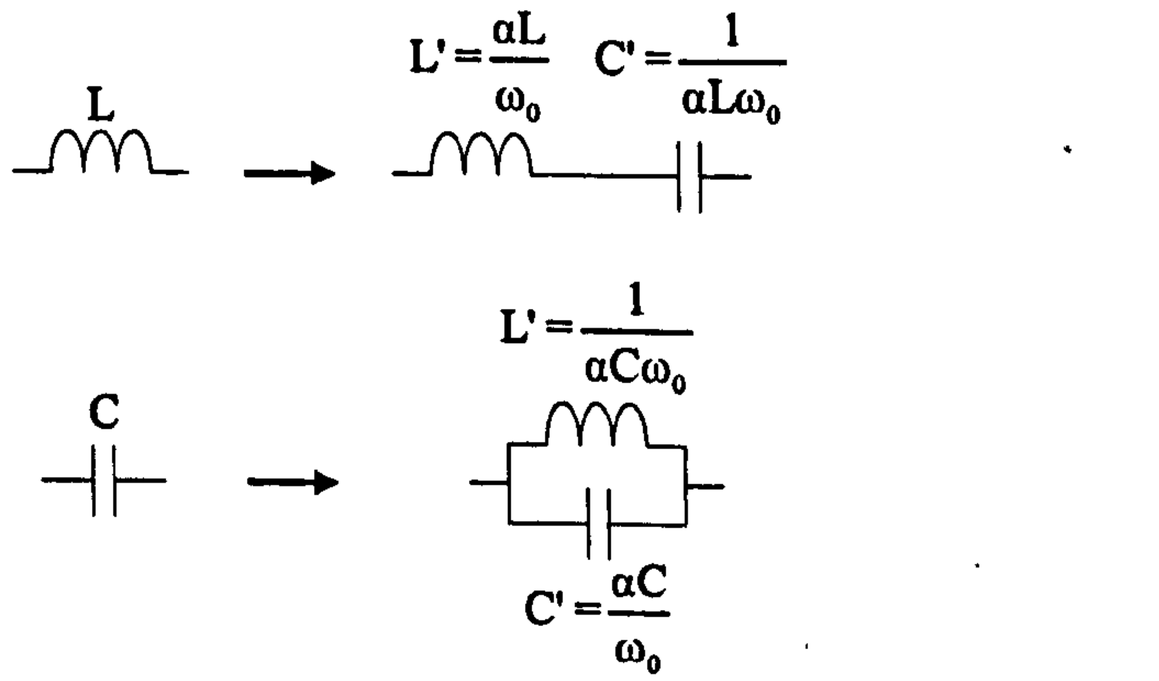

Figure 2.5: Bandstop transformation of an inductor and capacitor

2.5 Transfer Functions

The transfer function of a two-port network can be written as:

$$|S_{21}(j\omega)|^2 = \frac{1}{1+\varepsilon^2 {F_n}^2(\omega)} \tag{2.6}$$

where ε is a ripple constant, $F_n(\omega)$ represents a filtering or characteristic function and ω is a frequency variable. For the transfer function in equation 2.6, the insertion loss response of the filter can be solved using:

$$L_A(\omega) = 10\log\frac{1}{|S_{21}(j\omega)|^2}\ \text{dB} \tag{2.7}$$

Since $|S_{11}(j\omega)|^2 + |S_{21}(j\omega)|^2 = 1$ for a lossless, passive two-port network, the return loss of the filter is

$$L_R(\omega) = 10\log(1 - |S_{21}(j\omega)|^2) \text{ dB} \tag{2.8}$$

2.5.1 Butterworth or Maximally Flat Approximation

The butterworth response is the simplest approximation to an ideal low pass filter. The response is flat at d.c. and rolls off to 3 dB at $\omega = 1$ before flattening out again at infinity as shown in figure 2.6.

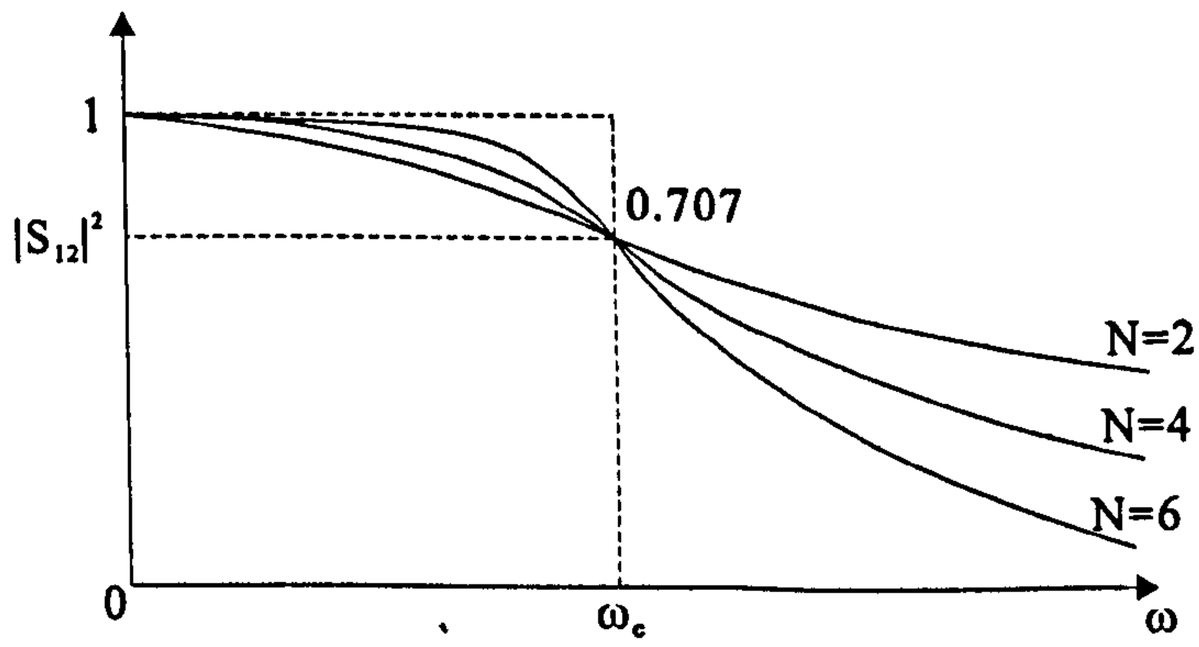

Figure 2.6: Frequency response of butterworth lowpass filter for varying N

The transfer function describing this response is given by:

$$|S_{21}(j\omega)|^2 = \frac{1}{1+\omega^{2N}} \tag{2.9}$$

and the insertion loss is

$$L_A(\omega) = 10\log(1+\omega^{2N}) \text{ dB} \tag{2.10}$$

where N is the degree of the network.

Design formulae for both lowpass prototypes for a general Nth degree with inverters separated by inductors or capacitors, shown in figures 2.3 (a) and (b) respectively, are given for the element values, G_r, below.

$$G_r = L_r \text{ or } C_r = 2\sin\left[\frac{(2_r - 1)\pi}{2N}\right] \quad (r = 1, ..., N) \tag{2.11}$$

$$K_{r,r+1} = 1 \quad (r = 1, ..., N-1) \tag{2.12}$$

2.5.2 Chebyshev Approximation

A better approximation than the maximally flat to the ideal transfer function is one containing a rippled response in the passband region. The response of a Chebyshev approximation is shown in figure 2.7 and the insertion loss at the ripple level is defined by

$$L_A = 10\log(1 + \omega^2 T_N^2(\omega)) \tag{2.13}$$

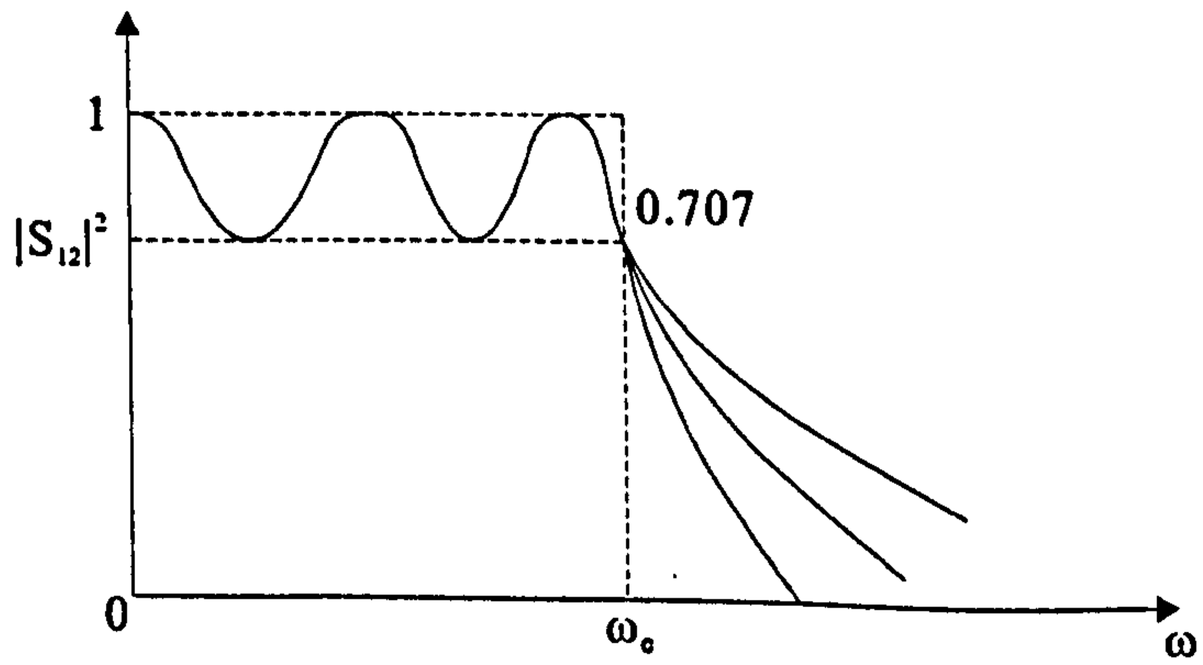

Figure 2.7: Frequency response of a Chebyshev lowpass filter

An expression for the transfer function of this response is given by

$$|S_{21}(j\omega)|^2 = \frac{1}{1 + \varepsilon^2 T_N^2(\omega)} \tag{2.14}$$

where the ripple level, ε, controls the ripple in the passband and is defined as

$$\varepsilon = (10^{L_R/10} - 1)^{-1/2} \tag{2.15}$$

where T_N is the N^{th} order Chebyshev polynomial and $\varepsilon < 1$ is a real constant. These polynomials are defined in terms of a real variable ω as

$$T_N(\omega) = \cos[N \cos^{-1}(\omega)] \tag{2.16}$$

Element values, in terms of η, are given below and can be applied to either of the N^{th} degree lowpass prototypes as for the butterworth design.

$$K_{R,R+1} = \frac{[\eta^2 + \sin^2(r\pi/N)]}{\eta} \quad r = 1, ..., N-1 \tag{2.17}$$

where $K_{R,R+1}$ is the impedance of the inverters.

$$L_r = \frac{2}{\eta} \sin\left[\frac{(2r-1)\pi}{2N}\right] \quad r = 1, ..., N \tag{2.18}$$

where

$$\eta = \sinh\left[\frac{1}{N} \sinh^{-1}\left(\frac{1}{\varepsilon}\right)\right] \tag{2.19}$$

2.5.3 Inverse Chebyshev Response

This approximation is the inverse of the normal Chebyshev in that it is maximally flat in the passband but is equiripple in the stopband as shown in figure 2.8. This function is used in applications where a non-infinite stopband attenuation is tolerated and a symmetrical stopband can be achieved by controlling the ripples in the stopband using zeros in a low pass transfer function.

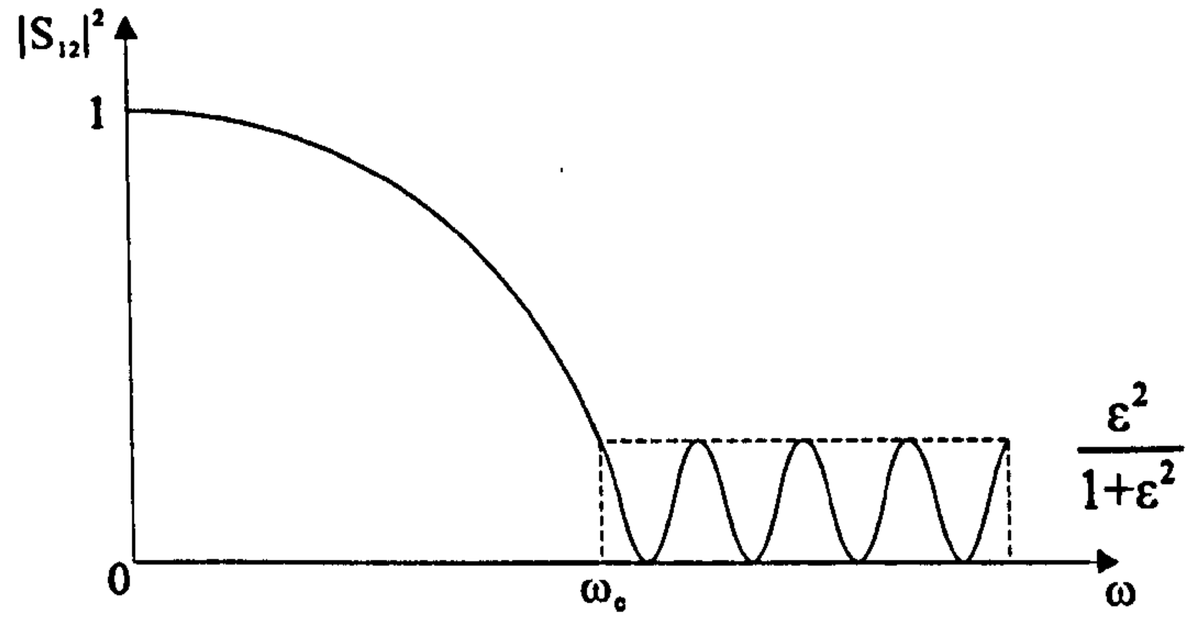

Figure 2.8: Frequency response of an inverse Chebyshev filter

The transfer function is defined as

$$|S_{21}(j\omega)|^2 = \frac{1}{1 + \dfrac{1}{\varepsilon^2 T_N^2(1/\omega)}} \tag{2.20}$$

and

$$L_A \approx 20 \log \frac{1}{\varepsilon} \tag{2.21}$$

A highpass prototype is shown in figure 2.9, [41], and the element values are calculated using

$$C_r = \frac{1}{2\eta \sin[(2r-1)\pi/2N]} \tag{2.22}$$

$$B_r = Cr \cos\left[\frac{(2r-1)\pi}{2N}\right] \tag{2.23}$$

$$K_{r,r+1} = 1 \tag{2.24}$$

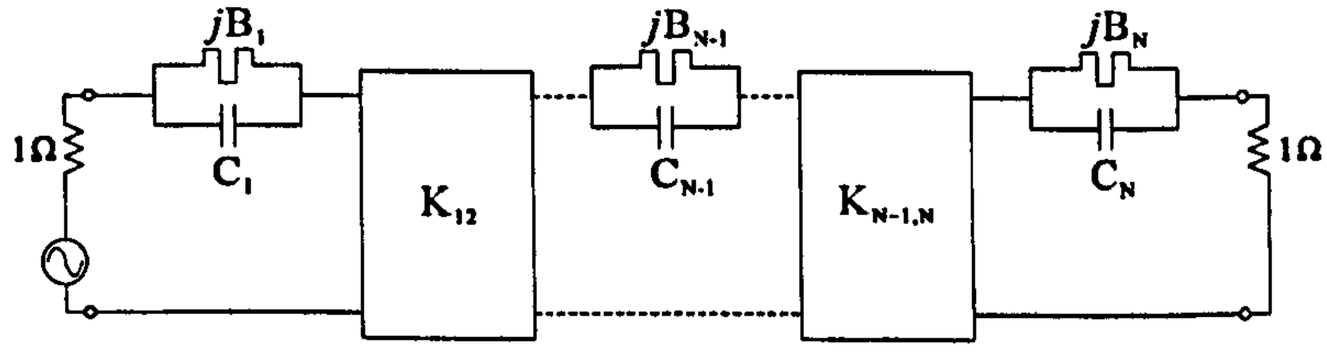

Figure 2.9: Highpass prototype for inverse Chebyshev filter

2.5.4 Generalised Chebyshev Response

It is possible to realise a polynomial function using extra resonators with non-adjacent cross couplings. The response of elliptic filters has rippled approximations in both the amplitude of the passband and stopband regions. This provides much more selective attenuation slopes as compared to any other filter of equal degree. The frequency response is as shown in figure 2.10 with finite-frequency transmission zeros present in the stopband.

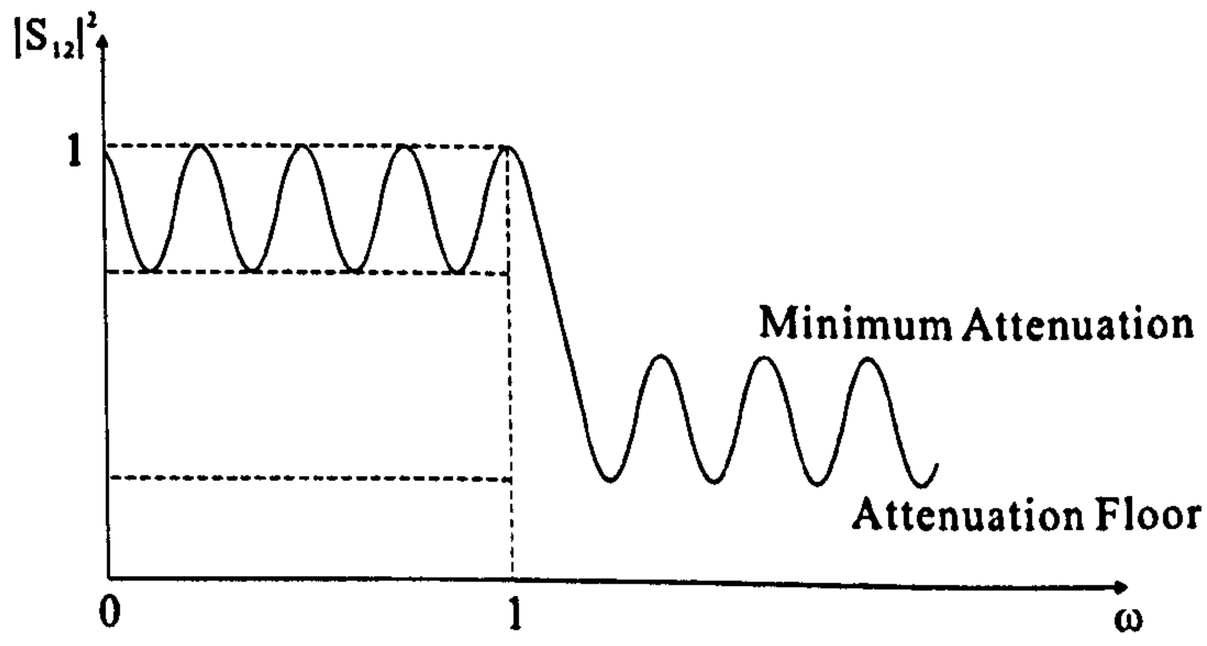

Figure 2.10: Frequency response of an elliptic lowpass filter

Unfortunately, a disadvantage of this response is transmission zeros are prescribed at certain frequencies. Thus, the basic Chebyshev polynomial is considered too simple for advanced filter designs. The generalised Chebyshev transfer response for a lowpass prototype is,

$$|S_{21}(j\omega)|^2 = \frac{1}{1+\varepsilon^2 F_N^2(\omega)} \tag{2.25}$$

with -1 < $F_N(\omega)$ < +1 for -1 < ω < +1

and $F_N(\omega_r)$ for r = 1,...,N

where ω_r is the frequency of the r^{th} transmission zero.

The cross couplings can be made in an inverter-coupled network where additional negative, capacitive, or positive, inductive, couplings add transmission zeros or poles to ther response. Adding real transmission zeros in the frequency doman can increase selectivity. The design for such a filter can be approached through the addition of cross-couplings to a Chebyshev prototype, performing an analysis and optimisation program to achieve the response. This technique is suitable for basic structures but for more complex designs requiring asymmetric or multiple pairs of transmission zeros, a further technique is required.

2.6 Direct-Coupled Bandstop Filters

In conventional Chebyshev bandstop filter designs, each resonant element is coupled at odd multiples of $\lambda/4$ to a main transmission line. An advanced approach can reduce the number of couplings between transmission line and resonant cavities dramatically, therefore, wideband performance is potentially better. Since the resonant frequencies are tuned within the stopband, the main signal need only travel through the input and output tap points, bypassing direct-coupled resonators to give high power handling and minimum insertion loss.

The technique stems from generating transfer polynomials and solving for the filter function as described in [40] following the Darlington synthesis procedure and revolves around the coupling matrix model, [31] and [42]. This can be applied to the asymmetric case and to singly and doubly terminated networks. That is, the method produces filter networks for any type of filter function including:

1. Even and odd degree
2. Prescribed transmission zeros
3. Asymmetric or symmetric characteristics

4. Singly or doubly terminated networks

An example of the 4th degree N+2 coupling matrix with all possible cross-couplings is shown in figures 2.11 and 2.12, [45]. The core 4x4 matrix describes the adjacent couplings between resonators and the whole matrix is symmetrical around the diagonal axis. From this matrix it is possible to calculate the element values in the circuit network using equations described in [47].

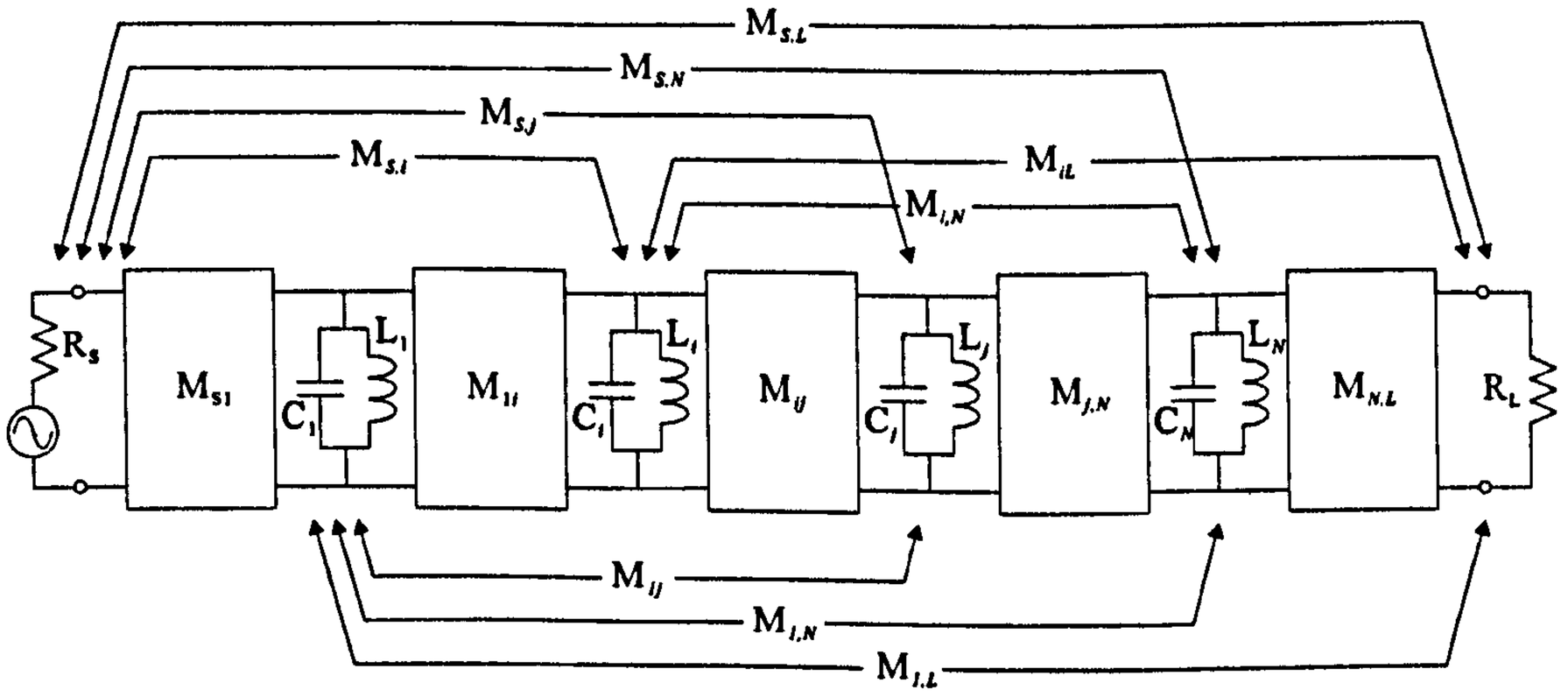

Figure 2.11: N+2 multicoupled resonator circuit

	S	*1*	*2*	*3*	*4*	*L*
S	M_{SS}	M_{S1}	M_{S2}	M_{S3}	M_{S4}	M_{SL}
1	M_{S1}	M_{11}	M_{12}	M_{13}	M_{14}	M_{1L}
2	M_{S2}	M_{12}	M_{22}	M_{23}	M_{24}	M_{2L}
3	M_{S3}	M_{13}	M_{23}	M_{33}	M_{34}	M_{3L}
4	M_{S4}	M_{14}	M_{24}	M_{34}	M_{44}	M_{4L}
L	M_{SL}	M_{1L}	M_{2L}	M_{3L}	M_{4L}	M_{LL}

Figure 2.12: 4th degree N+2 coupling matrix with all possible cross-couplings. Core NxN matrix within double lines

To generate the exact solution for the filter element values given a set of initial parameters, three essential steps are required:

1. Network synthesis
2. Generation of coupling matrix for N^{th} degree network
3. Reduction of matrix to represent realisable coupling elements

The network synthesis begins from first considering a lossless two-port network and defining the transfer and reflection functions as the ratio of two N^{th} degree polynomials, [45],

$$S_{11}(s) = \frac{F(s)/\varepsilon_R}{E(s)}, \quad S_{21}(s) = \frac{P(s)}{\varepsilon E(s)} \tag{2.26}$$

where ε is the passband equiripple from equation 2.19 and ε_R is unity for general cases except for canonical functions where all transmission zeros are prescribed at finite frequencies and ε_R is given as,

$$\varepsilon_R = \frac{\varepsilon}{\sqrt{\varepsilon^2 - 1}} \tag{2.27}$$

To develop the bandstop characteristic, the reflection and transfer coefficients and constants are exchanged to become,

$$S_{11}(s) = \frac{P(s)/\varepsilon}{E(s)}, \quad S_{21}(s) = \frac{F(s)}{\varepsilon_R E(s)} \tag{2.28}$$

The shared common denominator of both functions preserve the unitary condition for a passive lossless network,

$$S_{11}{}^2 + S_{21}{}^2 = 1 \tag{2.29}$$

In effect, with respect to a Chebyshev characteristic, the original equiripple return loss is now transformed to the transfer response and the minimum rejection level

is now equivalent to the original return loss level. As the degree for top and bottom of S_{21} are now equal, the synthesized network is now canonical, thus, the new numerator of S_{11} is the original transfer function polynomial and can realise any number of prescribed transmission zeros provided this figure is equal or less than the N^{th} degree. Note that $\varepsilon_R = 1$ for the number of zeros less than the degree. To form the polynomials for a bandstop filter, $P(s)/\varepsilon$ and $F(s)/\varepsilon_R$ are exchanged in the process to calculate the polynomials for a lowpass prototype, outlined below as described in [40].

For a lossless network,

$$S_{21}(\omega)^2 = \frac{1}{1+\varepsilon^2 C_N{}^2(\omega)} = \frac{1}{\left(1+j\frac{\varepsilon}{\varepsilon_R}C_N(\omega)\right)\left(1-j\frac{\varepsilon}{\varepsilon_R}C_N(\omega)\right)} \tag{2.30}$$

where

$$C_N(\omega) = \frac{F\omega}{P\omega}$$

To generate the polynomials and location of transmission zeros, the recursive technique is performed on the derived equation 2.31 for the general Chebyshev characteristic through mathematical techniques described in [45].

$$C_N(\omega) = \frac{1}{2}\left[\frac{\Pi_{n=1}^{N}[(\omega - 1/\omega_n) + \sqrt{(1-1/\omega_n^2)}\omega'] + \Pi_{n=1}^{N}[(\omega - 1/\omega_n) - \sqrt{(1-1/\omega_n^2)}\omega']}{\Pi_{n=1}^{N}(1-\omega/\omega_n)}\right] \tag{2.31}$$

where $\omega' = (\omega^2 - 1)^{1/2}$ and ω_n are the prescribed transmission zeros. These must be symmetrical about the imaginary axis of the s-plane for $F(\omega)$ and $P(\omega)$ to be purely real and the number of zeros must be of order no greater than N-2 to implement the physical filter. The polynomial, $C_N(\omega)$, is of N^{th} degree and the remaining zeros must be placed at infinity. The recursive technique is performed from n = 1 to the N^{th} degree to yield the polynomials for $F(\omega)$. $P_N(\omega)$ may now

be derived as the denominator of $C_N(\omega)$,

$$P_N(\omega) = \Pi_{n=1}^{N} \left[1 - \frac{\omega}{\omega_n}\right] \tag{2.32}$$

The next polynomial $E(\omega)$ is more complex and requires the Hurwitz polynomial condition that all roots have negative real parts in the s-plane so that they are now located on the left hand side of the imaginary axis. The complex polynomial $P(\omega)/\varepsilon - jF(\omega)/\varepsilon_R$ is formed and the roots are found positioned alternately and symmetrically on the top and bottom of the ω plane. The conjugate of a root is taken through multiplying by j and $E(\omega)$ may now be obtained. The coupling matrix may now be synthesised from finding the admittance parameters, $y_{21}(s)$ and $y_{21}(s)$, for a two-port short-circuit network. As an example, for an even network with 1 Ω source and load impedances,

$$y_{21}(s) = \frac{y_{21n}(s)}{y_d(s)} = \frac{(F(s)/\varepsilon_R)}{m_1(s)} \tag{2.33}$$

$$y_{22}(s) = \frac{y_{22n}(s)}{y_d(s)} = \frac{n_1(s)}{m_1(s)} \tag{2.34}$$

where

$$m_1(s) = Re(e_0 + p_0) + jIm(e_1 + p_1)s + Re(e_2 + p_2)s^2 + \cdots$$

$$n_1(s) = jIm(e_0 + p_0) + Re(e_1 + p_1)s + jIm(e_2 + p_2)s^2 + \cdots$$

and e_i and p_i, i = 0,1,2,3,...,N, are the complex coefficients of E(s) and P(s)/ε respectively. The coupling matrix is synthesised with one noticeable exception since $S_{21}(s)$ is now fully canonical, the direct source-load coupling M_{SL} is calculated from,

$$jM_{SL} = \frac{y_{21}(s)}{y_d(s)} = \frac{n_1(s)}{m_1(s)} \tag{2.35}$$

For the noncanonical case where the number of transmission zeros is less than the N^{th} degree, $P_N = 0$, and from the equations above, $y_d(s) = 1$. Together with the properties that the leading coefficient *F(s)* is unity for Chebyshev characteristics, along with ε_R for noncanonical designs, therefore, $M_{SL} = 1$. This provides the direct-coupled property where the source and load coupled inverter have the same characteristic impedance and can be modelled as a $\lambda/4$ uniform transmission line. Note that for the fully canonical case, M_{SL} will have a value slightly below unity providing the finite return loss at infinite frequency. The synthesis technique proceeds by finding the residues and eigenvalues of the admittance functions to construct the coupling matrix. This coupling matrix is then reduced to folded form using similarity transforms, such that it represents the coupling network of the physical filter. An example of a symmetric 4^{th} degree bandstop filter in folded form is shown in figure 2.13 demonstrating the signal path is directly coupled, M_{SL}.

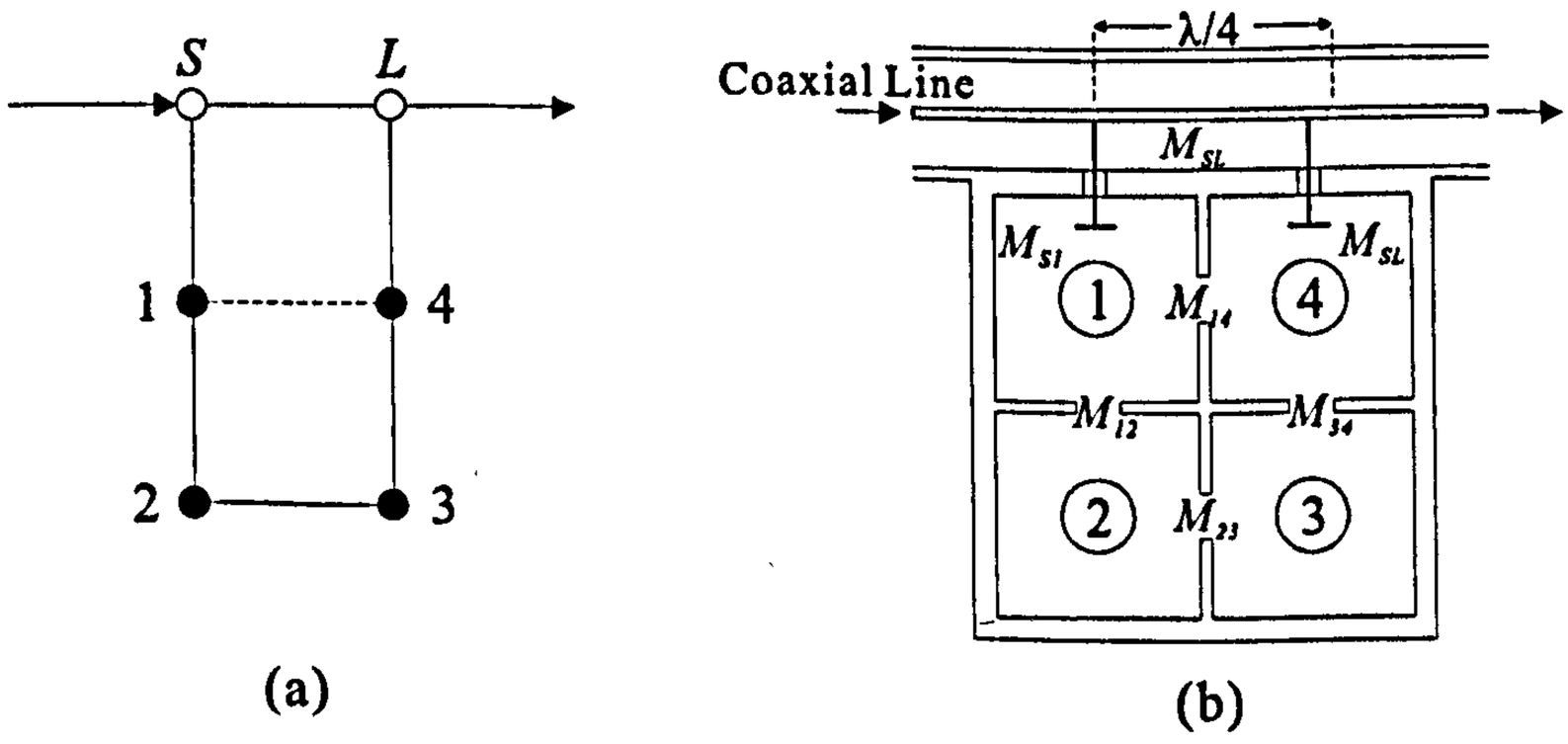

(a) (b)

Figure 2.13: Direct coupled (4-2) bandstop filter, [48]: (a) coupling-routing diagram (b) realisation with coaxial cavities

For a doubly terminated network between source and load impedances and if the order of reflection zeros is less than the N^{th} degree, then a cul-de-sac configuration may be formed by adding two unity impedance 45° phase lengths at either end

of the network. This represents multiplying the $F(s)$ and $P(s)$ polynomials by j that only introduces a 90° phase change without changing the overall transfer and reflection response of the network. A typical configuration for the bandstop filter is illustrated in figure 2.14 and clearly shows the core quartet of resonators in a square formation removing the need for diagonal cross-couplings, even for asymmetric characteristics. As for the original direct-coupled form, M_{SL} is unity for the number of reflection zeros less than the N^{th} degree meaning only a $\lambda/4$ transmission line is required between the input and output. The form is defined by the last resonator in each of the two chains having no output coupling, hence the name for this form.

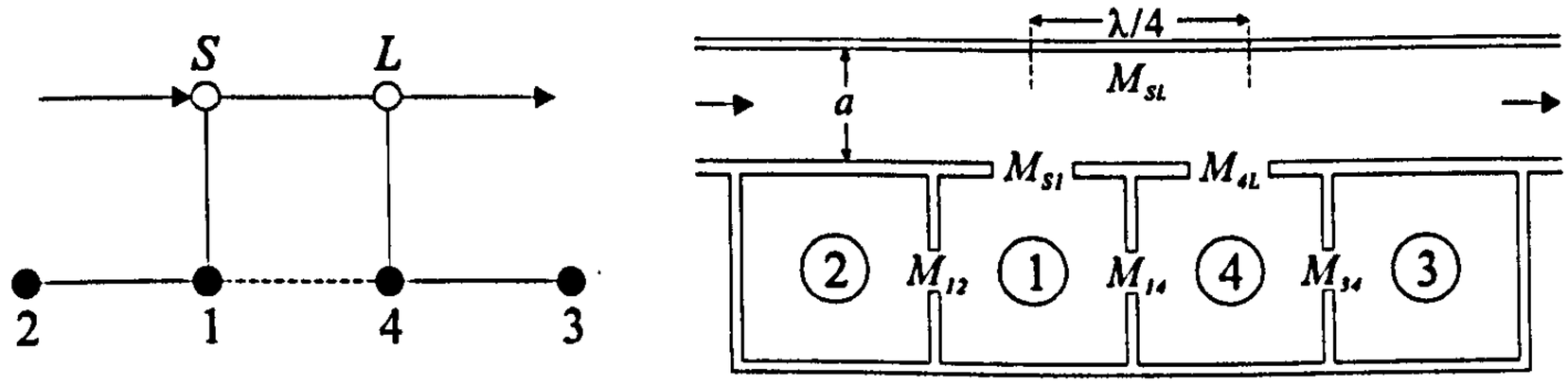

(a) (b)

Figure 2.14: Direct coupled (4-2) bandstop filter, [48]: (a) coupling-routing diagram (b) realisation with waveguide cavities

These two configurations demonstrate that only a $\lambda/4$ length of uniform transmission line is needed to form a multi-resonator bandstop filter. This asserts the advantage of reduced transmission phase lengths between resonator to transmission line tap points removing the need to tune these phase lengths and reduce transmission line dispersion. In addition, matrix operations can be applied to reconfigure the topology and performance of the simulated circuit.

2.6.1 Quality Factor

Practical filters have components with finite resistance producing loss in the system. This loss can be accounted for by the Q of the filter. In Chebyshev prototypes, for an N^{th} degree bandpass filter of centre frequency, f_0, and bandwidth

Δf, the unloaded Q is given by

$$Q_u = \frac{4.343 f_0}{\Delta f I_L} \sum_{r=1}^{N} g_r \tag{2.36}$$

where I_L is the midband insertion loss and g_r is the value of the r^{th} element of the lowpass prototype. External losses are also evident due to coupling fields from input probes to the filter and is attributed to an external quality factor, Q_L. The loaded quality factor, Q_L relates any external and internal losses and is an important design parameter for bandpass and bandstop filter structures. It is defined as

$$\frac{1}{Q_L} = \frac{1}{Q_U} + \frac{1}{Q_{ext}} \tag{2.37}$$

LEEDS UNIVERSITY LIBRARY

Chapter 3

Dielectric Resonator Filters

3.1 Basic Properties of Dielectric Resonators

Resonators are important components in microwave systems acting as filtering, frequency selection in oscilloscopes, amplifiers and tuners. At resonance, stored electric and magnetic fields energies are equal leading to maximum energy storage by internal resonator fields. Since reactance is proportional to the difference between electric and magnetic energy storage, the input impedance at the resonant frequency is purely real. A dielectric object with free-space boundaries can resonate in various modes due to internal reflections of electromagnetic waves at the high dielectric constant material/air boundary. The dimensions of a DR are on the order of one wavelength in the dielectric material for the fundamental mode of resonance. As $\lambda_d = \lambda\sqrt{\varepsilon_r}$, where λ_d is the wavelength associated with the dielectric, λ is the wavelength in freespace and ε_r is the relative dielectric constant, the resonator dimensions become smaller when compared to λ as ε_r increases. Since the dimensions of an air-filled cavity are of the order of λ, a DR has much smaller dimensions than the cavity resonator.

During the previous decade, many advances in dielectric materials have led to the successful combinations of high Qs, high dielectric constant and small temperature drift in materials suitable for use at microwave frequencies. High Q materials with dielectric constants ranging from 20 to 90 are now commercially

available from various manufacturers. At microwave frequencies, the classical dispersion theory of dielectric materials states that the dielectric loss increases with frequency, f, whilst ε_r remains unchanged, [49]. Therefore, the product of Q and f can be used to classify the fundamental properties for each dielectric material. Table 3.1 lists the characteristics of dielectric materials currently available. These materials not only have high-Q values and high dielectric constants but also good temperature stability. By adjusting proportions of the compounds in the material and allowing for the linear expansion of the ceramic, perfect temperature compensation is possible. The temperature coefficient of the resonant frequency of the dielectric material, τ_f, combines three independent factors that include temperature cofficient of the dielectric, τ_e, thermal expansion of the material, α_L, and thermal expansion of the environment in which the resonator is mounted. Resonant frequency shifts due to intrinsic material parameters are related by the above temperature coefficients in the equation below,

$$\tau_f \approx -\frac{\tau_e}{2} - \alpha_L \tag{3.1}$$

To advance the technology of these materials, the properties of the material must be measured accurately. Hakki and Coleman provided a method to measure the loss tangent of the dielectric, [51], which was later improved upon by Kobayashi and Katoh with greater accuracy, [52]. The technique involved measuring the microwave dielectric properties of a dielectric rod resonator short circuited at both ends by two parallel conducting plates. This allowed the advancement of new materials.

3.2 Quality Factor

Practical filters have components of finite resistance that produce a degradation in performance. The effects of this resistance can be related directly to the Q

Materials	ϵ_r	Q	τ_f(ppm)/°C	f(GHz)
$MgTiO_3$-$CaTiO_3$	21	8000	0	7
$Ba(Mg,Ta)O_3$	25	16000	3	10
$Ba(Mg,Ta)O_3$	25	35000	4	10
$Ba(Sn,Mg,Ta)O_3$	25	20000	0	10
$Ba(Mg,Ta)O_3$-$Ba(Zn,Ta)O_3$	27	15000	0	10
$Ba(Zn,Nb)O_3$-$Ba(Zn,Ta)O_3$	30	14000	0	12
$Ba(Zr,Zn,Ta)O_3$	30	10000	0	10
$(Ca,Sr,Ba)ZrO_3$	30	4000	5	11
BaO-TiO_2-WO_3	37	8800	2	6
$(Zr,Sa)TiO_4$	38	7000	0	7
$Ba_2Ti_9O_{20}$	40	8000	2	6
$Sr(Zn,Nb)O_3$-$SrTiO_3$	43	5000	-5 $+5$	5
BaO-Sm_2O_3-$5TiO_2$	77	4000	15	2
BaO-PbO-Nd_2O_3-TiO_2	90	5000	0	1
TiO_2	104	40000(Qf)	+460	–
$CaTiO_3$	180	70000(Qf)	+910	–
$SRTiO_3$	304	33000(Qf)	+1700	–

Table 3.1: High-Q dielectric materials, [50]

factor. The definition of the Q factor is given by,

$$Q = \omega \frac{\text{energy stored in resonator}}{\text{energy dissipated}} = 2\pi \frac{\text{energy stored in resonator}}{\text{energy dissipated per cycle}} \tag{3.2}$$

where Q is dimensionless providing a figure of merit of loss in the circuit. In order to excite the resonator, energy must be coupled into the resonator with either magnetic or electric coupling. To take into account the effects of input/output loading, the quality factor of a structure can be broken down into different factors, namely the unloaded Q, Q_u, the external Q, Q_e and the loaded Q, Q_L. The first unloaded Q_u accounts for internal losses and the external Q accounts for external losses when the resonator is part of an external circuit. The loaded Q is the quality factor taking into account the loading effects of any external circuits on the resonator itself and includes both internal and external losses. This figure may be measured easily, however, Q_u and Q_e can only be extrapolated. In cavity resonators, the dielectric medium, conductor loss and radiation can contribute to the unloaded Q. These losses can be individually classified. If the dielectric

constant is high and the DR is physically remote from the walls of the enclosure, the electric and magnetic fields of a given resonant mode will be confined in and around the vicinity of the material forming a resonant structure. These fields will attenuate to negligible values within a small distance relative to the freespace wavelength. As a result, radiation losses become minimal and the unloaded Q of the filter is primarily determined by the loss tangent of the dielectric material used to construct the DR filter. The loss tangent for a dielectric material is defined by

$$\tan\delta = \frac{\sigma}{\omega\varepsilon_0\varepsilon_r} \tag{3.3}$$

where $\varepsilon_0\varepsilon_r$ is the dielectric constant, σ is the conductivity of the medium and ω is the radian frequency. Note that Q is inversely proportional to fractional bandwidth allowing DR filters with high-Q to have narrow bandwidths. If all the electric energy of the resonant mode is stored inside the DR and no losses occur due to external fields, the unloaded Q is

$$Q_u = \frac{1}{\tan\delta} \tag{3.4}$$

Dielectric losses then become dominant and largely dependent on Q_u. For all practical DRs, external losses will always occur due to some form of radiation or dissipation in a surrounding metal shield. These losses will reduce Q_u, however, external stored energy will increase Q_u. For a permittivity greater than 100 or higher, these effects are negligible and equation 3.4 becomes a good approximation for the unloaded Q of a DR. The benefit of this is that an unloaded Q of 50 000 can be obtained in a reasonable volume, of which, would be impossible for metallic waveguide filters.

For a resonator in bandpass, or bandstop configuration, with resistive matched source and load impedances, the loaded quality factor can be obtained from measuring the 3 dB bandwidth of the S_{21}, or S_{11} as shown below,

$$Q_L = \frac{f_0}{\Delta f_{3dB}} \tag{3.5}$$

where f_0 is the resonant frequency and Δf_{3dB} is the 3 dB bandwidth of the S_{21}, or S_{11}, response. A typical transmission response is shown in figure 3.1.

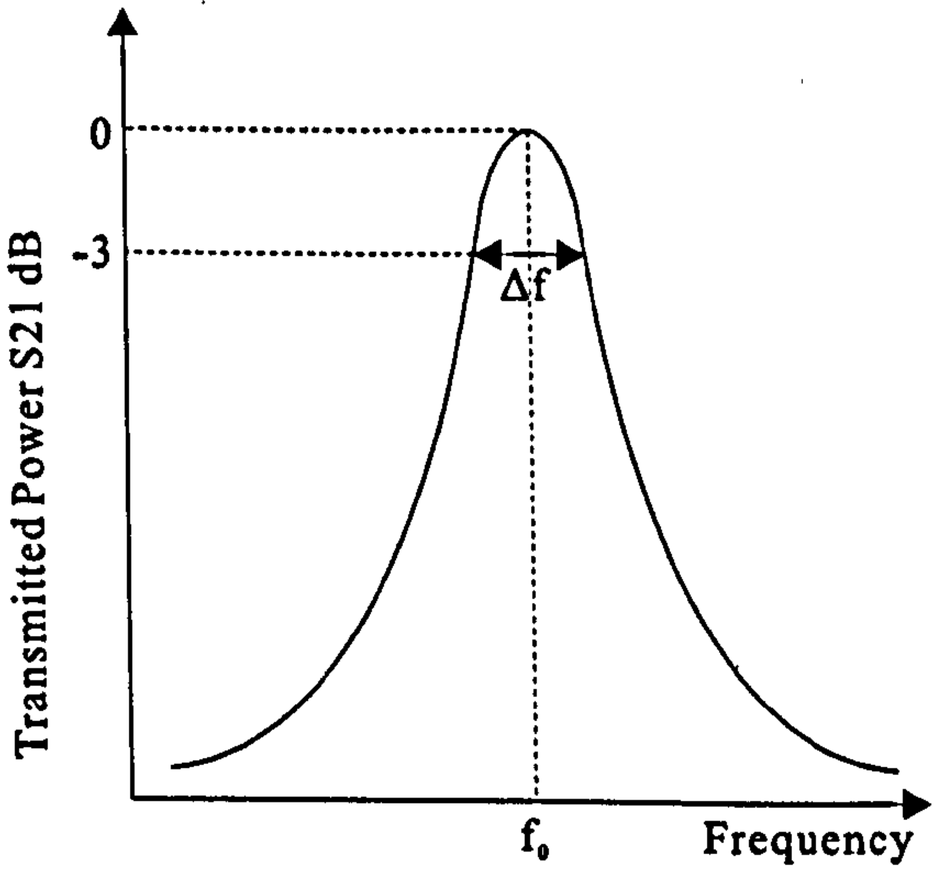

Figure 3.1: Transmission response displaying resonant frequency and 3 dB bandwidth

The external Q can then be obtained from Q_L and the insertion loss of the resonator at the resonant frequency by solving,

$$Q_e = \frac{Q_L}{S_{21}(f_0)} \text{ or } \left(Q_e = \frac{Q_L}{S_{11}(f_0)}\right) \tag{3.6}$$

where S_{21} is the transmission and S_{11} the reflection coefficient at resonance, f_0, for a bandpass and bandstop resonator respectively. The unloaded Q can then be found from,

$$Q_u = \frac{Q_L}{1 - S_{21}(f_0)} \text{ or } \left(Q_e = \frac{Q_L}{1 - S_{11}(f_0)}\right) \tag{3.7}$$

For accurate measurements, the coupling should be weak such that any influence from the loss of the feedline structure has negligible impact on extrapolation of the unloaded Q. The above three definitions can be related by

$$\frac{1}{Q_u} = \frac{1}{Q_L} - \frac{1}{Q_e} \tag{3.8}$$

Thus, the Q_u of a resonator can be measured.

3.3 Coupling to a transmission line

An advantage of DRs is the ease with which they can couple to common transmission lines. A typical DR operating in the $TE_{01\delta}$ mode can be transversely inserted into a rectangular waveguide and by coupling to the magnetic field, a simple bandstop filter is formed as shown in figure 3.2. Coupling to the magnetic field in the waveguide can be adjusted by rotating the resonator or moving the resonator towards the side of the waveguide. In microstrip line applications, the

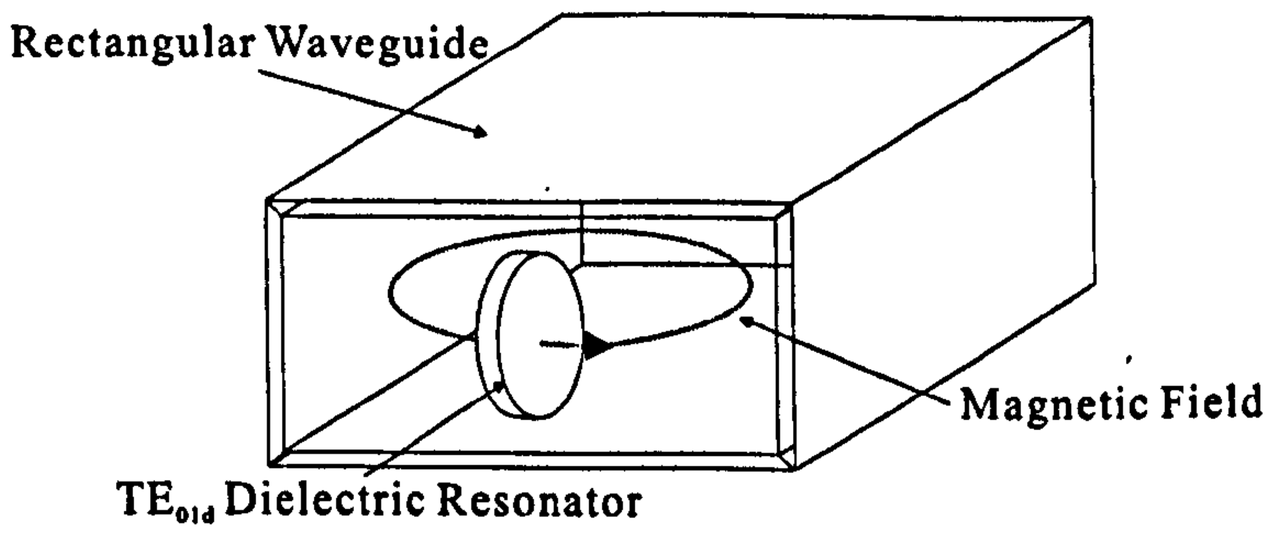

Figure 3.2: Magnetic field coupling of a DR to rectangular waveguide

same DR couples magnetically and forms a bandstop filter as shown in figure 3.3. This is the simplest way to incorporate a DR into a microwave network. In this case, the coupling is adjusted by lateral movement of the resonator from the microstrip line. A low-loss support with low dielectric constant material may be used to raise the resonator which would increase the Q. In order to prevent losses due to radiation, the entire device is enclosed in a metallic box, often aluminium. The resonant frequency may be calculated using equations from [53] and may be increased through perturbing the magnetic field via a tuning screw, or metal plate, above the resonator or shifted down in frequency by moving the resonator

away from the ground plane. A typical tuning range of 10% is possible, however, care must be taken to avoid degrading Q or temperature performance of the resonator by moving the metal plates in close proximity to the DR.

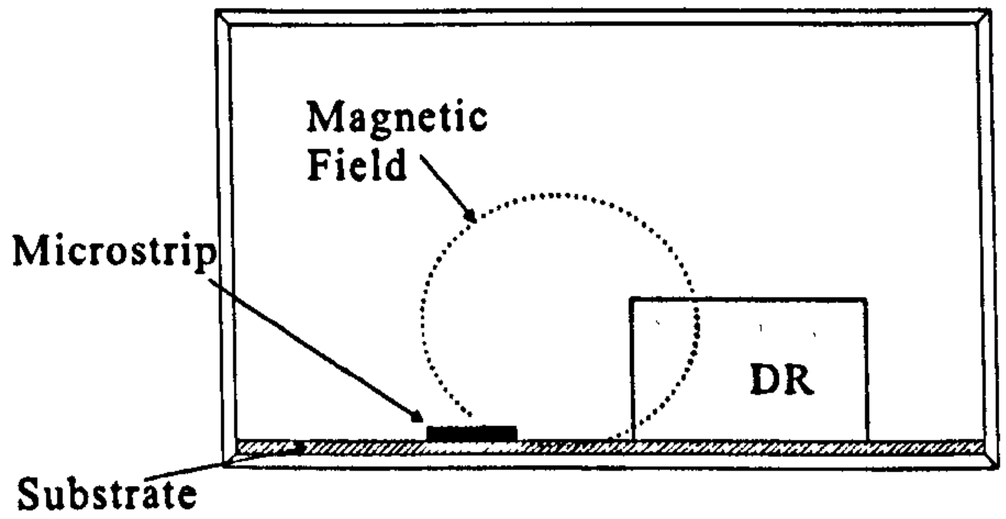

Figure 3.3: Magnetic field coupling of a DR to microstrip line

3.4 Configurations

DRs are the basic building blocks in DR filters. Fields inside a resonator store energy at the resonant frequency where equal storage of electric and magnetic energy occurs. An advantage of DRs over corresponding metal wall cavities is they can be shaped to perturb the fields inside the evanescent cavity, whereas, it is impossible to shape a hollow cavity without inserting extra materials. Typically, DRs have a disc form that can be modified to include notches, chamfers and holes to control spurious modes and in multiple-order devices, these perturbations may address issues of inter-modal couplings. Three conventional shapes for a DR are shown in figure 3.4 and among the theoretically explored geometries, the cylindrical shape, L < D, is considered the most advantageous as a resonator element in filter structures.

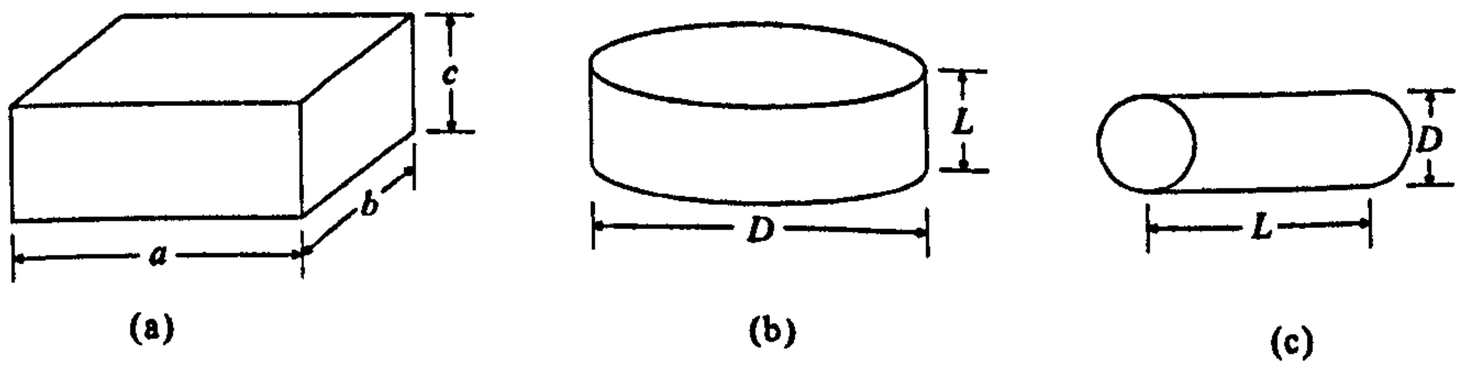

Figure 3.4: Three DR configurations: (a) rectangular resonator, (b) cylindrical resonator, L < D, and (c) cylindrical resonator, L > D

At microwave frequencies, any physical entity can be used to realise a resonator, whereby, the shape, size and boundary conditions applied will determine the internal electric and magnetic fields. The most common type of DR structure is the cylindrical suspended DR structure as shown in figure 3.5. A shielding is used as an enclosure to prevent losses from radiation and typical metals used include aluminium and copper. If the walls of the outer conductor are moved closer to the resonator, the resonant frequency of the $TE_{01\delta}$ mode is increased due to the cavity perturbation theory. This theory states that when a metal wall of a resonant cavity is moved inward, the resonant frequency decreases if the stored energy of the displaced field is predominantly electric. Otherwise, if the majority of displaced fields are magnetic, the resonant frequency increases as is the case here for the $TE_{01\delta}$ mode resonator. The relative dielectric constant is typically between 20 to 80 and the DR is remote from conductive walls, usually about twice the largest dimension of the DR. This is important as any current induced on the metallic surface by the external field of the resonator may incur serious adverse effects on the resonant frequency and also reduce the high intrinsic Q of the resonator.

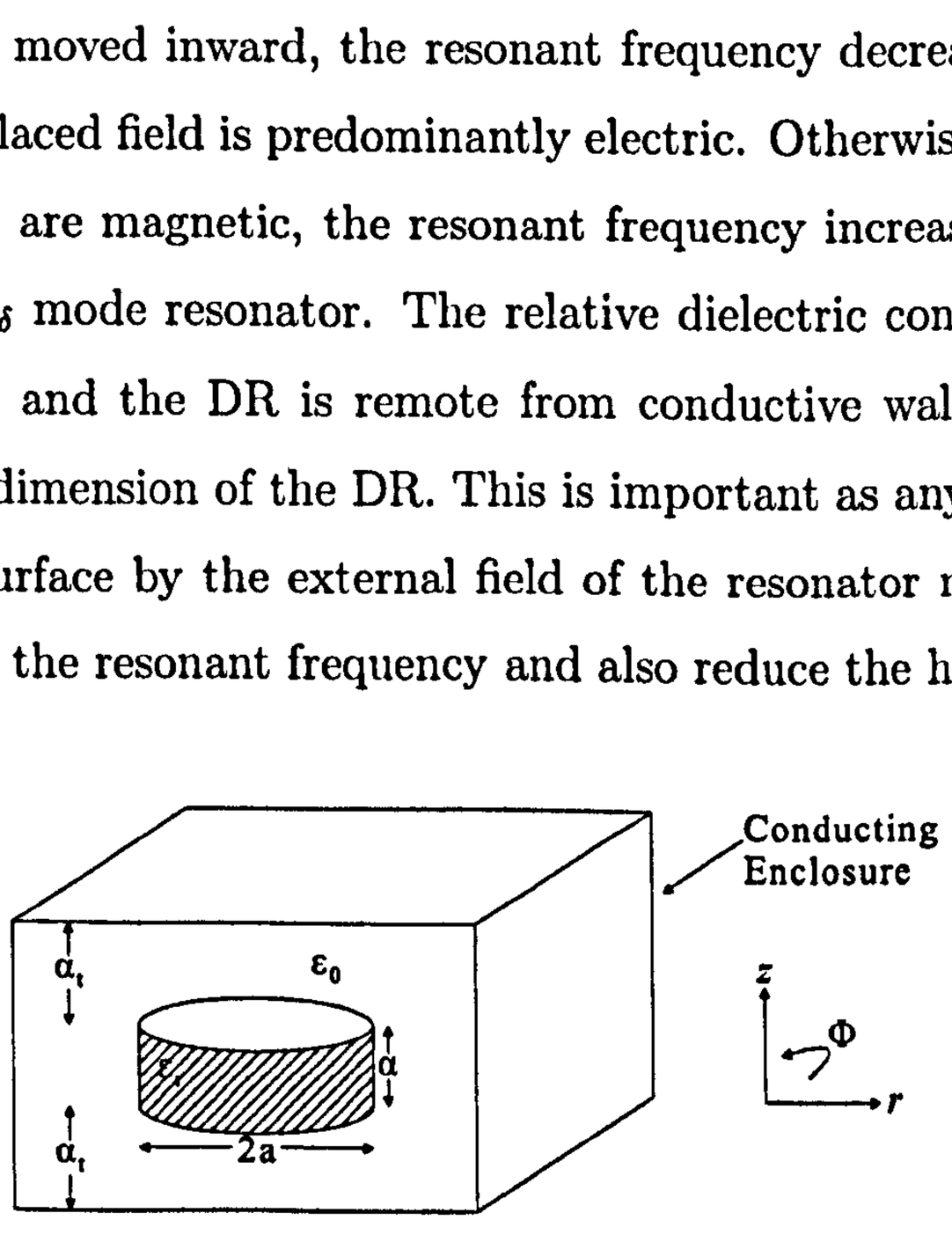

Figure 3.5: Commonly used DR structure, [28]

Since most of the electromagnetic energy is stored within the dielectric at the resonant frequency, this frequency is largely controlled by the dimensions and dielectic constant of the dielectric material itself. By assuming that the lateral surface of the DR behaves as an ideal magnetic boundary, the resonant frequency and field patterns may be approximately calculated since it is now assumed there is zero tangential magnetic component on the curved surface of the DR. In all filter configurations, preventing Q degradation requires mounting the dielectric

resonator on special supports.

3.5 Resonant Modes

Similar to conventional metal wall cavities, an infinite number of operating modes exist and may be excited in DRs satisfying boundary conditions. These modes may be classified into three distinct groups known as transverse electric (TE), transverse magnetic (TM), and hybrid electromagnetic (HE) modes. Each of these three families has an infinite variety of individual modes, thus, particular modes will suit individual applications. Plots of the field distributions for these modes are shown in figure 3.6, [54]. For a puck where L < D, the lowest frequency resonant mode is the $TE_{01\delta}$ mode which has a circular electric field distribution. The magnetic field is strongest on the axis of the puck and maintains a magnitude to a sufficient distance outside the puck. The field resembles that of an axial magnetic dipole and this mode is commonly used. For L > D, the fundamental mode is the $TM_{01\delta}$ mode which has an equivalent magnetic dipole moment transverse to the axis. The other mode of interest is the $HE_{11\delta}$ in which both the electric and magnetic field vary over the azimuthal direction. This dual-mode configuration has distinct advantages over single-modes offering better performance, smaller size and less weight than classical fundamental TE or TM mode filters, [55].

Comprehensive studies of modes in DRs have produced mode charts for the cylindrical system and a few examples are illustrated in, [56], [57], [58], [16] and [59]. These charts are important design tools for filters and other applications. A typical mode chart is shown in figure 3.7, [28].

The most commonly used mode in a DR is the $TE_{01\delta}$ mode in a cylindrical resonator, or the $TE_{11\delta}$ mode in a rectangular resonator since the former has the lowest resonant frequency, for certain diameter/length, D/L, ratios, and is ,therefore, classified as the fundamental mode. The $HE_{11\delta}$ degenerate hybrid mode offers the advantage of smaller volume and weight, half the number of cavities,

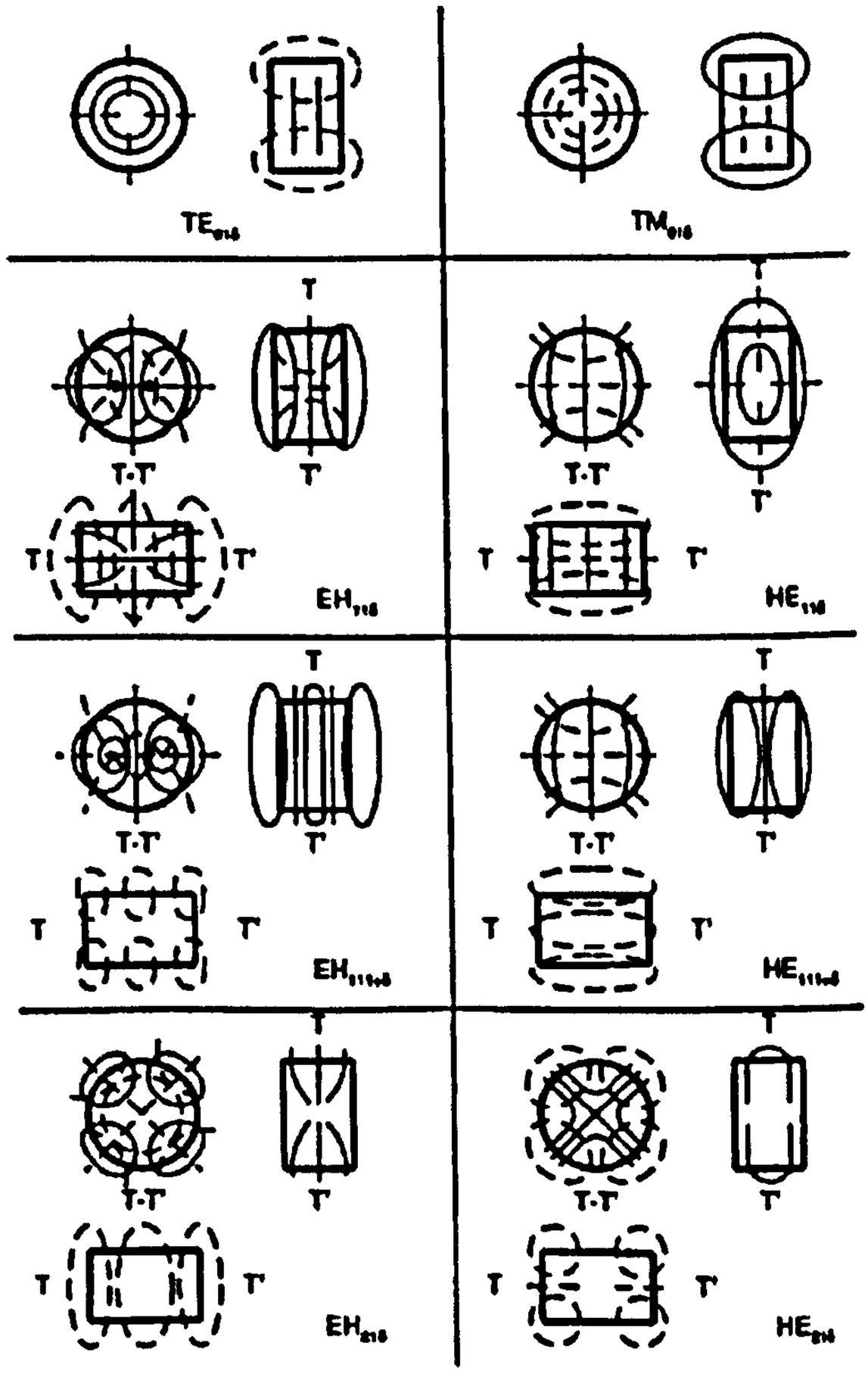

Figure 3.6: Field plots of common DR modes, [54]

when compared to single-mode devices. This is possible since each resonator resonates in two orthogonal and independent modes. A drawback of the DR is proximity of resonant modes to each other and in order to make the DR useful for practical applications, a goal in resonator design is to separate the resonant frequency of the operating mode as far as possible from higher frequency modes. Side walls were shown to exhibit little effect when placed at a distance greater than the diameter of the DR, however, the aspect ratio of the puck can have a positive effect in improving the spurious performance. In $TE_{01\delta}$ mode operation, a choice of height over the diameter, H/D, of around 0.4 is recommended for both

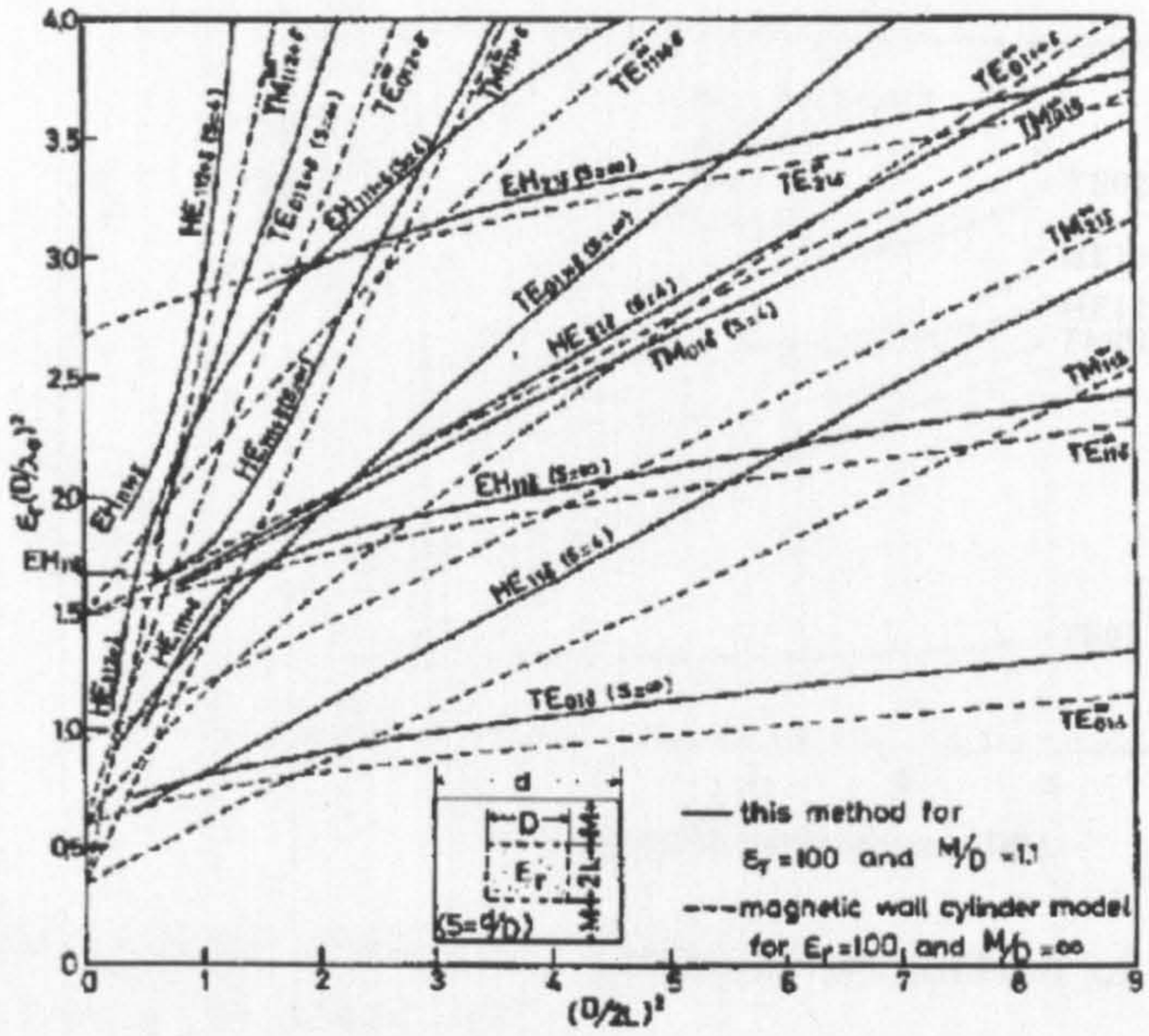

Figure 3.7: Typical DR mode chart, [28]

optimum Q and minimal interference of spurious modes. A chart depicting this is shown, figure 3.8, [24]. By introducing a hole at the centre of the DR, the spurious separation between the fundamental $TE_{01\delta}$ mode and higher-order modes can be improved. Figure 3.9 shows how the spurious characteristics are improved as a function of ring diameter, [17]. This property can be used to improve the spurious performance of dielectric loaded filters.

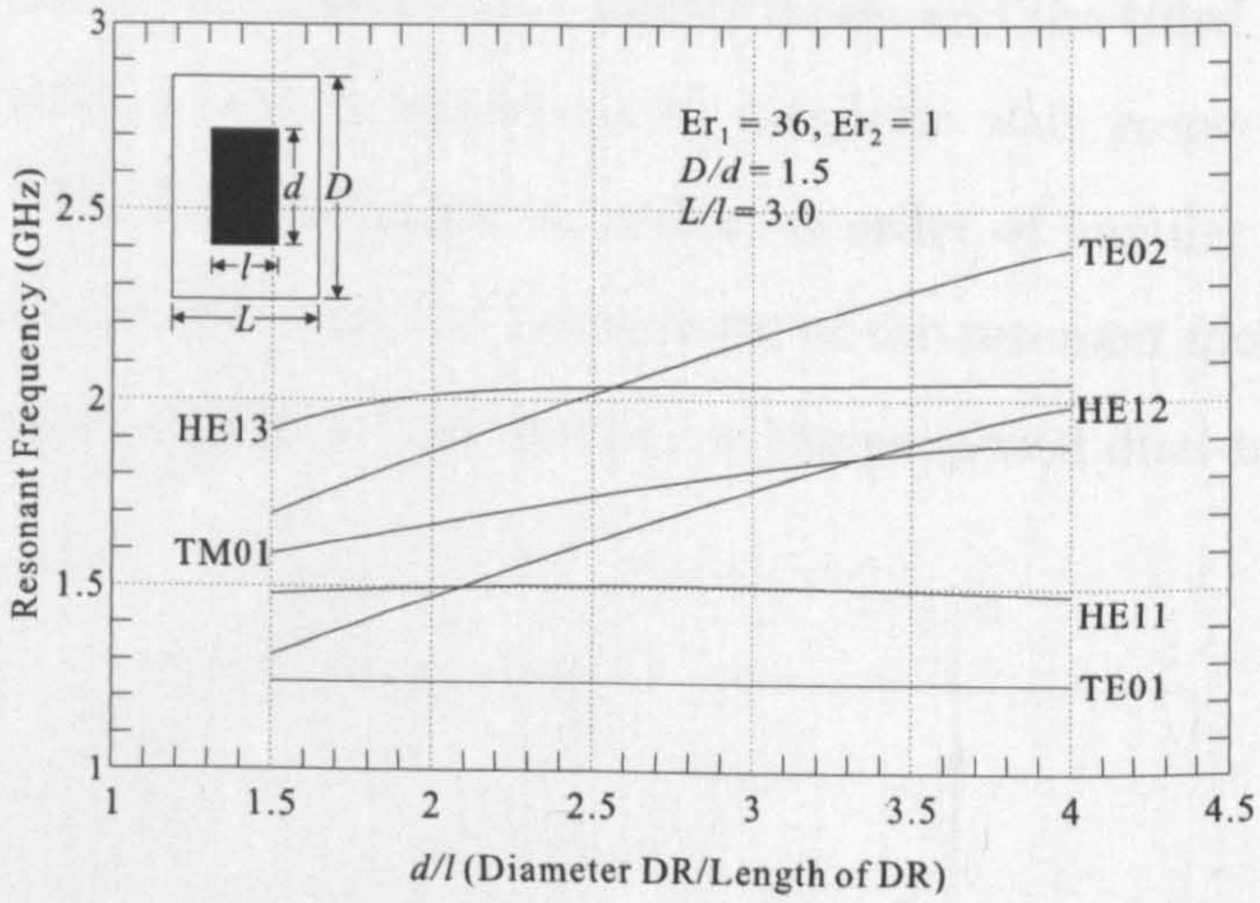

Figure 3.8: Mode chart of a DR in cavity as a function of aspect ratio, [24]

Even for a radially symmetrical mode such as the $TE_{01\delta}$, which only has three

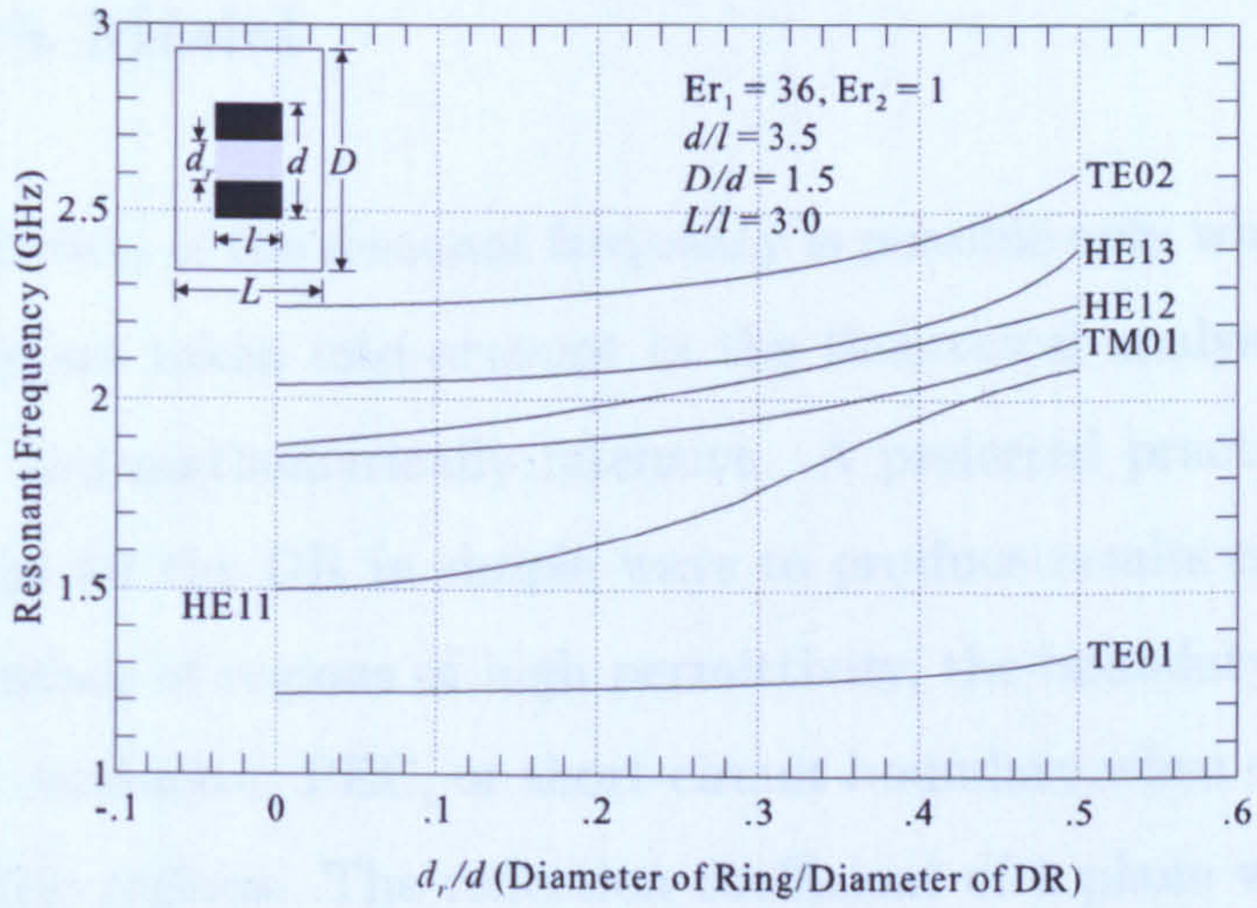

Figure 3.9: Mode chart of a DR in cavity as a function of aspect ratio with improved spurious performance, [17]

components of the electromagnetic field, rigorous analysis is still a problem and various simplifying assumptions are required. The situation is more complex for higher order modes that are generally hybrid, usually degenerate, and have all six components of the electromagnetic field. To identify and distinguish the hybrid modes with strong axial magnetic or electric fields, Kobayashi proposed a naming convention using EH and HE notations, [58], respectively. A modern classification system proposed by Zaki, [59], is more simple and defines HEE_{nm} and HEH_{nm} with the first two letters indicating a hybrid mode and the third letter, E or H, if the symmetry wall, z = 0, is an electric or magnetic wall, respectively, as shown in figure 3.10. The first subscript, n, indicates order of angular variation of the fields and the second subscript, m, is the order of the resonant mode. This system is used in the study of the hybrid modes for the proposed dual-mode resonator.

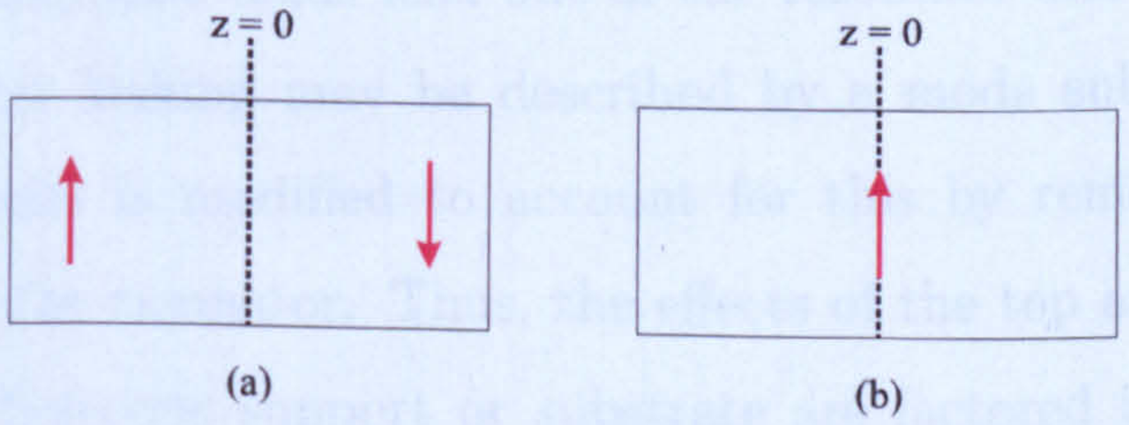

Figure 3.10: Classification of HE modes showing E-field component for (a) electric wall (b) magnetic wall

3.5.1 Cohn's Model

An accurate prediction of the resonant frequency is possible only when all boundary perturbations are taken into account in the theoretical analysis and is rigorously complex and mathematically intensive. A preferred practical approach is to find solutions for the DR in simple ways to produce results close to actual values. At the surface of regions of high permittivity, the boundary behaves like a perfect electric conductor, PEC, or short-circuit boundary when observed from the air to dielectric regions. The reflection coefficient of a plane wave normally incident at the dielectric to air boundary is given by,

$$\Gamma = \frac{\eta_0 - \eta}{\eta_0 + \eta} = \frac{\sqrt{\varepsilon_r} - 1}{\sqrt{\varepsilon_r} + 1} \approx +1 \tag{3.9}$$

where η_0 and η are the wave impedance of air and dielectric, respectively, and $\varepsilon_r \gg 1$. The boundary, when observed from dielectric to air, can now be approximated by a hypothetical perfect magnetic conductor, PMC, on which the normal components of the electric field and tangential components of the magnetic field vanish at the boundary. This causes total internal reflections resulting in the confinement of energy in the high permittivity object. To a first approximation, a DR can be explained as a hypothetical perfect magnetic conductor, PMC, waveguide cavity, therefore, the field distribution and resonant frequencies for such a resonator can be calculated analytically. The magnetic wall waveguide below cutoff with a dielectric resonator situated in the middle is as shown in figure 3.11.

In reality, electromagnetic fields leak out of the resonator and eventually decay exponentially. This leaking may be described by a mode subscript δ and the magnetic wall model is modified to account for this by removing two lateral magnetic walls of the resonator. Thus, the effects of the top and bottom covers of the puck and dielectric support or substrate are factored in to improve the accuracy of the model as shown in figure 3.12. A simple mathematical model of a magnetic waveguide below cutoff is introduced in which a second-order model

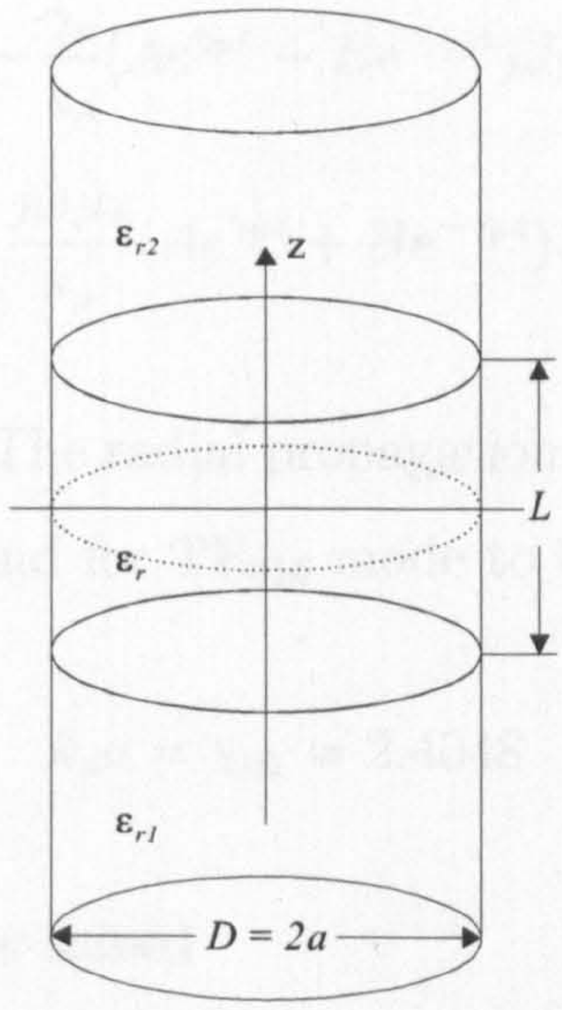

Figure 3.11: Cohn's second-order DR model showing a DR inside a magnetic-wall waveguide below cutoff

of a cylindrical DR is used, [11] and [60]. This model reduces to Cohn's standard model when the two plates are moved to infinity, $L_1 = \infty$ and $L_2 = \infty$ with air occupying spaces on each side of the dielectric, $\varepsilon_{r1} = 1$ and $\varepsilon_{r2} = 1$. Thus, an isolated resonator in free space is assumed. Both the $TE_{01\delta}$ and $HE_{11\delta}$ modes of a DR can be solved using the modified Cohn's model. A calculated frequency accuracy for the $TE_{01\delta}$ mode is approximately 6%, [61].

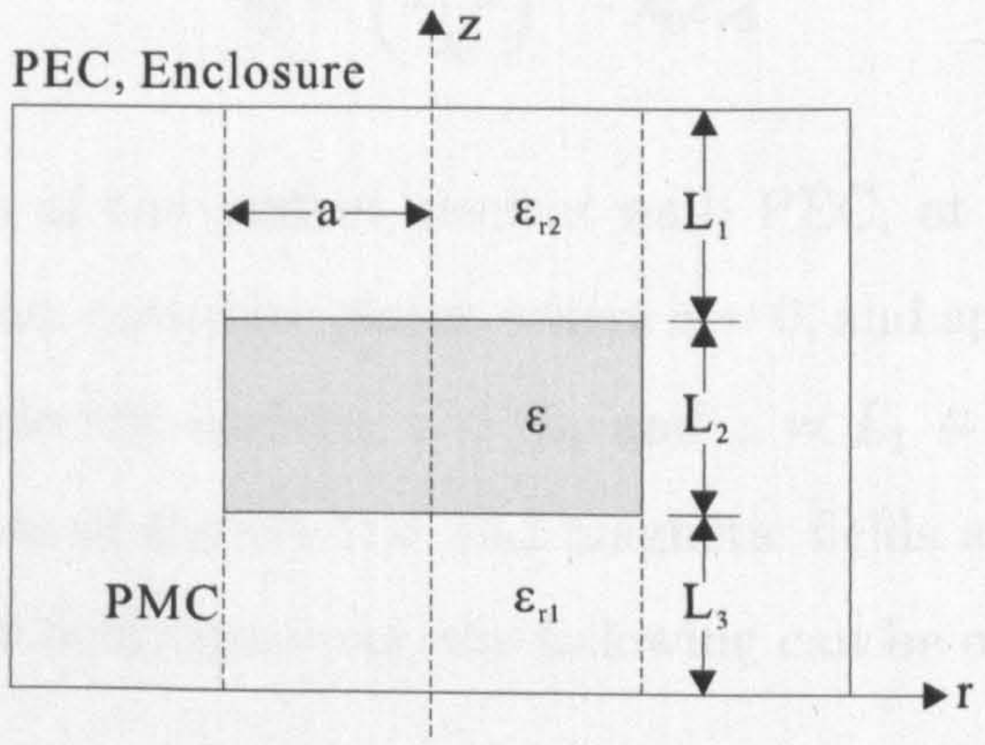

Figure 3.12: Improved model for a shielded DR

The EM field within each region can be expressed as

$$H_z = (Ae^{\gamma_p z} + Be^{-\gamma_p z})J_0(k_\rho \rho)) \tag{3.10}$$

$$H_\rho = -\frac{\gamma_\rho}{k_\rho}(Ae^{\gamma_p z} - Be^{-\gamma_p z})J_1(k_\rho \rho)) \tag{3.11}$$

$$E_\phi = -\frac{j\omega\mu_o}{k_\rho}(Ae^{\gamma_p z} + Be^{-\gamma_p z})J_1(k_\rho \rho)) \tag{3.12}$$

where p is the region index. The radial propagation constant of the mode is fixed by the PMC wall at $\rho = a$, and for $TE_{01\delta}$ mode to be solved,

$$k_\rho a = \chi_{01} = 2.4048 \tag{3.13}$$

and for the $HE_{11\delta}$ mode to be solved

$$k_\rho a = \chi_{11} = 3.832 \tag{3.14}$$

The separation constants are

$$\beta^2 = -\gamma^2 = k_0^2\varepsilon_r - \left(\frac{\chi_{m1}}{a}\right)^2 \tag{3.15}$$

$$\gamma_1^2 = \left(\frac{\chi_{m1}}{a}\right)^2 - k_0^2\varepsilon_{r1} \tag{3.16}$$

$$\gamma_2^2 = \left(\frac{\chi_{m1}}{a}\right)^2 - k_0^2\varepsilon_{r2} \tag{3.17}$$

Using the properties of the perfect electric wall, PEC, at the top, where $z = L_1+L+L_2$, and bottom enclosure plates, where $z = 0$, and applying the boundary conditions at the dielectric surface, $z = L_1$ and $z = L_1 + L$. This ensures the tangential components of the electric and magnetic fields are continuous at the interface. Solving the field equations, the following can be obtained.

$$\frac{\phi_1}{2} = \tan^{-1}\left(\frac{\gamma_1}{\beta}\coth\gamma_1 L_1\right) \tag{3.18}$$

$$\frac{\phi_1}{2} = \tan^{-1}\left(\frac{\gamma_2}{\beta}\coth\gamma_2 L_2\right) \tag{3.19}$$

$$\beta L = \frac{\phi_1}{2} + \frac{\phi_2}{2} + l\pi, \quad l = 0, 1, 2, 3, \ldots \tag{3.20}$$

For generality, the added angle $l\pi$ gives all possible resonance conditions. When $l = 0$, the mode is the lowest fundamental mode $TE_{01\delta}$ or $TE_{11\delta}$ with the desired radial propation constant, where δ signifies a nonintegral number, smaller than unity. As shown, for the lowest mode, $l = 0$ of the desired radial propagation constant, the field variation in a DR undergoes less than a half wavelength within the resonator length, L, due to the end effects of the air-filled region. This model was further improved by removing the circular wall leading to calculations of the resonant frequency to an accuracy within 1-2%, [62] and [61].

3.5.2 Mode-Matching Model

A simple DR model is helpful during the initial stages of the analysis or design process but lacks the accuracy needed for modern microwave circuit design. In actual resonator configurations, a metal-wall cavity or housing is necessary to prevent radiation of the electromagnetic field resulting in degradation of Q. Due to recent progress in computer technology and computer aided design, CAD, tools for microwave engineering, many EM simulation software and methods have been developed and can be used to compute the exact resonant frequency and field patterns for a DR. The model described previously was modified leading to accurate formulae for resonant frequency and electromagnetic field distribution in the structure through mode matching method, [63] and [53].

The radial mode matching method is used to analyse any cylindrical DR configuration as described in [64] using a general multilayer configuration with adjustable number of material layers in both longitudinal and radial directions as shown in figure 3.13. The resonator structure is partitioned into a succession of waveguides terminated by appropriate boundaries. Region ij of the resonator is filled with a dielectric material with relative permittivity, ε_{rij}, and loss tangent, $\tan\delta_{ij}$. The number of layers and material properties can be assigned individually according to the resonator structure. The top and bottom planes of the structure can be either perfect electric conductor, PEC, or perfect magnetic conductor, PMC.

The variations of the TE and TM fields of the modes contributing to resonance are first expressed in each radial region and are matched at each interface to establish the continuity of the fields tangential to a discountinuity of the medium. To simplify the analysis, the normal mode fields are decomposed into two orthogonal sets of solutions. These are the TE_z modes, where $E_z = 0$, and TM_z modes, where $H_z = 0$. Finally, the orthogonality property of the modes is applied providing an infinite set of linear equations. These are then rearranged and truncated to form a matrix whose determinant will be zero at the resonant frequencies of the cavity. The field coefficients of each mode can then be solved to obtain the field distribution and unloaded Q.

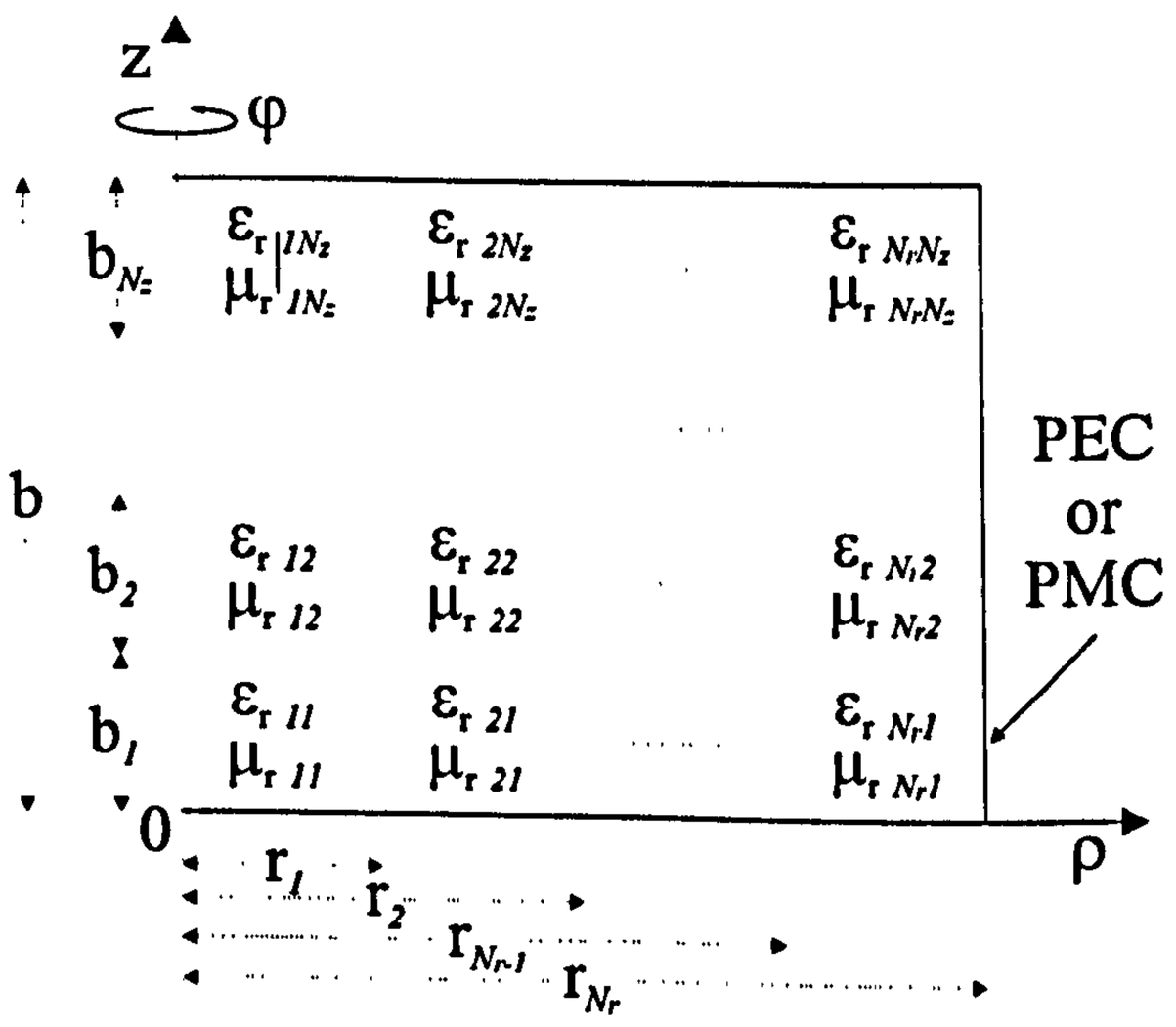

Figure 3.13: Generalized multilayer cylindrical DR, [64]

In advanced models, additional factors such as dielectric supports and tuning mechanisms are taken into account. The resonant frequency of the DR in these configurations can be calculated using the mode matching method with accuracies better than 1%. Recently available electromagnetic simulation programs enable additional improvements in the calculations of relatively complex structures. Using such programs, the resonator housing, tuning and coupling elements can be precisely modelled obtaining accurate results taking into account practical aspects of the design. An additional advantage is the electromagnetic field dis-

tribution, dissipated power, etc. can be visualised and plotted easily. Table 3.2 presents the resonant frequencies of several DRs computed by both Cohn's simple model and rigorous mode matching method.

Mode	ε_r	DR Radius (mm)	DR Length (mm)	L1,L2 (mm)	Cohn's Model	MM Method	Measured (MHz)
TE_{01}	36.2	3.015	4.16	3.411	7419	7941	7940 [61]
TE_{01}	36.2	3.995	2.14	4.43	7159	7758	7790 [61]
HE_{11}	37.6	8.00	6.90	inf	4373	4210	4196 [30]
HE_{11}	38.2	6.80	5.60	inf	5152	4980	4994 [30]

Table 3.2: Computed and measured resonant frequencies of DRs, [65]

This method is one of the most efficient and precise methods for DR analysis and design but for complex three-dimensional designs, 3D, with non homogeneous media, this method is time consuming where there is a need to vary a number of parameters dynamically.

3.5.3 HFSS Finite Element Model

The finite element method, FEM, is used to solve Maxwell's equations in the volume of arbitrary three-dimensional structure and, from this, the transfinite element method can be used to determine the two-dimensional field solution to input and output ports, [66]. This method has been successfully used to analyse dielectric-loaded cavity resonators using one-dimensional FEM and is economical for dielectrics extended along the length of the cavity, [67]. 2D and 3D FEM have been applied to evaluate and design high quality TM and hybrid DR modes and a need for the analysis of a full 3D structure is shown for greater accuracy of asymmetric devices, [68]. Resonant frequencies for TE and TM modes of axisymmetric structures containing common dielectric resonators have been calculated in different environments with tuning screws, [69].

HFSS is a software simulation package that uses the generality strength of FEM to analyse arbitrary, complex voluminous or planar 3D closed device with var-

ious levels of resolution in the problem space. This allows the user to address minute problems in large problem spaces efficiently based on the adaptive mesh refinement method. The inner materials must be homogeneous and linear but can be anisotropic and possess dielectric or metallic losses. The studied structure is generally closed by perfect magnetic and electrical conditions or excited by transmission lines or waveguides. The obvious advantage is the ability to visualise the fields of resonant modes, thus, the structure may be modified to include or suppress modes. This tool approximates the true fields in the problem space by discretizing the field domain into basic elements that are roughly 1/10 of a guide wavelength. The finite elements are contactual and of the simplest form such as line elements in 1D domains, triangular in 2D domains and tetrahedral volume elements in 3D problems. The advantage for these simple elements is their flexibility to subdivide any arbitrary geometry, figure 3.14.

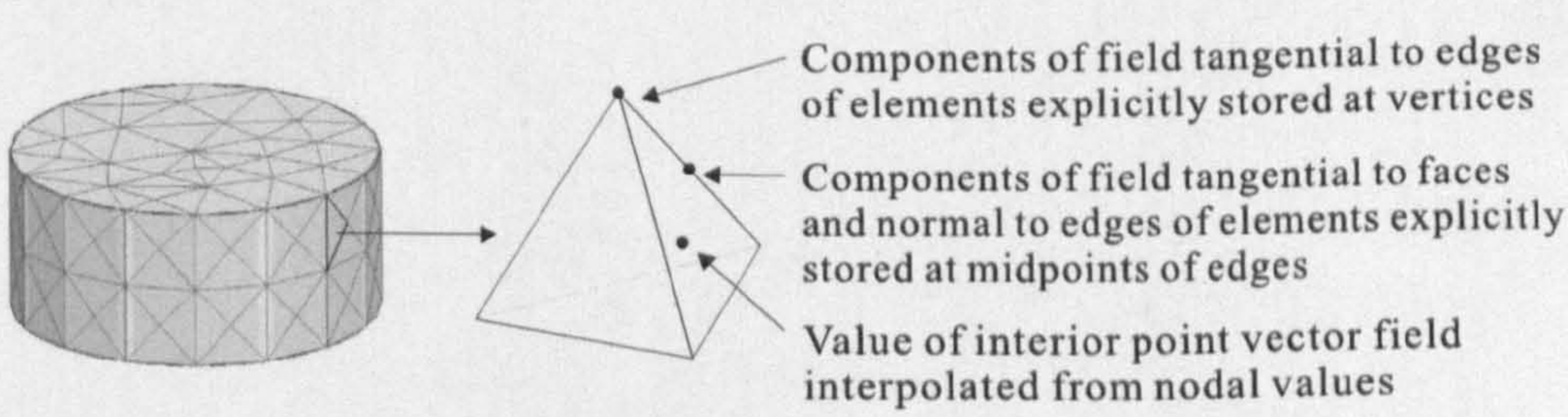

Figure 3.14: Mesh with tetrahedral elements for maximum flexibility to approximate shape of 3D dielectric puck

The solution is found by summing the magnitude of the fields or potentials at each junction of elements. It computes the eigenmodes at each port by using the number of modes chosen by the user and the S-parameters, for the structure, are calculated to within a tolerance set by the user. The finite-element mesh is refined over a number of passes until the desired tolerance is achieved. Once a mesh is created at one frequency, the same mesh can be used to sweep a range of proximate frequencies and the impedances are calculated at each port for each set of S-parameters. An adaptive pass is run at the frequency of interest to create a finite-element mesh and a frequency sweep is performed acrosss the interested spectral range. Adaptive passes can be run at the end frequencies to check the

validity of the mesh.

HFSS has different frequency domain solvers. For a driven problem, an external source of energy is applied at a physical access port and a matrix is built and inverted to find the solution at each frequency of interest, of which the scattering parameters are calculated. A sourceless problem can also be solved using an eigenmode solver with defined short circuited planes. The solutions to the solver are derived from stationary field configurations and formulate cutoff frequencies and propagation constants for waveguide structures and natural resonant frequencies, field plots and Q_us of resonators. For a dielectric resonator puck situated in a cavity, one can produce mode charts of variations between resonant frequency and any variable of the resonator.

The mesh algorithm allows it to predict the required mesh density for particular boundary topologies and in the vicinity of a singularity of the solution, the energy density becomes high, thus, the value of the functional is very sensitive to the coefficients in that area. This requires finer subdivisions for better accuracy as depicted in figure 3.15(b). The resolution of the mesh can be varied for greater accuracy as shown in figure 3.15(c) where the elements are 0.1λ in comparison to elements of 0.2λ in figure 3.15(b). The compromise for greater resolution is a longer computational time is required. Also, to ensure the accuracy of each adaptive mesh, a convergence value is required that also has a compromise between accuracy and computational time.

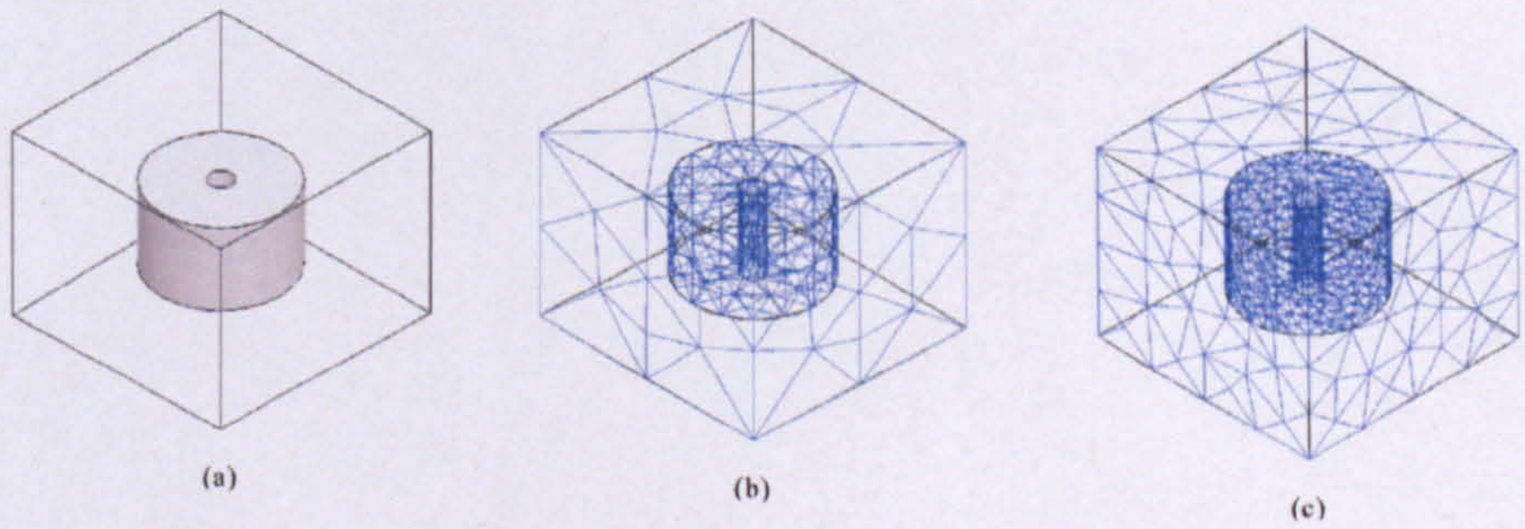

Figure 3.15: Finite element method analysis of dielectric puck with axial hole: (a) basic geometry, (b) view of mesh with 0.2λ mesh, (c) view of mesh with 0.1λ mesh

There are some drawbacks to HFSS, notably performing a frequency sweep with eigenmodes dependent on frequency. Eigenmodes are calculated at each frequency and ordered according to the propagation constant but in HFSS, the mode numbering may become erroneous towards a higher frequency. For example, eigenmode 1 and 2 will remain in order at low frequency until an extra mode is shown in the structure that has a frequency less than eigenmode 2. This new mode will now replace and will be labelled as eigenmode 2. Furthermore, impedances are not calculated in HFSS unless impedance lines are defined on the ports. These are lines connecting the points of maximum voltage difference at each port and are different for each mode. Only one set of impedance lines are defined for all the frequencies in a sweep and must be defined in the same order as the corresponding modes. When modes are switched during a switch, the impedance lines are no longer valid at each frequency and no impedances will be calculated. Computation time is a factor as the simulation must subdivide the whole volume, thus, more solutions are required at each node in the mesh. The material properties of dielectric resonators in HFSS, [70], and design of DR filters, [71], have been analysed. For the latter, a combination of the accuracy of HFSS and rigorous analysis of inter-resonator couplings has produced slotted-DR filters without tuning. Unfortunately, a frequency shift of 0.2% between simulated and measured responses shows that although HFSS is promisingly accurate in 3D simulations, for dielectric-loaded cavity resonators, tuning must be present to compensate for practical imperfections. With regards to this, sensitivity simulations should be performed to understand the effect of physical tolerances on the response of the device.

Chapter 4

Dielectric-Loaded Compact Bandstop Filter

4.1 Introduction

Proposing the use of dielectric loading within waveguide sections is not uncommon, [72] and [50], as the size of resonant sections in filters and other components are dramatically reduced. However, energy is now strictly confined to metallized sides and the Q values are reduced by at least the ratio of $1/\sqrt{\epsilon_r}$ neglecting metal losses. Since resonances are fully supported within the dielectric region, high Q performance exceeds that of a conductor-loaded or cavity metal resonator. This is because energy is not in substantial contact with metal except on enclosure walls. A bandstop filter realised by means of rectangular dielectric-loaded resonators coupled to the inner rod of a coaxial transmission line with square outer conductor is described. Commonly, coaxial resonators are normally realised for base station filters but conventional waveguide components are used as they offer lower loss. The existence of a dielectric-loaded waveguide allows for near perfect magnetic walls. For example, when a hollow waveguide is transversely cut, the open ends radiate but in the presence of a high ϵ_r medium, the open ends approximate a near perfect magnetic wall and will not radiate, although a small percentage of leaky fields are present. Maximum reduction is obtained by the complete loading of the rectangular waveguide resonator cavities and although Q_u values are smaller, calculated values are acceptable for mobile base station

applications. This physical arrangement allows a simplicity in the mechanical design where rectangular dielectric-loaded resonators are fitted into prescribed cavities coupled to the coaxial line. The narrow rectangular resonators allow for inter-resonator spacings of $\lambda/4$ offering further miniaturisation. For example, conventional waveguide resonators and dielectric pucks, when coupled to a transmission line, require $3\lambda/4$ spacings, [73] and [3]. The design adds flexibility in that the resonators may be positioned at any distance along the transmission line for adjustable phase lengths. Also, the cavities may be easily machined to include different shaped dielectric resonators, metal-loaded or completely unloaded resonators. Initial narrowband designs have focused on dielectric slabs of permittivity, 44, exciting the $TE_{10\delta}$ mode at 2 GHz. Preliminary simulation data have produced 3 dB coupling bandwidths in the region of 25 MHz for a 4^{th} degree filter. Possible applications for this device include UMTS base stations and other communication applications where rejection of signals is necessary. The advantages of this filter are that more complex designs can be carried out based upon this simple structure, i.e. layering coaxial lines and resonators on top of each other forming multiple instances of bandstop behaviour over a broad frequency range with layout similar to end-coupled bandpass filters. The physical structure also allows ease of positioning of tuning screws for both input coupling and resonant frequency which is neccessary to ensure the response meets the required specifications. In all practical designs, fabrication tolerances can make the measured response different to the simulated response, thus, some form of tuning is required.

4.2 $TE_{10\delta}$ Rectangular Waveguide Resonator

The design for the $TE_{10\delta}$ dielectric-loaded rectangular resonator begins by finding the dimensions for the required resonant frequency. The rectangular waveguide is a hollow-pipe waveguide where an air-filled, or dielectric, region of width, a, height, b, and length, l extend indefinitely in the axial, z, direction and is enclosed

by conducting boundaries on four sides. In this one-conductor guiding structure, no transverse electromagnetic, TEM, wave exists since no axial field components exist, unlike for TE and TM modes which do propagate through this waveguide. The TE_{10} is the dominant propagating mode in this waveguide for $a > b$ since it is the lowest cutoff in this rectangular structure, figure 4.1. By shorting the two ends of a segment of waveguide, a rectangular cavity resonator is formed with two groups of resonant modes, TE_{mnp} and TM_{mnp}, and these correspond to TE_{mn} and TM_{mn} propagation modes in open-ended waveguides, respectively. The first two subscripts, m and n, follow from TE_{mn} and TM_{mn} modes, representing the changing cycles along the x and y directions. The third subscript, p, denotes changing cycles along the z axis. The TE_{101} mode corresponds to the lowest fundamental mode for $b < a < l$ of which the field solutions are, [74],

$$E_y = -2\frac{A\omega\mu a}{\pi}\sin\left(\frac{\pi x}{a}\right)\sin\left(\frac{\pi z}{l}\right) \tag{4.1}$$

$$H_x = j\frac{Aa}{l}\sin\left(\frac{\pi x}{a}\right)\cos\left(\frac{\pi z}{a}\right) \tag{4.2}$$

$$H_z = -j2A\cos\left(\frac{\pi x}{a}\right)\sin\left(\frac{\pi z}{l}\right) \tag{4.3}$$

$$E_x = E_z = H_y = 0 \tag{4.4}$$

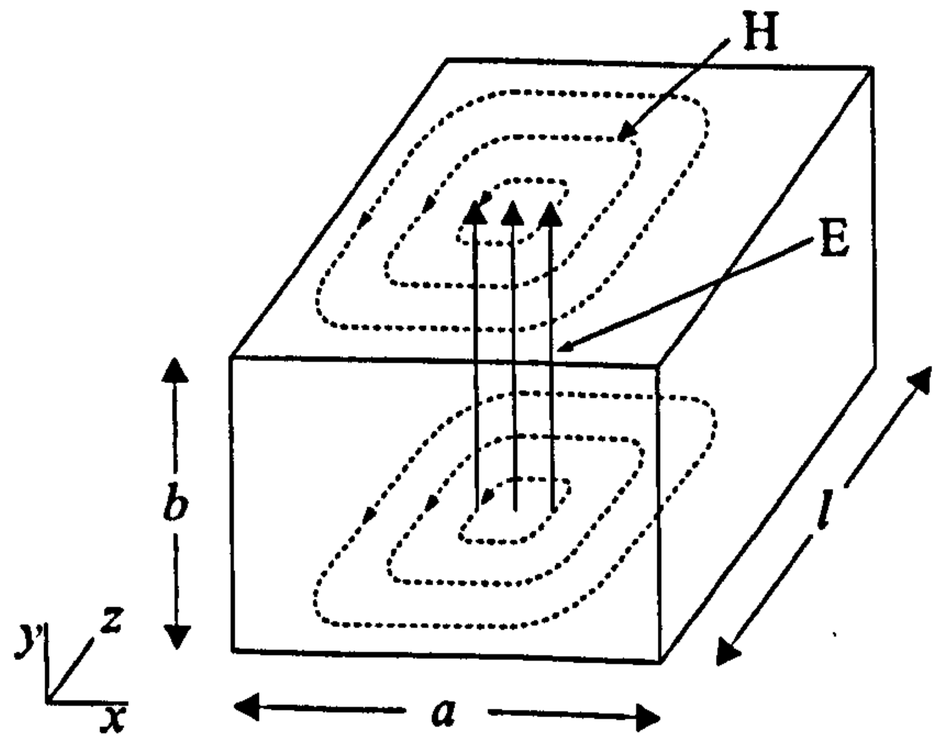

Figure 4.1: Field distribution of TE_{101} rectangular cavity

In such cavity resonators, the resonant frequency for a TE_{101} cavity may be

calculated from, [75],

$$f_{mnp} = \frac{c}{2\pi\sqrt{\mu_r\varepsilon_r}}\sqrt{\left(\frac{m\pi}{a}\right)^2 + \left(\frac{n\pi}{b}\right)^2 + \left(\frac{p\pi}{l}\right)^2} \tag{4.5}$$

The rectangular waveguide should be designed to operate at a considerably higher frequency than the cutoff frequency which is given as

$$\omega_c = v\left[\left(\frac{m\pi}{a}\right)^2 + \left(\frac{n\pi}{b}\right)^2\right]^{1/2} \tag{4.6}$$

where v is the velocity of light in a dielectric medium and for a typical aspect ratio of $a = 2b$ in free space, ω_c, is given by

$$\omega_c = \frac{c\pi}{a}(m^2 + 4n^2)^{1/2} \tag{4.7}$$

The reason for this design factor concerns the group velocity of the waveguide, v_g, given by

$$\lambda_g = \frac{d\omega}{d\beta} = v\left[1 - \left(\frac{\omega_c}{\omega}\right)^2\right]^{1/2} \tag{4.8}$$

As shown, as v_g approaches zero, ω approaches ω_c and β tends to zero leading to phase distortions as the signal frequency approaches too close to the cutoff frequency. The guide wavelength for a TE_{10} waveguide is defined as

$$\lambda_g = \frac{2\pi}{\beta} = \frac{\lambda_0}{[1 - (\omega_c/\omega)^2]^{1/2}} \tag{4.9}$$

where λ_0 is the free space wavelength, β is the propagation constant and ω_c is the cutoff frequency. For the E field to be zero at $z = 0$ and $z = l$ to form a TE_{101} mode cavity resonator, l must be one half-guide wavelength and knowing the cutoff frequency of a mode in a rectangular waveguide, this length is given as

$$l = \frac{\lambda_g}{2} = \frac{\lambda_0}{2[1-(\omega_c/\omega)^2]^{1/2}} = \frac{\lambda_0}{2[1-(\lambda_0/2a)^2]^{1/2}} \tag{4.10}$$

which allows the resonant frequency to be calculated from

$$f_0 = \frac{c}{\lambda_0} = \frac{c(a^2+l^2)^{1/2}}{2al} \tag{4.11}$$

The effects of finite losses in the conducting walls determine the unloaded Q of the resonator. This can be calculated by forming a volume integral of E_y to determine the stored energy and dividing it by the dissipated energy due to currents in the walls of the resonator, [76]. The quality factor of the resonance may be estimated from,

$$\begin{aligned} Q\frac{\delta}{\lambda_0} = \frac{abc}{4} \times \frac{\left[\left(\frac{m}{a}\right)^2+\left(\frac{n}{b}\right)^2\right]\left[\left(\frac{m}{a}\right)^2+\left(\frac{n}{b}\right)^2+\left(\frac{p}{c}\right)^2\right]^{\frac{3}{2}}}{ac\left\{\left(\frac{m}{a}\right)^2\left(\frac{p}{c}\right)^2+\left[\left(\frac{m}{a}\right)^2+\left(\frac{n}{b}\right)^2\right]^2\right\}} \\ +bc\left\{\left(\frac{n}{b}\right)^2\left(\frac{p}{c}\right)^2+\left[\left(\frac{m}{a}\right)^2+\left(\frac{n}{b}\right)^2\right]^2\right\} \\ +ab\left(\frac{p}{c}\right)^2\left[\left(\frac{m}{a}\right)^2+\left(\frac{n}{b}\right)^2\right] \end{aligned} \tag{4.12}$$

This leads to the following result for the unloaded Q for a TE_{101} mode cavity,

$$Q_{u101} = \frac{\lambda}{\delta}\frac{abl}{2}\frac{\left(\frac{1}{a^2}+\frac{1}{l^2}\right)^{3/2}}{\frac{l}{a^2}(a+2b)+\frac{a}{l^2}(l+2b)} \tag{4.13}$$

where λ/δ is the ratio of free space wavelength to the skin depth of the conductor at the resonant frequency. To find the overall Q, any losses in the lossy dielectric medium must be accounted for and is found from equation 3.4 and the total loss may be calculated from,

$$Q_{101} = \left(\frac{1}{Q_{u101}} + \frac{1}{Q_u}\right)^{-1} \tag{4.14}$$

The design equations above have produced initial dimensions based on a dielectric waveguide resonator with short-circuited ends to approximate the TE_{101} mode, however, the resonator used in this filter has open-circuited ends to allow coupling to the transmission line to produce the required attenuation transfer response. These open ends allow a small leakage of magnetic fields outside the dielectric boundary. Although the resonator length was designed to be $l = \lambda_g/2$, such that there was a half cycle in the z-direction, for classification correctness the mode is defined as the dielectric-loaded $TE_{10\delta}$ mode. The subscript, δ, denotes a noninteger ratio $2l/\lambda_g < 1$ in the z-axis to account for the leaky fields, however, calculations from this section are still applicable in the design of the initial dimensions of the $TE_{10\delta}$ mode dielectric-loaded resonator.

4.3 Configuration of Proposed Filter

The proposed filter follows the classical design of bandstop filters with a planar topology consisting of a main transmission line capacitively coupled to inductive stubs as shown figure 4.2, [73]. The same design can also be realised using a series of waveguide resonator cavities positioned periodically along a waveguide transmission line, figure 4.3. The principal objective is to load the waveguide resonator cavities with high ε_r dielectric material to reduce the volume of the resonant segments to form dielectric-loaded resonators coupled to a transmission line. From circuit theory, these segments must be spaced at odd multiples of a quarter wavelength to cover a relatively narrow bandwidth at the centre frequency.

As reported previously, [73], a disadvantage with the waveguide transmission line is a minimum resonator separation of $3\lambda/4$ is required to reduce interaction effects if the resonators are wide with respect to the transmission line. This increases the length of the transmission line but by using rectangular DRs, only $\lambda/4$ separa-

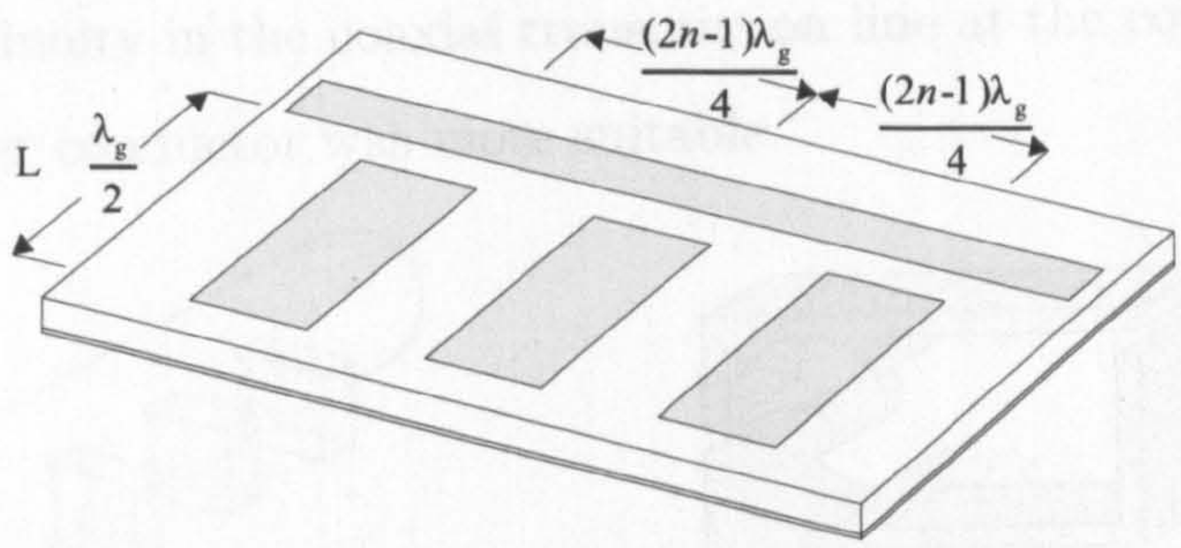

Figure 4.2: Schematic of third-degree strip transmission line bandstop filter

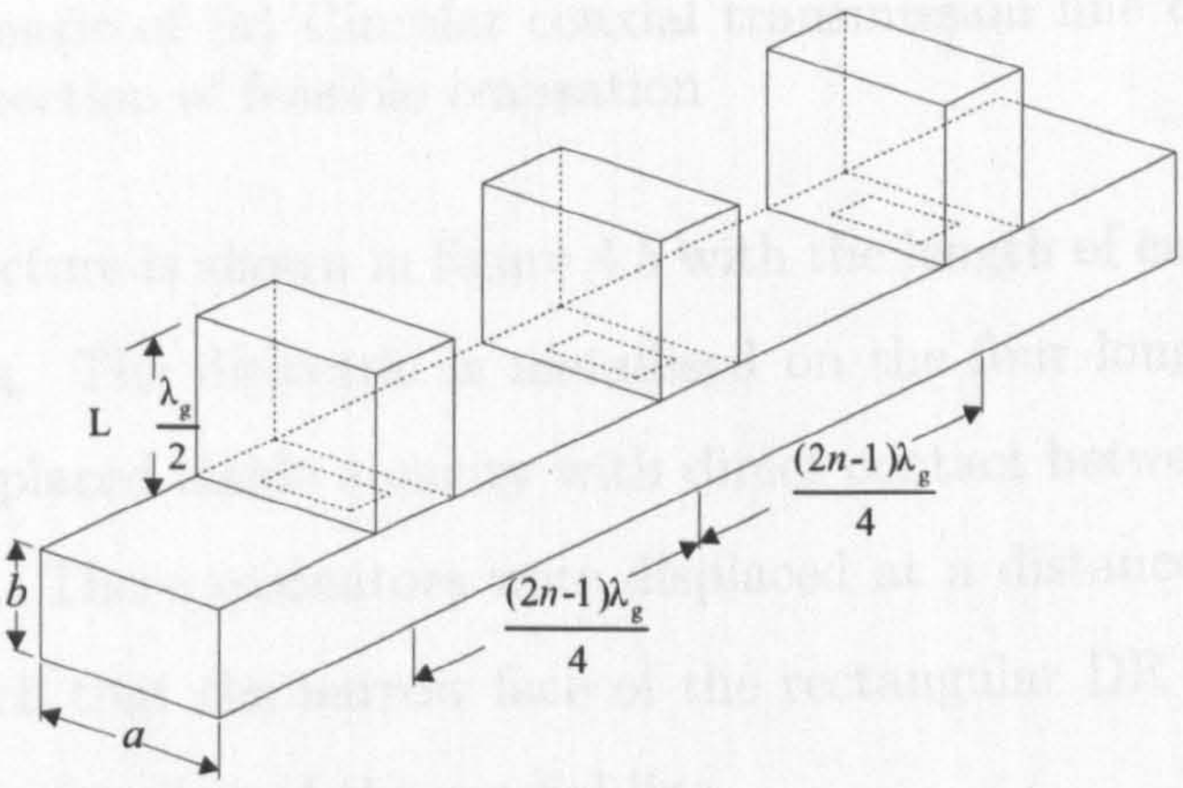

Figure 4.3: Schematic of third-degree cavity waveguide bandstop filter

tions would be needed reducing the length of the line leading to miniaturisation. For the $TE_{10\delta}$ DRs, a microstrip is possible but physical realisation would be complex and weak couplings between the resonators and transmission line would be problematic, even for narrowband designs. Also, shielding is needed to confine the fields leading to a larger volume. A coaxial line would be more advantageous as it is suitable for high power, allows ease of coupling and a uniform cross-section offers advanced configurations such as the broadband dielectric-loaded coaxial resonator, discussed later. An air-filled coaxial line with a square outer conductor, rather than circular, is chosen as the square shape compliments the rectangular DR waveguide for coupling purposes. If a conventional circular outer conductor was used, the fabricated lid would be positioned in the middle of the cross-section which will cause spurious effects in the transmission line, figure 4.4. In addition, portions of the outer circular coaxial conductor must be removed to enable a coupling window to the rectangular resonator. Removing this section

will cause a discontinuity in the coaxial transmission line at the coupling points. Thus, a square outer conductor was more suitable.

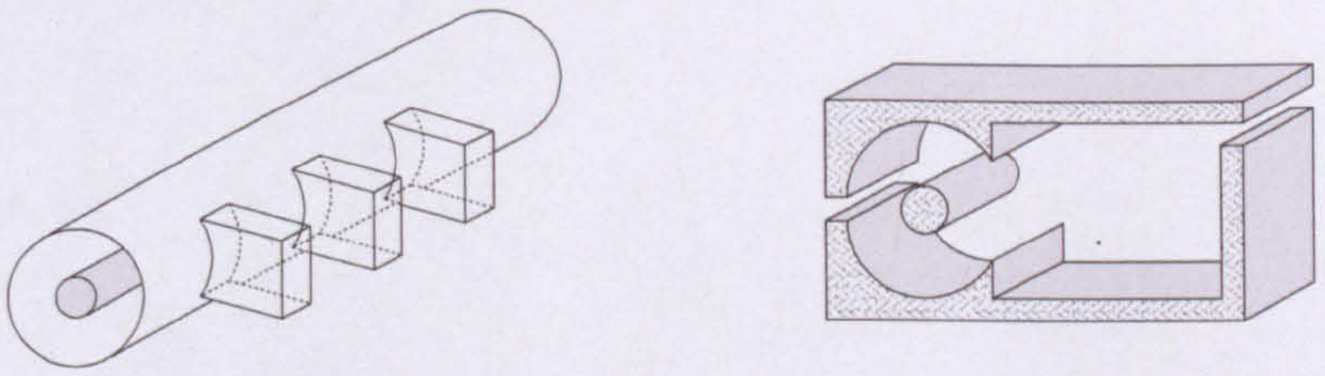

Figure 4.4: Schematic of (a) Circular coaxial transmission line coupled to DR cavities (b) Cross-section of feasible realisation

The resonator structure is shown in figure 4.5 with the length of each rectangular resonator $\lambda/2$ long. The dielectric is metallised on the four longer faces using silver plating and placed inside a cavity with direct contact between the sides of the DR and walls. These resonators were displaced at a distance from the line and positioned such that the narrow face of the rectangular DR was tangential to the propagation direction of the coaxial line.

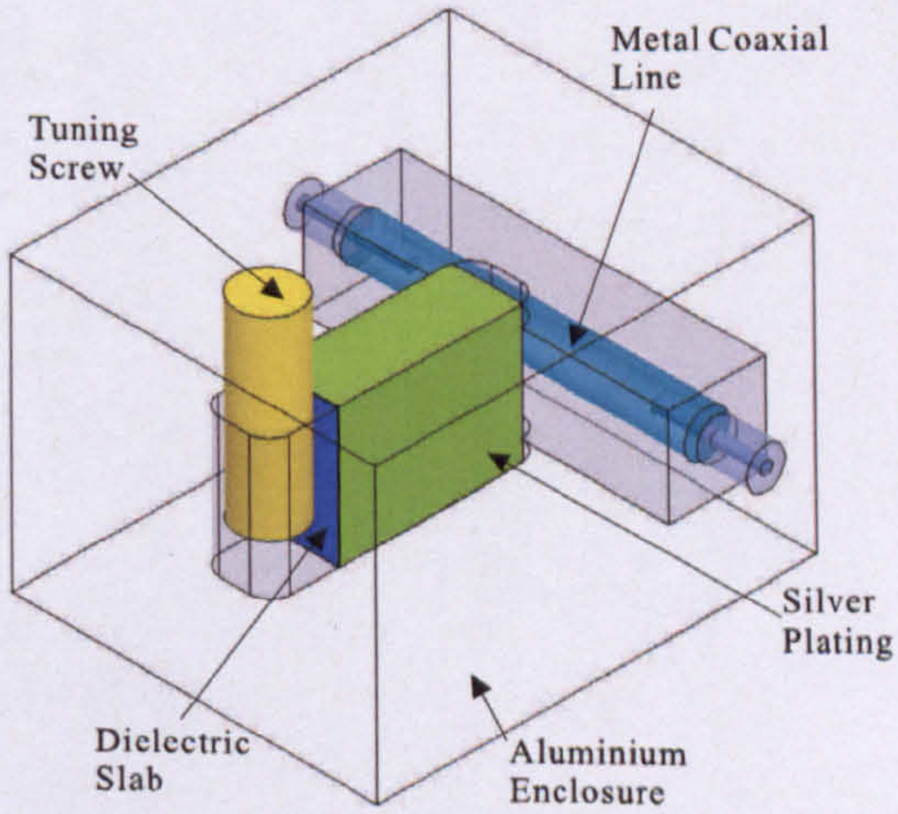

Figure 4.5: Structure of $TE_{10\delta}$ mode dielectric bandstop resonator

4.3.1 Single Resonator Design

The dielectric material was made from a compound of $CaTiO_3$-$NdAlO_3$ and have a permittivity of 44. They were manufactured with a measured $Q.f$ product of 41

000, therefore, at 2 GHz, a Q of 21 000 would be available. They also had a stable temperature coefficient of 1 ppm/°C in isolation. Initially, the dimensions for a rectangular waveguide operating in the $TE_{10\delta}$ mode with a resonant frequency of 2 GHz were calculated. To utilise the dominant mode, the width of the rectangular DR, a, was taken to be at least greater than $\lambda/2$. Taking into account the dielectric loading of the waveguide, the effective wavelength, λ_{eff}, is calculated from,

$$\lambda = \frac{c}{f} = \frac{3 \times 10^8}{2 \times 10^9} \quad \lambda_{eff} = \frac{\lambda}{\sqrt{\epsilon_r}} = \frac{15}{\sqrt{44}} = 22.6 \text{ mm} \tag{4.15}$$

However, this length should be kept near the minimum allowable value to ensure only the dominant mode propagates in the interested frequency range, therefore, higher-order modes are avoided. Thus, a was reduced to 14.1 mm and the height, b, was taken as approximately half the value of a, therefore, $b = 7.1$ mm. The length, l, of the resonator was then found by substituting these values into equation 4.11 to give,

$$l = \frac{\lambda_{eff}}{a[1 - (\lambda_{eff}/2a)^2]^{1/2}} = \frac{0.0226}{2[1 - (0.0226/0.0282)^2]^{1/2}} = 18.8 \text{ mm} \tag{4.16}$$

Using the above dimensions, the Q for this resonator was calculated, first by calculating the Q of the cavity with imperfect conducting walls and an ideal dielectric material with zero intrinsic loss. Taking into account that silver plating was used, at 2 GHz,

$$\frac{\lambda}{\delta} = \frac{1.479 \times 10^5}{\sqrt{f}} = 104581 \tag{4.17}$$

and substituting into equation 4.13,

$$Q_{u101} = 2586 \tag{4.18}$$

Hence, as $\tan\delta = 0.000048$,

$$Q_{u101} = \left(\frac{1}{Q_{u101}} + \frac{1}{Q_u}\right)^{-1} = 2302 \tag{4.19}$$

Thus, a large unloaded Q_u for a compact resonator is produced allowing the designer to achieve a narrowband response compensating for any losses that should occur such as coupling to a system, surface irregularities and other perturbations. The transmision line was a coaxial line enabling $\lambda/4$ separations between resonators coupled to the line. This enforces the objective to achieve miniaturisation since $3\lambda/4$ separations are needed in waveguide transmission lines to avoid unwanted inter-resonator couplings. To design the coaxial line, the empirical formula for a coaxial line with square outer conductor and round inner conductor is,

$$Z_0 = \frac{\eta_0}{2\pi\sqrt{\varepsilon_r}} \ln\left[(1.0787D/r)\right] \tag{4.20}$$

where η_0 is the wave impedance of free-space, D is the side of the square and r is the diameter of the inner conductor. A system impedance of 50 Ω and a dimension $D = 10$ mm was defined to give $r = 4.68$ mm and a simulated response as shown in figure 4.6. The coaxial transmission line achieved greater than 20 dB return loss over a 2 GHz bandwidth at an operation frequency of 2 GHz, thus, the transmission line was suitable for the design and these dimensions were used for the physical realisation. Details of the typical dimensions and physical performance for the resonator with coaxial connectors are shown in figure 4.7 and table 4.1. The position of the tuning screw has also been included, however, for simplicity, it was omitted in preliminary HFSS simulations.

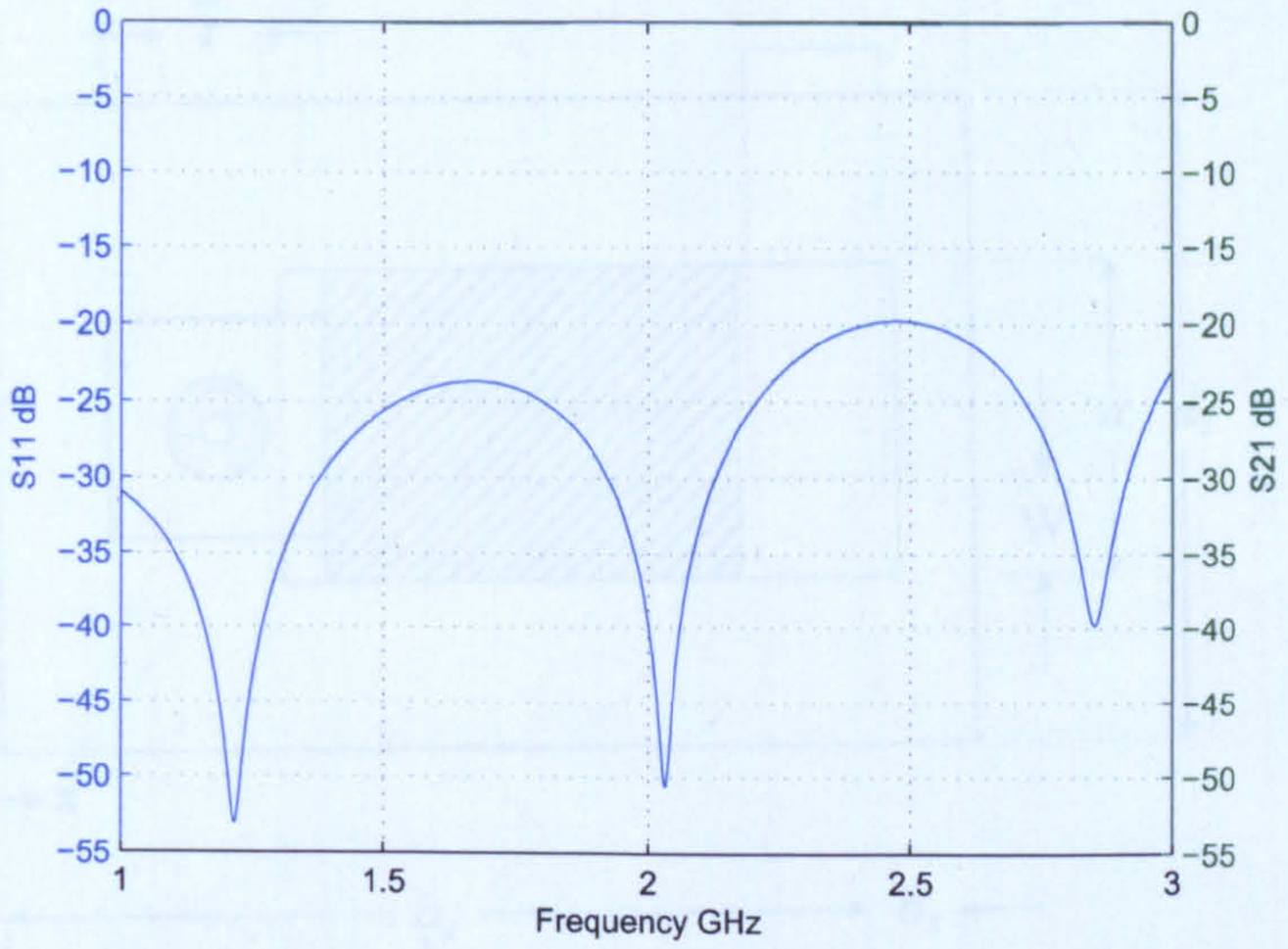

Figure 4.6: Frequency response of air-filled square coaxial TEM line with circular centre conductor, D = 10 mm and r = 4.68 mm

Typical Dimensions		Typical Performance
$a = 14.1$ mm	$l_1 = 45$ mm	$f_0 = 1.85$ GHz
$b = 7.1$ mm	$d_1 = 1.3$ mm	$\epsilon_r = 44$
$l = 18.1$ mm	$d_2 = 4.1$ mm	$Q_u = 2200$
$a_1 = 30$ mm	T = 1.7 mm	First spurious frequency 2.5 GHz
$b_1 = 45.1$ mm	s = 2.61 mm	
$b_2 = 47.1$ mm	D = 10 mm	
$b_3 = 5$ mm	r = 4.68 mm	

Table 4.1: Typical dimensions and performance of $TE_{10\delta}$ mode dielectric bandstop resonator

4.4 FEM Simulations

Electromagnetic field simulation has proved to be a useful tool for predicting the interaction of electromagnetic fields in microwave filter designs. By using the eigenmode solver of HFSS, FEM simulations of a $TE_{10\delta}$ mode rectangular DR with the calculated dimensions, produced field plots as shown in figures 4.8 and 4.9. The fields shown clearly represent those of a TE_{101} mode rectangular resonator as there are half-wave variations of the E component in both the x and z direction and no variations in the y direction. The tangential electric field

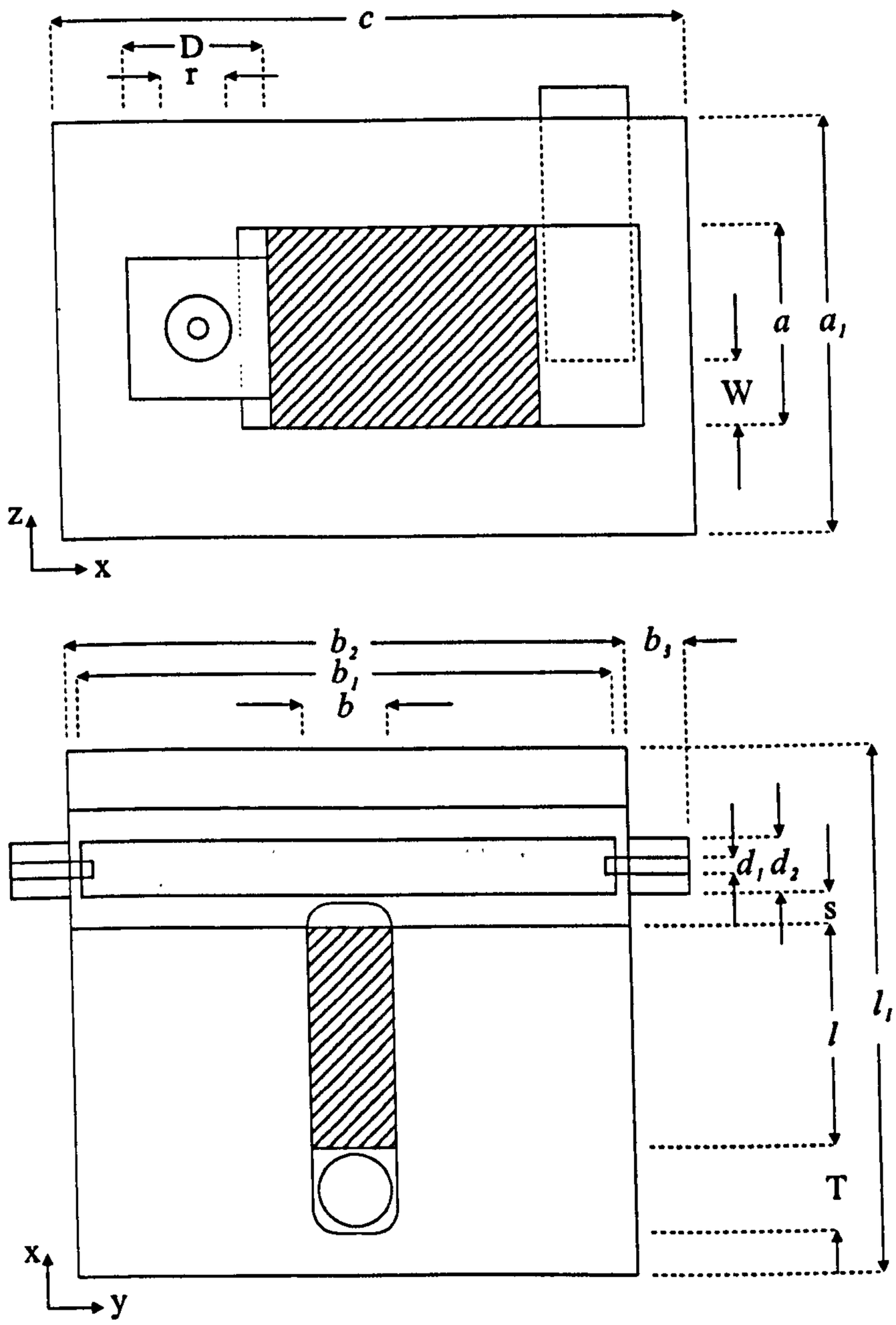

Figure 4.7: Details of $TE_{10\delta}$ mode dielectric bandstop resonator

vanishes at $x = 0$ and $x = l$ confirming the guide is one half wavelength long. Thus, the E field is zero at the end walls and has one maximum at the centre of the cavity. The figures also show how favourably the modal fields store electric energy within its boundary walls whereas magnetic energy is allowed to disperse beyond the air-dielectric interface. The natural frequencies of the first five modes were simulated and shown in table 4.2 showing the advantage of a broad first spurious response at 885 MHz above the fundamental frequency.

The dominant coupling between the transmission line and the rectangular DR was

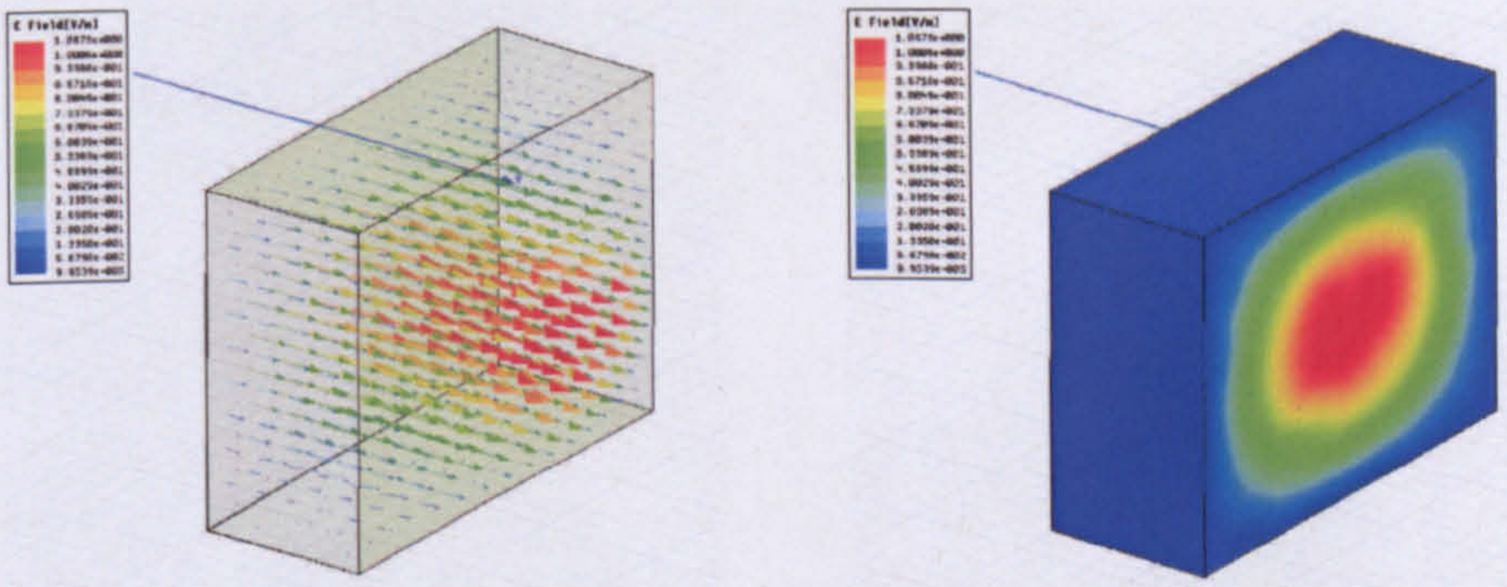

(a) (b)

Figure 4.8: Electric field of $TE_{10\delta}$ mode DR: (a)Vector Lines (b)Magnitude

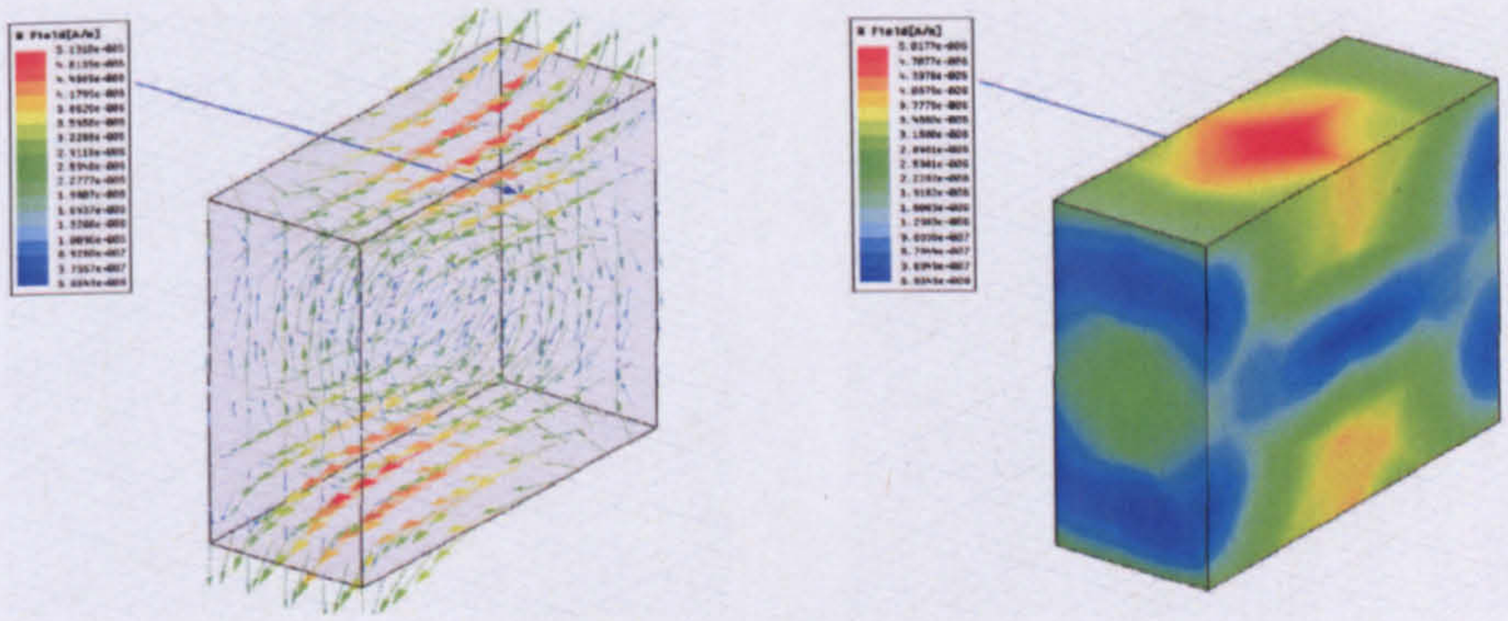

(a) (b)

Figure 4.9: Magnetic field of $TE_{10\delta}$ mode DR: (a)Vector Lines (b)Magnitude

Mode	Resonant Frequency GHz	Q_u
TE_{101}	2.0024	2554.1
TE_{102}	2.8847	3628.5
TE_{011}	3.3937	2457.6
TE_{201}	3.415	2879.1
TM_{110}	3.5533	3050.1

Table 4.2: Simulated resonant frequencies and Q_us of first five modes of isolated dielectric rectangular cavity resonator

magnetic since it has already been shown that the $TE_{10\delta}$ mode DR readily stores electric energy but allows magnetic fields to leak. Simulations for the field plots of transmission line to resonator couplings are shown in figure 4.10. To achieve the maximum coupling, the rectangular DRs were orientated such that the magnetic fields from both the resonator and transmission line were not orthogonal.

When the rectangular DR was coupled to the coaxial line, the resonant frequency

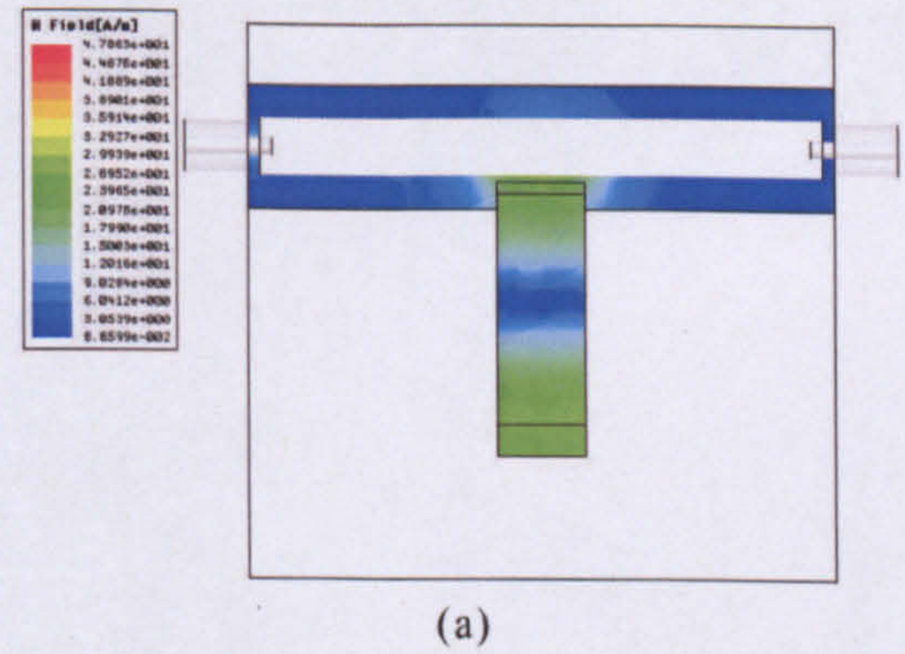

Figure 4.10: H-field plots of fundamental mode DR coupled to coaxial line: (a) Magnitude across transverse plan (b) Vector view cut through middle (c) Magnitude cut through middle

decreased in frequency from 2 GHz to 1.85 GHz. This was expected as the coupling was dominated by magnetic fields and inductance has an inverse relationship with frequency. The advantage of using an FEM solver is now apparent as fast simulations can be performed to observe the relationships between physical dimensions of the resonator and the required resonant frequency. It was found that the resonant frequency of the rectangular DRs was determined by their lengths with minimal dependence on the coupling distance to the coaxial line. Figure 4.11 shows the simulated resonant frequencies against DR length for different values of coupling spacing ranging from $s = 0.5$ mm to 10.5 mm. The 3 dB coupling bandwidth was simulated to find the coupling needed for different DR lengths ranging from $l = 12.8$ mm to 18.8 mm, figure 4.12. The simulation showed that for shorter DR lengths, greater coupling bandwidth can be attained, however, the compromise for this is the unloaded Q would decrease.

The first five modes and their resonant frequencies for the experimental resonator are shown in table 4.3. The mode classification has reverted back to classical

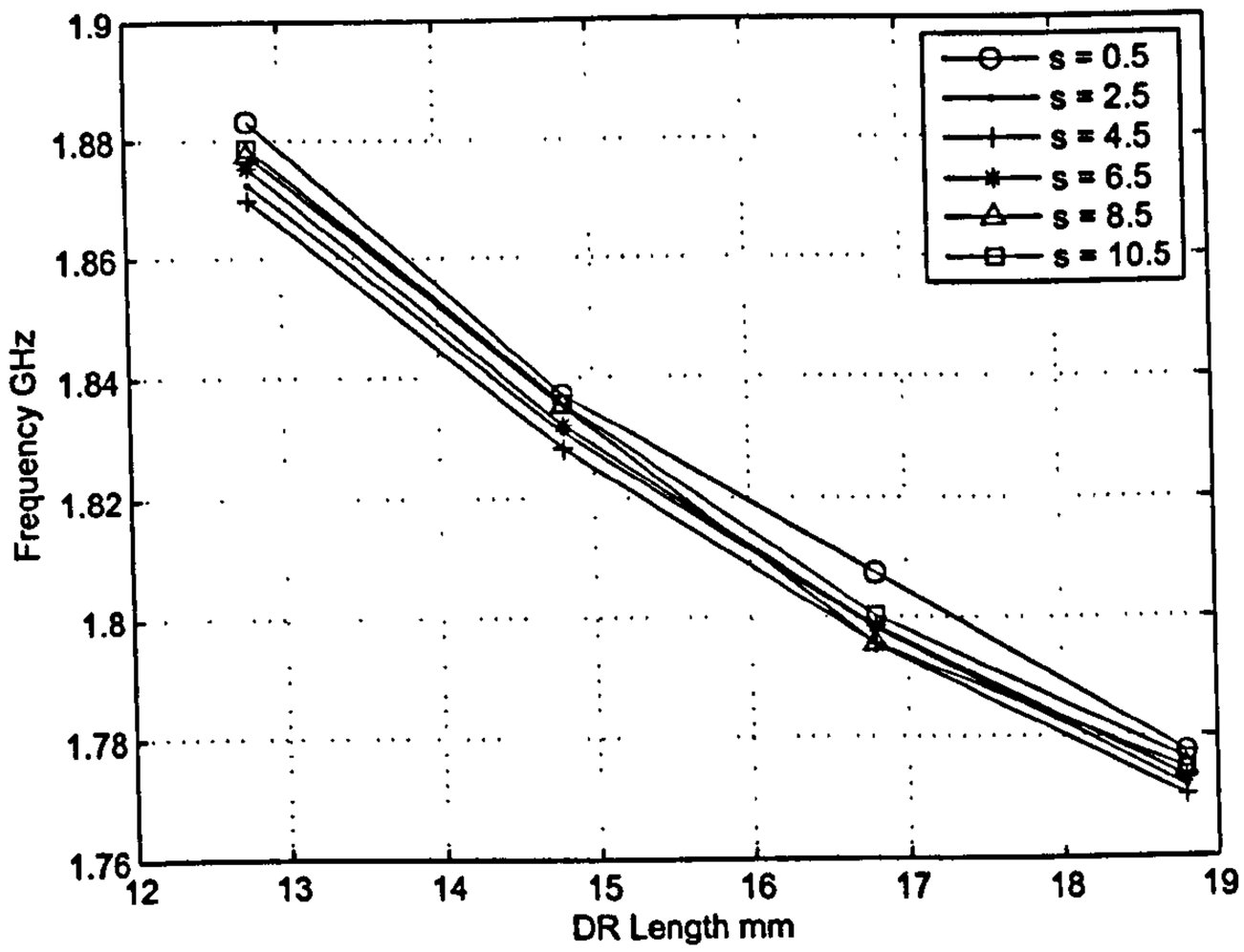

Figure 4.11: Resonant frequency versus DR length for various coupling gaps

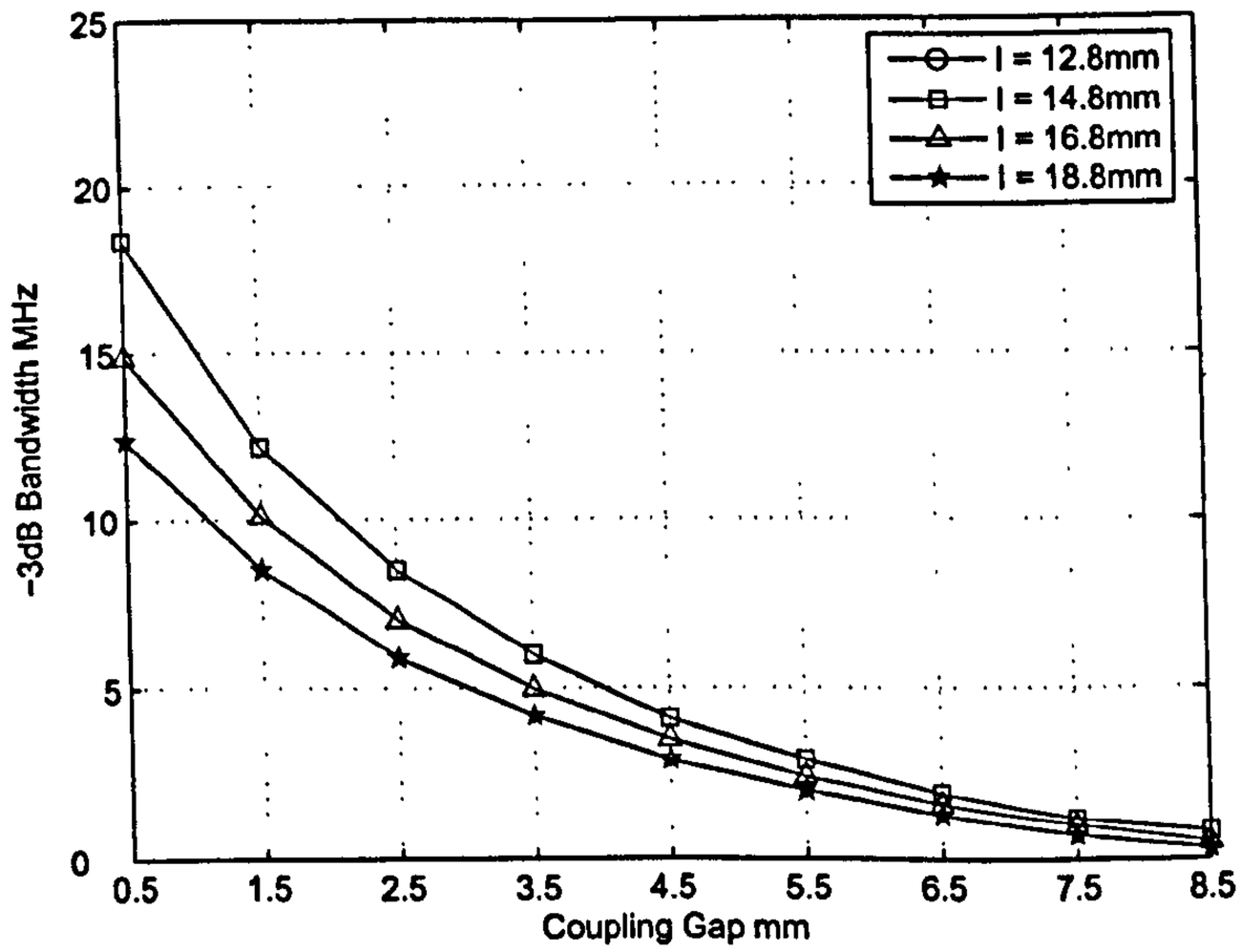

Figure 4.12: 3 dB bandwidth versus coupling gaps for different DR lengths

rectangular waveguide to distinguish between modes with wavelength variations in the z direction. The significant observation is the first spurious resonance has maintained a spurious-free bandwidth of approximately 650 MHz above the fundamental mode and confirms these resonators are superior to conventional DR resonators where poor spurious performance often gives rise to more complex

Mode No.	Name	Resonant Frequency GHz
1	TE_{101}	1.850
2	TE_{102}	2.494
3	TE_{011}	3.336
4	TE_{201}	3.356
5	TE_{103}	3.363

Table 4.3: First five resonant modes of prototype resonator

designs, [77].

4.5 4^{th} Degree Chebyshev Design

A Chebyshev prototype was designed using a shunt capacitor, inverter-coupled network to synthesise the network, figure 2.3 (b). The design follows that from [39]. The specifications of the filter were assumed to have a centre frequency of 1.85 GHz and a stopband insertion loss greater than 40 dB at 3 MHz bandwidth. The complete specifications were as shown in table 4.4. At 1.85 GHz, the separations between the transmission line to resonator tap points were calculated to be a quarter wavelength long to avoid unwanted inter-resonator coupling.

Filter Specifications	
Centre frequency	1.85 GHz
Passband bandwidth	d.c. - 1.844 GHz, 1.861 GHz - 2.5 GHz
Passband return loss (L_R)	20 dB
Stopband bandwidth	3 MHz
Stopband insertion loss (L_A)	> 40 dB
System Impedance	1 Ω

Table 4.4: Filter specifications

The degree of the filter needed to meet the requirements was calculated from, [39],

$$N \geq \frac{L_A + L_R + 6}{20 \log_{10}[S + (S^2 - 1)^{1/2}]} \geq 3.68 \tag{4.21}$$

where N is the order required and selectivity, S, is defined as the ratio of passband to stopband, therefore, a 4^{th} degree network was required and the ripple level, ε, was calculated from the following equation for a lowpass prototype,

$$\varepsilon = (10^{L_R/10} - 1)^{-1/2} = 0.1005 \tag{4.22}$$

Hence

$$\eta = \sinh\left[\frac{1}{N}\sinh^{-1}(1/\varepsilon)\right] = 0.8201 \tag{4.23}$$

Using,

$$C_r = \frac{2}{\eta}\sin\left[\frac{(2r-1)\pi}{2N}\right] \tag{4.24}$$

$$K_{r,r+1} = \frac{[\eta^2 + \sin^2(r\pi/N)]^{1/2}}{\eta} \tag{4.25}$$

giving

$$C_1 = C_4 = 0.9332 \tag{4.26}$$

$$C_2 = C_3 = 2.253 \tag{4.27}$$

$$K_{12} = K_{34} = 1.3204 \tag{4.28}$$

$$K_{23} = 1.5769 \tag{4.29}$$

For unity admittance inverters, a technique is used to scale the nodal admittance matrix for a ladder network to force the inverters to have the same value. A typical ladder network is shown in figure 4.13 with N + 2 nodes.

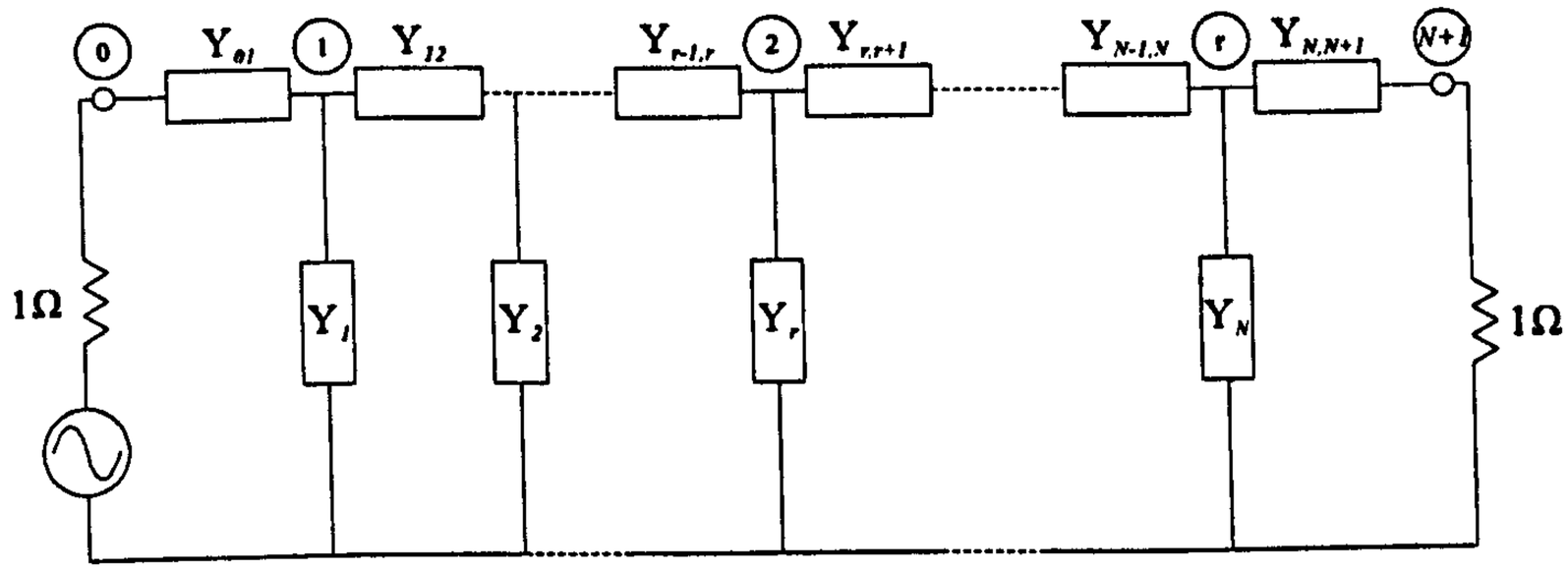

Figure 4.13: Ladder network

The general admittance matrix for the ladder network is,

$$[Y] = \begin{bmatrix}
Y_{00} & -Y_{01} & 0 & 0 & \cdots & & & & \\
-Y_{01} & Y_{11} & -Y_{12} & 0 & & & & & \\
0 & -Y_{12} & Y_{22} & & & & & & \\
0 & & \ddots & & & & & & \\
\vdots & & & -Y_{r-1,r} & & & & & \\
 & & -Y_{r-1,r} & Y_{rr} & Y_{r,r+1} & & & & \\
 & & & Y_{r,r+1} & & & & & \\
 & & & & \ddots & -Y_{N-1,N} & & & \\
 & & & & -Y_{N-1,N} & Y_{NN} & -Y_{N,N+1} & & \\
 & & & & & -Y_{N,N+1} & Y_{N+1,N+1} &
\end{bmatrix}$$

By multiplying each r^{th} row and column using the required constants, the internal nodal admittances can be scaled with negligible effect on the terminal characteristics of the network. Note that it is not possible to scale the input and output nodes, 0 and N+1 respectively, as transformers at the source and loads must be appropriately scaled independently. The inverters may be constructed from a single length of transmission line with no discontinuities and isolated from the resonators for improved response. Consider the nodal admittance matrix for the design,

$$[Y] = \begin{bmatrix} C_1p & -jK_{12} & 0 & 0 \\ -jK_{12} & C_2p & -jK_{23} & 0 \\ 0 & -jK_{23} & C_3p & -jK_{34} \end{bmatrix}$$

The scaling is performed through multiplying each row and column by a constant factor, A and B respectively. In this case, appropriate scaling is performed on the first and last nodes, therefore, the technique was also performed on the first and last columns in the matrix.

$$[Y] = \begin{array}{c} \begin{array}{cccc} \downarrow A & \downarrow B & \downarrow B & \downarrow A \end{array} \\ \begin{bmatrix} C_1p & -jK_{12} & 0 & 0 \\ -jK_{12} & C_2p & -jK_{23} & 0 \\ 0 & -jK_{23} & C_3p & -jK_{34} \\ 0 & 0 & -jK_{34} & C_4p \end{bmatrix} \end{array} \begin{array}{l} \leftarrow A \\ \leftarrow B \\ \leftarrow B \\ \leftarrow A \end{array}$$

$$[Y] = \begin{bmatrix} A^2C_1p & -jABK_{12} & 0 & 0 \\ -jABK_{12} & B^2C_2p & -jB^2K_{23} & 0 \\ 0 & -jB^2K_{23} & B^2C_3p & -jABK_{34} \\ 0 & 0 & -jABK_{34} & A^2C_4p \end{bmatrix}$$

Scaling the middle two rows and columns, the following equations are obtained and from equations 4.30 and 4.31, values for the constants, A and B, are found that satisfy the condition for unity inverters. The constant, A, was used to scale the source and load impedances in the circuit simulations for the correct impedance.

$$K_{23}B^2 = 1, \quad B = 0.7963 \tag{4.30}$$

$$K_{12}AB = 1, \quad A = 0.9511 \tag{4.31}$$

The new element values with unit inverters were then calculated

$$C_1 = C_4 = 0.8441 \tag{4.32}$$

$$C_2 = C_3 = 1.4287 \tag{4.33}$$

$$K_{12} = K_{23} = K_{34} = 1 \tag{4.34}$$

These element values have been calculated for a broadband lowpass prototype. For this particular design, the $TE_{10\delta}$ filter is coupled to the transmission line through magnetic coupling and is narrowband, approximately 5%, therefore, the lowpass prototype was modified by the reactance slope parameter method. The reactance slope parameter determines the rate of change of the reactance with frequency. A steep gradient expresses a fast changing reactance when varying the frequency, which corresponds to a high-Q resonator. A comparison of two resonators having the same resonant frequency, f_c, is shown in figure 4.14(a). A high Q resonator equates to a steeper reactance slope. The reactance slope parameter is a useful tool to relate the resonance properties of any circuit to a simple lumped circuit. Any dual types of resonator with the same reactance slope demonstrates a similar frequency response. For a series resonant circuit, the general definition of the reactance slope parameter, x, can be written as, [57],

$$x = \frac{\omega_0}{2}\frac{dX}{d\omega}\bigg|_{\omega_0} \quad \Omega \tag{4.35}$$

By forcing the impedance inverters to be fixed at unity to allow a broader out-of-band bandpass response, it is necessary to use a decoupled structure to control the coupling between transmission line and resonator. Although the DR should, strictly, be modelled as an open circuit stub of length $\lambda/2$, calculated elements

for a magnetic coupled resonator is used in the circuit model to simulate the inductive coupling between the transmission line and DR. The two circuits in figure 4.14(b) are now considered.

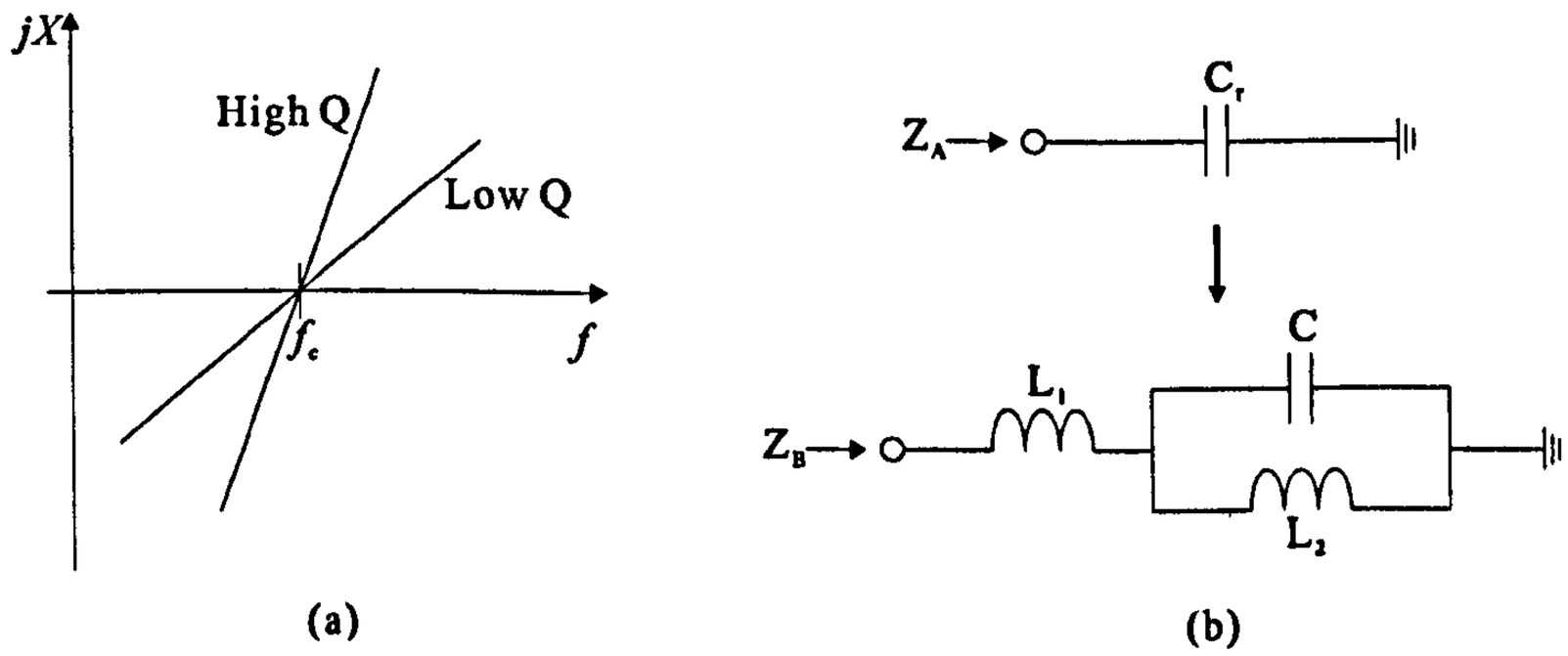

Figure 4.14: Transforming resonators of equivalent Q (a) Reactance slope parameter (b) Transformation of capacitor to magnetically-coupled resonator

For two circuits to have the same Q value, it is required that their reactance slope should be equal. Z_A is an input impedance to a lowpass to bandstop transformed capacitor using equation 2.3, which may be expressed as

$$Z_A(j\omega) = \frac{\alpha}{C_r}\left(\frac{\omega}{\omega_0} - \frac{\omega_0}{\omega}\right) \tag{4.36}$$

Z_B is the input impedance of the magnetically-coupled transmission line resonator, which can be expressed as

$$Z_B(p) = L_1 p + \frac{1}{C + 1/L_2 p} \tag{4.37}$$

$$= \frac{L_1 p + L_2 p + C L_1 L_2 p^3}{1 + C L_2 p^2} \tag{4.38}$$

Hence

$$Z_B(j\omega) = \frac{j\left[\omega(L_1 + L_2) - \omega^3 C L_1 L_2\right]}{1 - \omega^2 C L_2} \tag{4.39}$$

Equation (4.35) states the reactance slope of the resonator can be found by differentiating the reactance expression of such a resonator, thus

$$\frac{dZ_A(j\omega)}{d\omega} = \frac{\alpha}{C_r}\left(\frac{1}{\omega_0} + \frac{\omega_0}{\omega^2}\right) \tag{4.40}$$

and

$$\left.\frac{dZ_A(j\omega)}{d\omega}\right|_{\omega=\omega_0} = \frac{2\alpha}{C_r\omega_0} \tag{4.41}$$

Also,

$$\left.\frac{dZ_B(j\omega)}{d\omega}\right|_{\omega=\omega_0} = 2L_1^2\left(\frac{L_1+L_2}{L_1L_2}\right) \tag{4.42}$$

At resonance, $Z_B = 0$, thus

$$\omega_0 = \sqrt{\frac{L_1+L_2}{CL_1L_2}} \tag{4.43}$$

Substituting equation (4.43) into (4.42) and equating with (4.41) yields

$$\frac{\alpha_0}{C_r\omega_0} = \omega_0^2 CL_1^2 \tag{4.44}$$

The value of C can be chosen for physical realisabilty and L_1 and L_2 are found through solving equations (4.43) and (4.44) simultaneously.

From (4.43)

$$\frac{L_1+L_2}{L_1L_2} = \omega_0^2 C \tag{4.45}$$

and from (4.44) and (4.45)

$$\frac{L_1 + L_2}{L_1 L_2} = \frac{\alpha}{\omega_0 C_r L_1^2 = \omega_0^2 C} \tag{4.46}$$

Hence

$$L_{1r} = \sqrt{\frac{\alpha}{\omega_0^3 C_r C}} \tag{4.47}$$

and

$$L_{2r} = \frac{L_{1r}}{\omega_0^2 C L_{1r} - 1} \tag{4.48}$$

The bandwidth scaling factor is $\alpha = f_0/\Delta f$, and choosing all the capacitors to be 3 pF in a 1 Ω system, the transformed element values are calculated from equations (4.47) and (4.48)

$$L_{11} = L_{14} = 8.80 \text{ nH} \tag{4.49}$$

$$L_{12} = L_{13} = 6.76 \text{ nH} \tag{4.50}$$

$$L_{21} = L_{24} = 3.43 \text{ nH} \tag{4.51}$$

$$L_{22} = L_{23} = 3.88 \text{ nH} \tag{4.52}$$

The final prototype circuit is shown in figure 4.15 with all unit elements a quarter wavelength long at the centre frequency and have characteristic impedance of 50 Ω. A circuit simulation produced a frequency repsonse of the ideal 4^{th} degree Chebyshev bandstop filter, figure 4.16.

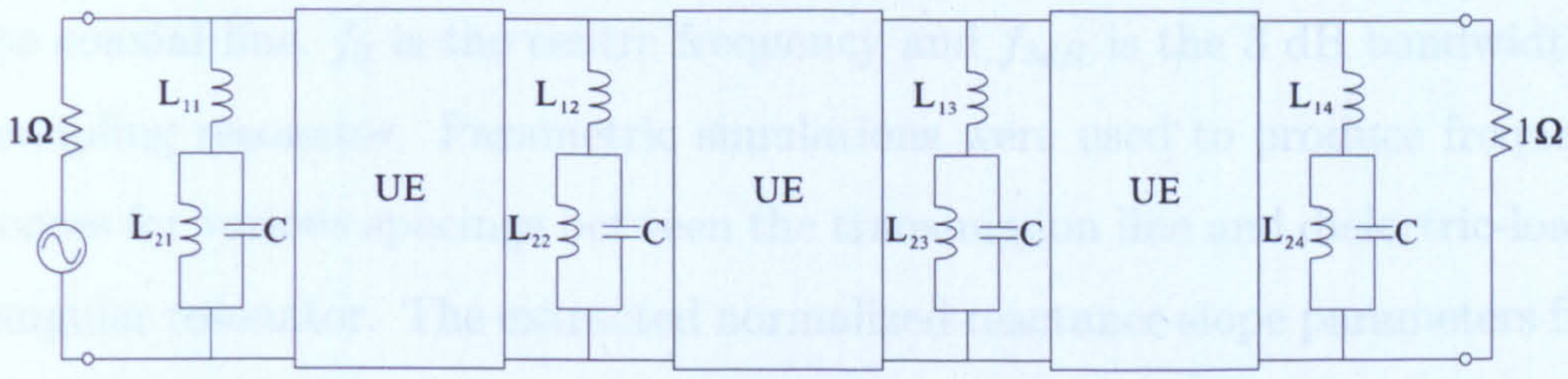

Figure 4.15: Prototype circuit for 4^{th} degree Chebyshev bandstop filter

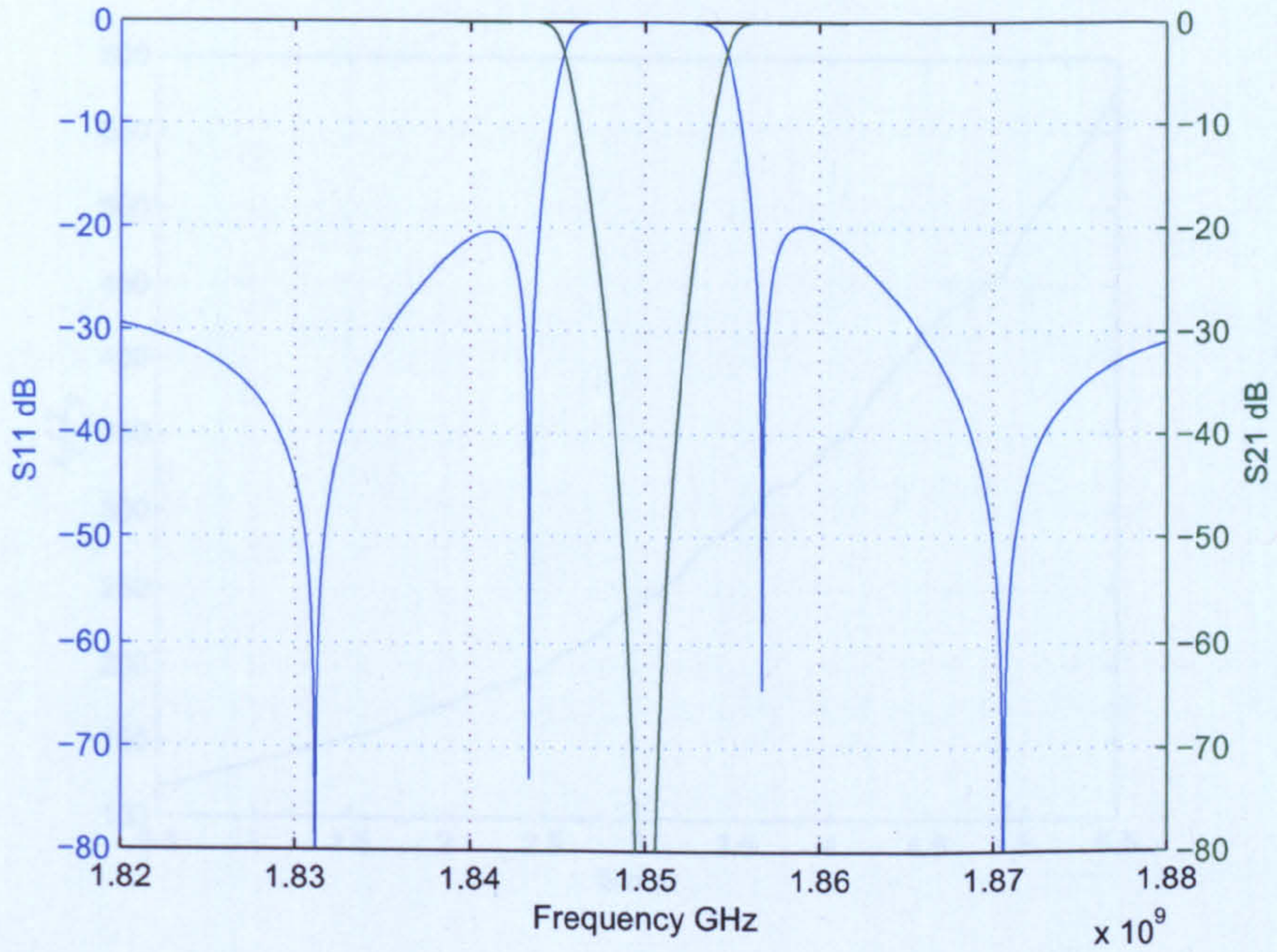

Figure 4.16: Simulated results of prototype network for 4^{th} degree Chebyshev bandstop filter

In order to realise the dielectric filter, a technique was used to equate equivalent normalized reactance slope parameters of individual resonators between the circuit and EM simulated models, commonly used to design microstrip bandstop filters, [78]. The required coupling between each resonator to the transmission line was dependent on the spacing determined by finding the normalized reactance slope parameter from the following expression,

$$\frac{x_i}{Z_0} = \frac{f_0}{2\Delta f_{3dB}} \tag{4.53}$$

where x_i/Z_0 is the normalized reactance slope parameter of a resonator coupled

to the coaxial line, f_0 is the centre frequency and f_{3dB} is the 3 dB bandwidth of the coupling resonator. Parametric simulations were used to produce frequency responses for various spacings between the transmission line and dielectric-loaded rectangular resonator. The extracted normalized reactance slope parameters from these frequency responses were taken from which the desired coupling gap was interpolated from figure 4.17.

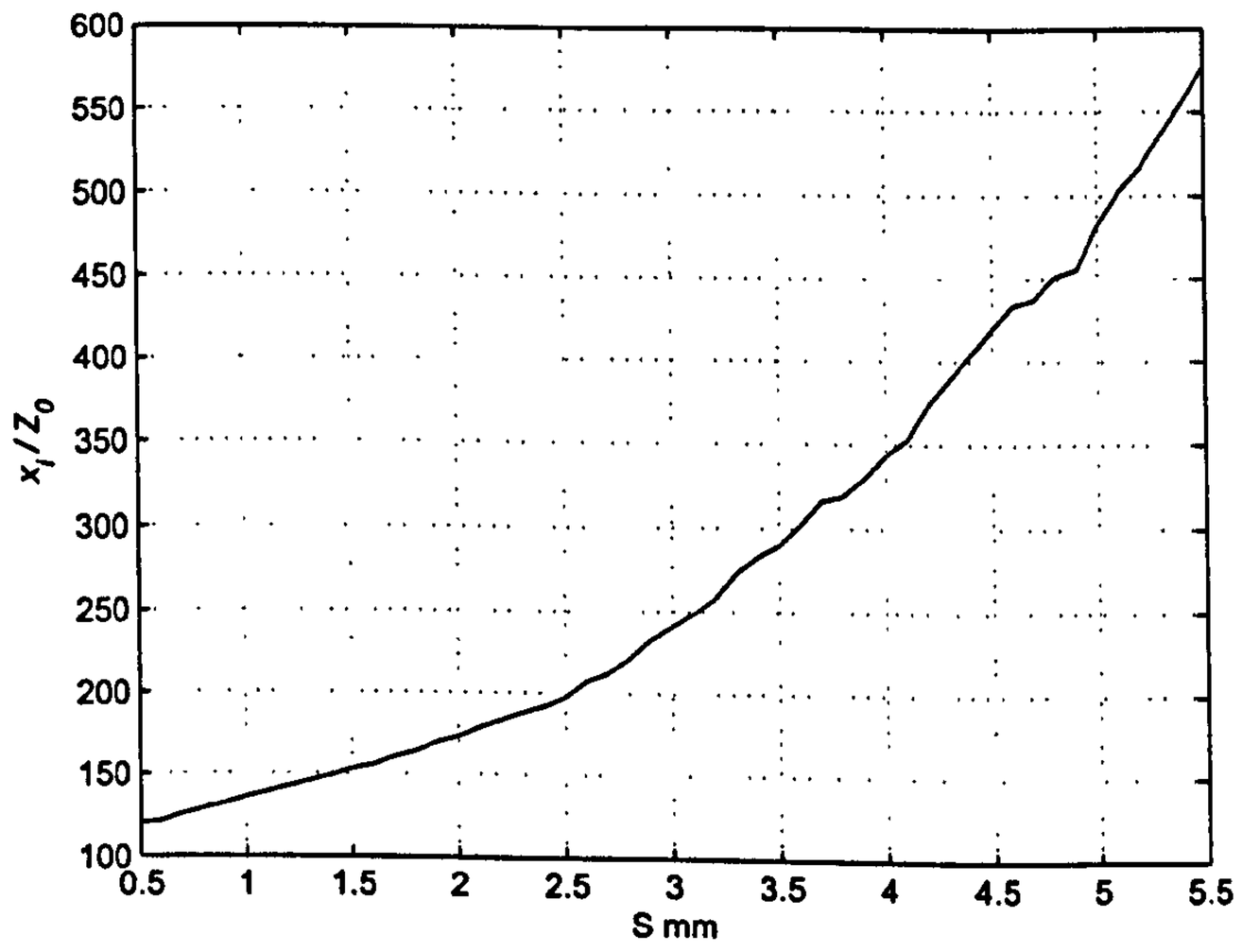

Figure 4.17: Normalized reactance slope parameter against spacing of resonator from coaxial line

It is important to know the physical parameters that control the frequency and bandwidth for each resonator independently. The coupling bandwidth was determined by the distance between the DR and coaxial transmission line and the resonant frequency was at first determined by the space between the end wall and the open end of the resonator that could accomodate a tuning screw. Following this, the resonant frequency was determined by the depth of the tuning screw. An advantage with FEM solvers is simulations can be performed to observe variations in parameters to obtain the optimised dimensions needed. A limiting factor in the accuracy of these simualations is determined by computing power, thus, these simulations only provide, at best, optimum solutions. As the filter was symmetrical, only simulations for the first two resonators for optimisation were

required, figure 4.18.

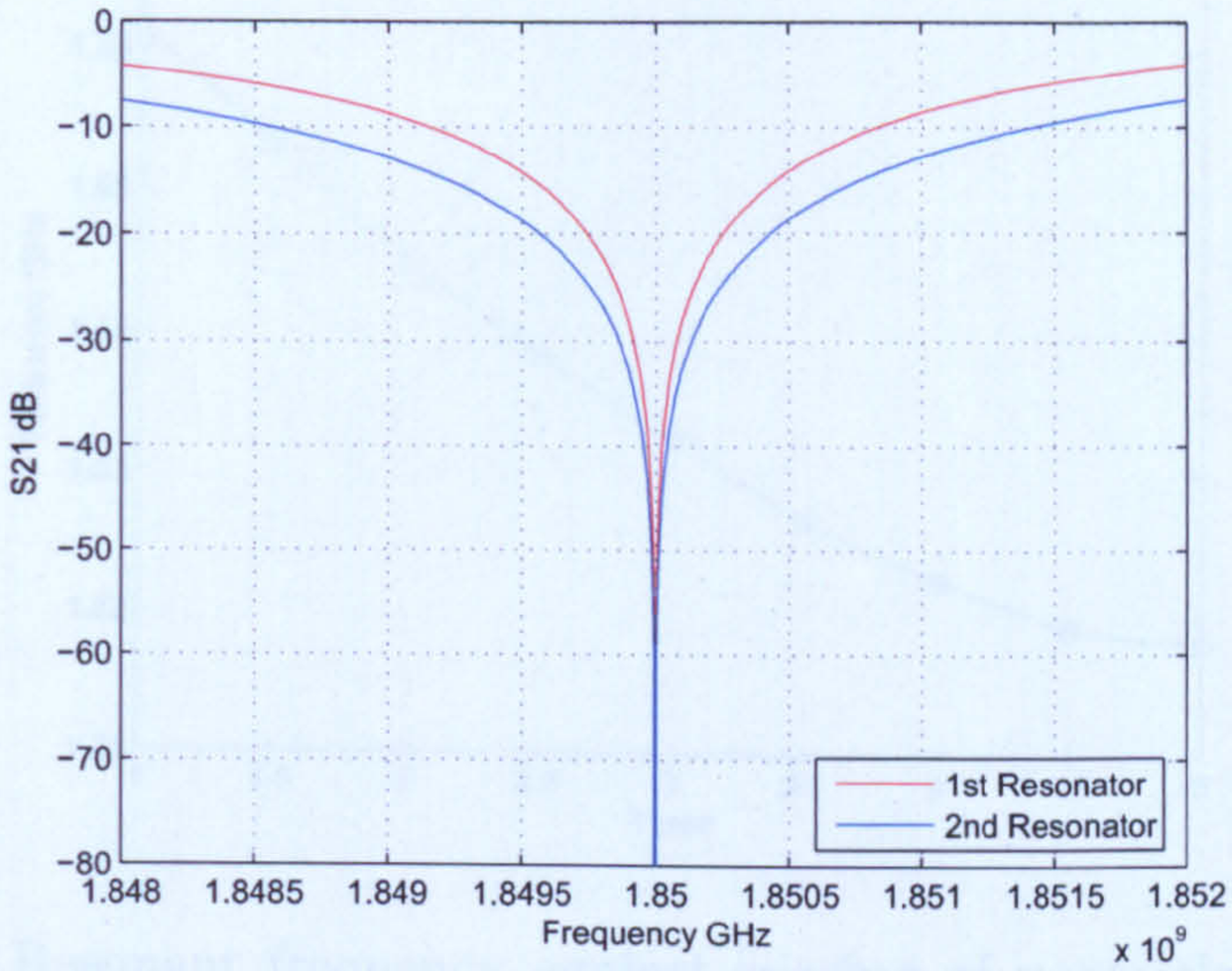

Figure 4.18: 3 dB bandwidth of 1^{st} = 5.1 MHz and 2^{nd} = 8.6 MHz resonator in Chebyshev design with f_0 = 1.85 GHz

The relationship between the resonant frequency and spacing between the uncoupled side of the resonator and wall of cavity is shown in figure 4.19. Fields in this region may be modelled as a series inductance, thus, a tuning screw inserted here will effectively increase the resonant frequency. The end cavity wall must, therefore, be at a greater distance from the open face of the rectangular resonator such that the resonant frequency is lower than centre frequency in order to tune up to the correct frequency. A plot of resonant frequency against tuning screw depth is shown in figure 4.20.

The next step was to optimise the dimensions of the dielectric resonator and the tuning screw such that the simulated response curve closely matched the ideal response of the circuit model. As shown from figure 4.21 and figure 4.22, a close approximation between the circuit model response and 3D model response was achieved for individual first and second resonators. The length of separations between each resonator, initally calculated from $\lambda/4$, provided an asymmetrical response and was corrected through an optimised separation of 91°. The final filter was simulated in HFSS meeting the specifications of the bandstop filter as

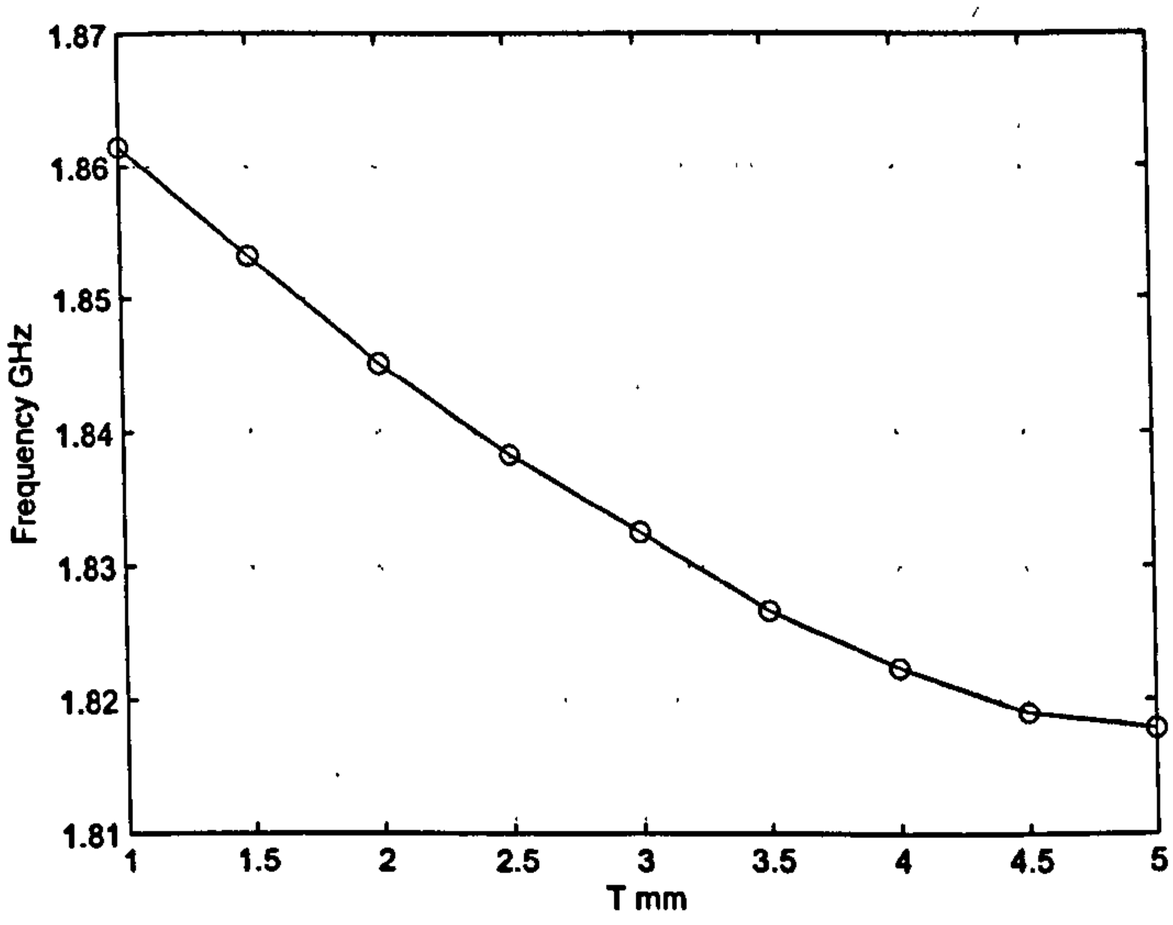

Figure 4.19: Resonant frequency against spacing of uncoupled dielectric side with sidewall

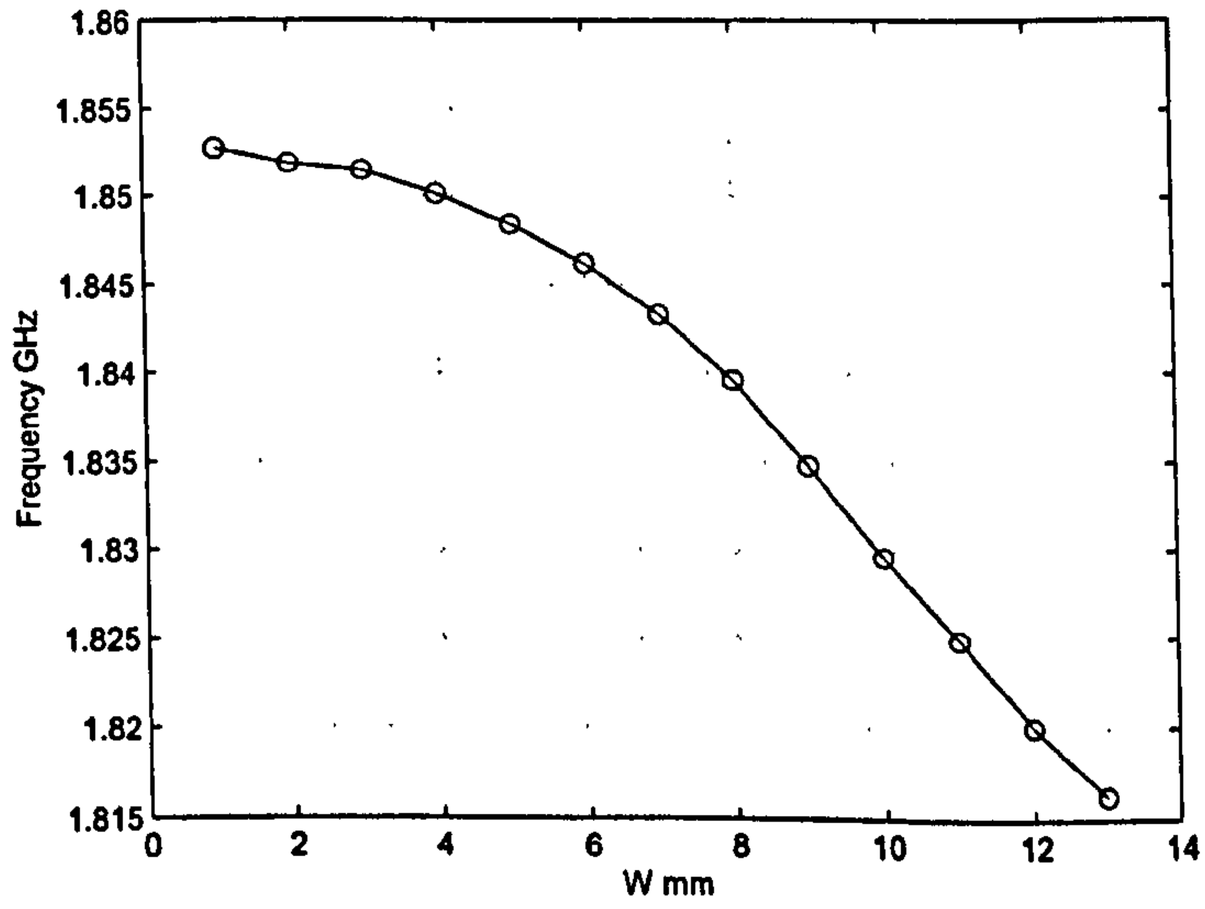

Figure 4.20: Simulated resonant frequency against depth of tuning screw

shown in figure 4.23.

The final practical filter was simulated with the optimised tuning screws as shown in figure 4.24 and the simulation showed a 3 dB bandwidth of 10.9 MHz at centre frequency of 1.85 GHz. The input and output couplings were also optimised to achieve low loss in out-of-band performance and a 1 mm gap was the optimised distance between the inner coaxial conductor and the outer cavity walls.

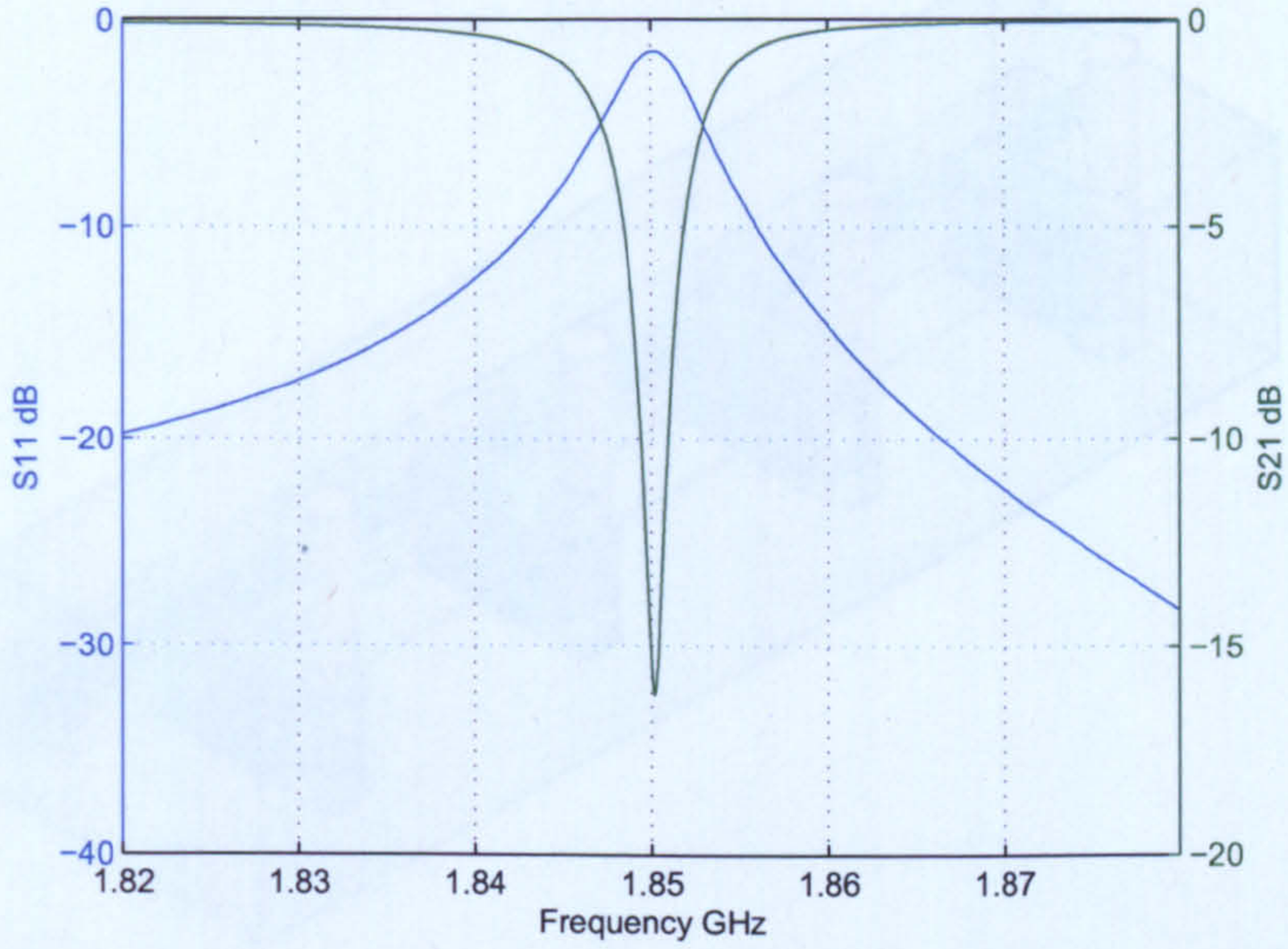

Figure 4.21: HFSS simulated tuned 1st resonator, 3 dB bandwidth = 5.11 MHz and f_0 = 1.8502 GHz

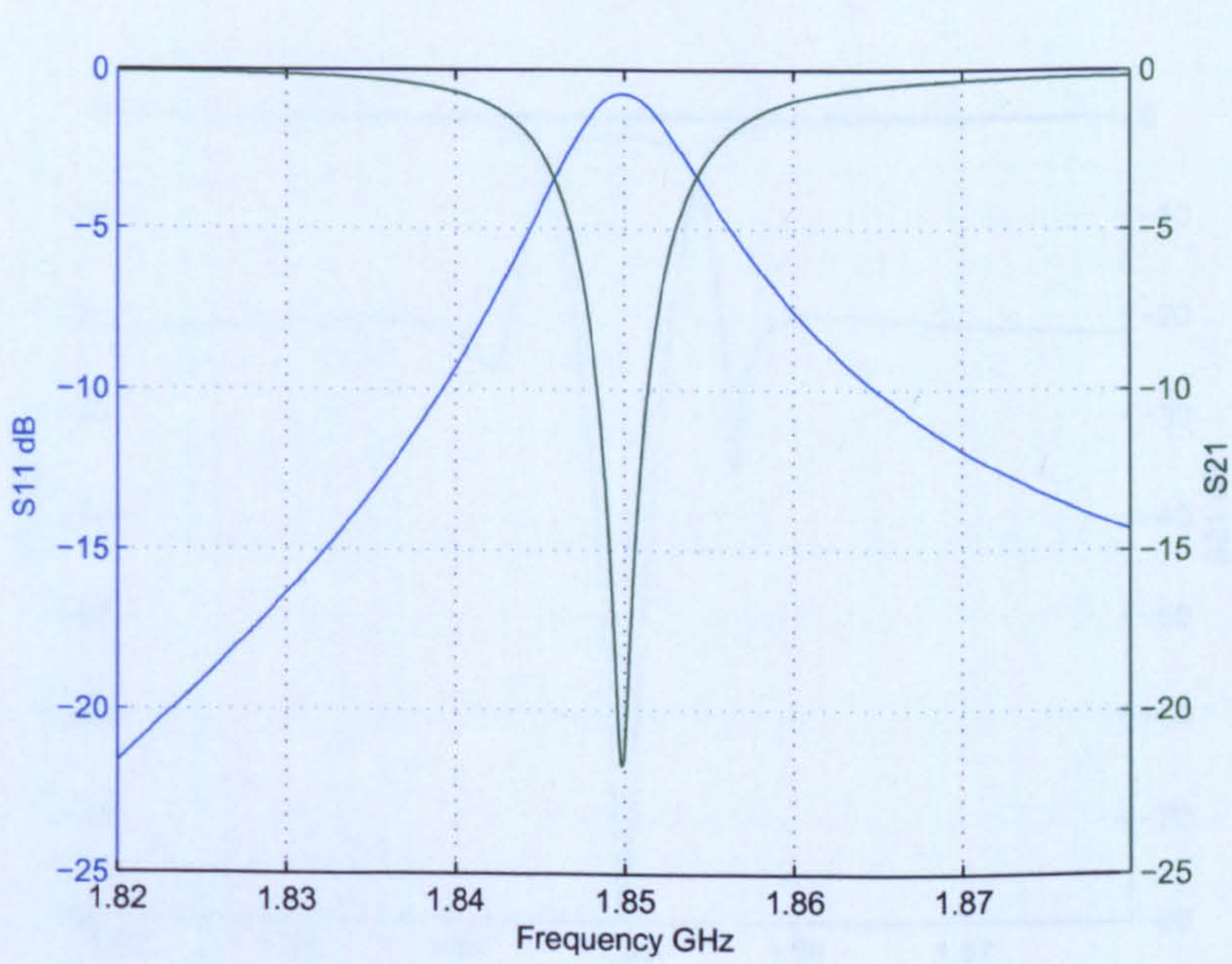

Figure 4.22: HFSS simulated tuned 2nd resonator, 3 dB bandwidth = 9 MHz and f_0 = 1.8498 GHz

A wideband response was also simulated for and the location of the next spurious mode was situated at 2.49 GHz, thus, leaving a 640 MHz spurious free window as shown in figure 4.25. Compared to DR filters, this spurious free band was quite

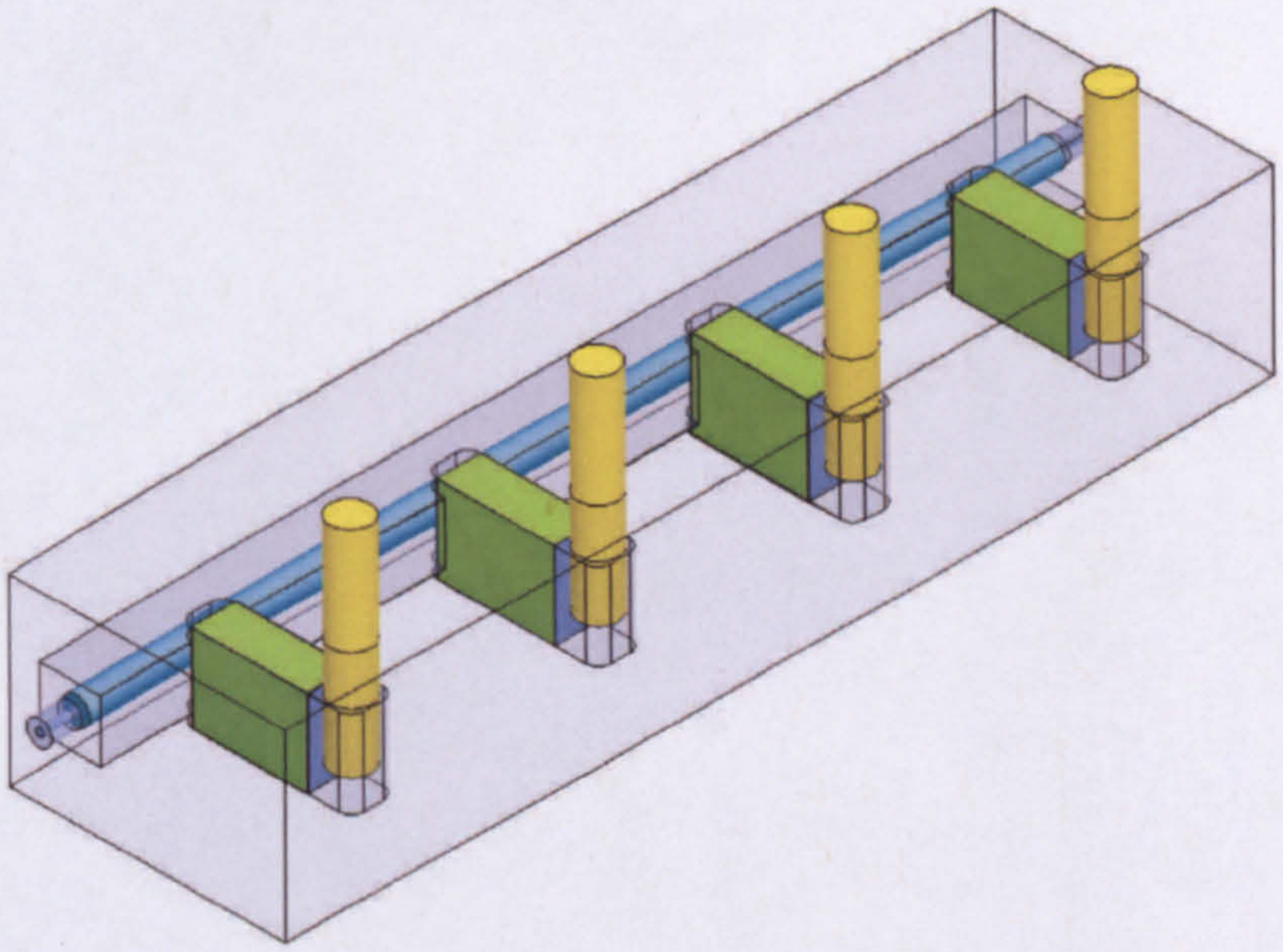

Figure 4.23: Schematic of HFSS design of final filter

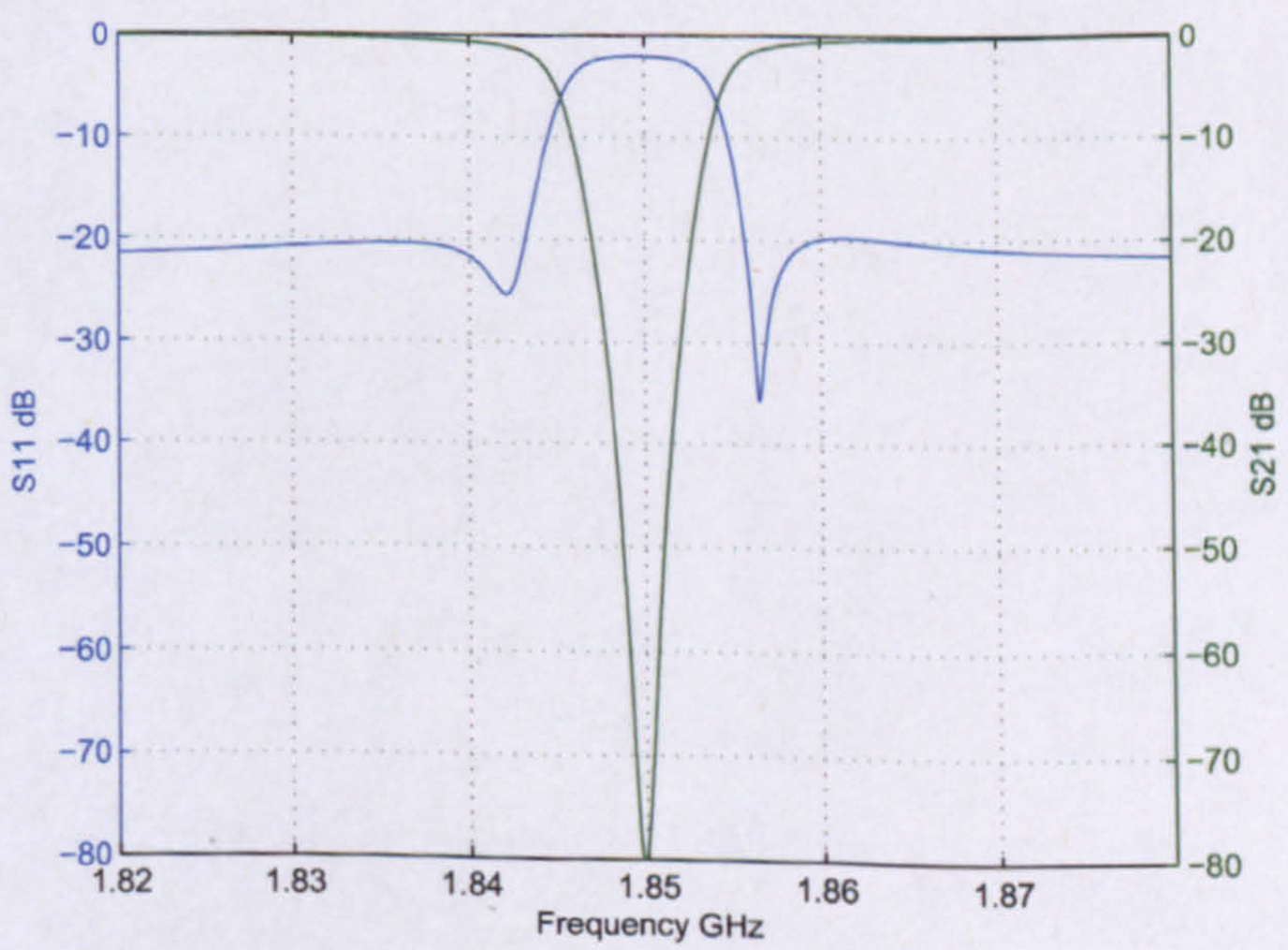

Figure 4.24: HFSS simulated response of filter to be fabricated

high considering typical DR filter designs require modifications to improve their spurious-free performance.

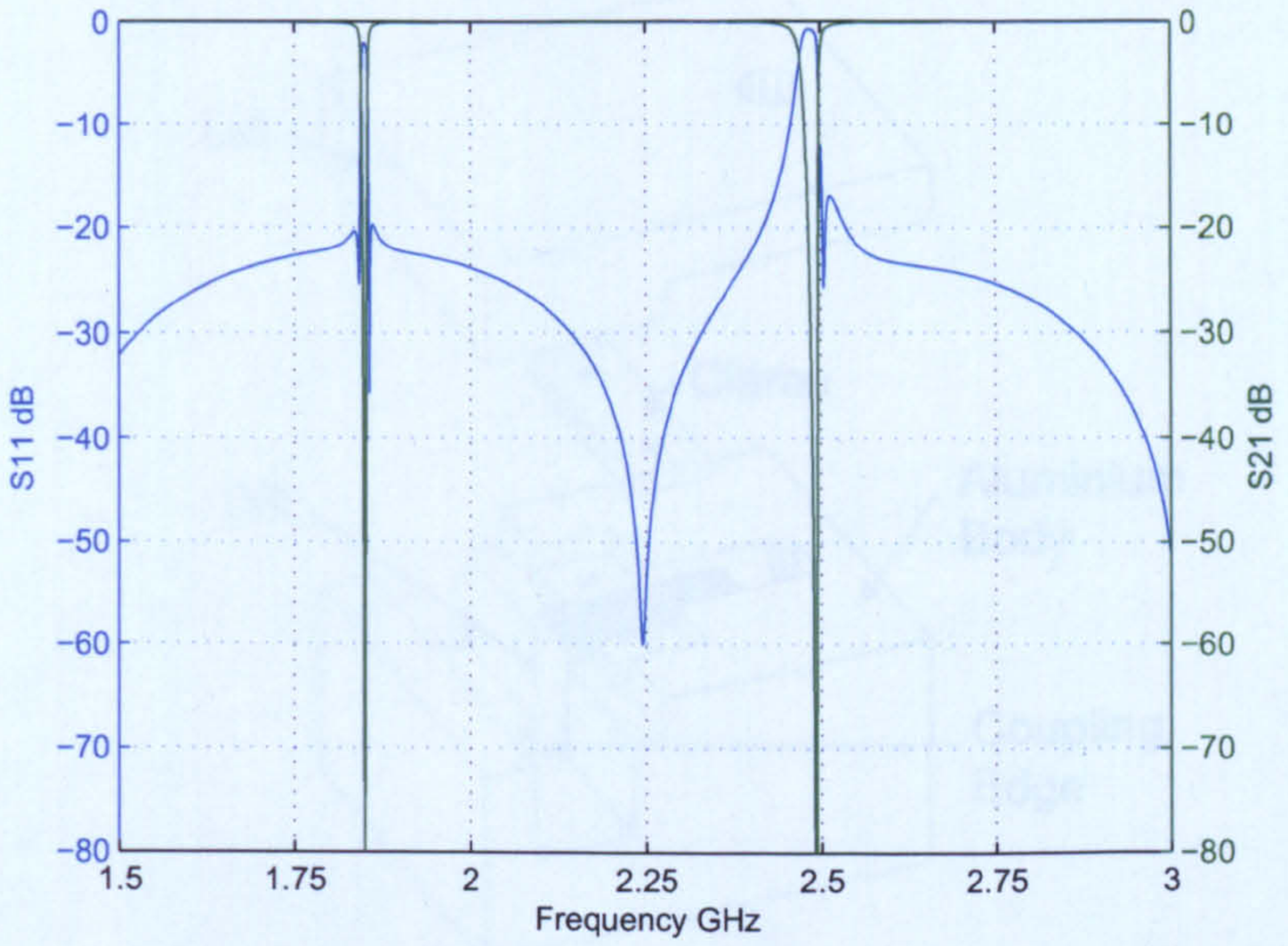

Figure 4.25: HFSS simulated wideband response of filter to be fabricated

4.6 Fabrication of Filter

It was essential the filter was precisely machined since any discrepancy could cause unwanted frequency shifts and couplings. To ensure the resonators were fixed at the required coupling distances from the transmission line, two fabrication techniques were implemented as shown in figure 4.26. Since the cross-sectional height of the coaxial line was designed to be smaller than the height of the rectangular resonator, an indent was machined into the base and lid of the sections in the vicinity between the transmission line and DR. This ridge prevented the dielectric resonator from shifting too close to the coaxial line, therefore, maintaining its coupling bandwidth. In addition, small aluminium plates were machined and secured the rectangular resonators in position using small screws. The fabricated filter is illustrated in figure 4.27 with brass tuning screws. A picture of the interior of the filter is also provided as shown in figure 4.28.

The measured response is shown in figure 4.29 with 3 dB bandwidth of 19.6 MHz at a centre frequency 1.8501 GHz. At 40 dB, the stopband bandwidth was measured to be 3 MHz which achieved the required specifications. However, a low Q

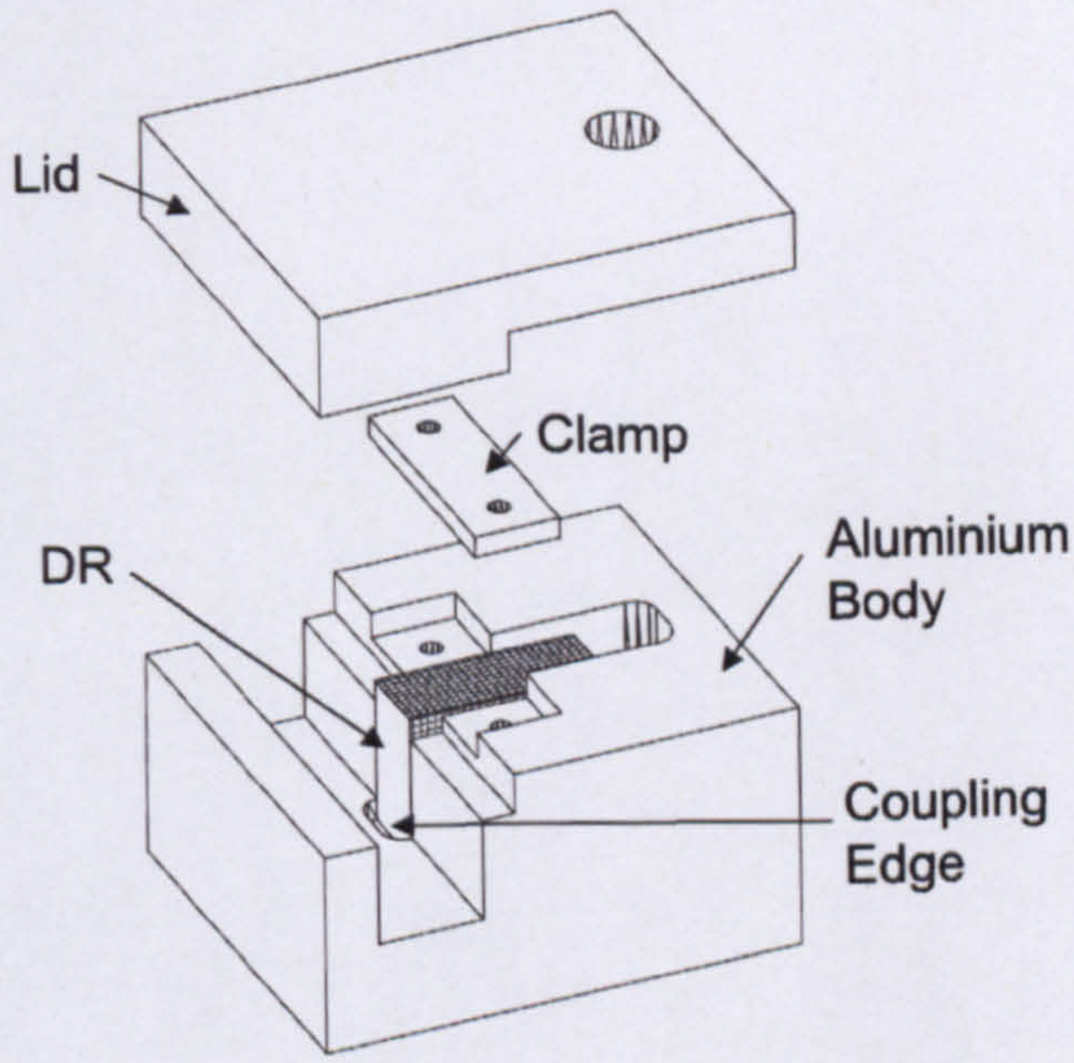

Figure 4.26: Practical resonator design

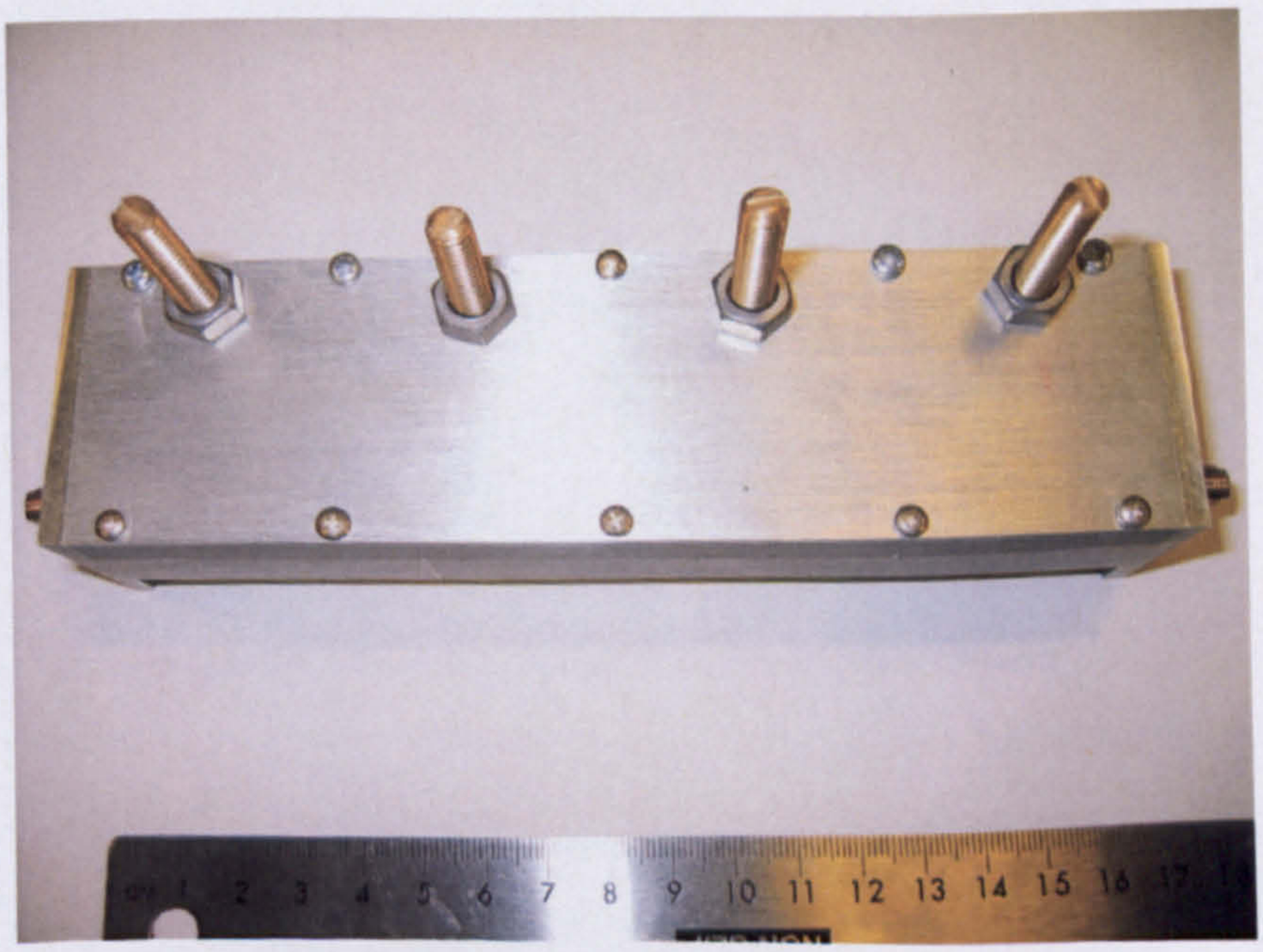

Figure 4.27: Fabricated 4^{th} degree Chebyshev bandstop filter

of only 216 was measured. This was largely due to the poor silver metallisation of the rectangular dielectric resonator and air gaps were also apparent between the dielectric slabs and the cavities they were placed in leading to poor electrical grounding. To improve the Q, improved metallisation techniques are required such as spattering rather than a hybrid metallisation using a sticking Nickel com-

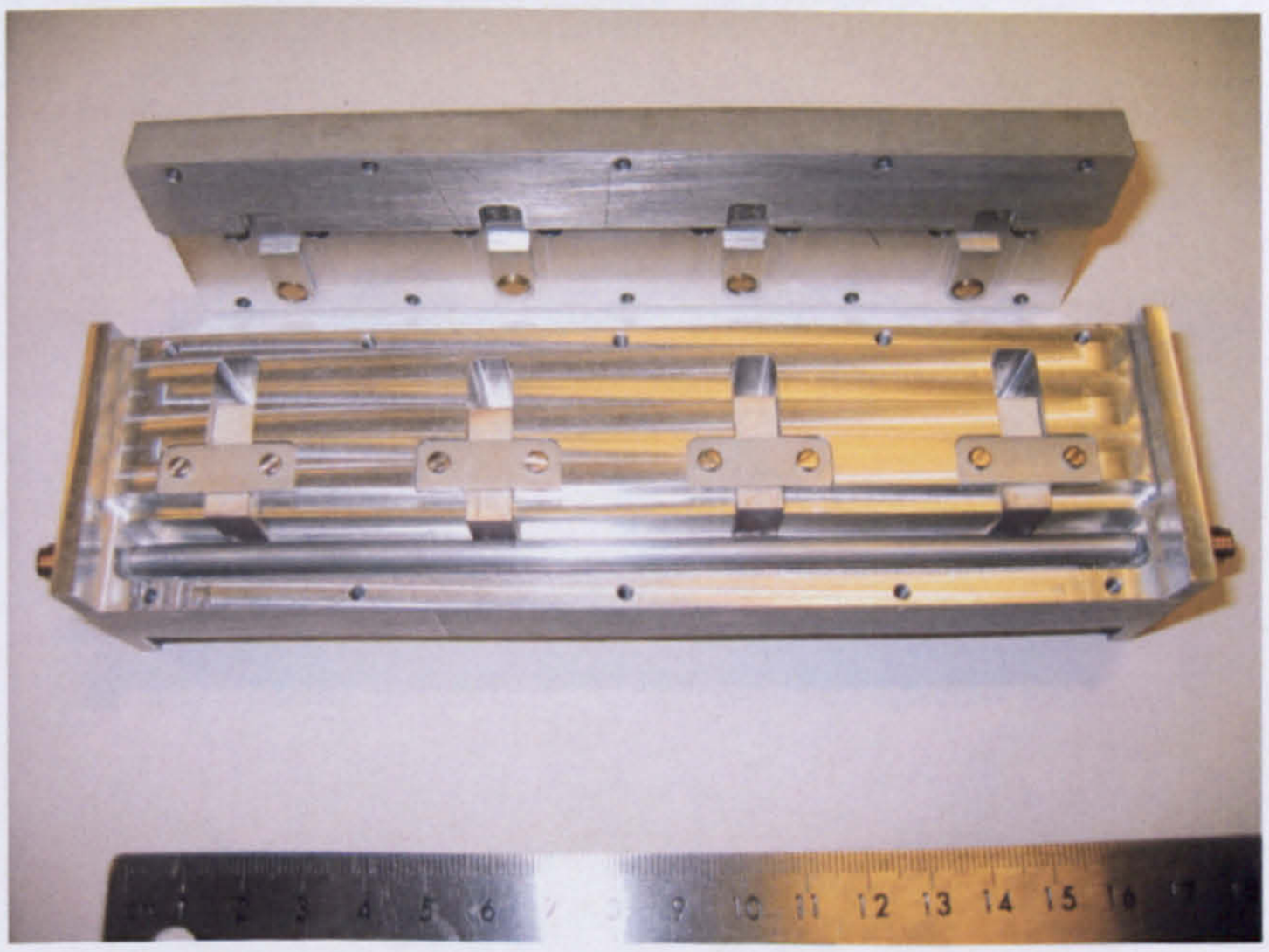

Figure 4.28: Interior of fabricated 4th degree Chebyshev bandstop filter

pound before silver. It may also be feasible to solder the DR into its resonator space, thus, proper grounding will be obtained.

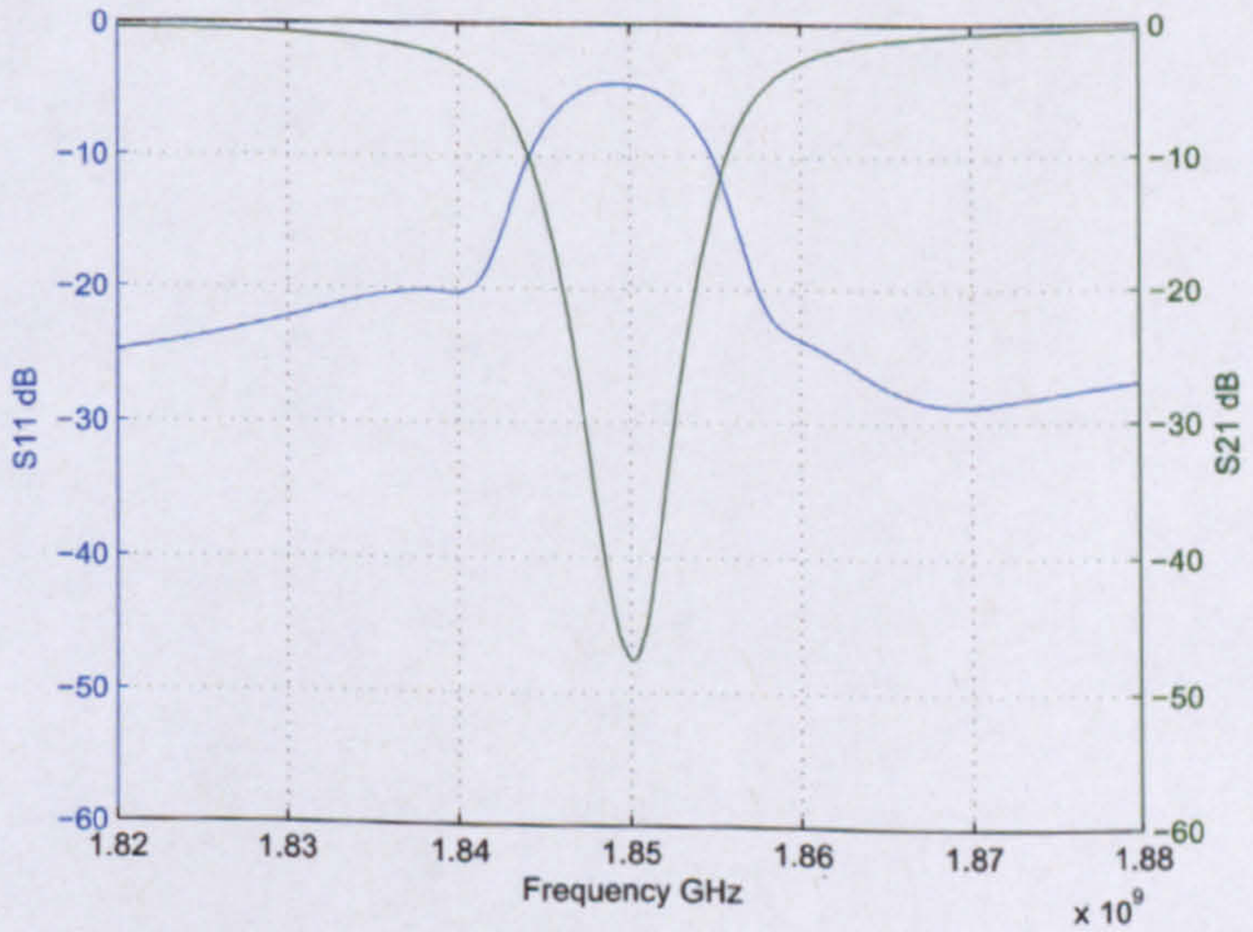

Figure 4.29: Measured frequency response of Chebyshev bandstop filter

The spurious performance of the filter is also examined. The TE_{102} mode was observed at 2.44 GHz leaving a spurious-free range of 590 MHz as shown in figure 4.30. Thus, a favourable spurious-free range is achieved without the need for

physical improvements as commonly required in DR filters. The filter demonstrated the principle of a compact high-Q bandstop using dielectric-loaded rectangular waveguides and the high unloaded Q allows miniaturisation over coaxial or cavity designs.

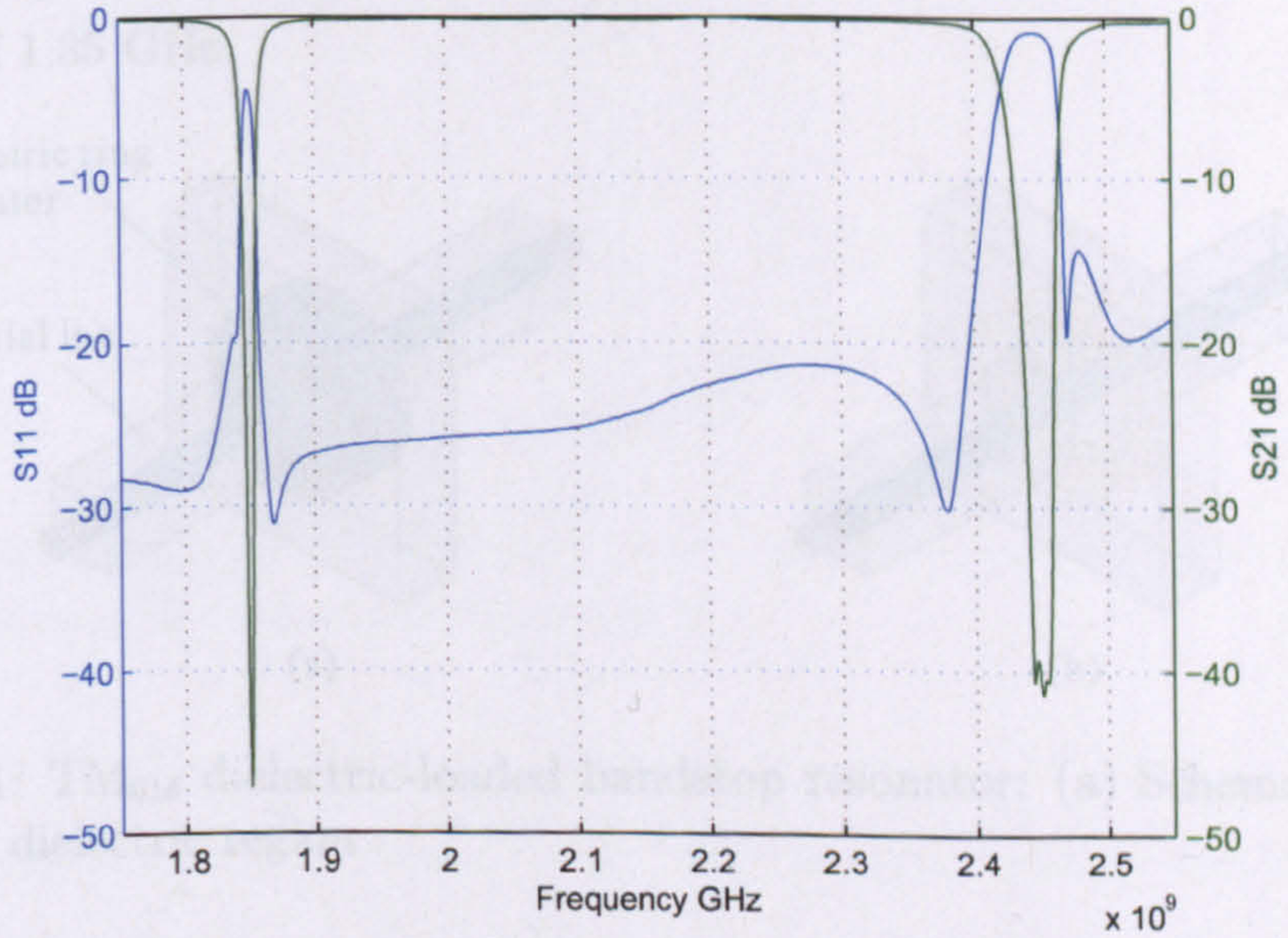

Figure 4.30: Measured wideband frequency response of Chebyshev bandstop filter

4.7 Coaxial Dielectric-Loaded Bandstop Resonator

Although the $TE_{10\delta}$ dielectric-loaded rectangular bandstop resonator is suitable for designs requiring narrow bandwidth, for applications requiring greater bandwidths, the coupling space between the resonator and transmission line provides a limitation on maximum bandwidth. It is possible to intersect the rectangular resonator with the coaxial line to improve coupling but it is difficult to insert the coaxial line through the rectangular resonator at the optimum position for maximum coupling. A better option would be to use dielectric pucks to take advantage of their radial field pattern. An experimental novel broadband bandstop resonator is shown in figure 4.31 with the H-field plot of the dielectric ring displaying the fundamental $TM_{01\delta}$ mode. The structure comprises a coaxial transmission line

coupled to a cylindrical dielectric ring resonator replacing the rectangular resonator. The DR had the same material properties as for $TE_{10\delta}$ mode resonator and dimensions of radius, 13 mm, height, 9 mm, inner hole radius, 5 mm, and the same coaxial transmission line, with outer diameter 10 mm and inner diameter 4.68 mm, was also used. These dimensions allowed a fundamental resonant frequency of 1.85 GHz.

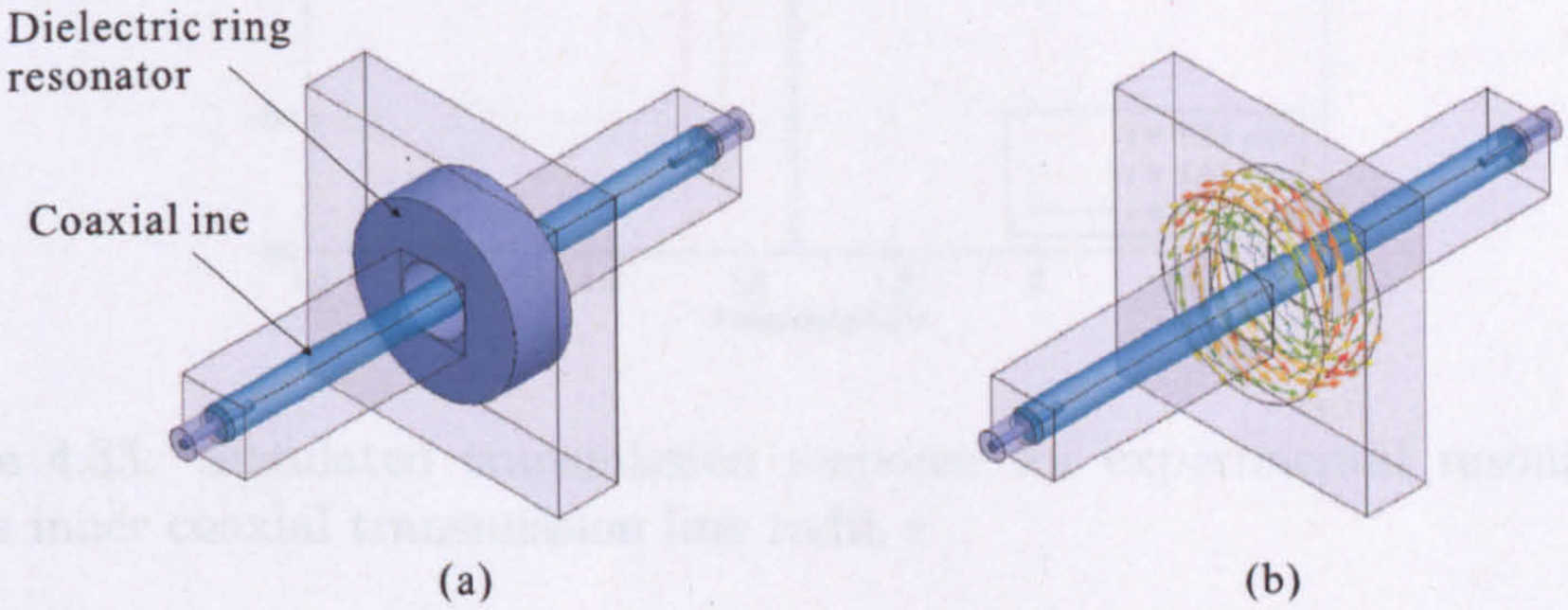

Figure 4.31: $TM_{01\delta}$ dielectric-loaded bandstop resonator: (a) Schematic (b) H-field plot in dielectric region

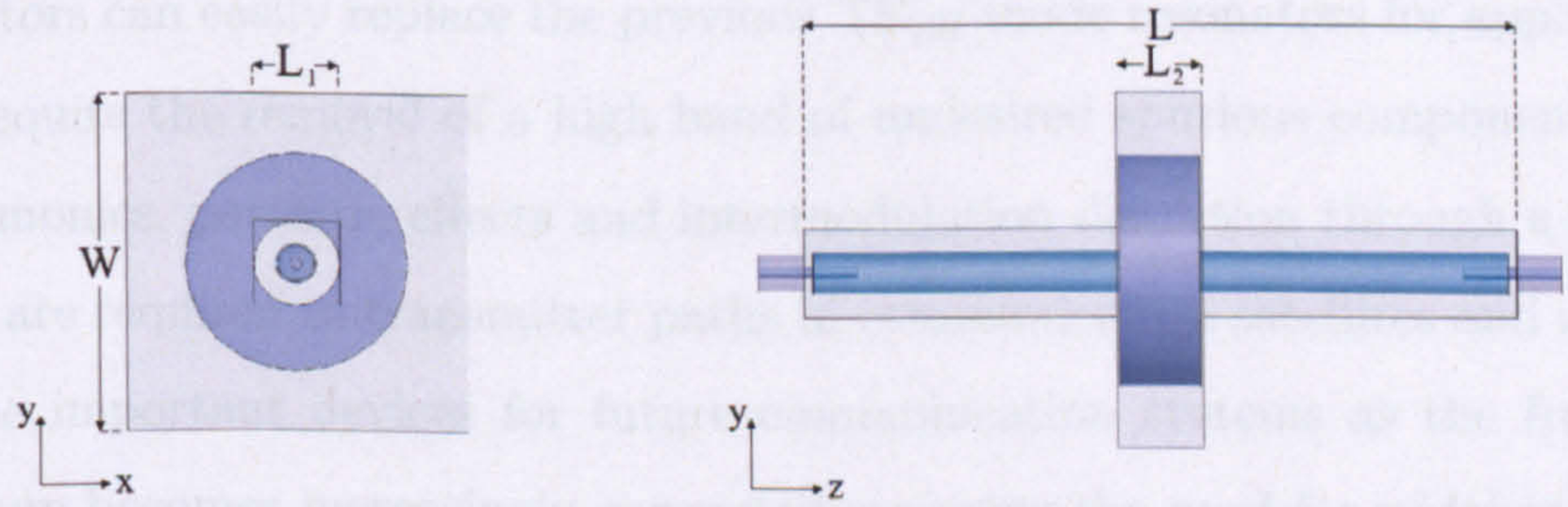

Figure 4.32: Dimensions for experimental coaxial dielectric-loaded resonator, L = 80mm, W = 40 mm, L_1 = 10 mm, L_2 = 9.57 mm

Due to the discontinuity at the dielectric resonator intersection, the TEM properties of the coaxial transmission line become distorted and is affected by dielectric loading. HFSS simulations can optimise the dimensions of the coaxial line to address these problems such as matching the discontinuity segments and also improve the selectivity of the rejection skirts. This is shown in figure 4.33 where coupling bandwidth of 200 MHz is possible for a smaller inner conductor radius at the transmission line to DR junction. An eignenmode solver calculated the unloaded Q of this structure to be 2670. The coupling bandwidth is superior to the

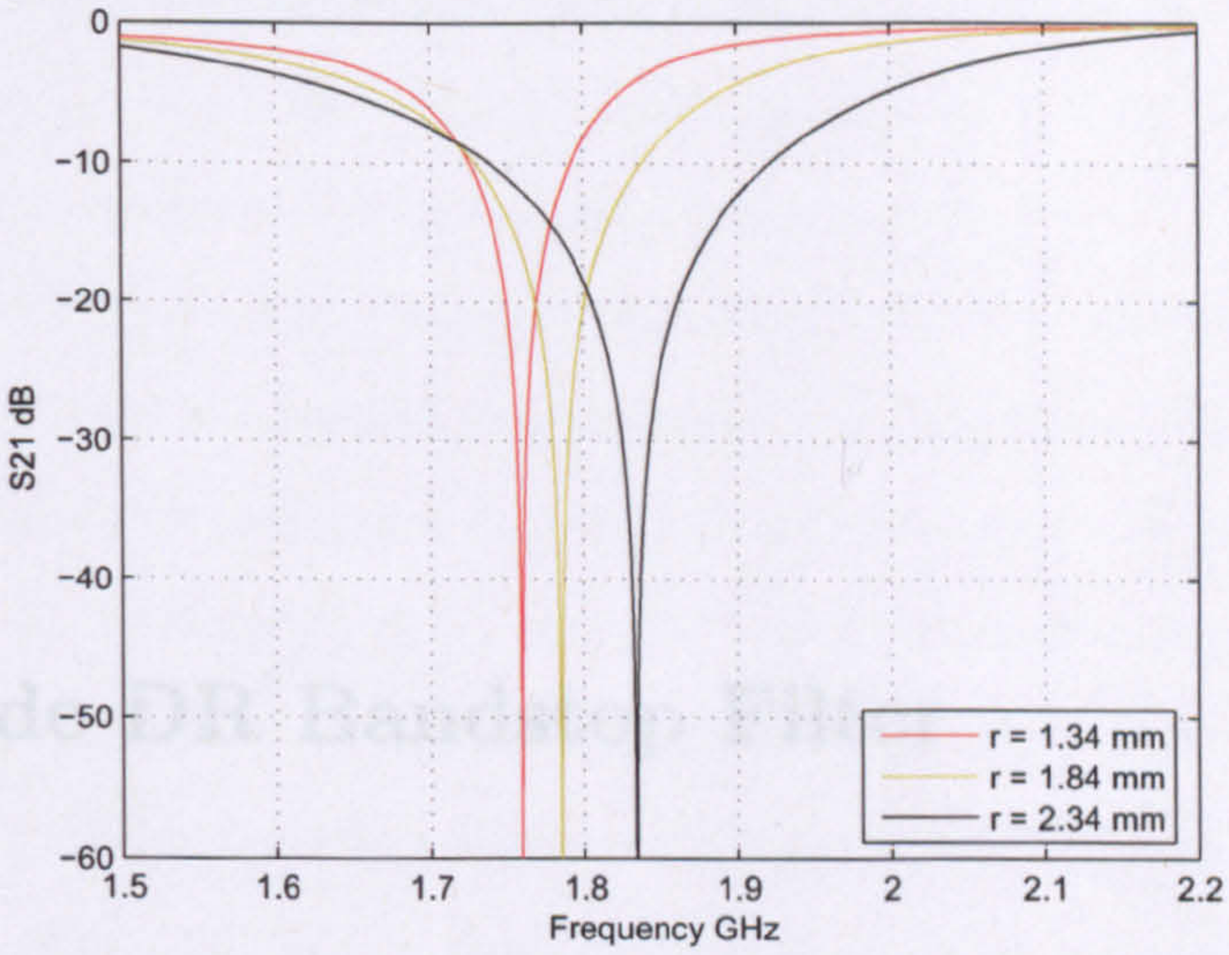

Figure 4.33: Simulated transmission response for experimental resonator for various inner coaxial transmission line radii, r

$TE_{10\delta}$ dielectric-loaded rectangular resonator where only 18 MHz is possible for 0.5 mm spacing, figure 4.12, thus, $TM_{01\delta}$ mode coaxial dieletric-loaded bandstop resonators can easily replace the previous $TE_{10\delta}$ mode resonators for applications that require the removal of a high band of undesired spurious components, such as harmonics, parasitic effects and intermodulation distortion through a system. These are required in transmitter paths in communication satellites and also will become important devices for future communication systems as the frequency spectrum becomes increasingly congested requiring the need for wideband interference suppression in front end of communication systems. Using these high Q resonators will also provide miniaturisation and reduce costs, a paramount objective for commercial filter design.

Chapter 5

Dual-Mode DR Bandstop Filter

5.1 Introduction

A novel dual-mode DR bandstop filter is described in this chapter offering a high Q, better performance, small volume and less weight compared to conventional air-filled cavity filters and TE- TM-mode filters. These benefits are due to the dimensions of the filter reduced by a factor of $1/\sqrt{\epsilon_r}$ and the high Q_u property of dielectric materials compared to an empty metallic enclosure. Although dual-mode DRs are commonly used in bandpass filters, there has been very little published material in the bandstop sector and only mono-mode DR bandstop structures have been investigated, [5]. It is the aim of this chapter to present the advantages of a dual-mode bandstop resonator compared to a mono-mode structure and its flexibity to realise advanced filter functions. One distinct drawback for such a structure is the complexity in the realisation process and these are highlighted throughout from FEM simulations to fabrication. The DR structure considers a dielectric puck situated in a waveguide cavity below cutoff coupled to a transmission line through coupling elements. The fundamental resonance is the dual-degenerate HEE_{11} mode and FEM simulations have been used to generate field patterns for this resonator and perform frequency response simulations aiding in the design of the filter. Bandstop filters are necessary in rejecting unwanted signals and interference. When low cost, size, weight and simplicity are required,

the design at high frequencies of such filters can meet cost targets using DRs with their superior large Qs. The new filter structure is well suited for rejecting unwanted carrier frequencies of a communications system. Although the construction process may seem arduous, the design itself is incredibly robust using metal coupling posts as opposed to magnetic coupling wires, where vibration and impact in a mobile environment can distort the frequency behaviour. The main transmission line is isolated from the DRs, thus, reducing impact of unwanted interference from stray coupling fields that were a problem seen in open transmission line designs. This isolation and miniature coaxial coupling tap points allows the resonators to be spaced $\lambda/4$ apart, unlike in open-transmission line structures where $3\lambda/4$ spacings are obligatory to avoid transmission line, inter-resonator, distortion of the signal.

5.2 Dual degenerate HEE_{11} mode

To understand the properties of the hybrid mode HEE_{11} dielectric resonator, the resonant modes must be studied. An initial FEM eigenmode solver calculated the first five resonant modes for a dielectric puck of height 23 mm, radius 18.5 mm and dielectric permittivity of 44, table 5.1. For accurate HFSS simulation results, the puck was enclosed within a 100 mm^3 airbox and perfect magnetic layer, PML, boundaries were introduced on the airbox as absorbing conditions for the open puck in free space. The $TE_{01\delta}$ mode is the fundamental for the specified dielectric puck but for different aspect ratios of diameter to length of the dielectric puck, the HEE_{11} mode can be the fundamental mode in shielded cavities.

The fields for a single degenerate polarisation of HEE_{11}, have been generated figure 5.1. The orthogonal polarisation has identical field plots but are normal to the plots shown. Coupling between these two polarisations may be controlled by introducing a suitable perturbation either internally in the puck, [35] and [71], or in the surroundings, located at 45° angle with respect to the direction of each excitation. Tuning screws have generally been used but recent advances have

Mode No.	Name	Resonant Frequency GHz
1	$TE_{01\delta}$	1.178
2	HEE_{11}	1.342
3	HEH_{11}	1.649
4	$TM_{01\delta}$	1.740
5	HEE_{21}	1.771

Table 5.1: First five resonant modes of a dielectric puck

included metallising the exterior of dielectric shapes, [79].

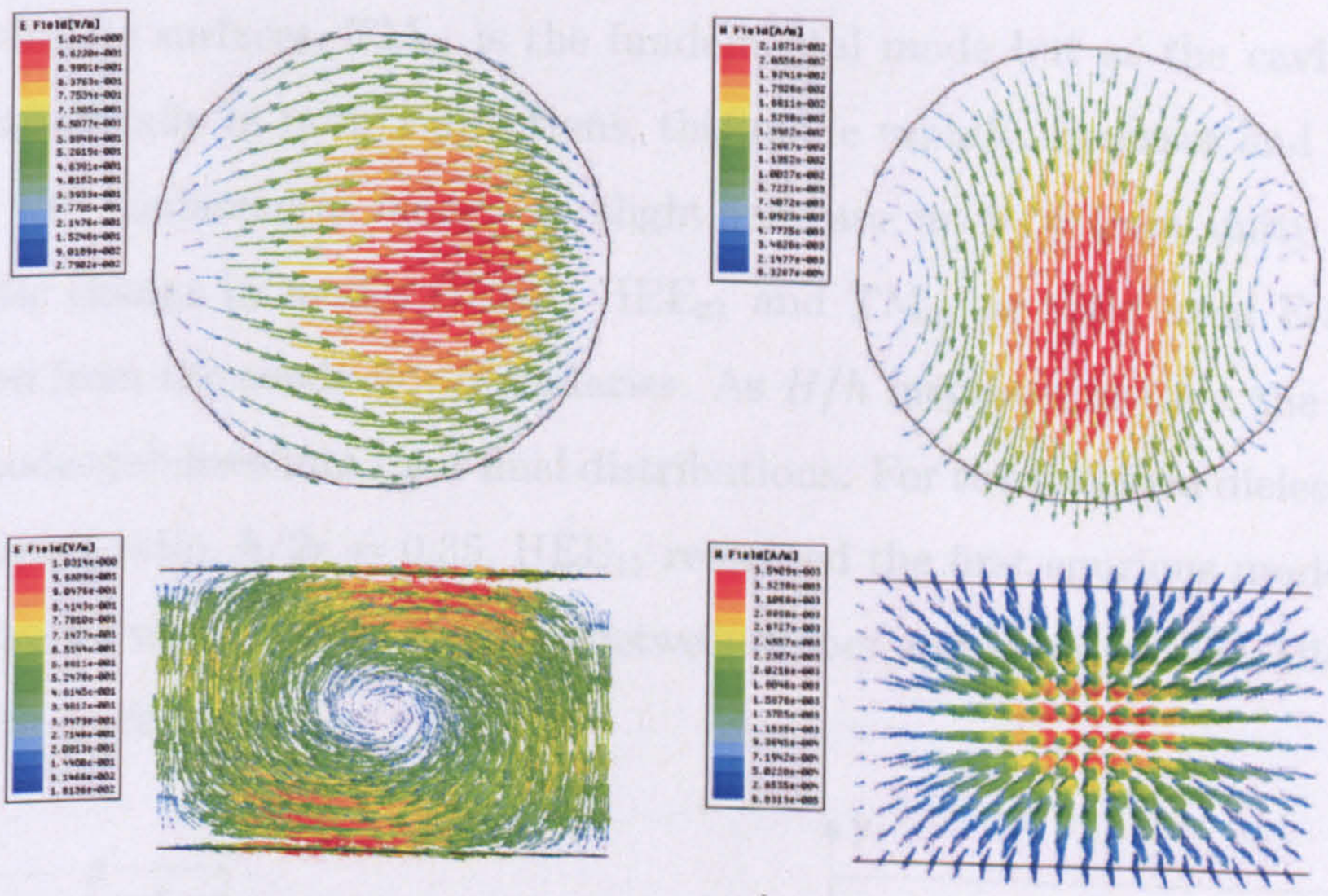

(a) (b)

Figure 5.1: Field distributions of HEE_{11} dual mode (a) E-field plots (b) H-field plots

5.3 Configuration of Proposed Resonator

In the design of a microwave bandstop resonator, mode charts are essential to understand the behaviour of the resonant frequency in the proposed DR structure which are prerequisites in the design of bandstop filters. A cylindrical dielectric puck suspended in a cavity is the common configuration for a DR but, unfortunately, in such a structure the fundamental mode is the $TE_{01\delta}$ mode, figure 5.2. A FEM simulation is produced to understand the frequency behaviour of the di-

electric modes in a cavity when the spacings between the respective faces of the top and bottom cavity walls relative to the dieletric puck surfaces, are varied, figure 5.3. The dielectric puck used was as before and placed in an air-filled, cavity box with perfect conducting walls of widths, $2W = 65$ mm and height, $H = 63$ mm. With consideration to realisation, the dielectric puck would be supported by a relatively low dielectric constant support but as its effect is insignificant compared to the resonator, its effect was removed for the mode chart simulations. In the range $H/h < 1.2$, with the top and bottom walls close to the dielectric surfaces, TM_{01} is the fundamental mode but as the cavity height increases equally in both z-directions, this mode rapidly increases and TE_{01} becomes the fundamental mode. A slight increase in H/h from unity causes a dramatic change in modes HEE_{11}, HEE_{21} and TM_{01} as their axial E-fields are removed from the conductor boundaries. As H/h increases further, the fields for each mode stabilizes into their final distributions. For the specified dielectric puck with aspect ratio, $h/2r = 0.35$, HEE_{11} remained the first spurious mode for this structure for various equal spacings between upper and lower cavity walls and the dielectric puck.

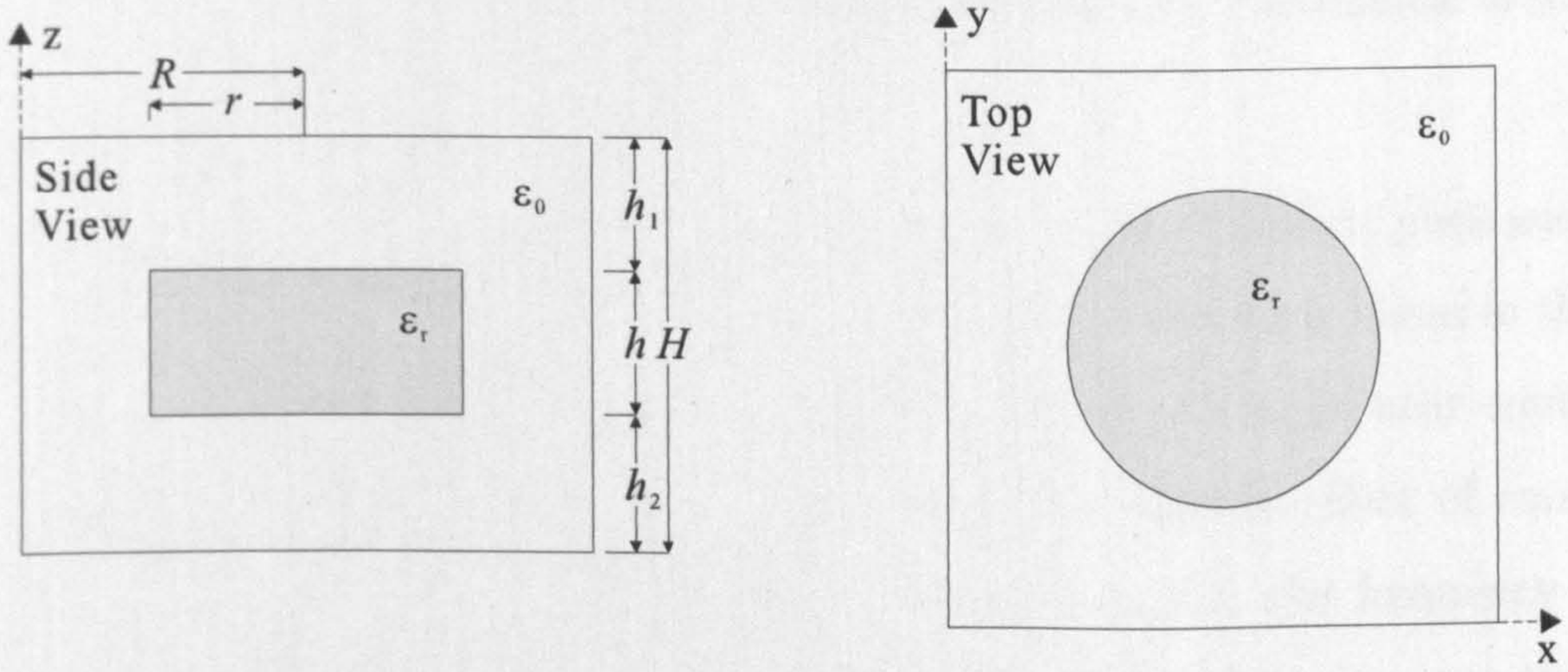

Figure 5.2: Diagram of dielectric puck in perfect conductor cavity

Although a dielectric puck with different r/h aspect ratio could force HEE_{11} to be the fundamental mode, to preserve the dimensions of the puck, an alternative method is to lower the puck to the cavity floor reducing $h_2 = 0$ whilst $h_1 = 20$ mm and $R = 32.5$ mm are kept constant. This increases the frequency of TM_{01} below

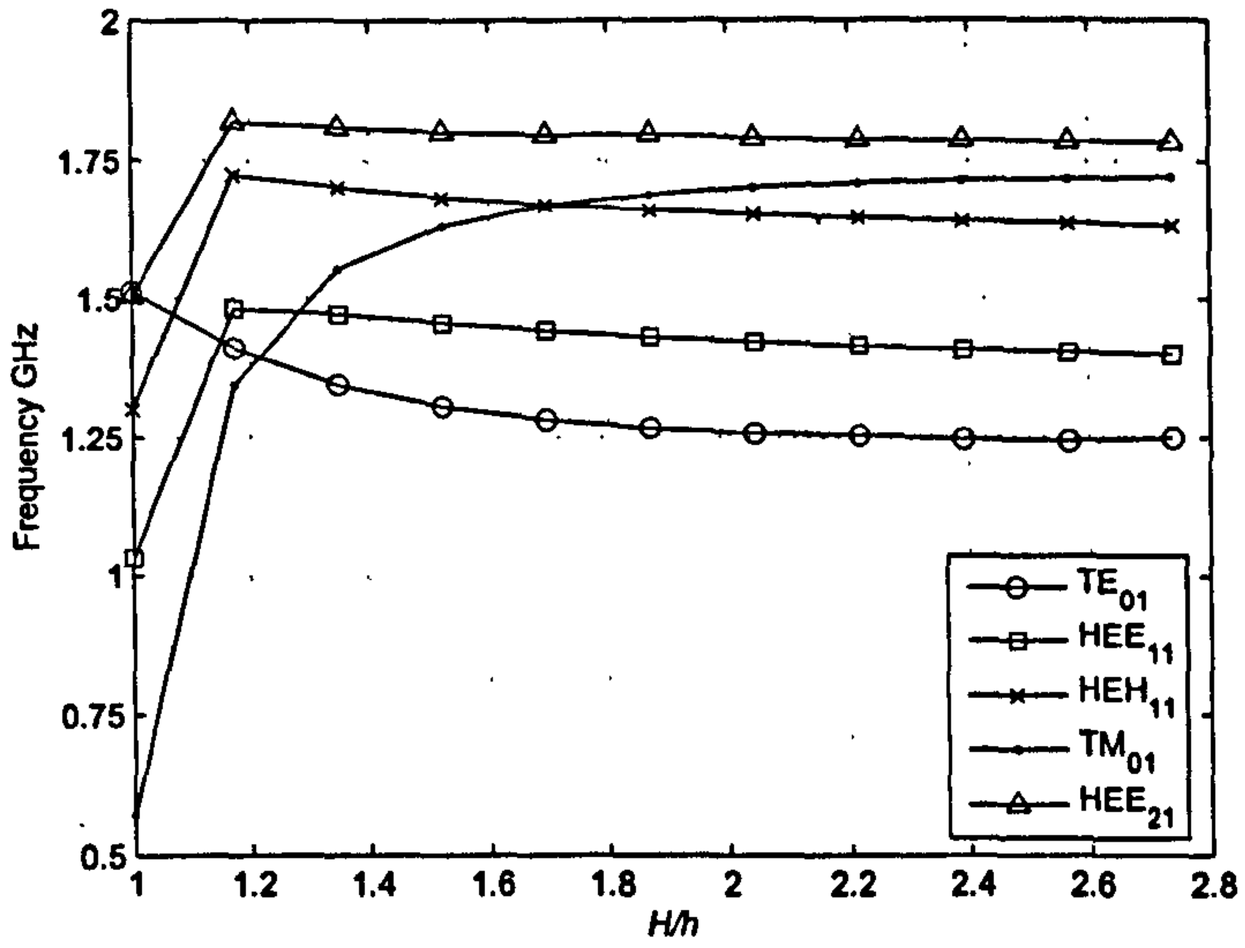

Figure 5.3: Mode chart variation of H/h with frequency

$h_2/h_1 < 0.8$ and leaves the resonant frequency of HEE_{11} relatively unchanged as the new fundamental mode and TE_{01} becomes the first spurious mode, figure 5.4. The disadvantage of this is that Q_u will decrease due to the interaction between the bottom face of the dielectric puck and cavity wall but by lowering both the puck and height of the cavity, further volume reduction is gained and reduces the need for a dielectric support. Thus, a solid foundation for mechanical stability is provided.

The conductor sidewalls must be at a distance from the dielectric puck such that the fields are concentrated at the dielectric region and resulting losses in the conductor walls are minimised, however, the sidewalls must also be near enough for miniaturisation to be effective. A mode chart showing the effect of conductor sidewalls on the DR shows that in the range $R/r < 1.3$, the frequency of the modes are vastly affected by the conductor walls due to their near proximity to the dielectric puck, figure 5.5. For $R/r > 1.5$, the resonant frequency for HEE_{11} mode varies constantly with conductor walls indicating the fields are concentrated within the puck and only weak evanescent fields exist in the vicinity of the conductor walls.

In conventional bandstop configurations, each resonator is located at an odd mul-

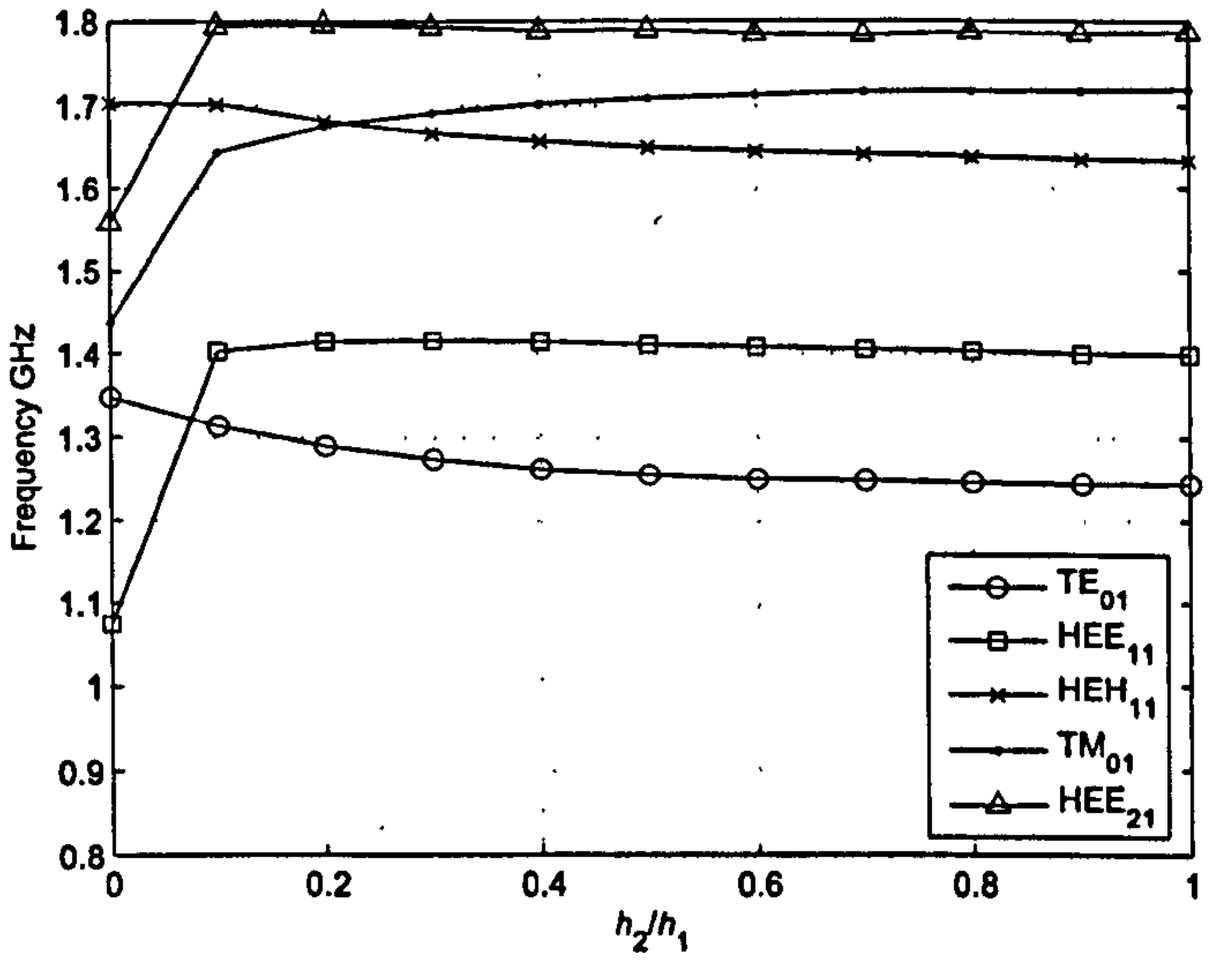

Figure 5.4: Mode chart variation of h_2/h_1 with frequency

tiple of a quarter-wavelength along a transmission line travelling in one direction. For the dual-mode configuration, the conventional design produces two physical topogies but with experimental coupling probes offset by $\lambda/4$, figure 5.6 (a), the coupling fields are not focused on the surface of the puck and resulting coupling bandwidths would be too poor for filtering applications. The height of the coupling probes may be raised such that they extend over the upper surface of the puck for increased coupling surface, however, this would cause increased spurious coupling between both probes. The coupling bandwidths may be increased by placing the input couplings perpindicular to each other such that the probe faces are normal to the puck, figure 5.6 (b), but the $\lambda/4$ separation between the resonant probes would be difficult to realise at the transmission line and extra probe lengths would cause higher loss within the cavity. The solution was to bend the transmission line 90° around the lateral face of the puck, figure 5.7. This is similar to input and output ports required for canonical dual-mode DR bandpass filters, [18], and allows minimum length coupling probes to directly excite each orthogonal dual mode for maximum coupling in a square cavity. A small disadvantage with this is the nature of the transmission line curve would cause a slight discontinuity in the transmission response, however, FEM simulations can

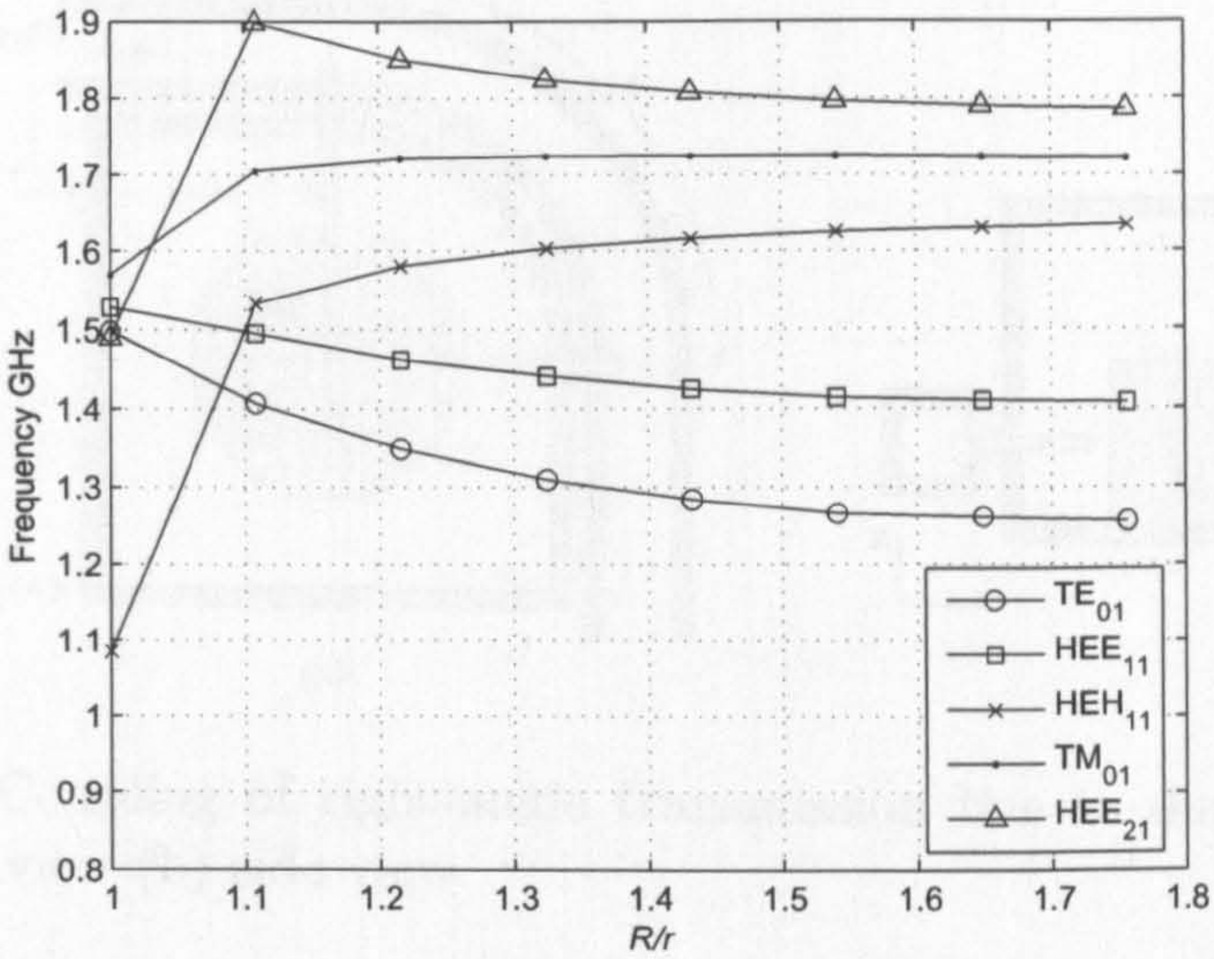

Figure 5.5: Mode chart variation of R/r with frequency

optimise the dimensions for the optimum frequency response.

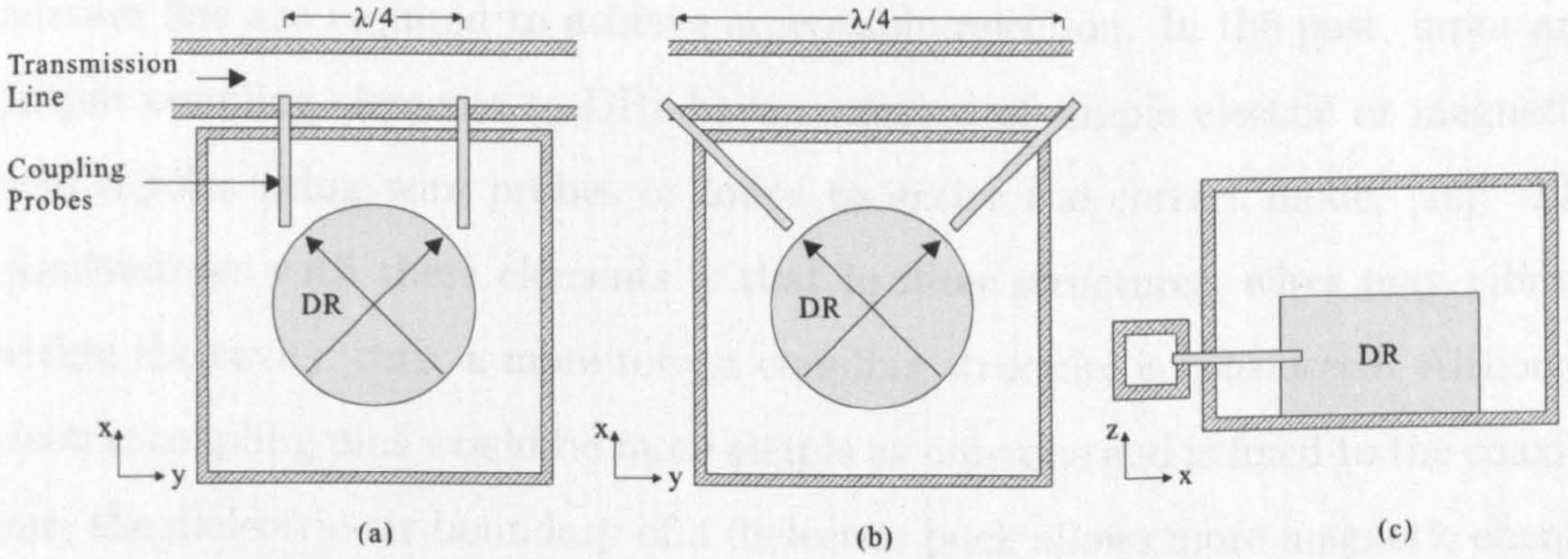

Figure 5.6: Topologies for coupling of transmission line to dual-mode dielectric puck: (a) weakly coupled probes (b) probes for maximum coupling (c) side view

A waveguide transmission line is commonly coupled to a DR situated in a cavity using irises but require $3\lambda/4$ separations to avoid transmission line spurious inter-resonator couplings which increases resonator volume and transmission line dispersion. A coaxial transmission line with square outer conducter and circular inner conductor, as described from the $TE_{10\delta}$ filter in the previous chapter, would be ideal. The physical benefits are it offers a uniform cross-section, when shaped into a curve, and coupling elements may be rigidly supported through direct contact to the inner coaxial conductor. A coupling mechanism to isolate the

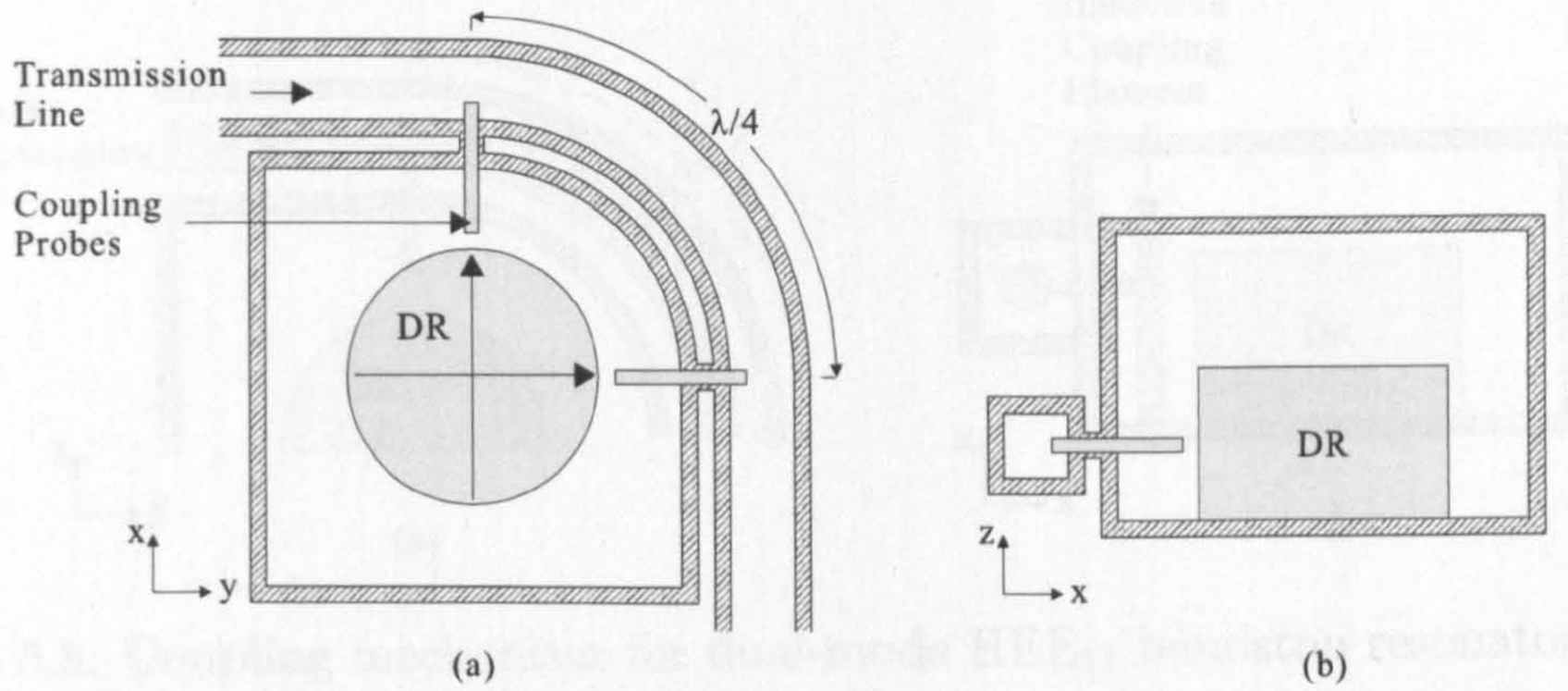

Figure 5.7: Coupling of right-angle transmission line to dual-mode dielectric puck: (a) top view (b) side view

degenerate mode excitations and provide controllable coupling is required. The design of the coaxial probe can also be isolated from the transmission line such that dielectric loading is insignificant and no physical changes in the main transmission line are required to achieve acceptable rejection. In the past, input and output coupling elements to DRs have consisted of simple electric or magnetic-field dipoles using wire probes or loops to excite the correct mode, [26]. The disadvantage with these elements is that in filter structures, wires may vibrate within the cavity, thus, a more robust coupling structure is considered. Although electric coupling pins would be more simple as only one end is fixed to the coaxial line, the dielectric-air boundary of a dielectric puck allows more magnetic energy to couple out. Thus, it was beneficial to make use of magnetic coupling to maximise the coupling bandwidth available. The coupling mechansim was designed as a coaxial probe tapped to a metal post and grounded to the base of the cavity as shown in figure 5.8.

A tuning element was also needed to correct any imperfections in the realised design, therefore, coupling screws were also introduced to tune the capacitive element of the probe. A circuit model for the coupling model is shown in figure 5.9. This is equivalent to a resonant circuit such that as the tuning screw approaches the inductive post, the capacitance increases, effectively reducing the resonance of the post allowing more coupling from the transmission line to the dielectric

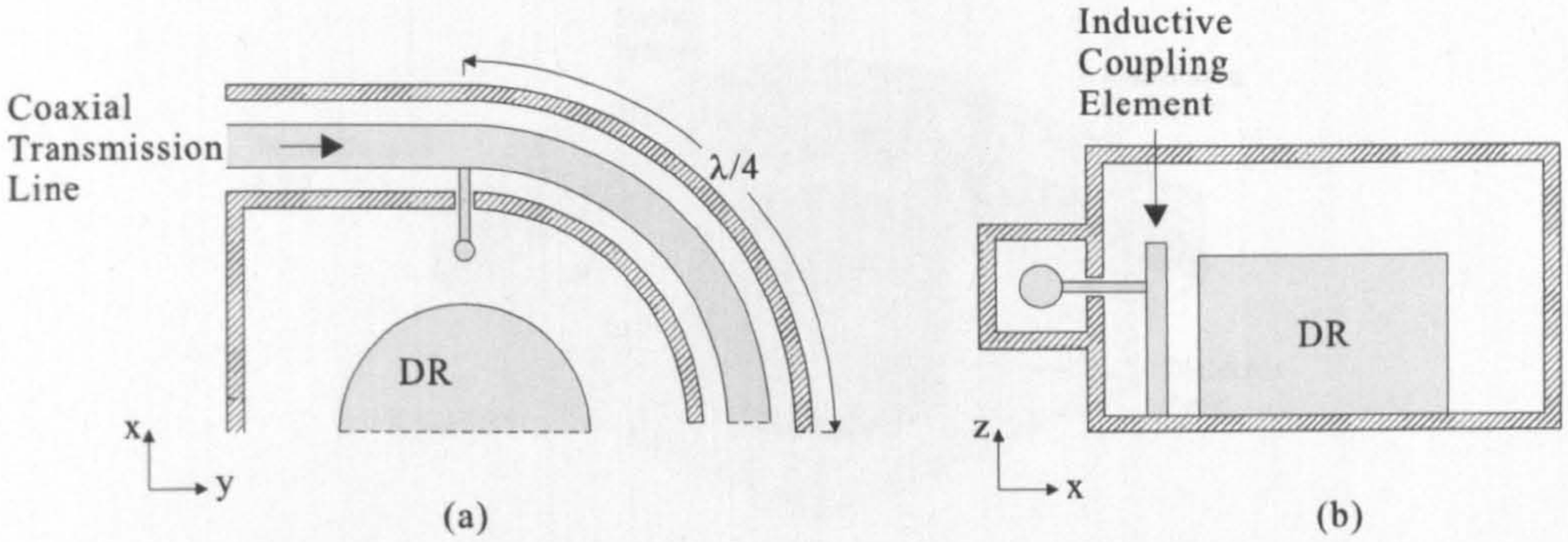

Figure 5.8: Coupling mechanism for dual-mode HEE_{11} bandstop resonator: (a) top view (b) side view

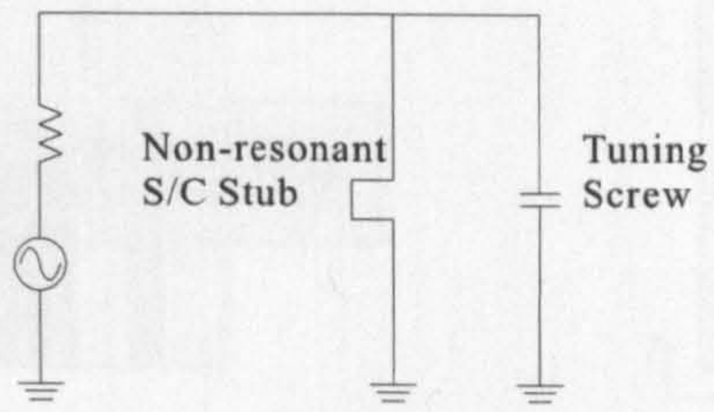

Figure 5.9: Circuit model for coupling post

puck. To aid with the positioning of the puck on the cavity floor, a centre hole was introduced in the puck. The final proposed HEE_{11} bandstop structure is shown in figure 5.10.

5.4 Single Cavity Design

The dimensions for a single cavity dual-mode resonator were calculated based on the same properties of the dielectric puck in the previous section with an additional circular hole along the axis of the puck. This modification was for positional purposes to align the puck at the centre of the cavity but to ensure the spurious performance was unaffected, a mode chart was produced, figure 5.11. This showed there was insignificant variation in resonant frequency against increasing hole diameter for both HEE_{11} and TE_{01} modes, thus, the spurious-free bandwidth of 250 MHz was conserved. It is interesting to note that for operation of TE_{01} mode, a hole will improve spurious performance since TM_{01} mode increases in frequency due to removal of the axial electric fields of the TM_{01} mode.

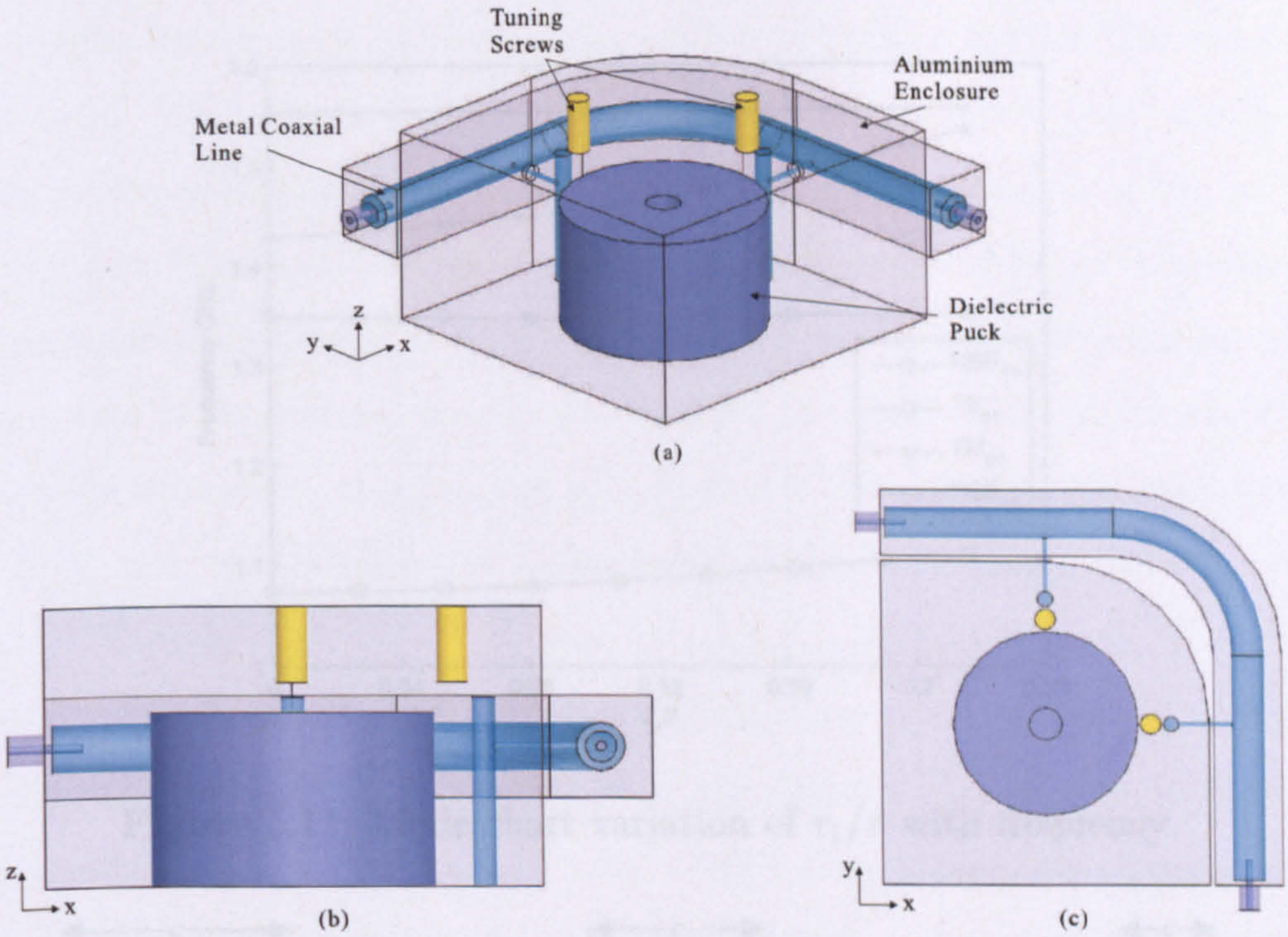

Figure 5.10: Structure of HEE_{11} mode dielectric bandstop resonator: (a) Corner view (b) Cross section (c) Top view

For ease of design, the sidewalls of the cavity were fixed to accomodate the right-angle coaxial transmission line. In the design for this particular dielectric puck of diameter, $2r = 37$ mm, a suitable cavity diameter providing a factor greater than 1.5 of $2R = 65$ mm was suitable to minimise the effect of conductor losses. A prescribed cavity height spacing of $h_1 = 20$ mm gave a resonant frequency of 1.07 GHz for the HEE_{11} mode, figure 5.4. One should note that this frequency was simulated for a puck in a box-shaped cavity but future simulations shows there is minimal change in frequency when a cavity corner is curved inwards to accomodate the transmission line bend. This frequency was used to calculate the length of transmission line separation between the two modes as $\lambda/4 = 7$ cm. The coaxial transmission line needed to be large enough to accomodate the coaxial probe and the dimensions were calculated from equation 4.20. A square outer conductor of width 13.5 mm and round inner conductor of 6.35 mm were defined with a 1 mm thick conductor wall between outer coaxial conductor and cavity sides.

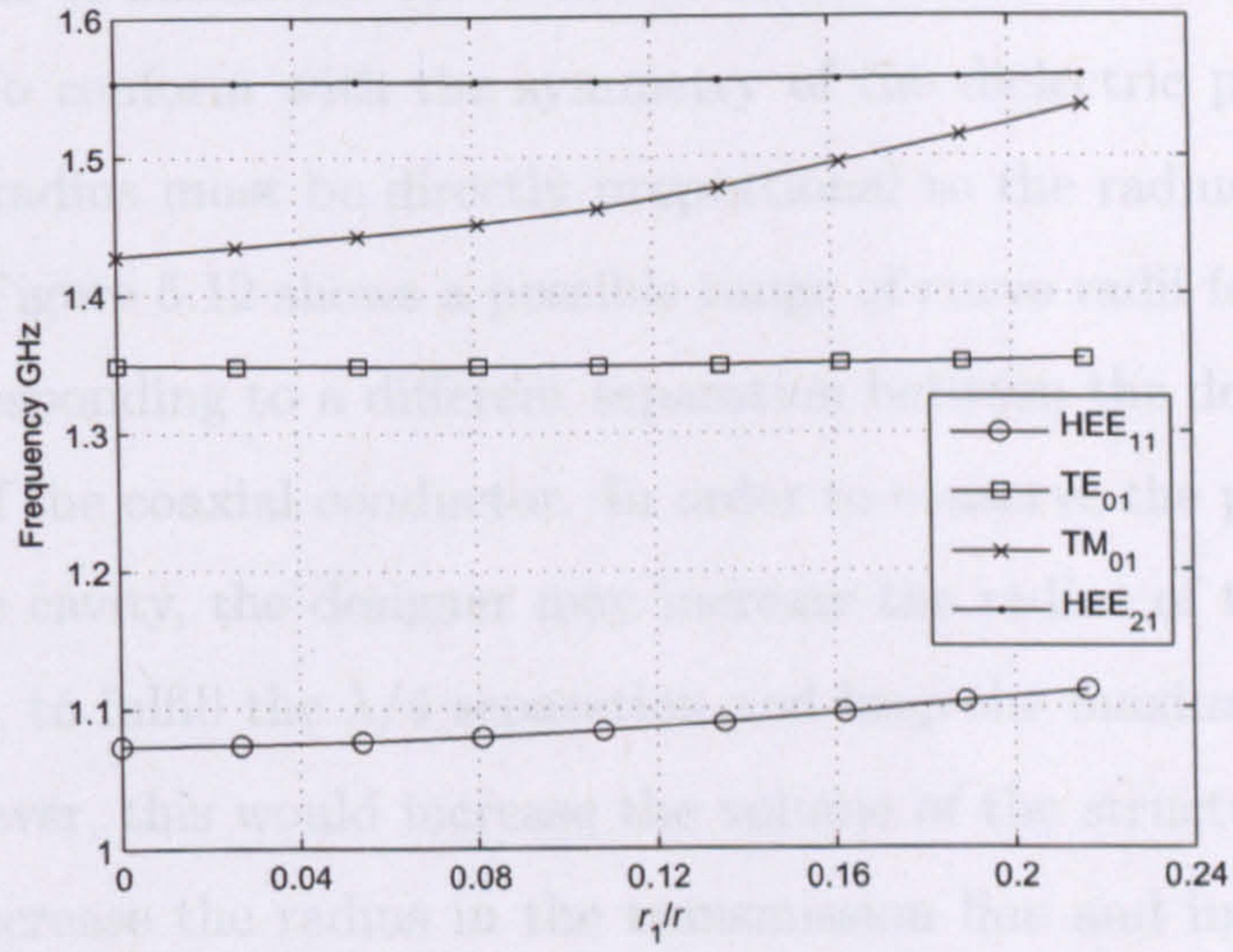

Figure 5.11: Mode chart variation of r_1/r with frequency

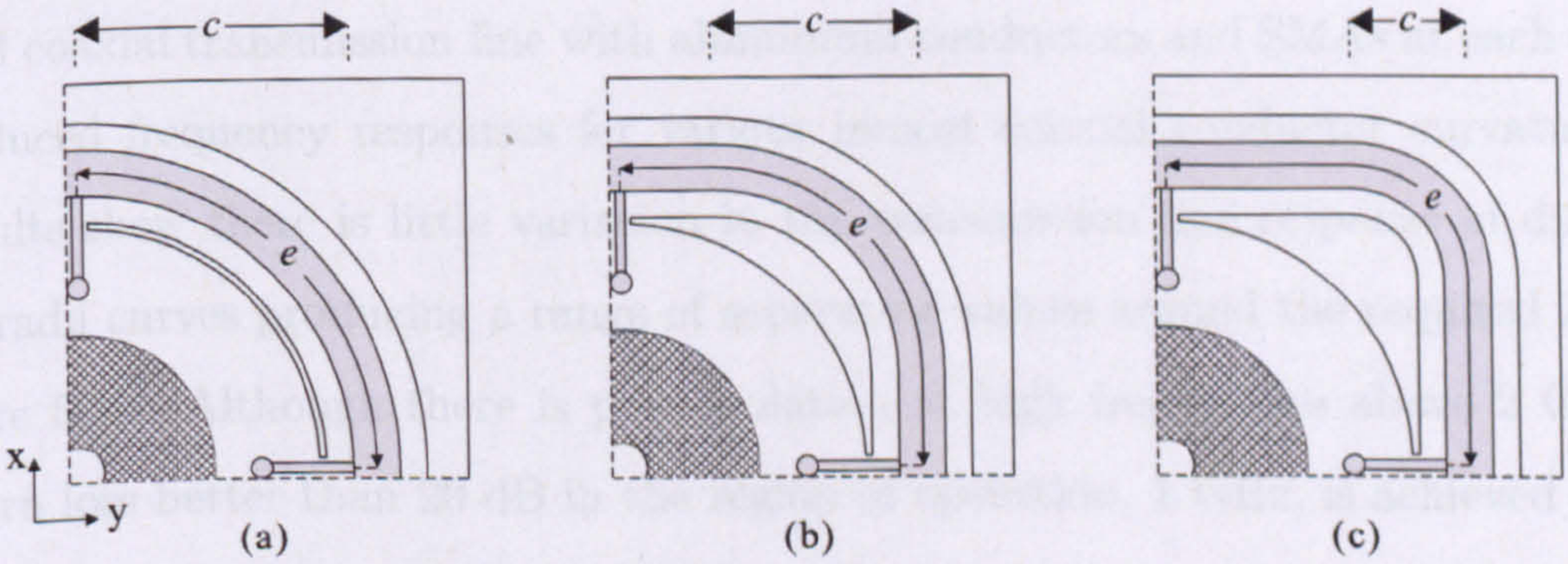

Figure 5.12: Coaxial transmission line with various centre conductor curvature radii (a) $c = 40.25$ mm, $e = 63.2$ mm (b) $c = 29$ mm, $e = 68.1$ mm (c) $c = 19$ mm, $e = 72.77$ mm

The complexity in the design of this structure is now shown as the total length of inter-mode transmission line separation, including the right-angle bend, must position the coupling tap points at the centre of their respective cavity sidewalls. This can be controlled by determining the length of transmission line to undergo the right-angle transformation. Ideally, the transmission line is straight but deviating from this into a curve causes a discontinuity at which point, the pure TEM mode breaks down into components of electric and magnetic fields along the axis of the bend. It was reported that the bend causes changes in the electromagnetic fields inversely proportional to the radius of the curvature, [80], therefore, a

transmission line of maximum curvature radius is desired to limit the sharpness of the bend. To conform with the symmetry of the dielectric puck and cavity, the maximum radius must be directly proportional to the radius of the puck at the sidewalls. Figure 5.12 shows a possible range of curve radii for this structure with each corresponding to a different separation between the degenerate modes at the centre of the coaxial conductor. In order to conserve the properties of the puck inside the cavity, the designer may increase the radius of the transmission line, 40.25 mm, to fulfill the $\lambda/4$ separation and keep the maximum curvature of the bend, however, this would increase the volume of the structure. The second option is to decrease the radius in the transmission line and introduce straight line sections to preserve the 1 mm cavity wall between the cavity sidewall and outer coaxial conductor, figure 5.12 (c). FEM simulations for a practical air-filled coaxial transmission line with aluminium conductors and SMAs at each end produced frequency responses for various inmost coaxial conductor curvatures. Results show there is little variation in the transmission line response of different radii curves producing a range of separation values around the required $\lambda/4$, figure 5.13. Although there is poor isolation at high frequencies above 2 GHz, return loss better than 20 dB in the region of operation, 1 GHz, is achieved and the second option was used to minimise volume.

Dimensions for the tuning element must also be considered to provide the correct bandwidth coupling to the DR puck. Coupling probes of miminum size were ideal to avoid impedance loading of the transmission line and unwanted spurious effects in the cavity at the coupling tap points. The well-known coaxial impedance line equation was used to calculate the initial diameters for the circular coaxial coupling points. These were initially configured to be 1.3 mm and 3 mm for the inner and outer conductor, repectively. An introductory rod length between the coaxial inner conductor and tuning post was 10.8 mm and the post diameter was 3 mm. Based on the above discussions, the typical dimensions for a single cavity dual-mode HEE_{11} bandstop filter are shown in table 5.2.

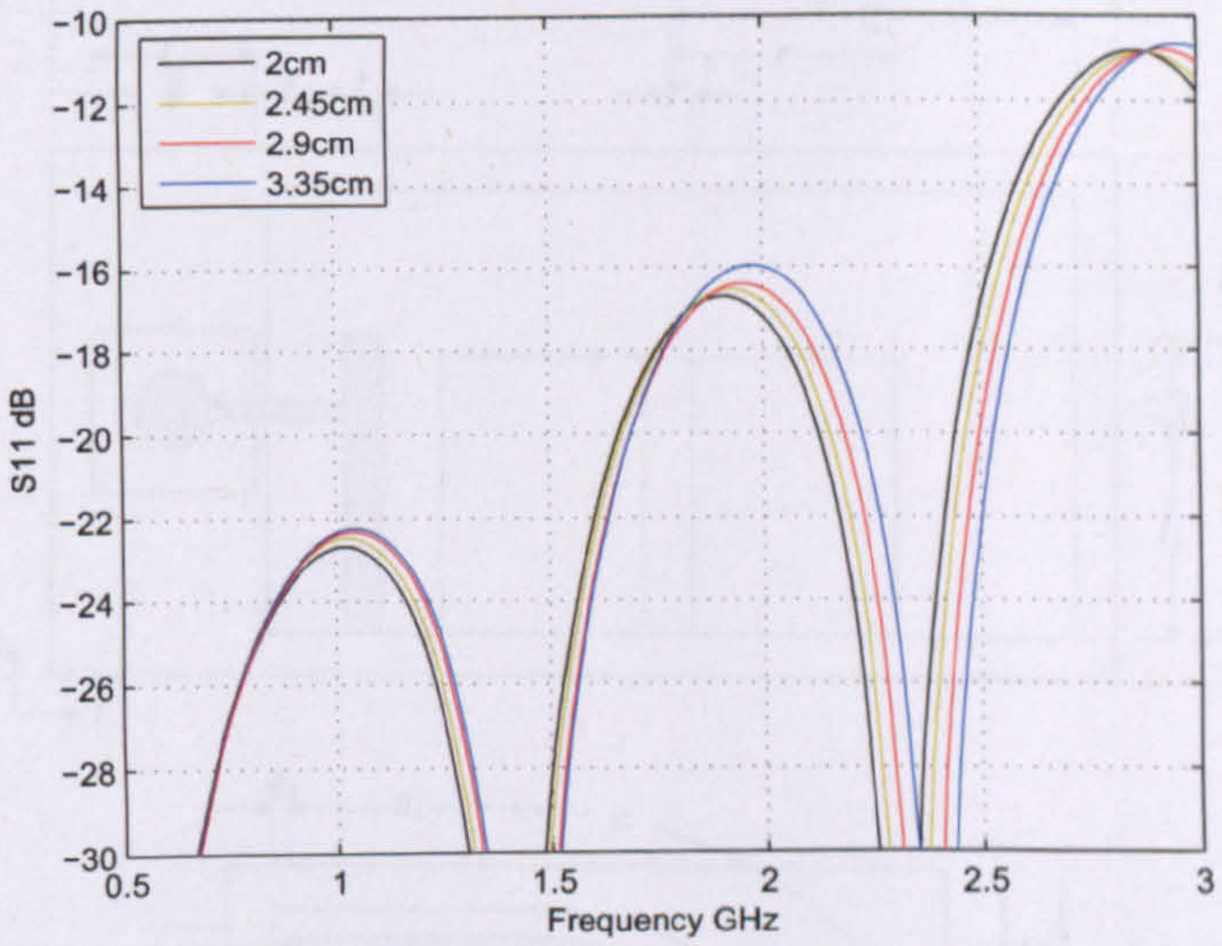

Figure 5.13: Frequency response of coaxial transmission line, outer and inner conductor diameters, 13.5 mm and 6 mm respectively, for various radii of inmost coaxial conductor wall curvatures

Typical Dimensions		Typical Performance
$h = 23$ mm	$l_1 = 18.5$ mm	$f_0 = 1.07$ GHz
$r = 18.5$ mm	$l_2 = 10.8$ mm	$\epsilon_r = 44$
$r_1 = 6.5$ mm	$l_3 = 3$ mm	$Q_u = 9000$
$c = 65$ mm	$l_4 = 1.5$ mm	First spurious frequency 1.35 GHz
$R = 52.5$ mm	$l_5 = 1.3$ mm	
$H = 57$ mm	$d_1 = 1.3$ mm	
$l = 25$ mm	$d_2 = 4.1$ mm	
$h_1 = 14$ mm	$e = 71.7$ mm	
G = 13.5 mm	$e_1 = 19$ mm	
g = 6.35 mm	$g_1 = 1$ mm	

Table 5.2: Typical dimensions and performance of HEE_{11} dual-mode dielectric bandstop resonator

5.4.1 FEM Simulations for single cavity

To confirm the ideas behind the proposed dual-mode bandstop filter, it is useful to understand the behaviour of the fields of the proposed resonator cavity using 3D FEM simulations. The coupling posts excite radial magnetic fields in the two orthogonal dual-modes. The field plots for a single HEE_{11} degenerate mode show the radial E-field is maximum near the centre of the top surface, and at

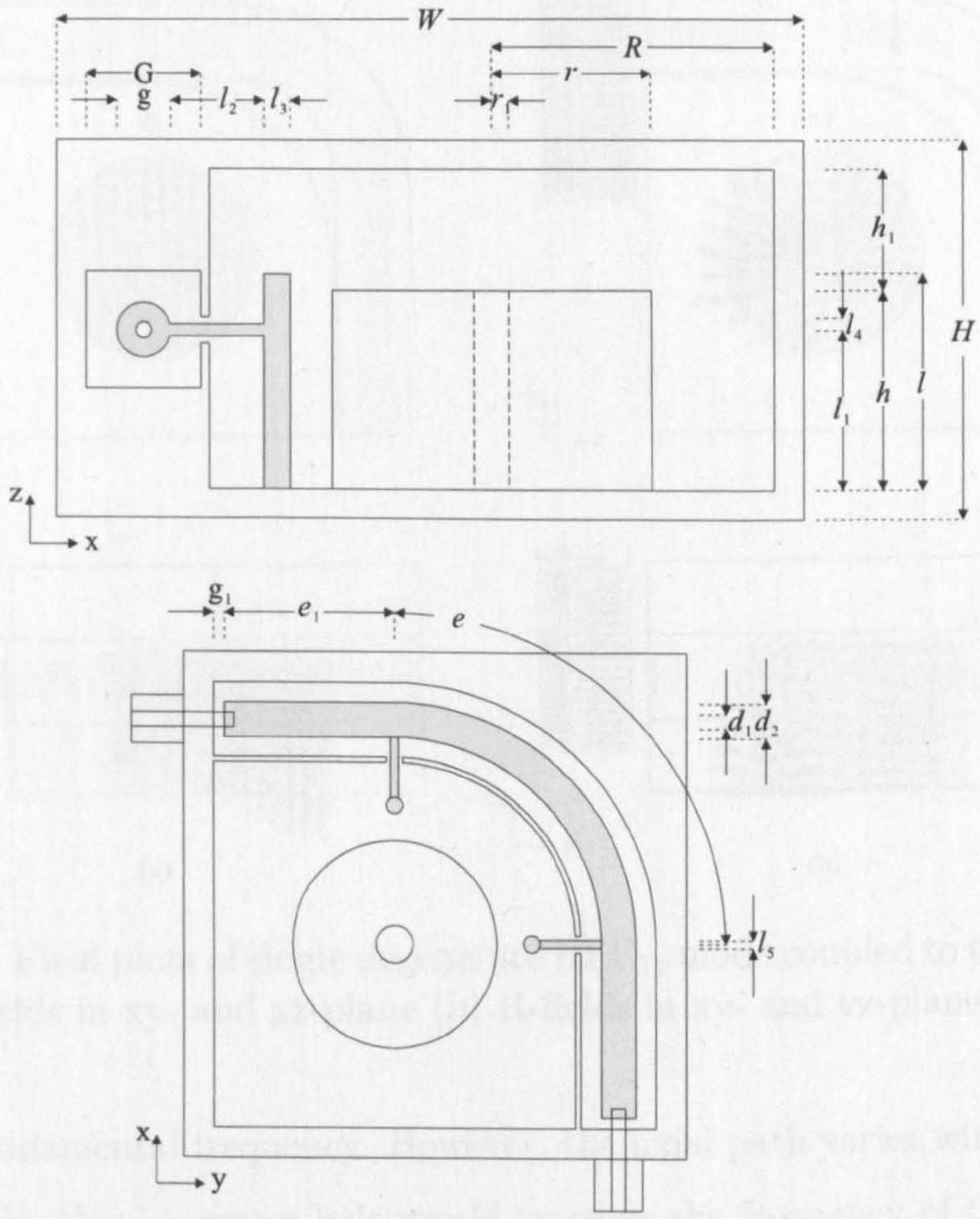

Figure 5.14: Details of HEE_{11} mode dielectric bandstop resonator

the circumference of the bottom puck. The H-field is concentrated through the centre of the transverse plane towards the cavity base, figure 5.15. There is greater variation of the fields dissecting the z-axis than in the axial direction of the puck which indicates that, in a fixed cavity, ε_r and the diameter of the puck have more effect on the resonant frequency than the puck height.

The eigenmode solver was used to simulate the resonant frequencies of the first five modes of the DR bandstop resonator, table 5.3, with dimensions from table 5.2. For the structure described, HEE_{11} is the fundamental mode but the resonant frequency increased from 1.07 GHz to 1.11 GHz caused by the interaction between the coupling posts. The Q_u of the fundamental mode was 8100 as the bottom face of the puck was now in direct contact with the cavity. The spurious response for DRs is generally poor and the first spurious $TE_{01\delta}$ mode occurred at 247 MHz

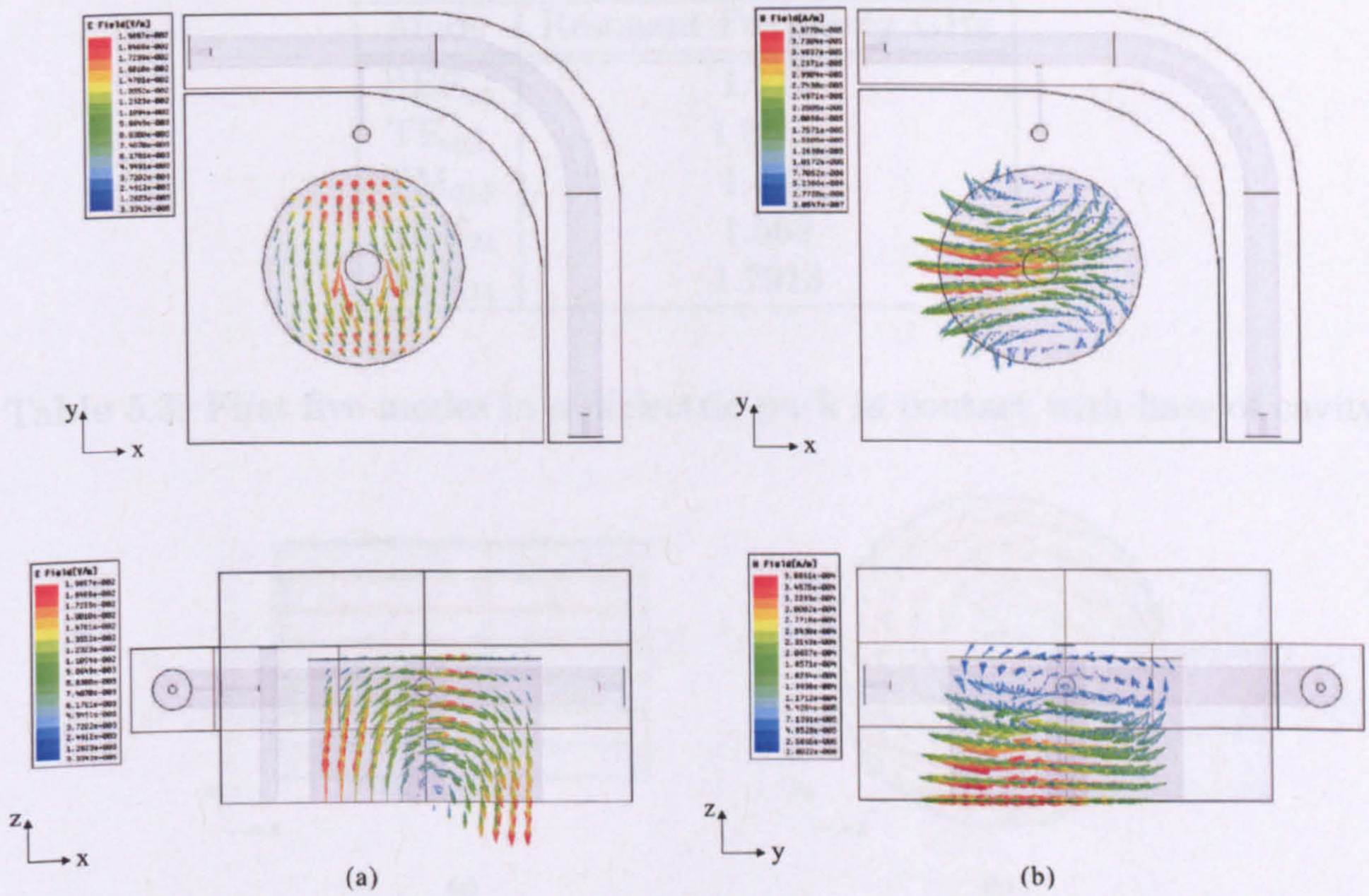

Figure 5.15: Field plots of single degenerate HEE_{11} mode coupled to transmission line: (a) E-fields in xy- and xz-plane (b) H-fields in xy- and yz-plane

above the fundamental frequency. However, the axial path varies with the TM_{01} spurious mode, thus, a centre hole would increase the frequency of this spurious mode. It is possible to improve the spurious response by removing portions of the puck where E-fields of spurious modes exist, [81]. The fields for the spurious $TE_{01\delta}$ are shown in figure 5.16. By removing sections to terminate the E-field paths, the spurious-free bandwidth will increase. An example is shown of the same dielectric puck used in the design with a small ring removed, figure 5.17. The dimensions of the ring are outer radius, 14 mm, inner radius, 7 mm, and height of 5 mm situated at 5 mm below the top surface of the puck. This modification produced a 50 MHz increase in the spurious bandwidth without affecting the fundamental frequency.

Figure 5.18 presents the tuning screw arrangement required for dual-mode cavity designs, [30]. The orthogonal modes are initially uncoupled but for cross-coupled designs, the bandwidth of this coupling may be controlled by placing a metallic screw opposite the perturbed edge of the cavity at 45° with respect to the two

Mode	Resonant Frequency GHz
HEE_{11}	1.111
$TE_{01\delta}$	1.3578
$TM_{01\delta}$	1.483
HEE_{21}	1.562
HEH_{11}	1.7913

Table 5.3: First five modes in a dielectric puck in contact with base of cavity

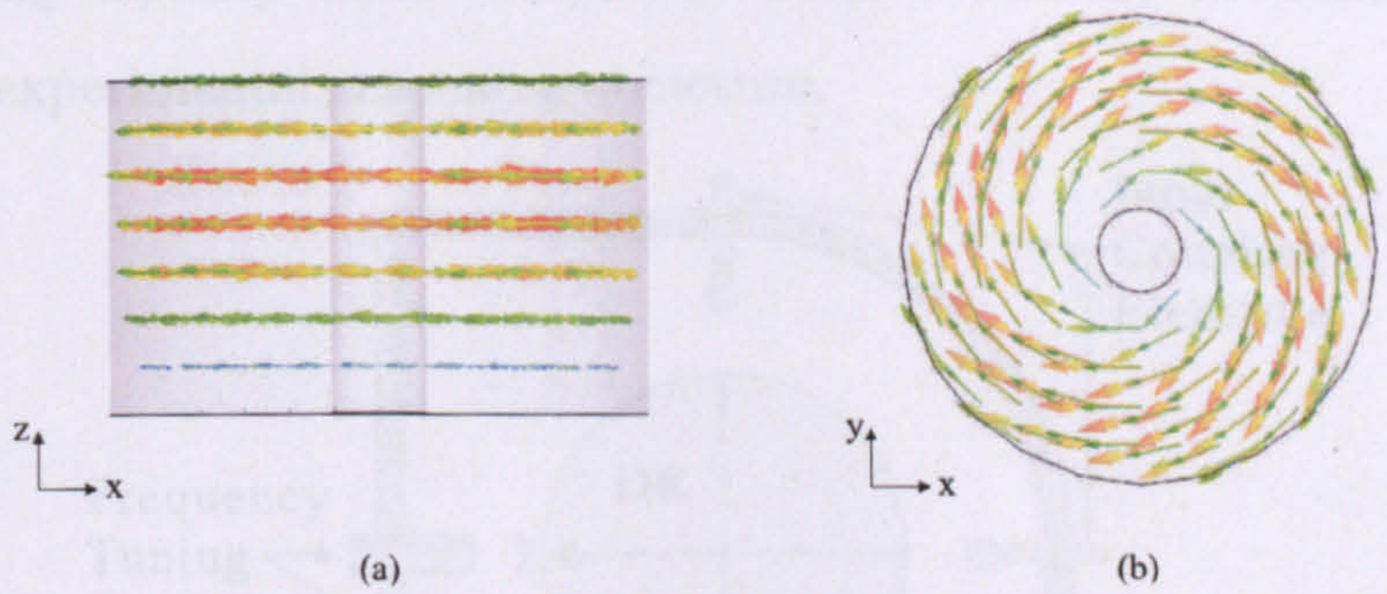

Figure 5.16: Field plot of first higher order spurious mode, $TE_{01\delta}$: (a) Side view (b) Top view (c)

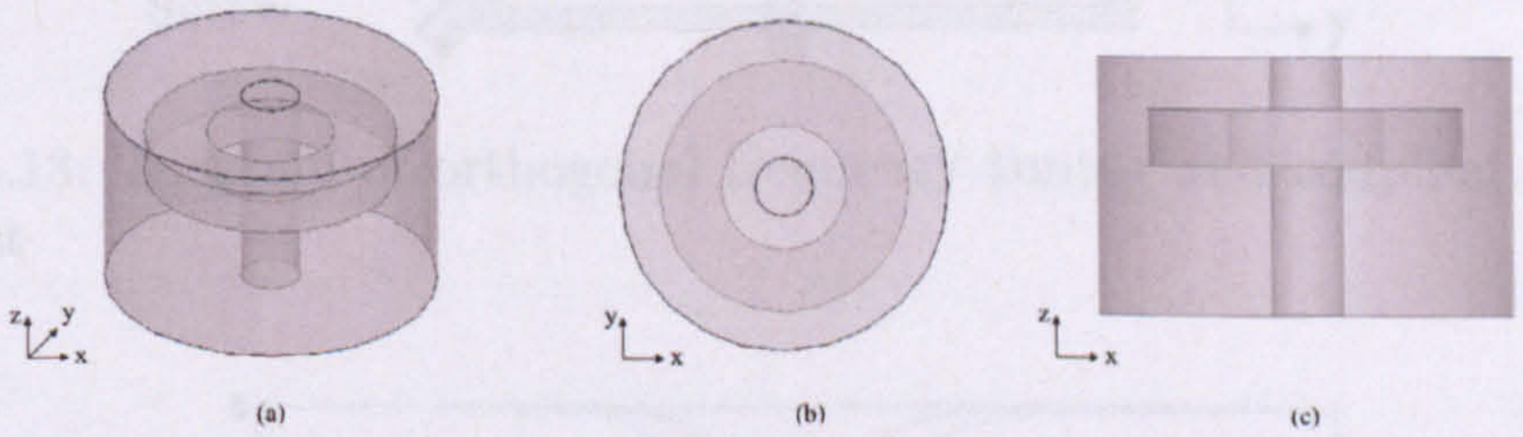

Figure 5.17: Dielectric puck with removed ring section for improved spurious: (a) 3D view (b) Top view (c) Side view

polarization axis. Tuning disks may also be used as the larger surface area will provide more tuning effect. As most of the fields lie within the dielectric, the screw must be tuned to close proximity to have a desired effect. This coupling variation can clearly be seen in figure 5.19 where a penetrating screw couples the two frequency modes together, splitting them further apart. The resonant frequency for each orthogonal mode may be controlled individually by placing tuning screws opposite each coupling post on the xy-plane. Figure 5.20 shows the effect of penetration of a tuning disk with a silver circular disk of 5 mm radius and 1 mm thickness attached on the end on mode 1. As the disk moves from 6.5 mm

inside the cavity to 14 mm towards the puck, the resonant frequency of mode 1, f1, decreases by over 3 MHz, while the frequency of mode 2, f2, increases slightly by 1.5%. For greater tuning bandwidth for each mode, a large screw is ideal but care must taken not to hugely distort the frequency of the second othogonal mode. Metal screws have a greater effect on frequency tuning but reduce the Q of the resonator. To maintain the Q, dielectric screws may be used but have a smaller tuning capacity when compared to metal screws. Metallic screws were used in the experimental resonator structure.

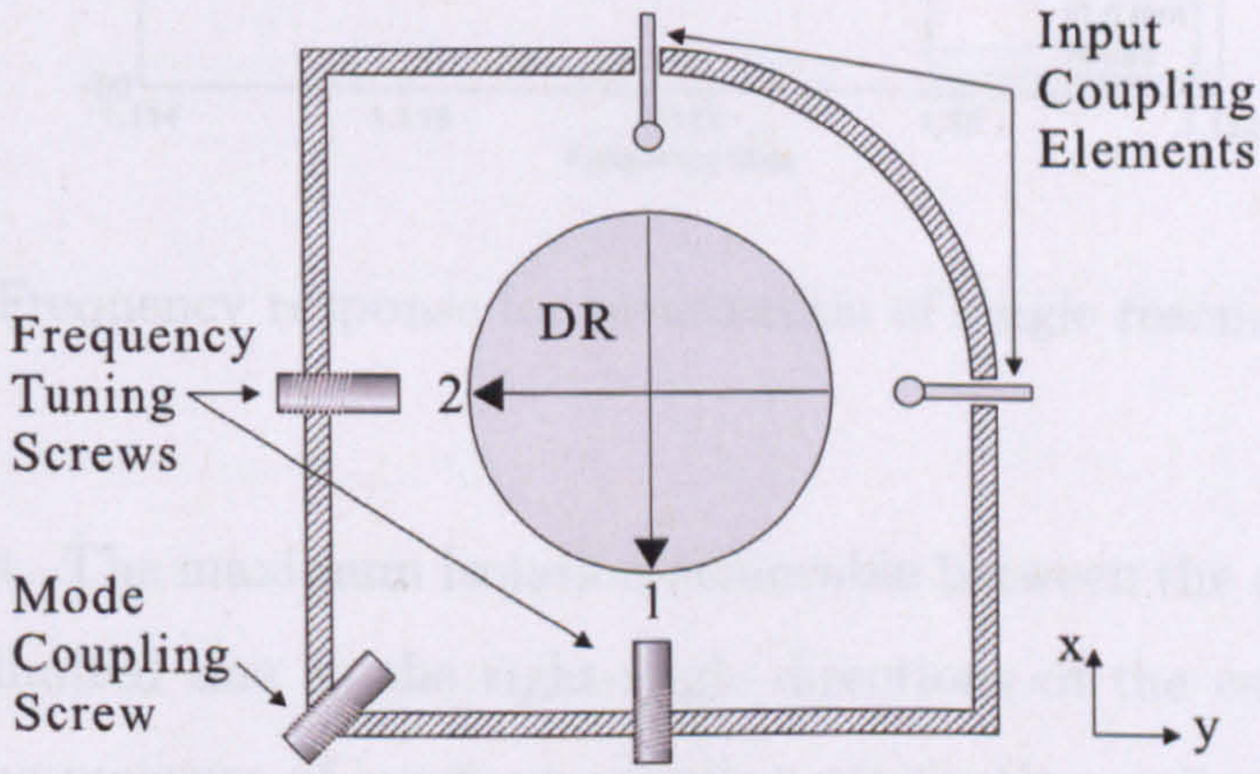

Figure 5.18: Diagram of orthogonal frequency tuning and coupling screws arrangement

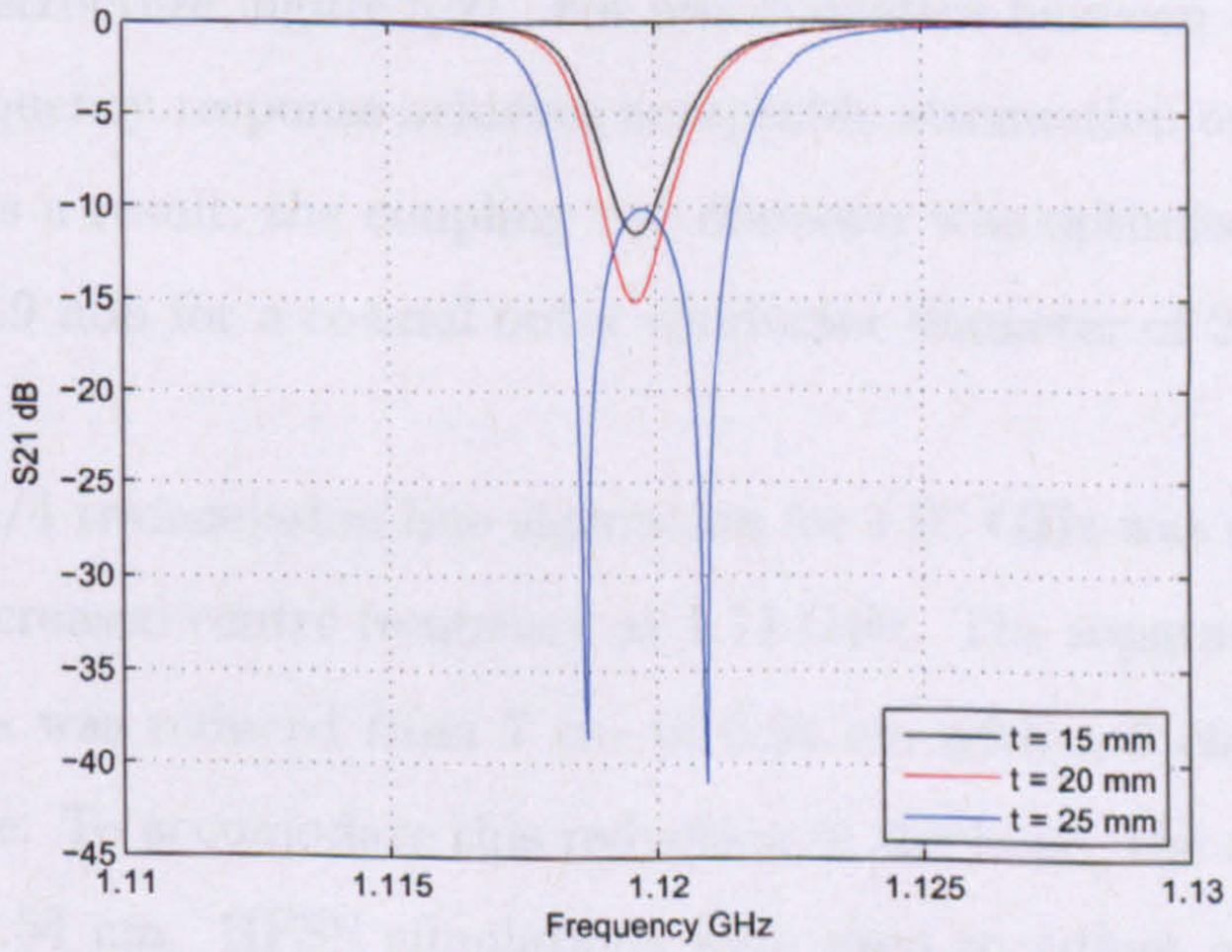

Figure 5.19: Frequency response for penetration of cross-coupling screw

The amount of bandwidth is controlled by the coupling rod length and the diam-

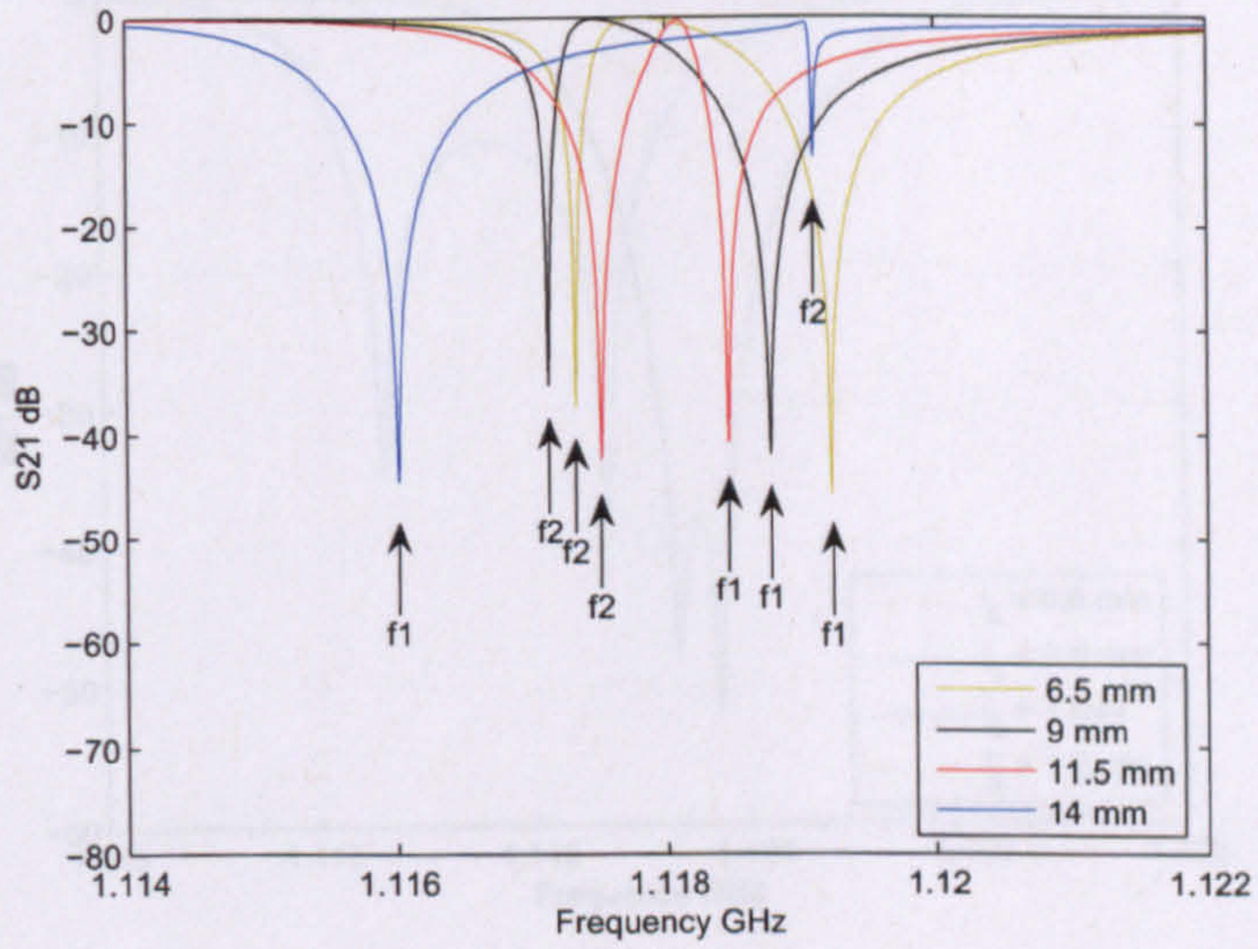

Figure 5.20: Frequency response for penetration of single resonant mode tuning screw

eter of the post. The maximum isolation achievable between the dual-mode input separation is limited due to the right-angle directions of the coupling elements producing some measure of spurious coupling within the cavity. This limits the bandstop attenuation but this problem can be reduced by optimising the size of the coupling elements, in particular the coupling rod diameters can be varied in the resonator structure, figure 5.21. For rod diameters between $l_5 = 0.8$ mm and 1 mm, the frequency response achieves acceptable attenuation over the bandstop bandwidth. As a result, the coupling rod diameter was optimised from 1.3 mm, table 5.2, to 0.9 mm for a coaxial outer conductor diameter of $2l_4 = 3$ mm.

The original $\lambda/4$ transmission line separation for 1.07 GHz was changed to accomodate the increased centre frequency at 1.11 GHz. The separation between the two tap points was reduced from 7 cm to 6.94 cm with a 2 cm radius bend in the coaxial line. To accomodate this reduction in the bend, the cavity walls were increased to 6.54 cm. HFSS simulations were used to adjust all these physical parameters and a single cavity resonator was simulated with a coupling distance of 5 mm between the inductive post and the puck. All dimensions were optimised in HFSS including the size of the cavity, the post sizes, input and output

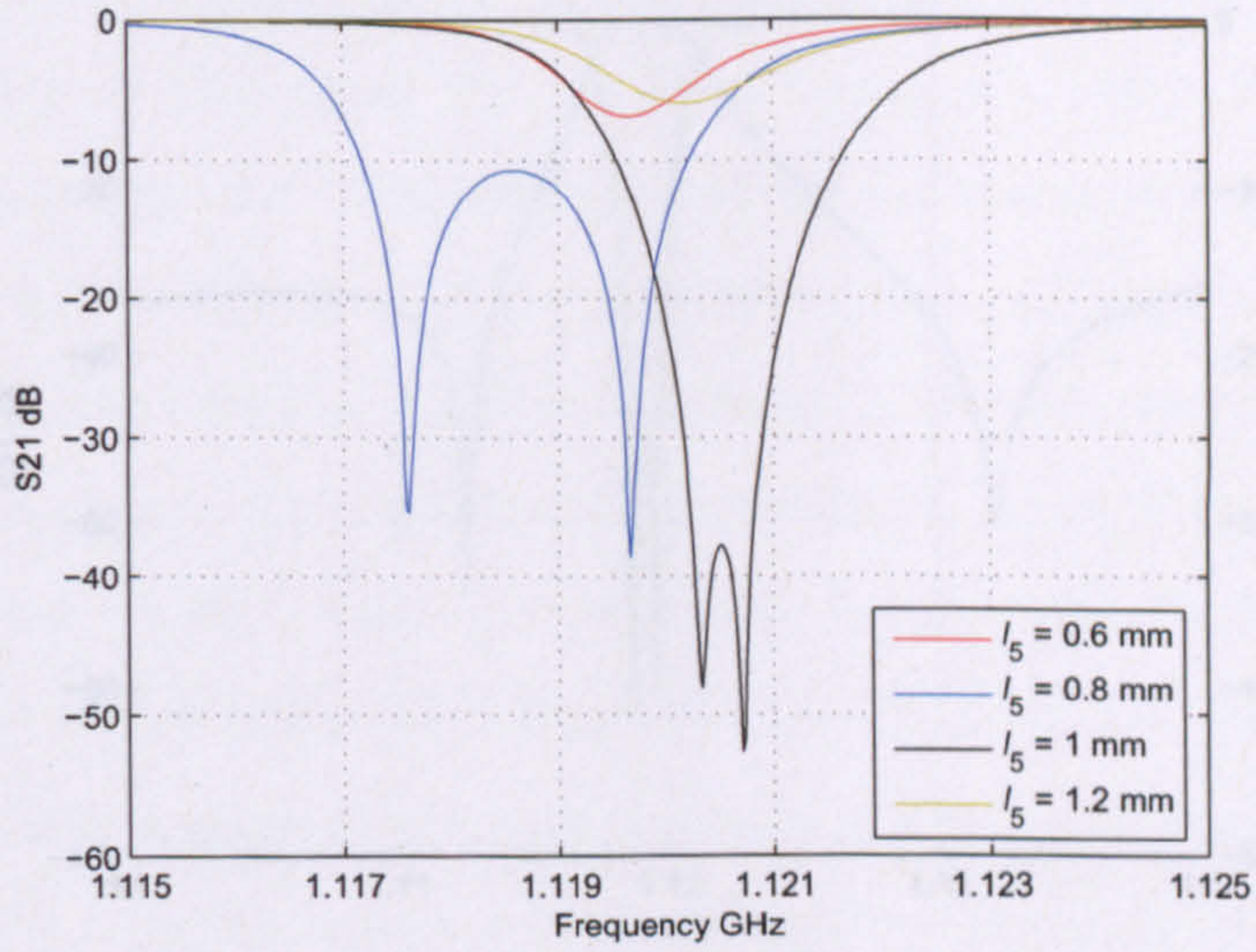

Figure 5.21: Optimisation of coupling rod diameter

couplings and phase separation was also changed. The frequency response of the experimental filter is shown in figure 5.22. The bend at one edge of the cavity to accomodate the right-angle coaxial line caused a reduction in the volume which, in turn, increased the frequency to 1.119 GHz. The simulation produced a 3 dB bandwidth of 3.6 MHz and a mid-band return loss of 0.18 dB. In addition, in dual-mode resonators, if the external surroundings are uniform and symmetrical, the frequencies of the degenerate modes can be identical leading to correct coupling between the two orthogonal modes. However, in cases where a discontinuity occurs in the cavity, such as an imperfection in the symmetry of the cavity or an external object being inserted, this would distort the orthogonality of the dual-modes affecting their coupling behaviour slightly. Tuning screws were introduced in the simulation to de-couple the modes.

The wideband performance of the filter was observed and a higher order mode occured at 1.432 GHz as shown in figure 5.23. This gave a spurious-free window of 313 MHz which is higher than the eigenmode solution. In fact, this mode was the TM_{01} from observation of the field pattern of this mode at its resonant frequency. The TE_{01} mode was not apparent because the inductive coupling post provided insufficient electric coupling.

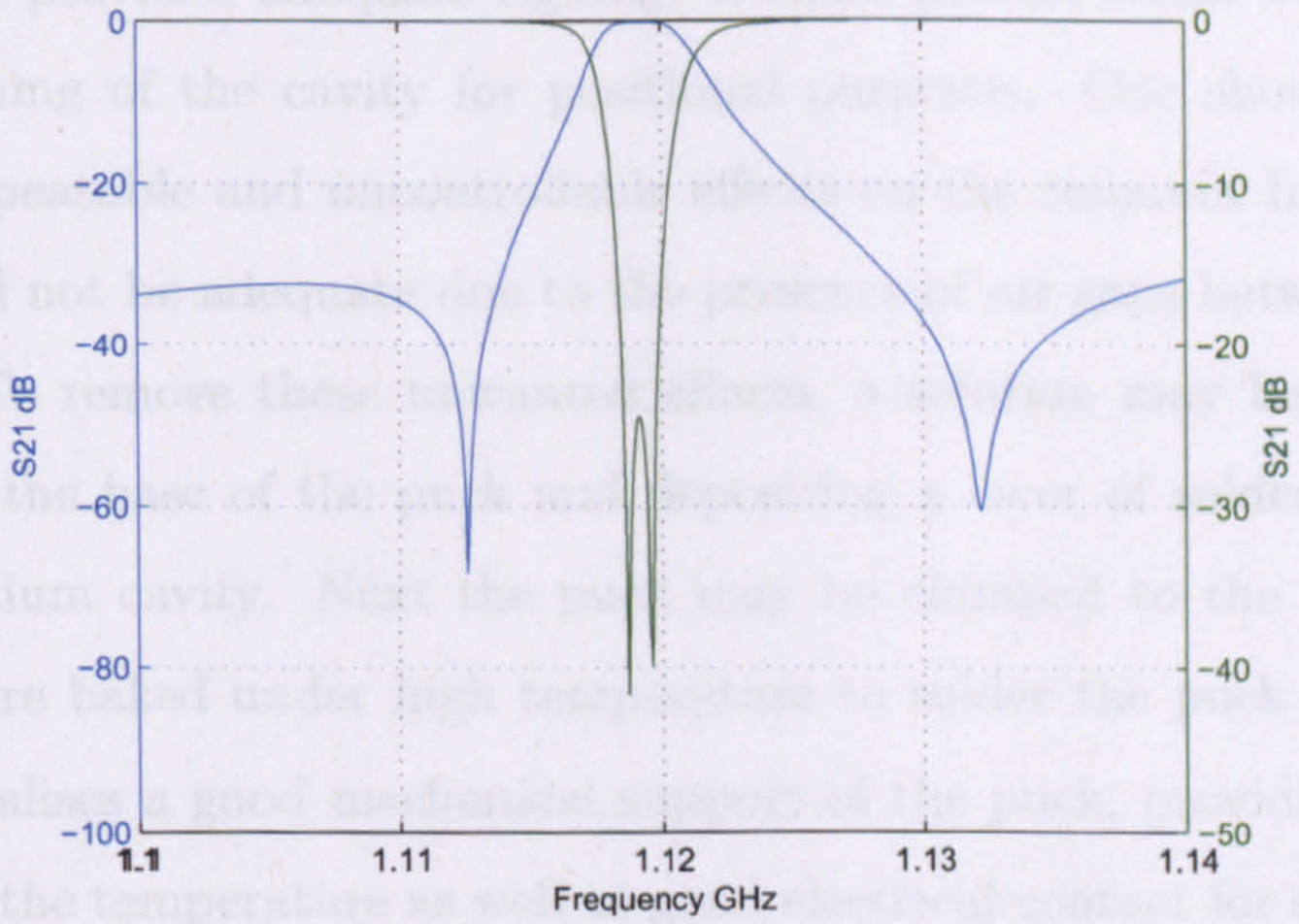

Figure 5.22: HFSS simulation of experimental filter for fabrication

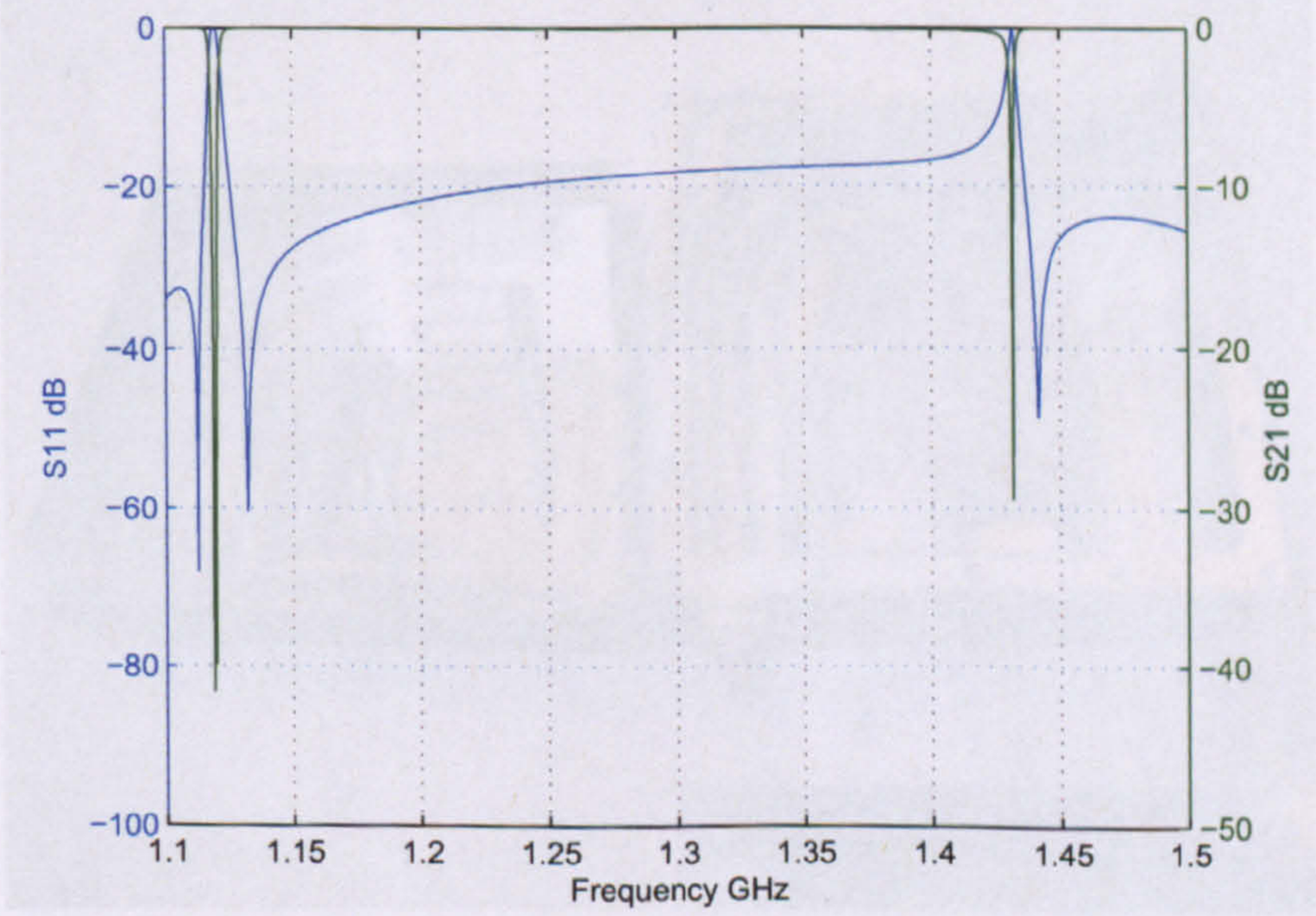

Figure 5.23: HFSS simulation of the spurious mode of the prototype filter for fabrication

5.4.2 Fabrication and measurements of dual-mode single cavity

The resonator mounting had to be mechanically robust and simple to fabricate. For this prototype it was found that applying a thin layer of glue between the

puck and base provided adequate rigidity. A small pocket island was also raised in the machining of the cavity for positional purposes. One should note that to avoid unrepeatable and uncontrollable effects on the resonant frequency, this method would not be adequate due to the presence of air gaps between the puck and cavity. To remove these unwanted effects, a solution may be provided by silver-plating the base of the puck and depositing a layer of solder on the base of the aluminium cavity. Next the puck may be clamped to the base and the whole structure baked under high temperature to solder the puck to the cavity base. This realises a good mechanical support of the puck, providing frequency stability over the temperature as well as good electrical contact for a high Q. The manufactured filter is shown in figure 5.24.

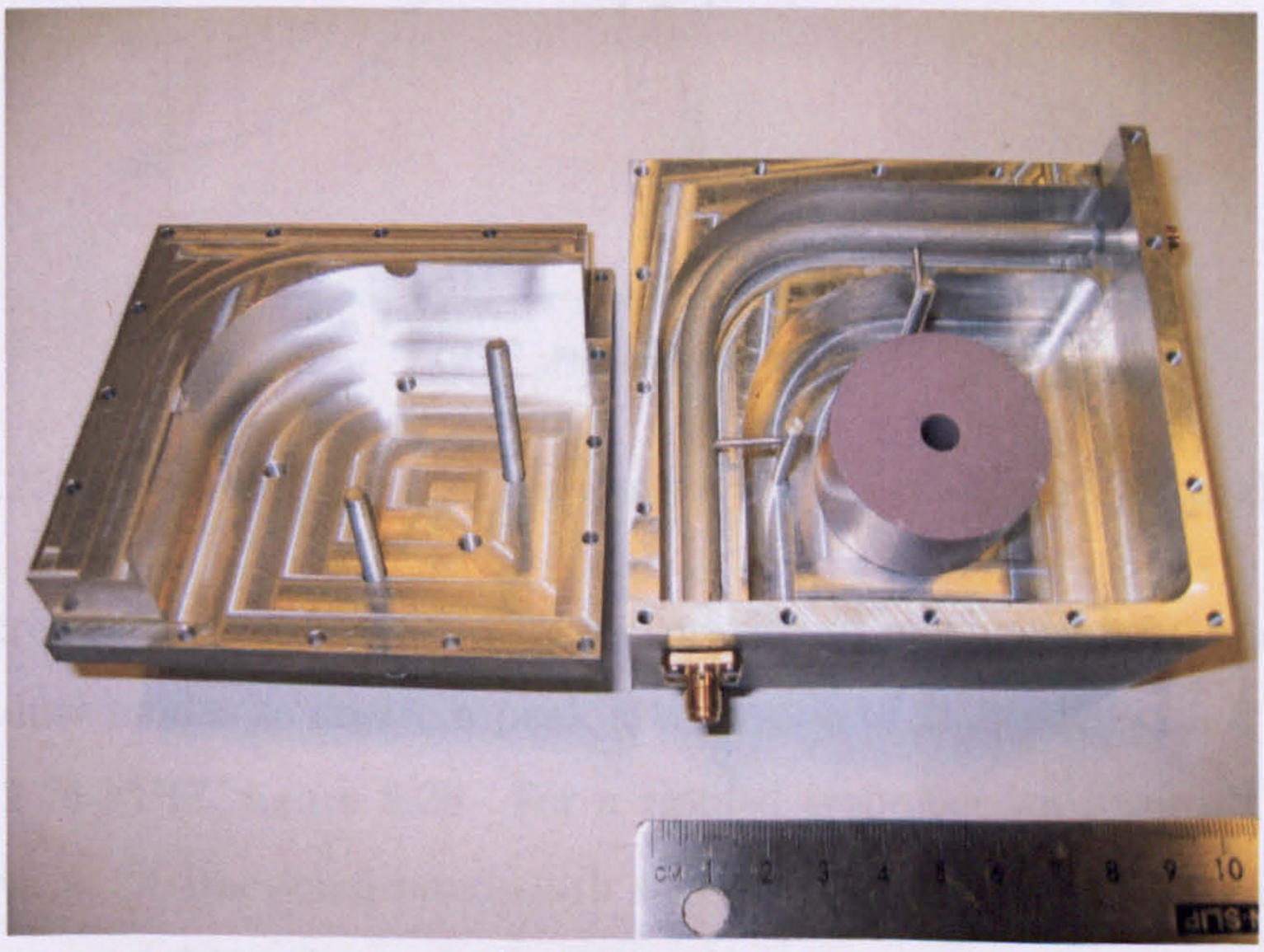

Figure 5.24: Fabricated single cavity of HEE_{11} dual-mode bandstop filter

The measured frequency response of the experimental bandstop filter is shown in figure 5.25. In this first measurement, no tuning screws were used and a centre frequency of 1.131 GHz was produced along with a 3 dB bandwidth of 4.59 MHz. The filter produced an attenuation of 18.56 dB. This figure incorporated any conductor losses and dielectric losses of the resonator and its surroundings. In particular, the air gap between the top plate of the filter and the body also creates

much loss, especially in the vicinity between the coaxial line and the main cavity. The losses here are due to the formation of the 1 mm diameter holes between the transmission line and cavity that are machined as two halves, one into the top and bottom of the enclosure. A small change in the symmetry here will create a discontinuity in the current flow along the face of the wall leading to loss.

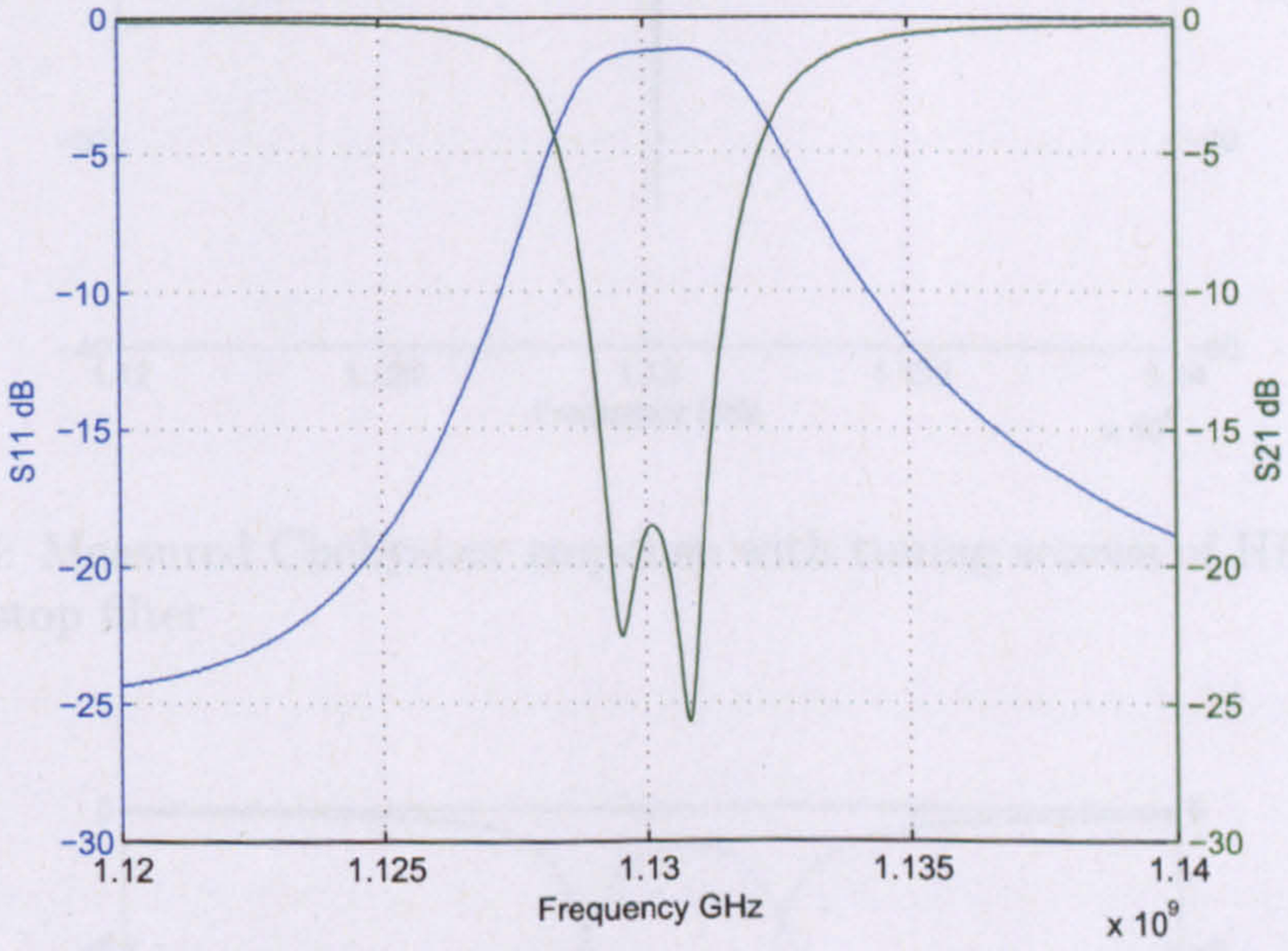

Figure 5.25: Measured frequency response of HEE_{11} experimental bandstop filter

Tuning screws were used to produce the maximum attenuation between the orthogonal dual modes to create a peak attenuation of 25.05 dB with 3 dB bandwidth of 2.74 MHZ, figure 5.26. For a rippled response, an inverse Chebyshev response with 1% fractional bandwidth was produced with a 3 dB bandwidth of 4.3 MHz at 1.13 GHz, figure 5.27. The spurious performance of the filter was measured with the next higher-order mode at 1.3689 GHz, figure 5.28, offering a spurious free passband of 240 MHz.

From these results, it was apparent how versatile this structure was since a number of filter functions can be realised through creating coupling paths between intra- or inter-cavity modes. However, for more complex functions, such as the elliptic approximation, the phase of the transmission line may be varied in the case of direct-coupled filters but for phase changes much smaller than $\lambda/4$, the

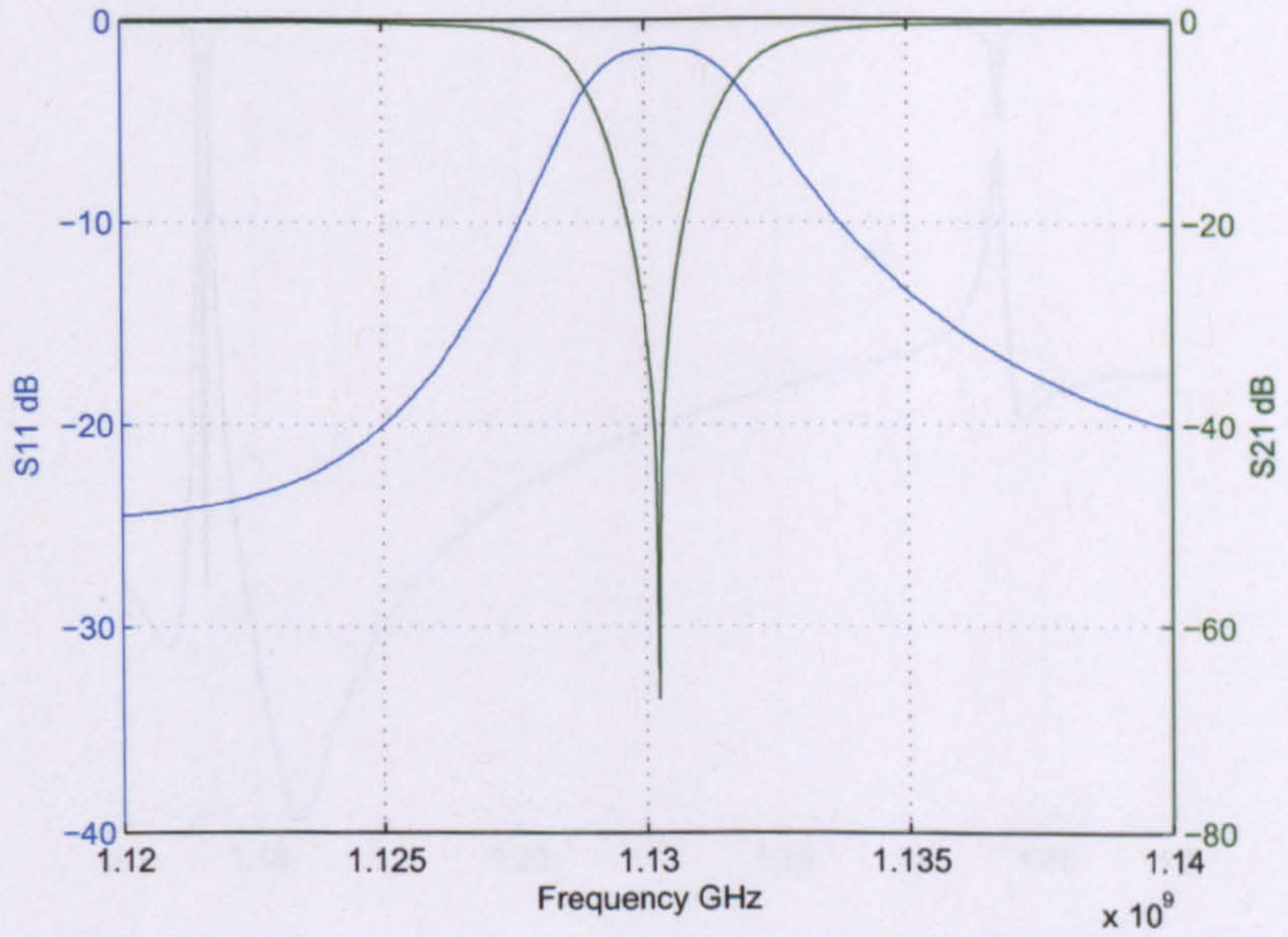

Figure 5.26: Measured Chebyshev response with tuning screws of HEE_{11} single cavity bandstop filter

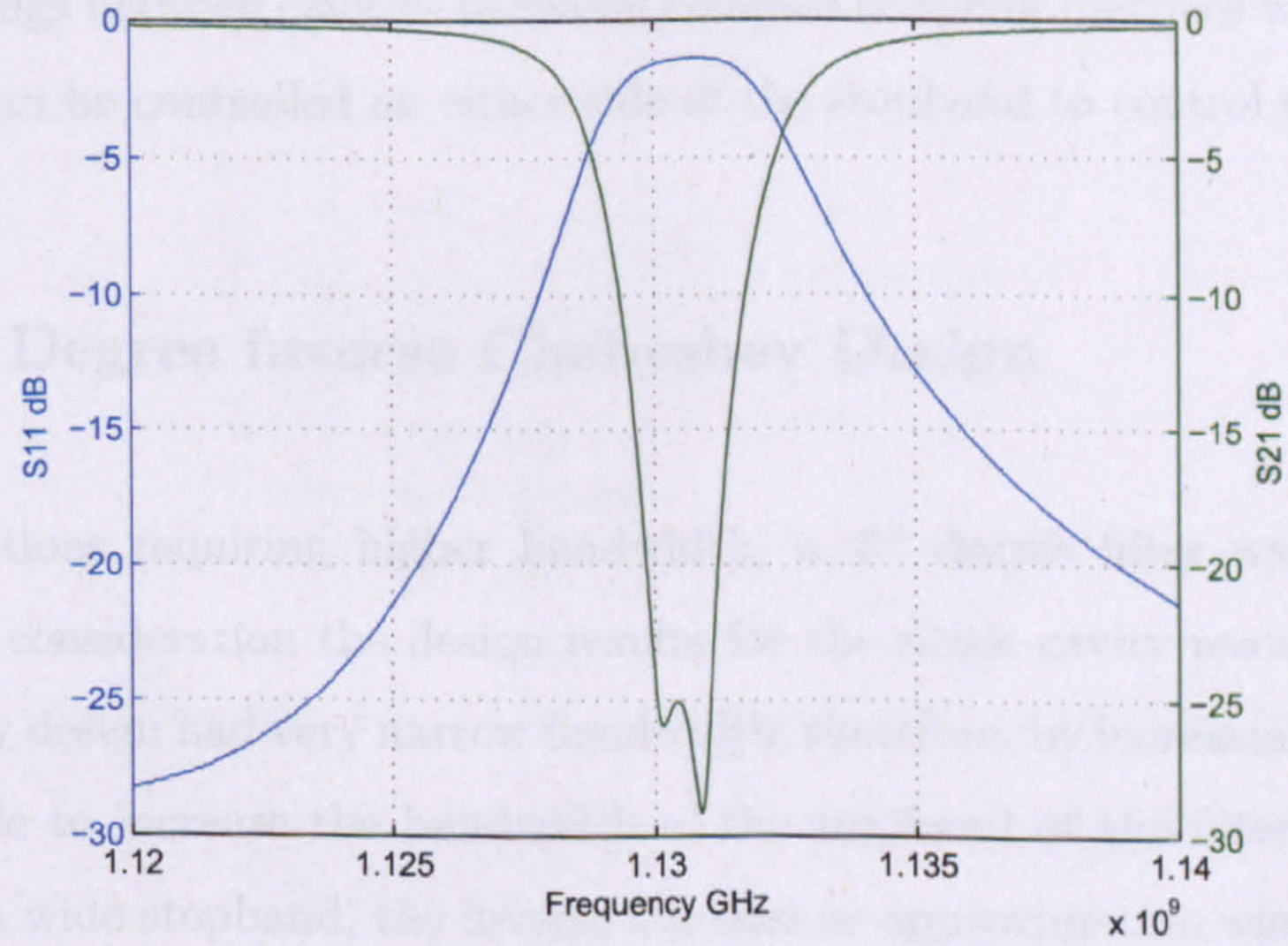

Figure 5.27: Inverse Chebyshev frequency response of HEE_{11} single cavity bandstop filter

transmission line may be scaled up by odd multiples of $\lambda/4$. In the HFSS simulations this was easily implemented through changing the radius of the transmission line bend which enabled the dual-mode separation to shift away from $\lambda/4$. By

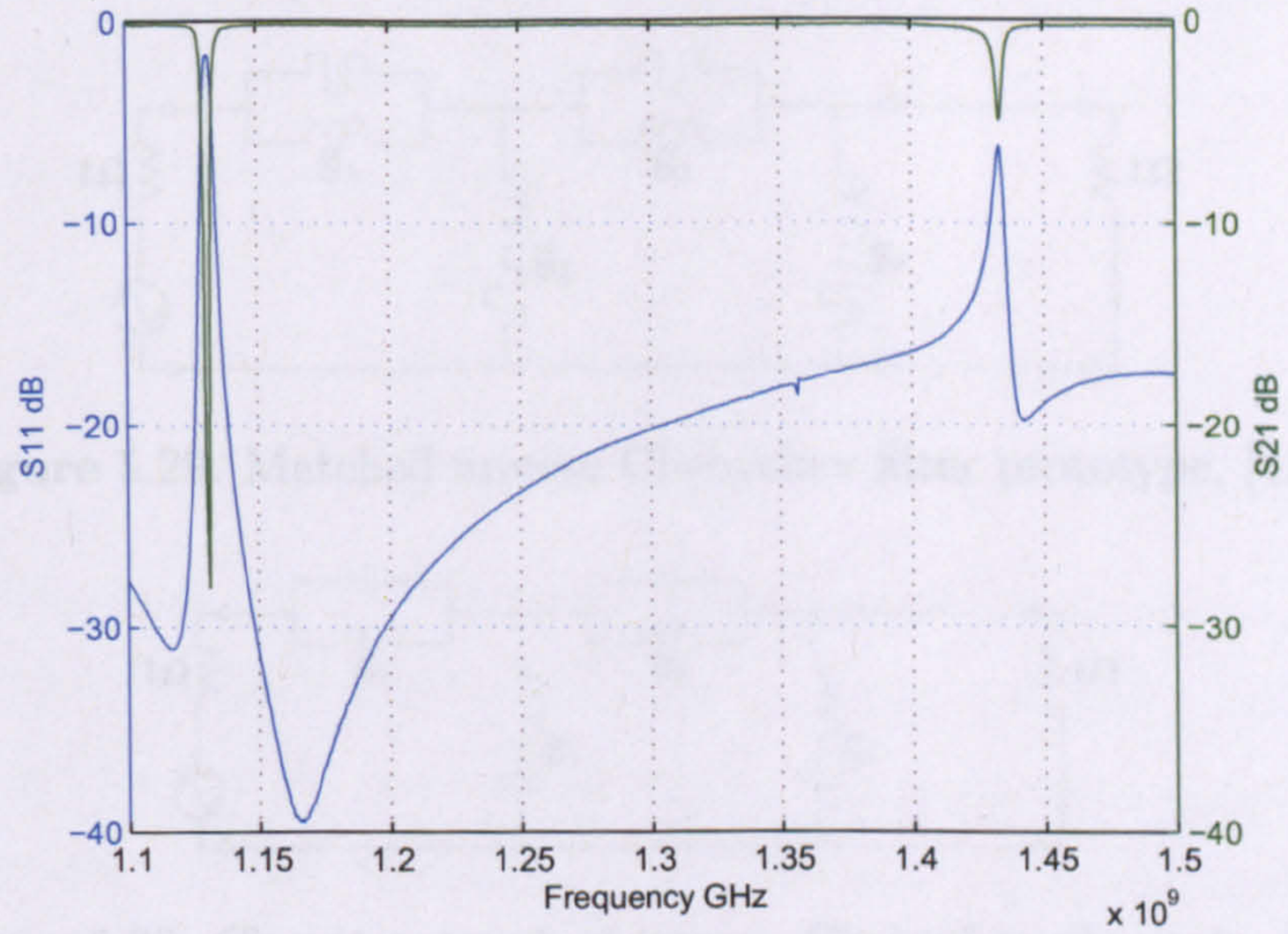

Figure 5.28: Spurious frequency response of HEE_{11} single cavity bandstop filter

cascading cavities, it is possible to create inter-cavity cross-couplings to create cross-couplings between cavities to model complex coupling matrices where rejection zeros can be controlled on either side of the stopband to control selectivity.

5.5 4^{th} Degree inverse Chebyshev Design

For applications requiring higher bandwidth, a 4^{th} degree filter was designed taking into consideration the design results for the single cavity resonator. The single cavity design had very narrow bandwidth, therefore, by increasing the order it is possible to increase the bandwidth of the stopband of the filter. In order to achieve a wide stopband, the inverse Chebyshev approximation was used as it offers a maximally flat passband and steep skirt to produce an equiripple stopband for a symmetrical response. The design follows from the transformation of a highpass matched inverse prototype, figure 5.29, to the ladder prototype network, figure 5.30, [41]. The network then translates to a symmetrical bandstop filter formed from an inverter-coupled network with each inverter equivalent to a unit element, figure 5.31. The filter specifications for the two cavity design are shown

in table 5.4.

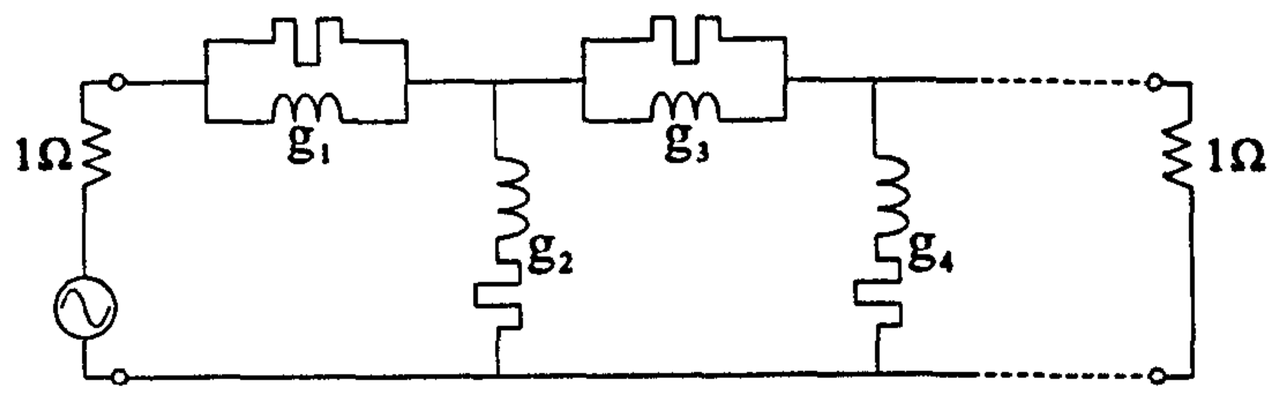

Figure 5.29: Matched inverse Chebyshev filter prototype, [41]

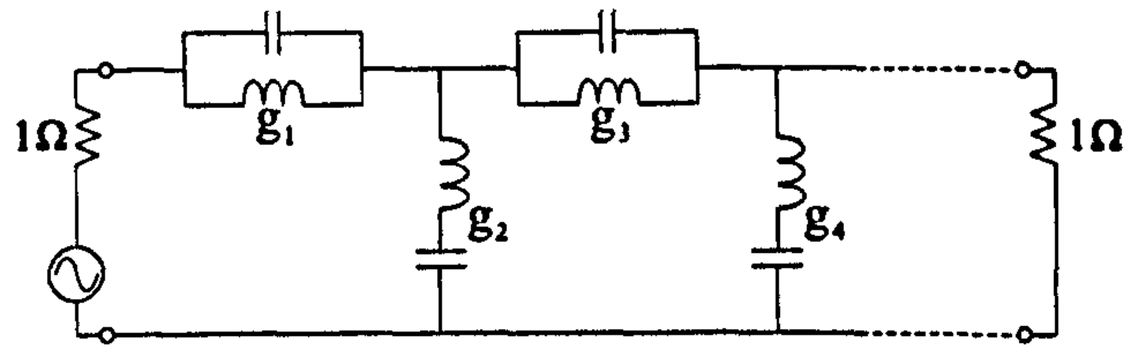

Figure 5.30: Circuit network of inverse Chebyshev elements, [41]

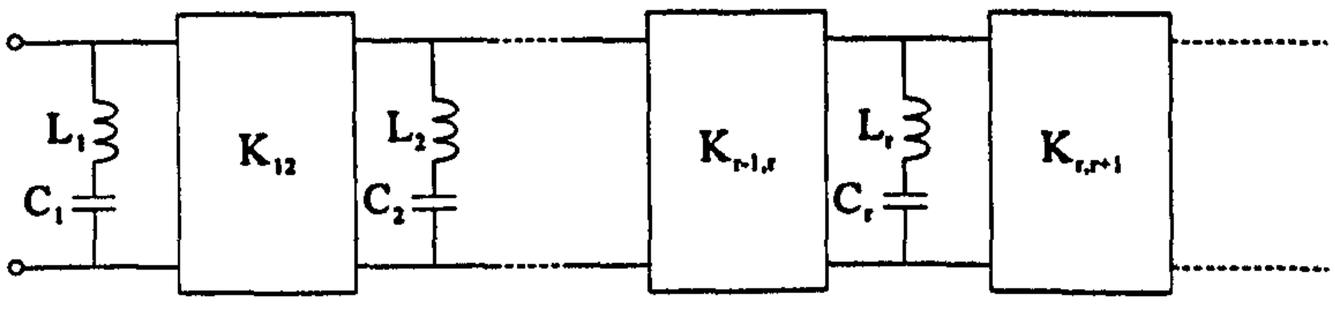

Figure 5.31: Inverse Chebyshev bandstop filter prototype, [82]

Filter Specifications	
Centre frequency	1.15 GHz
Passband bandwidth	24 MHz
Return loss (L_R)	20 dB
Stopband bandwidth	6 MHz
Insertion loss (L_A)	30 dB

Table 5.4: Filter specification for 4^{th} degree inverse Chebyshev bandstop filter

5.5.1 Inverse Chebyshev element values

The synthesis values for the design have been calculated from [41]. Specifications were produced that required a 4^{th} degree Chebyshev filter, equation 4.21,

$$N \geq \frac{30 + 20 + 6}{20 \log_{10}[4 + (4^2 - 1)^{1/2}]} \geq 3.68 \tag{5.1}$$

hence, a filter of degree 4 was required and a two cavity dual-mode structure was suitable. Next the bandwidth scaling factor, α, was calculated to be 191.7 and the element values were as follows,

$$\frac{1}{g_r} \approx Ap + \frac{B}{p} = Cp + \frac{1}{Lp} \tag{5.2}$$

The element values are derived from the following approximate frequency transformation to realise the frequency invariant reactance from figure 5.29. The transformation is based on the approximation that a lumped inductor or capacitor of equal reactance will behave similar to the frequency invariant reactance in the vicinity of $\omega_1 < \omega < \omega_2$ where $\omega_1 \approx \omega_2$. The immitance of the r^{th} element is calculated from

$$A = \frac{2\alpha + \cos\theta_r}{4\omega_0 \eta \sin\theta_r} \tag{5.3}$$

$$B = \frac{\omega_0(2\alpha - \cos\theta_r)}{4\eta \sin\theta_r} \tag{5.4}$$

for r = 1, $\theta = \pi/8$,

$$A_1 = L1 = 2.8185e \times 10^{-8} \text{ H} \tag{5.5}$$

for r = 2, $\theta = 3\pi/8$,

$$A_2 = L2 = 1.1658 \times 10^{-8} \text{ H} \tag{5.6}$$

for r = 3, $\theta = 5\pi/8$,

$$A_3 = L3 = 1.1635 \times 10^{-8} \text{ H} \tag{5.7}$$

for r = 4, $\theta = 7\pi/8$,

$$A_4 = L4 = 2.8049 \times 10^{-8} \text{ H} \tag{5.8}$$

The same θ values were used to calculate the rest of the elements.

$$B_1 = 1.4644 \times 10^{12}, C_1 = 6.8284 \times 10^{-13} \text{ F} \tag{5.9}$$

$$B_2 = 6.0745 \times 10^{11}, C_2 = 1.6462 \times 10^{-12} \text{ F} \tag{5.10}$$

$$B_3 = 6.0867 \times 10^{11}, C_3 = 1.6429 \times 10^{-12} \text{ F} \tag{5.11}$$

$$B_4 = 1.4715 \times 10^{12}, C_4 = 6.7957 \times 10^{-13} \text{ F} \tag{5.12}$$

In a 1 Ω system, the circuit model is shown in figure 5.32. The circuit approximation was simulated and the ideal inverse Chebyshev response is shown in figure 5.33.

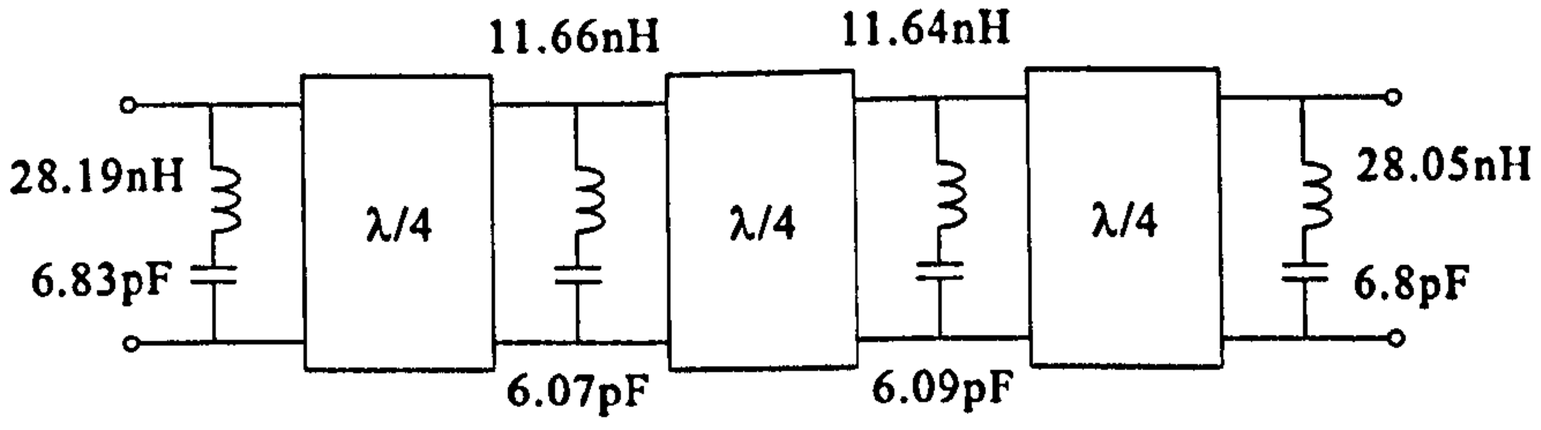

Figure 5.32: 4^{th} degree circuit model inverse Chebyshev bandstop filter

5.6 HFSS optimisation

The design was similar to the single cavity design using the same dielectric puck, coupling elements and coaxial transmission line, however, the cavity was modified to use a cylindrical waveguide cavity under cutoff conditions for efficient FEM simulations. This is useful as the symmetry of the structure and appropriate magnetic- or electric-wall boundaries allows the simulation time to reduce dramatically. A top view of the structure ahows the dimensions that were varied for

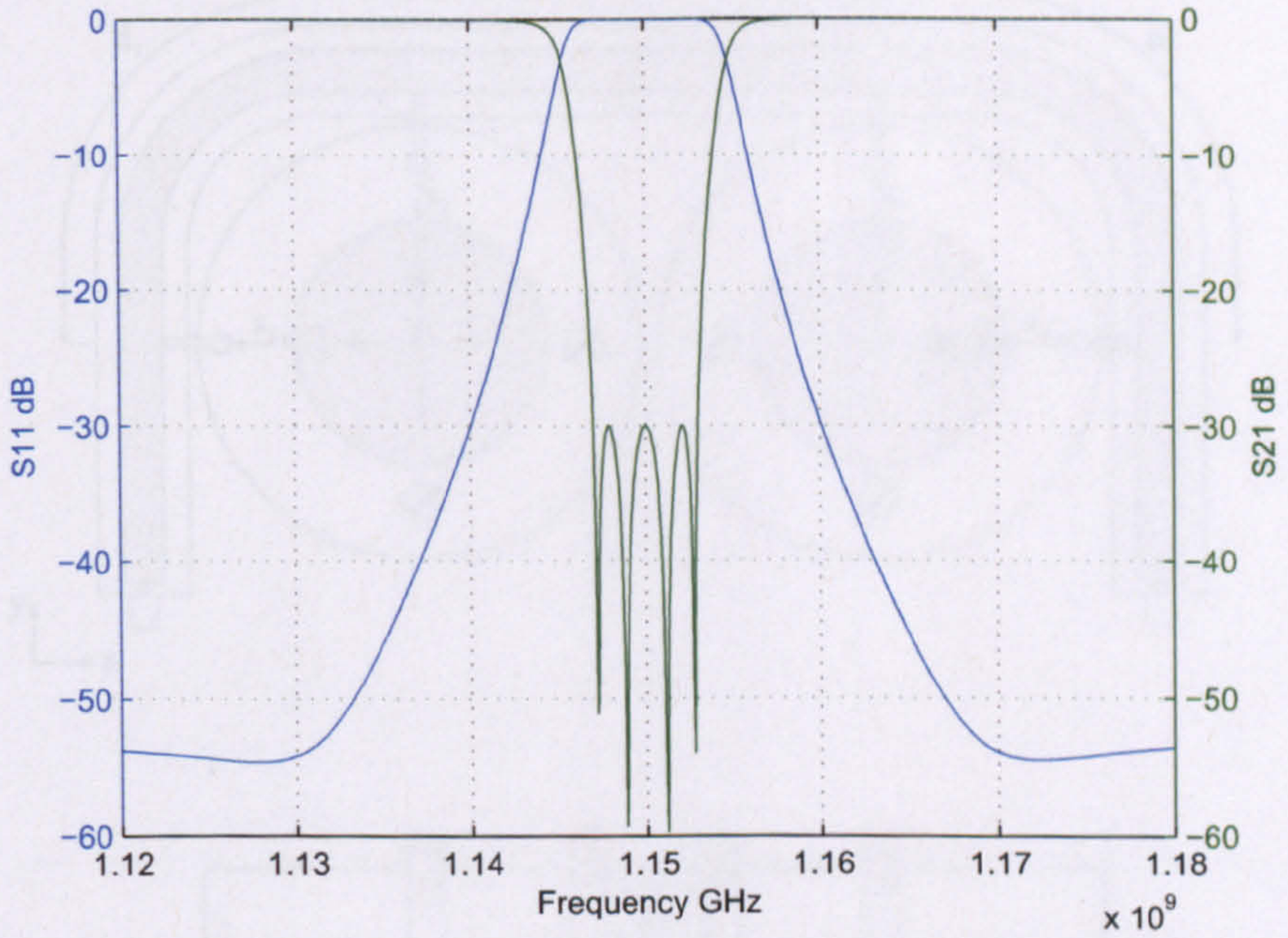

Figure 5.33: 4^{th} degree circuit model inverse Chebyshev bandstop filter

optimisation, in particular, for even heights in both cavities, the tuning depth is increased from the first to last resonant mode depicted by t_1 to t_4, figure 5.34. The coupling bandwidths for each tuning element was adjusted with spacings $s_1 = s_4$ and $s_2 = s_3$.

To aid the design, initial simulations were performed to find the optimum cavity height for the resonant frequency to be slightly above centre frequency to allow tuning down to the required resonant frequency, figure 5.35. For correct coupling bandwidths, a simulation of the tuning element spacing against coupling bandwidth was produced to extract the required spacings, figure 5.36.

The reactance slope parameter method, as used for the $TE_{10\delta}$ bandstop filter, was used to realise the physical filter from the circuit model, however, each resonance mode could not be treated individually due to spurious coupling between the degenerate modes in each cavity. The optimisation technique involved performing HFSS simulations to equate the frequency response and 3 dB bandwidth for each consecutive dual-resonator circuit from the prototype, figure 5.32, and required results shown in table 5.5. The first step was to observe the middle two resonators

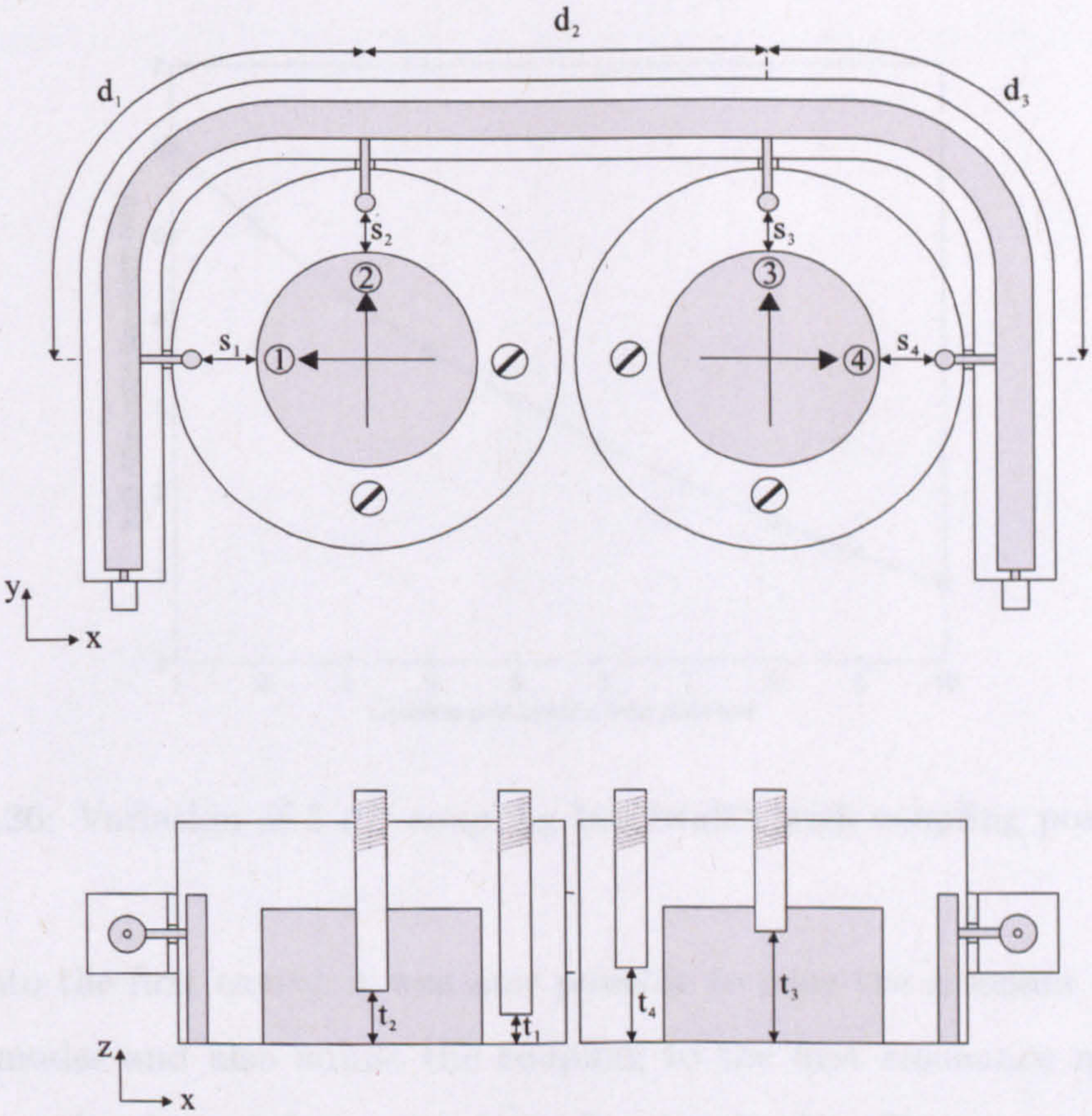

Figure 5.34: Top view of HFSS simulation with variables for optimisation

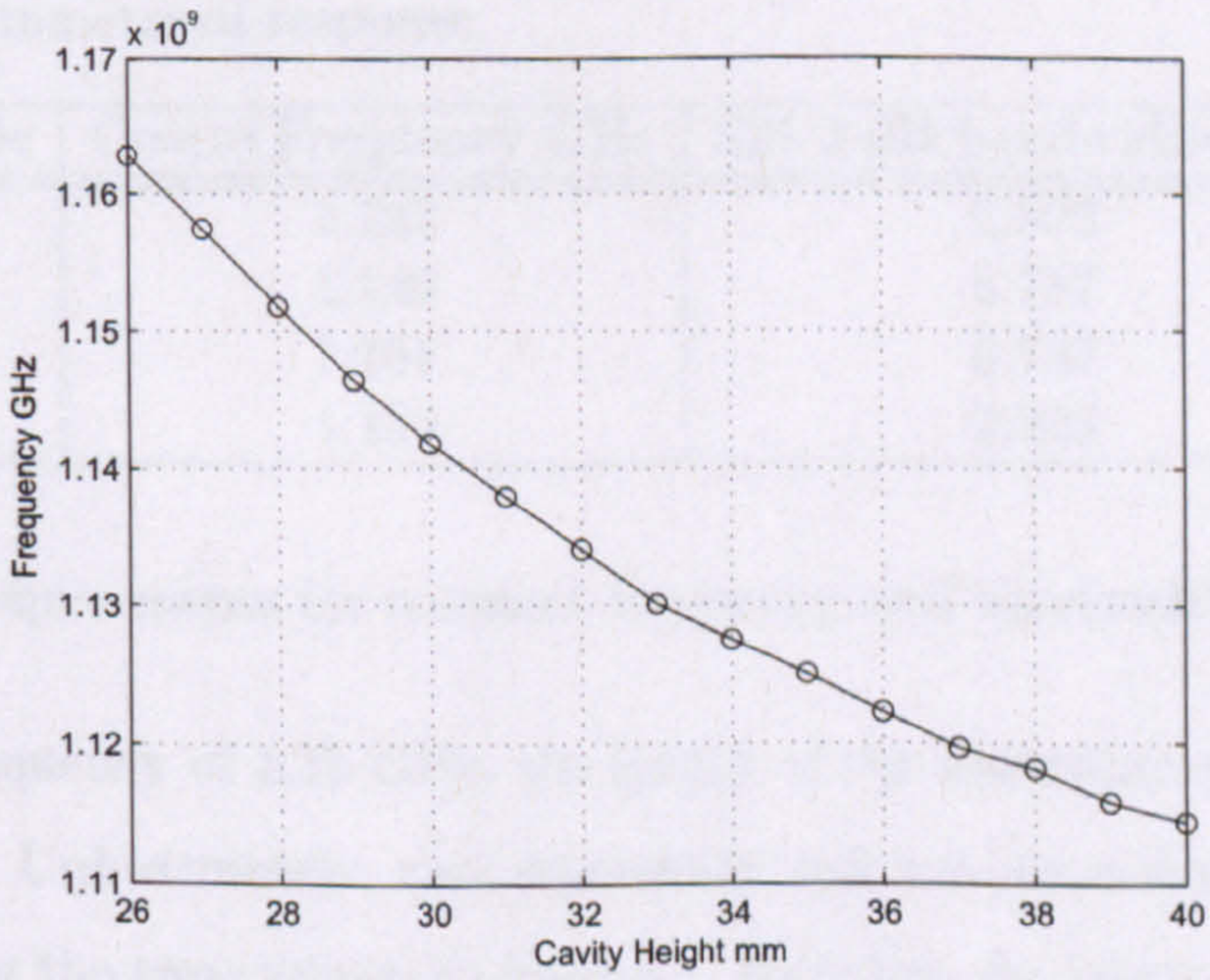

Figure 5.35: Variation of resonant frequency with DR circular cavity height

from the circuit since their symmetrical bandwidth and isolation within their respective cavity allowed the desired physical dimensions of their tuning elements.

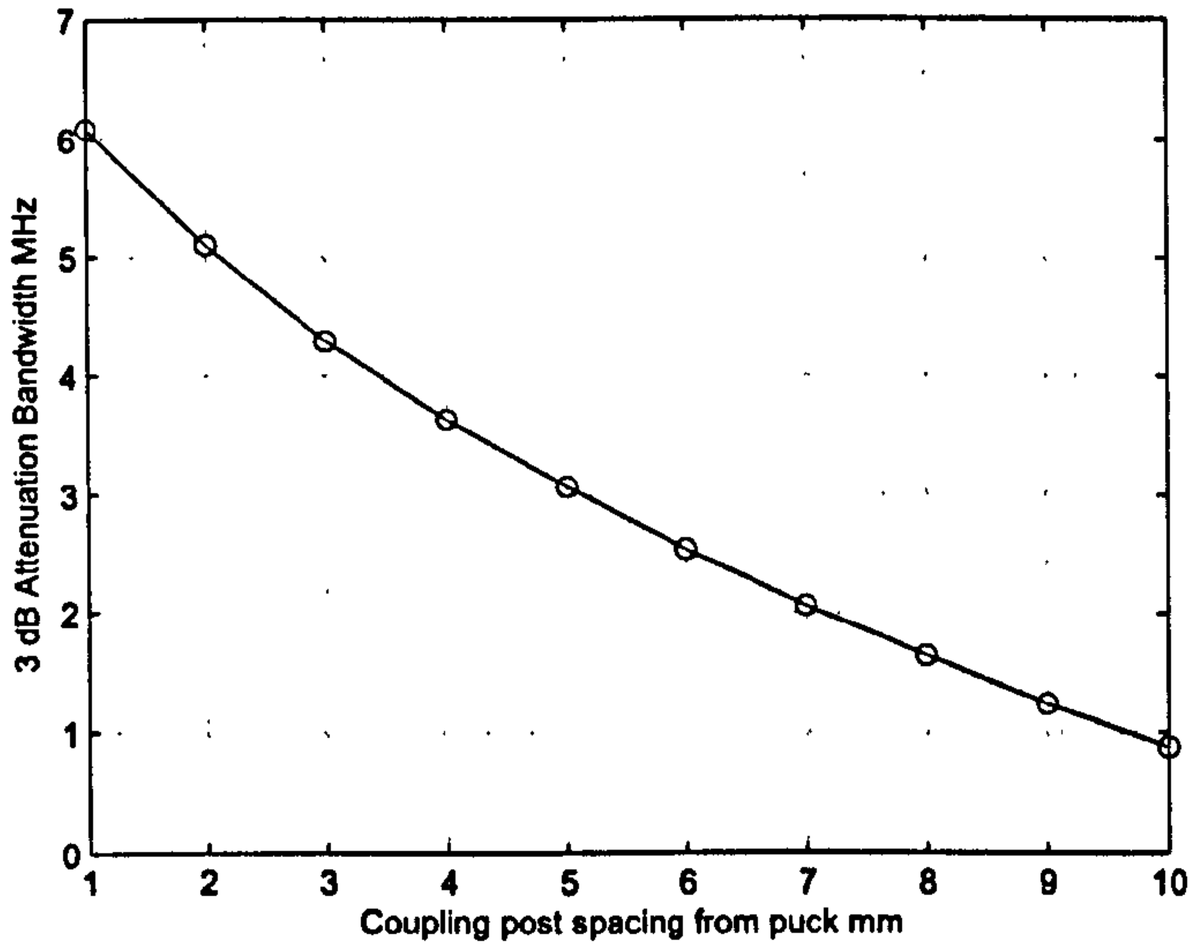

Figure 5.36: Variation of 3 dB coupling bandwidth with coupling post to puck spacing

Moving into the first cavity, it was now possible to tune the resonant frequency for both modes and also adjust the coupling to the first resonance mode such that both modes showed the required coupling bandwidth. The same process was applied to the second cavity and the last step was to adjust the $\lambda/4$ separations to achieve a symmetrical response.

Mode	Centre Frequency GHz	S21 3 dB bandwidth MHz
1	1.147	2.823
2	1.149	6.787
3	1.151	6.787
4	1.153	2.823

Table 5.5: Requirements for resonant frequency and bandwidth for each mode

At a centre frequency of 1.15 GHz, the length of the separations was taken to be 6.52 cm long. Unfortunately, this separation was too short for the middle resonators causing the two cavities to intersect, therefore, for fabrication purposes, a value of 6.7 cm was chosen to separate the two centre input taps. This was incorporated into the final HFSS 3D model, figure 5.37 and the optimised frequency response is produced in figure 5.38. The out-of-band asymmetry is caused by the 3% increase of the separation between the middle resonators. For future designs,

it is proposed that the cavity radii be decreased to accomodate the separations required.

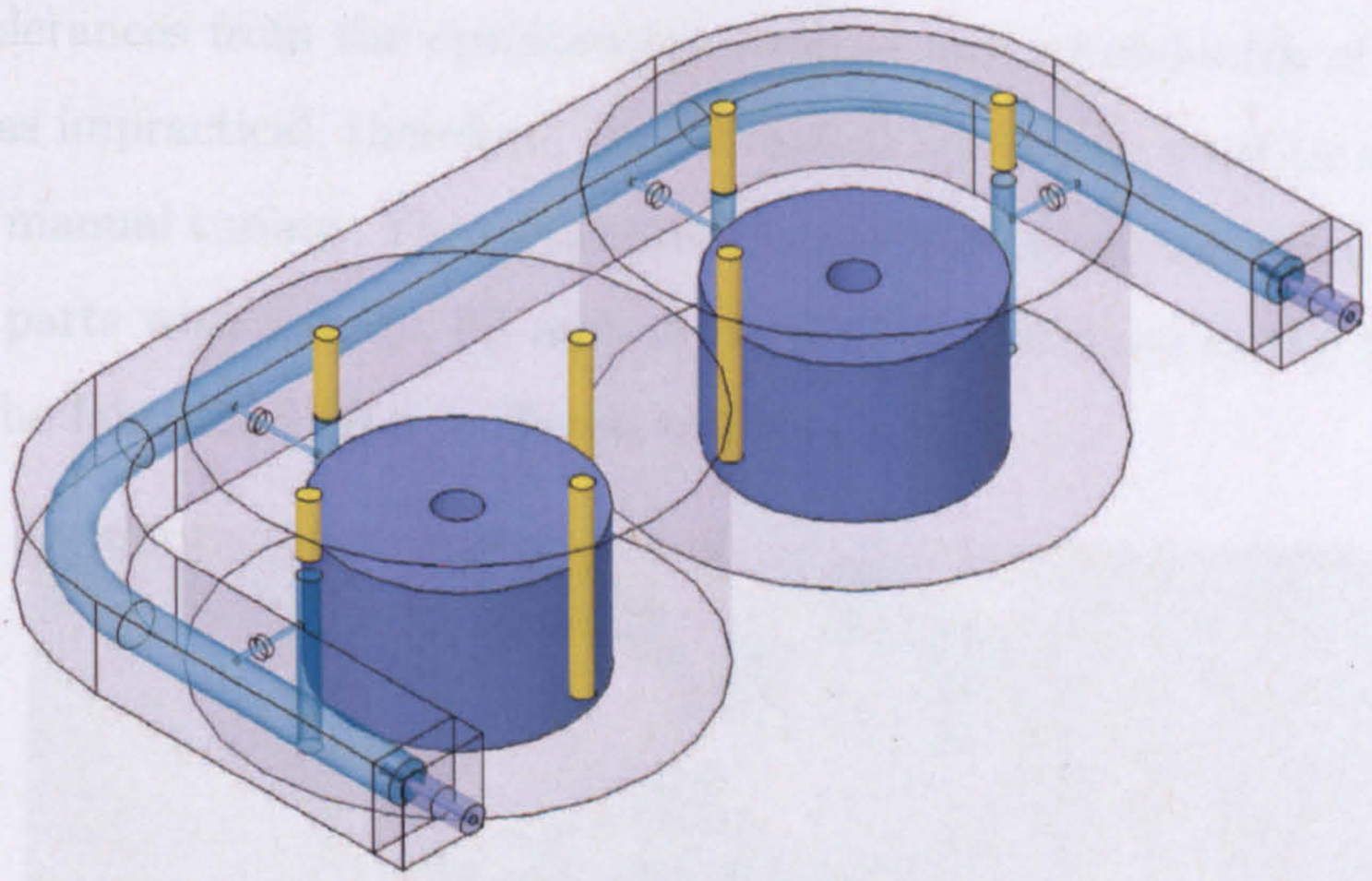

Figure 5.37: Final HFSS simulated model for inverse Chebyshev bandstop filter

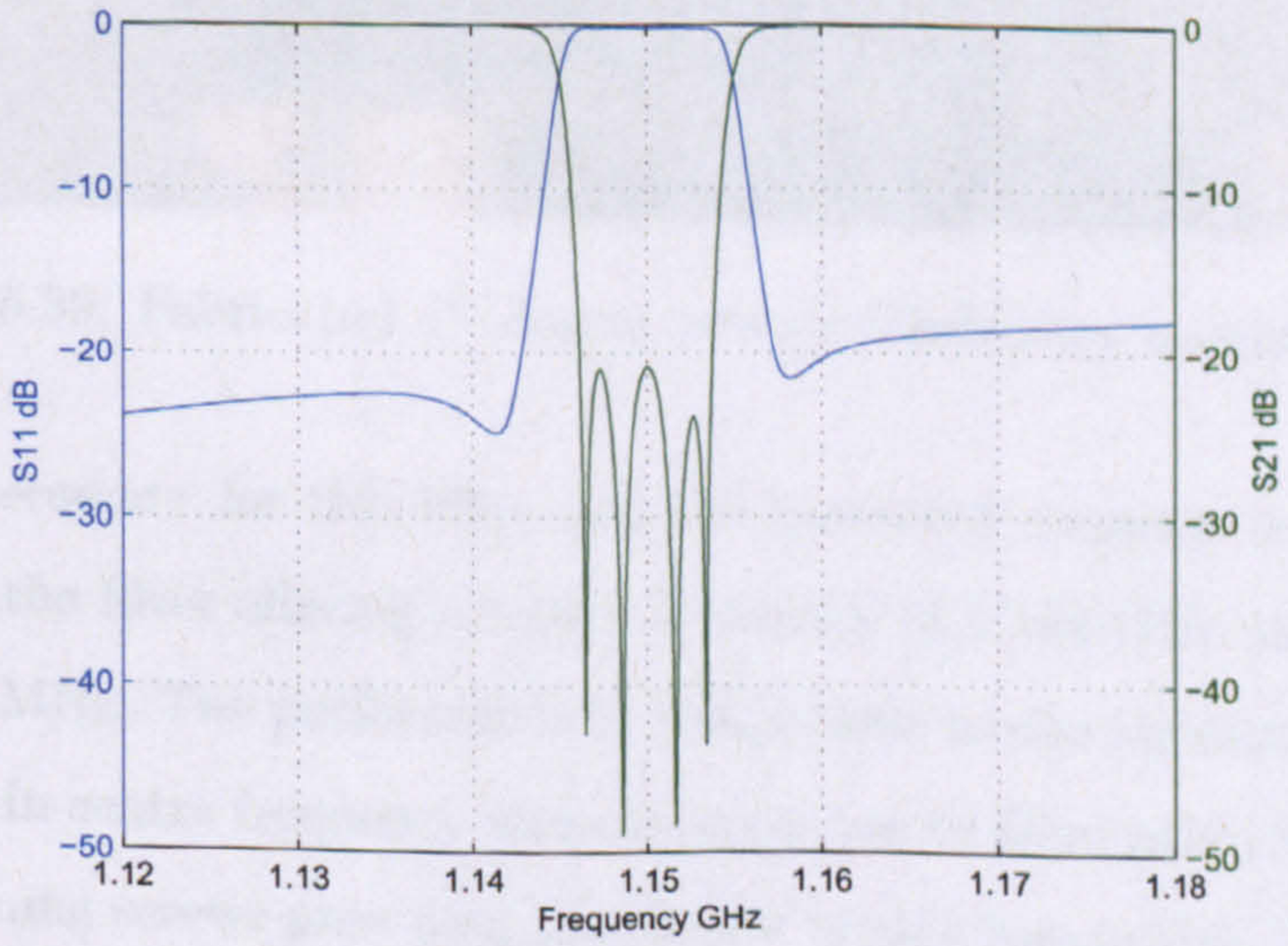

Figure 5.38: Frequency response of optimised HFSS design for inverse Chebyshev bandstop filter

5.7 Fabrication of filter

Precise machining was used for the desired dimensions and the dielectric pucks were mounted and positioned to the base of each cavity. The required dimensional tolerances from the optimisation process was a hundredth of a millimeter which was impractical, therefore, the fabricated tolerances must be accounted for through manual tuning. The enclosure was made from aluminium and was made in three parts with a body, lid and an aluminium rod fixed to the four coupling posts. The fabricated filter is shown in figure 5.39.

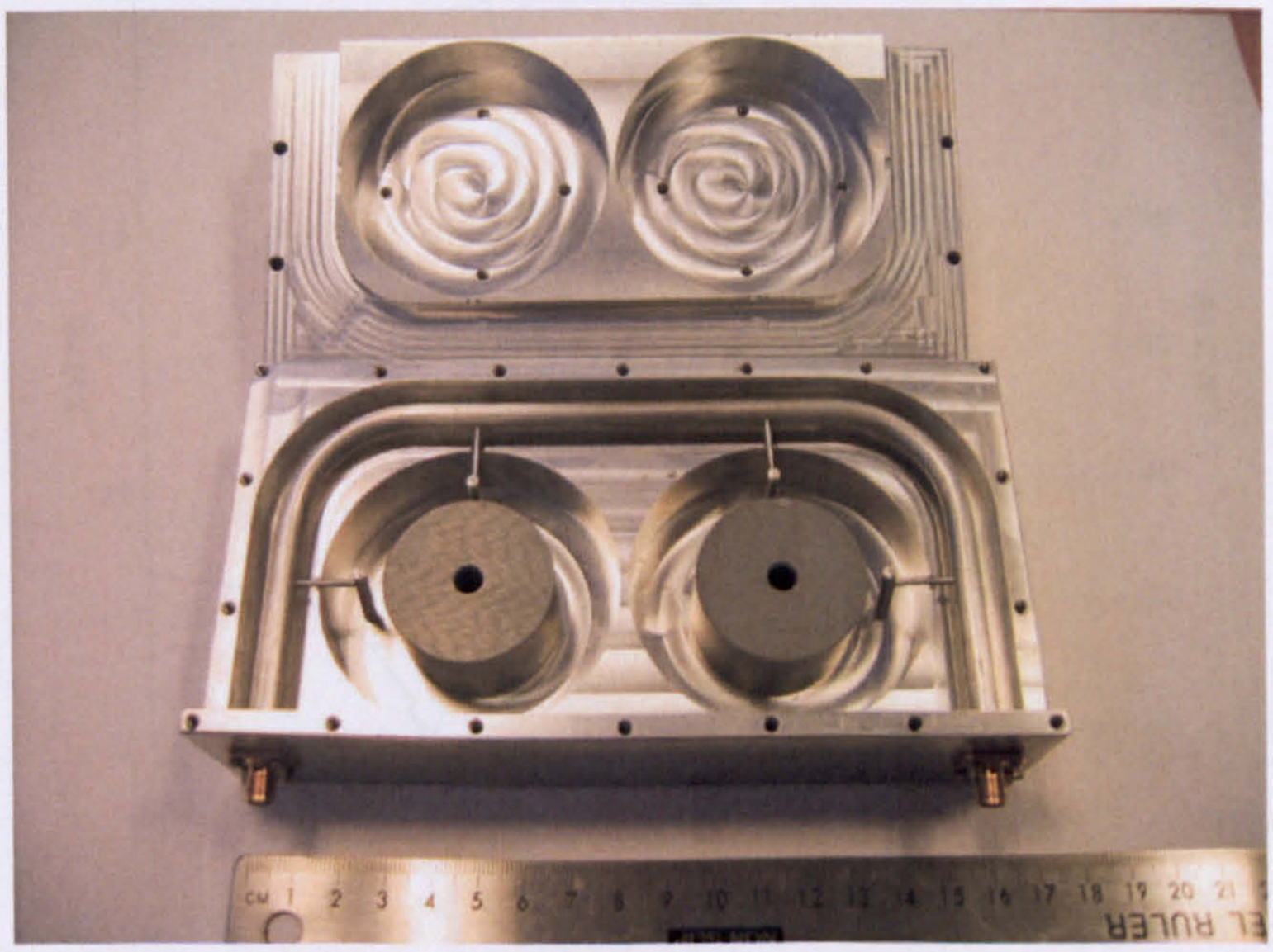

Figure 5.39: Fabricated 4^{th} degree inverse Chebyshev bandstop filter

Tuning was necessary for this filter and the measured response is shown in figure 5.40 with the filter offering a centre frequency of 1.164 GHz and 3 dB bandwidth of 16.3 MHz. The performance is comparable to the simulated results but a 1% increase in centre frequency was observed due to fabrication tolerances and inadequate tuning screws providing insufficient tuning bandwidth. For future designs, it is proposed that tuning disks with wide surface area to the dielectric puck be used for greater tuning effect. Losses were due to poor tuning screws and poor contact between the surface of the dielectric puck and the base of the cavity.

These can be improved by using silver screws and the interior of the cavity can be silver-plated ensuring conductor losses are minimised. The tuning mechanism also introduced loss as it increased conductor losses in the cavity. Of note, there is a reflection zero on the left side of the response caused by the shortening of the separation between the two middle resonators. The asymmetric behaviour is due to an occurrence of a susceptance in the transmission line. By changing the length of the line, this susceptance will be absorbed into the line producing the required symmetrical response.

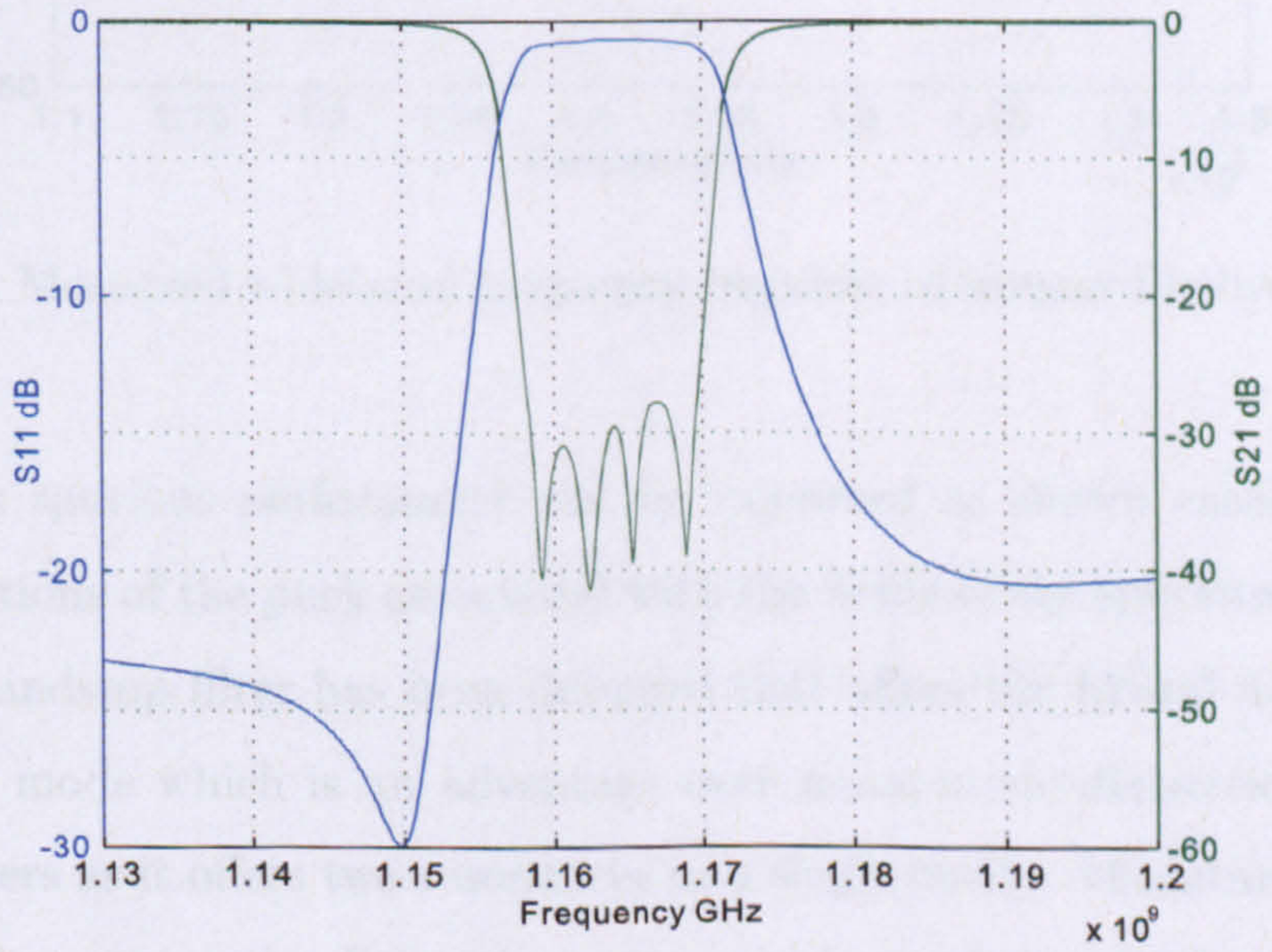

Figure 5.40: Measured frequency response of inverse Chebyshev bandstop filter

This filter demonstrated a significant improvement in bandwidth over the first bandstop design producing 16.3 MHz 3 dB attenuation bandwidth in contrast to 4.3 MHz for the single cavity filter. The wideband response showed the first spurious mode, TM_{01}, occurring at 1.516 GHz in the 4^{th} degree DR filter giving a spurious free window of 352 MHz, figure 5.41. This spurious frequency has been driven down along with the fundamental frequency as the puck was moved towards the base of the cavity. Although adequate for narrowband communication

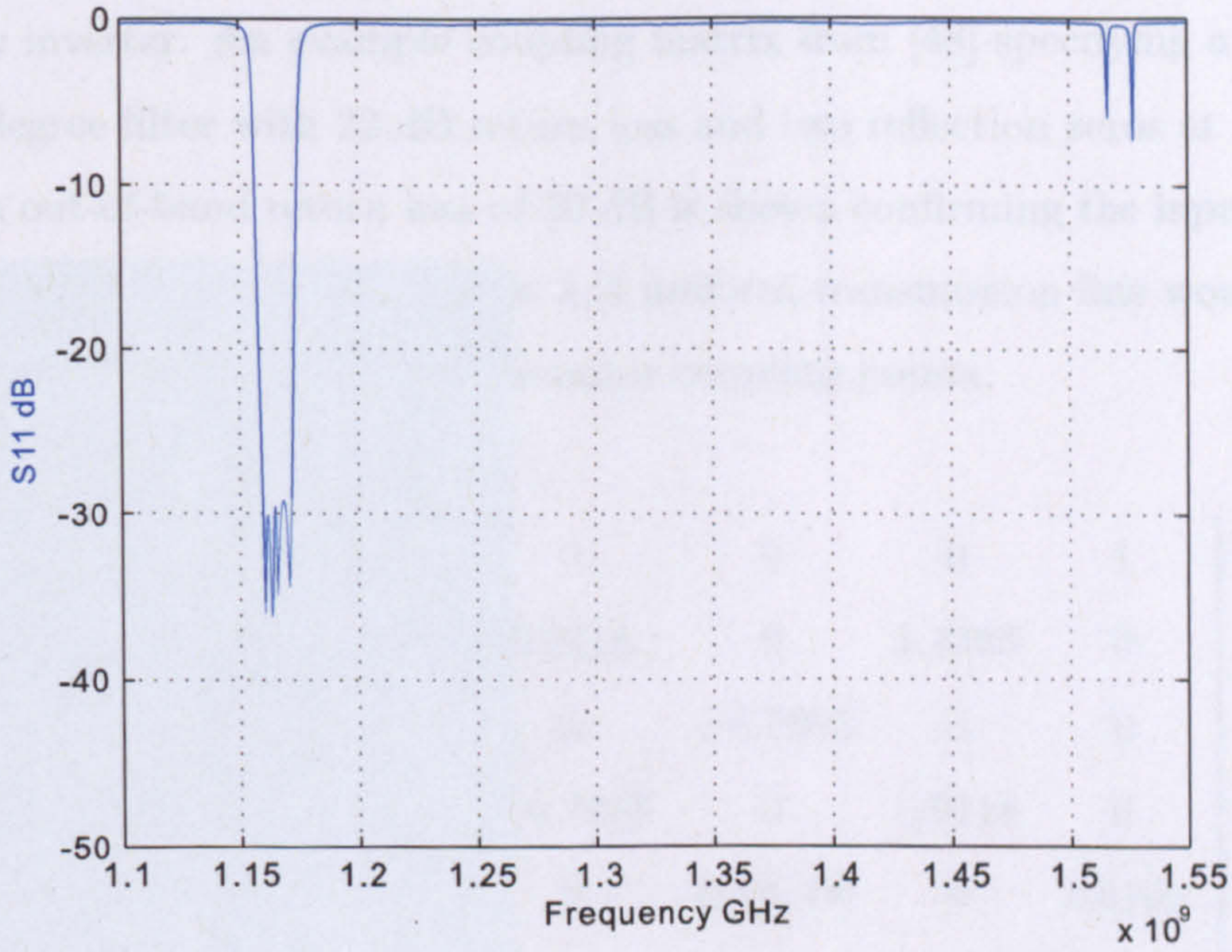

Figure 5.41: Measured wideband frequency response of inverse Chebyshev bandstop filter

systems, this spurious performance can be improved as shown earlier through removing sections of the puck associated with the fields of the spurious modes. A dual-mode bandstop filter has been designed that offers the hybrid mode as the fundamental mode which is an advantage over mono-mode dielectric resonator bandstop filters as it offers two resonances in a single cavity. Miniaturisation has been shown by moving the dielectric puck to the base of the cavity, thus, nearly half the cavity has been removed and the filter structure exhibits an unloaded high Q of 9000.

5.8 Direct-coupled DR bandstop filter

In this section the dual-mode bandstop configuration is used to realise a network synthesis technique that generates a bandstop function from the regular lowpass polynomials as described in chapter 2. The beauty of this technique is that the coupling matrix formed produces a folded configuration of a 4^{th} degree bandstop filter and the main transmission line is of uniform impedance and can be modelled

as a unity inverter. An example coupling matrix from [48] specifying a symmetrical 4th degree filter with 22 dB return loss and two reflection zeros at $\pm j2.0107$ to give an out-of-band return loss of 30 dB is shown confirming the input/output coupling is unity, therefore, a simple $\lambda/4$ uniform transmission line would suffice between the transmission line-to-resonator coupling points.

$$M = \begin{bmatrix} 0 & 1.5109 & 0 & 0 & 0 & 1 \\ 1.5109 & 0 & 0.9118 & 0 & 1.3363 & 0 \\ 0 & 0.9118 & 0 & -0.7985 & 0 & 0 \\ 0 & 0 & -0.7985 & 0 & 0.9118 & 0 \\ 0 & 1.3363 & 0 & 0.98118 & 0 & 1.5109 \\ 1 & 0 & 0 & 0 & 1.5109 & 0 \end{bmatrix}$$

For bandstop transfer functions where the reflection zeros are less than the filter degree, a second solution is provided by performing the synthesis technique on the dual of the coupling matrix provided above. The dual network is established by multiplying the reflection numerator polynomials by -1, in effect adding unity inverters at the input and output. The coupling matrix is produced below showing the removal of the negative M_{23} coupling, to give positive values for all couplings. This is a unique solution to cross-coupled designs and removes the need for electric probes for negative coupling. The frequency response for both solutions is shown in figure 5.42.

$$M = \begin{bmatrix} 0 & 1.5109 & 0 & 0 & 0 & 1 \\ 1.5109 & 0 & 0.9118 & 0 & 0.9465 & 0 \\ 0 & 0.9118 & 0 & 0.7985 & 0 & 0 \\ 0 & 0 & 0.7985 & 0 & 0.9118 & 0 \\ 0 & 0.9465 & 0 & 0.98118 & 0 & 1.5109 \\ 1 & 0 & 0 & 0 & 1.5109 & 0 \end{bmatrix}$$

The coupling routing diagram for this matrix is shown in figure 5.43. The dual-

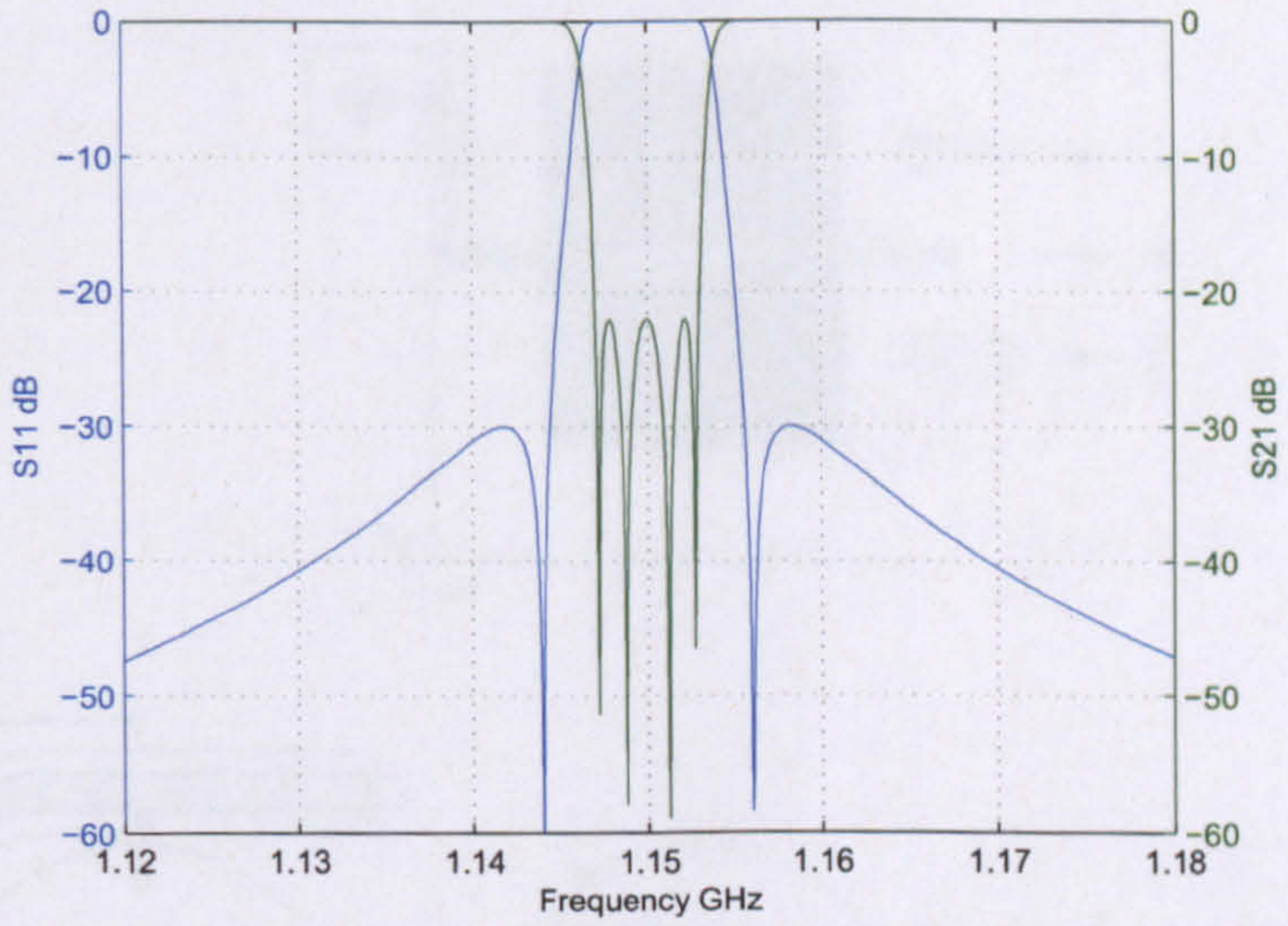

Figure 5.42: Frequency response of direct-coupled (4-2) bandstop filter

mode dielectric bandstop filter, already described, is perfectly suitable to realise this coupling matrix. A diagram of the possible realisation depicts the coupling paths between each othogonal mode and the cross-couplings required, figure 5.44. One should note that for practical realisation the bottom dielectric puck is now fixed to the top of its respective cavity, thus, a low permittivity dielectric support will be required to mount the puck. The filter is assumed to have the specifications in table 5.6.

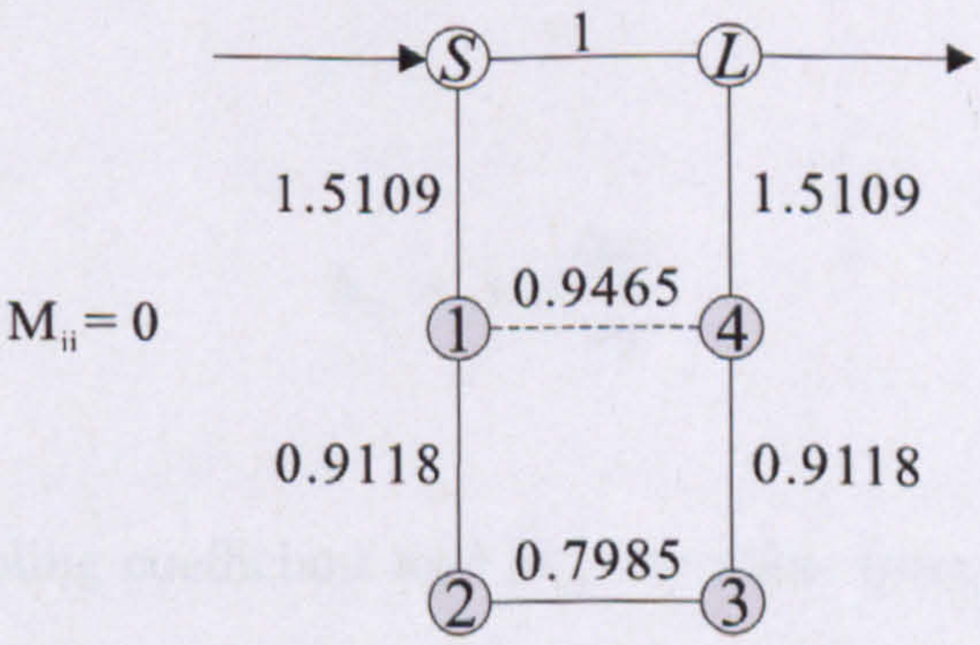

Figure 5.43: Coupling routing diagram of a direct-coupled (4-2) bandstop filter, [45]

The dimensions of the cavity and coaxial line and dielectric puck were identical to those from the previous design. To convert between the ccoupling matrix values and coupling bandwidth for each coupling in the physical model, the coupling

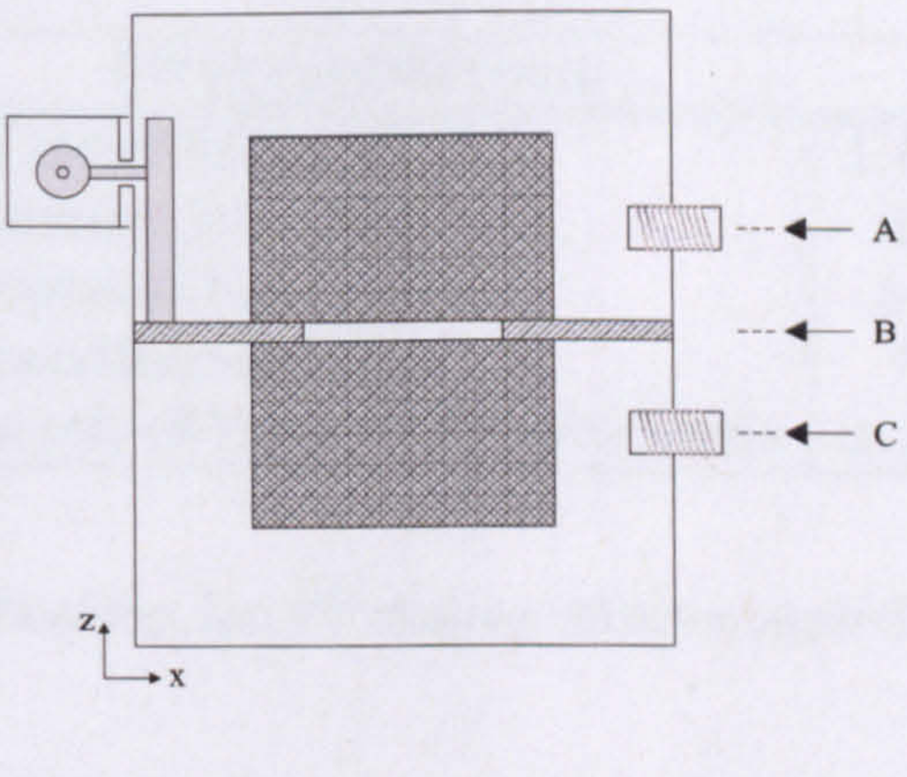

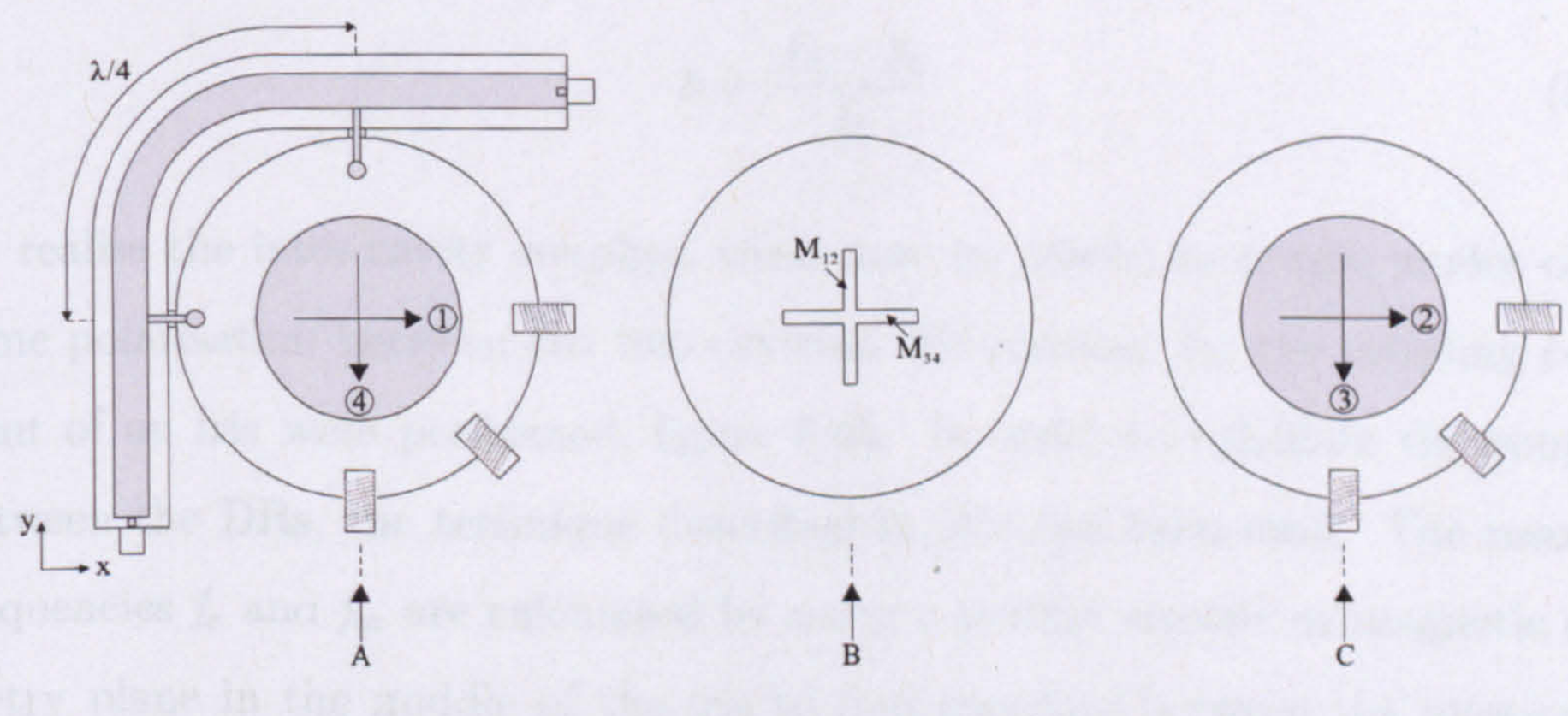

Figure 5.44: Configuration of HEE_{11} dual mode direct-coupled (4-2) dielectric bandstop filter

coefficient is calculated from, [47],

$$k_{ij} = M_{ij}\frac{\Delta\omega}{\omega_0} \tag{5.13}$$

where k_{ij} is the coupling coefficiant and M_{ij} the value from the coupling matrix. Intra-cavity couplings are now required from the coupling matrix and mode coupling tuning disks were used in the simulations. The coupling can be controlled by the physical dimensions of the disk such as the thickness and diameter but its position from the dielectric puck will cause the most variation. An eigenmode solver can easily compute the coupling coefficients within the dual-mode resonator cavity using, [45],

Filter Specifications	
Centre frequency	1.15 GHz
Return loss (L_R)	22 dB
Stopband bandwidth	5 MHz
Insertion loss (L_A)	30 dB
Reflection zeros out-of-band 30 dB lobe levels	$\pm$ j2.0107

Table 5.6: Filter specification for 4^{th} degree direct-coupled bandstop filter

$$k = \frac{f_2 - f_1}{f_2} \tag{5.14}$$

To realise the inter-cavity coupligs, irises may be placed to couple modes of the same polarisation between the two cavities. Simulations for the coupling coefficient of an iris were performed, figure 5.45. In order to calculate the coupling between the DRs, the technique described in [45] has been used. The resonant frequencies f_e and f_m are calculated by using a perfect electric or magnetic symmetry plane in the middle of the iris to find coupling between the inter-cavity modes. The coupling coefficient is found from the well-known equation,

$$k = \frac{{f_e}^2 - {f_m}^2}{{f_e}^2 + {f_m}^2} \tag{5.15}$$

This cross-coupling approach caused loading effects from the irises shifting the resonant frequency below the centre frequency. To increase the resonant frequency, the top cavity height was reduced from 37 mm to 30.5 mm and the bottom cavity height was reduced to 28.37 mm. The optimisation process began by observing the top cavity and adjusting the coupling element dimensions such that each produced the correct bandwidth. The lengths for the irises were calculated from figure 5.45 and for $K_{12} = K_{34} = 0.00246$, slot widths of 1.26 mm were required for irises of length 30 mm and thickness 20 mm. From these initial dimensions, it was possible to draw an initial model in HFSS and after lengthy fine tuning involving adjusting positions of tuning disks and heights of both cavities, the final simulation model and response are shown in figures 5.46 and 5.47 providing

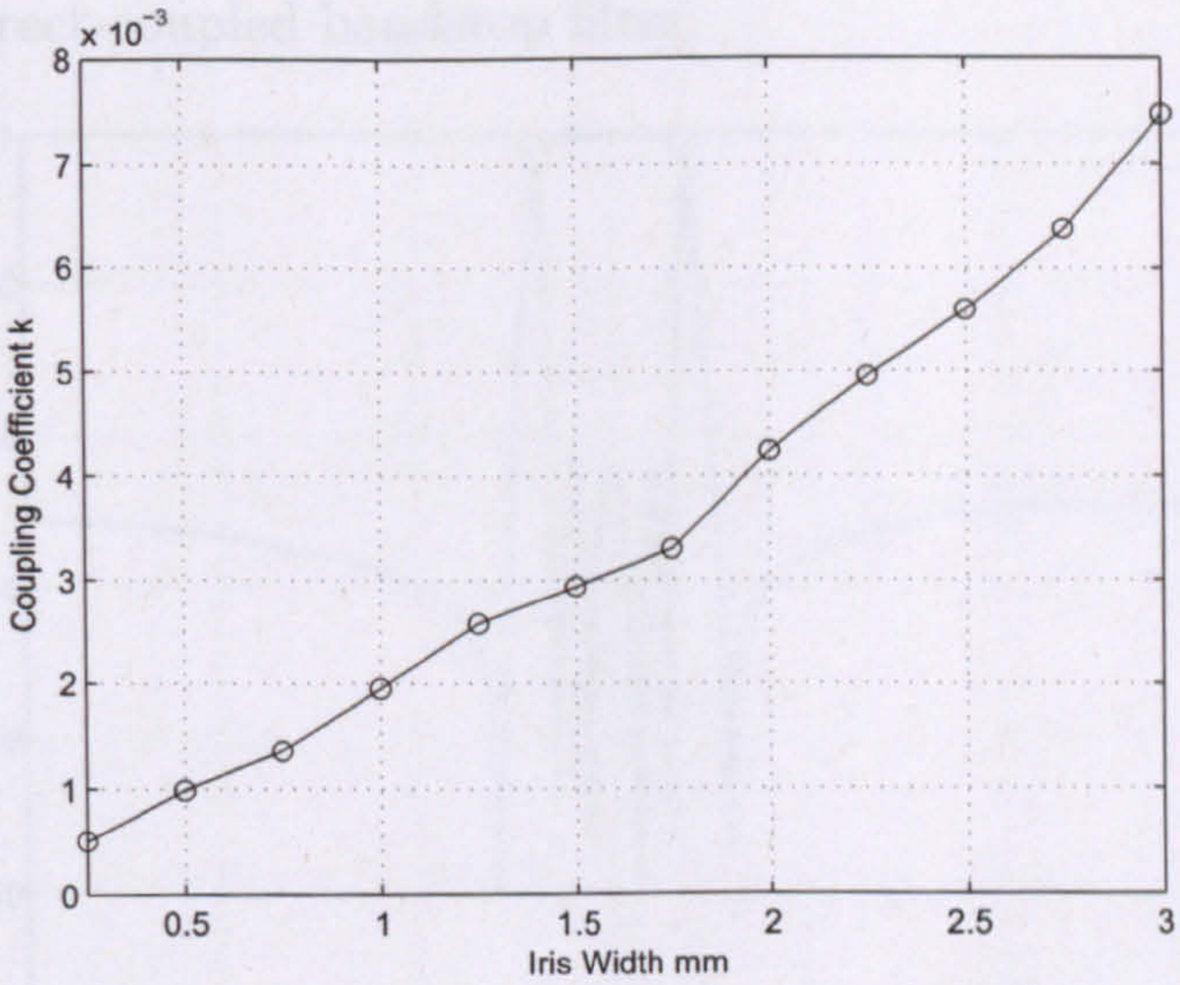

Figure 5.45: Variation of coupling coefficient with iris width of length 3 cm and thickness 2 cm

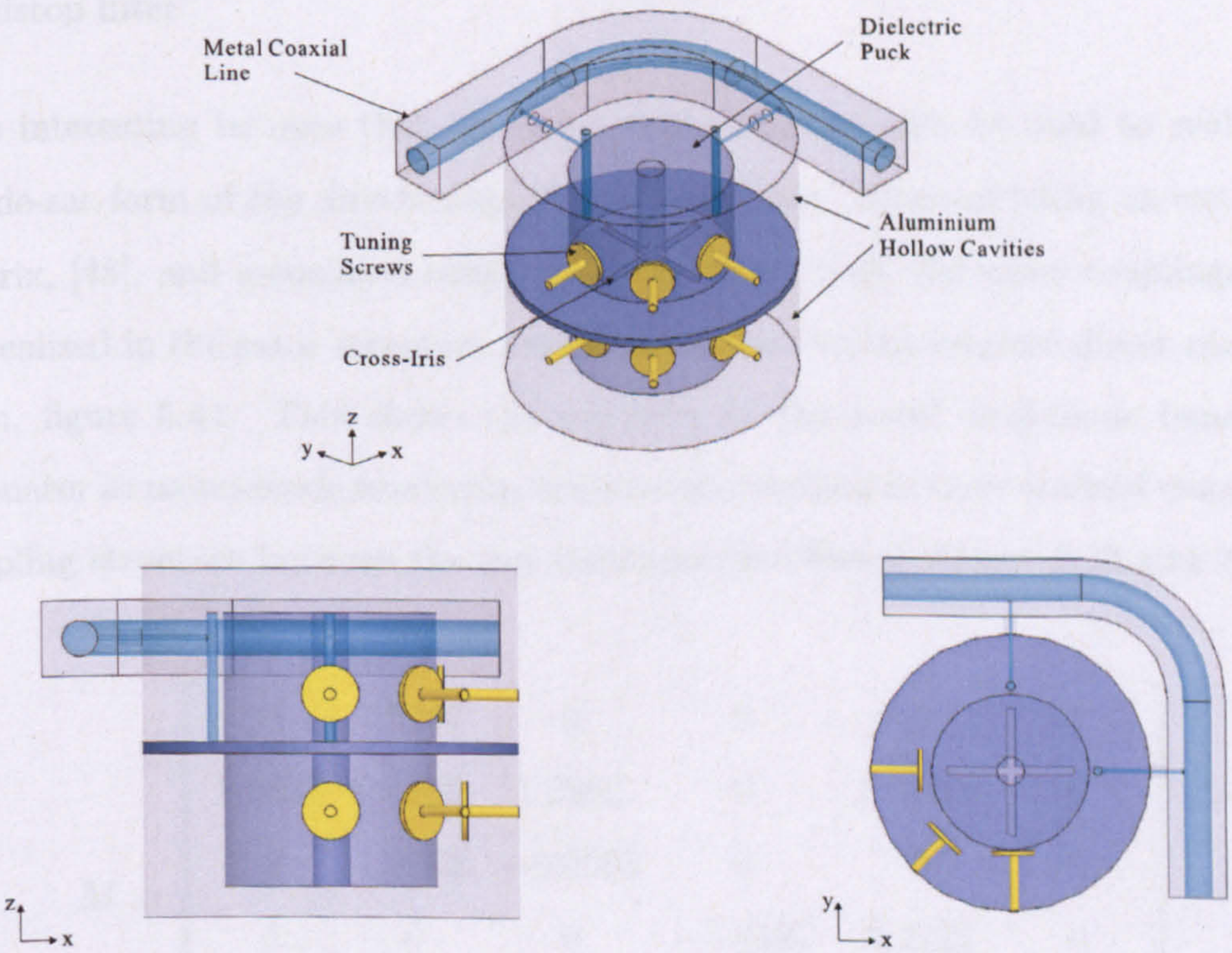

Figure 5.46: HFSS model of optimised direct-coupled HEE_{11} dual-mode bandstop filter

a good comparison to the ideal response. Thus, the HEE_{11} dual-mode bandstop resonator readily demonstrates the principle of the coupling matrix synthesis ap-

proach to the direct-coupled bandstop filter.

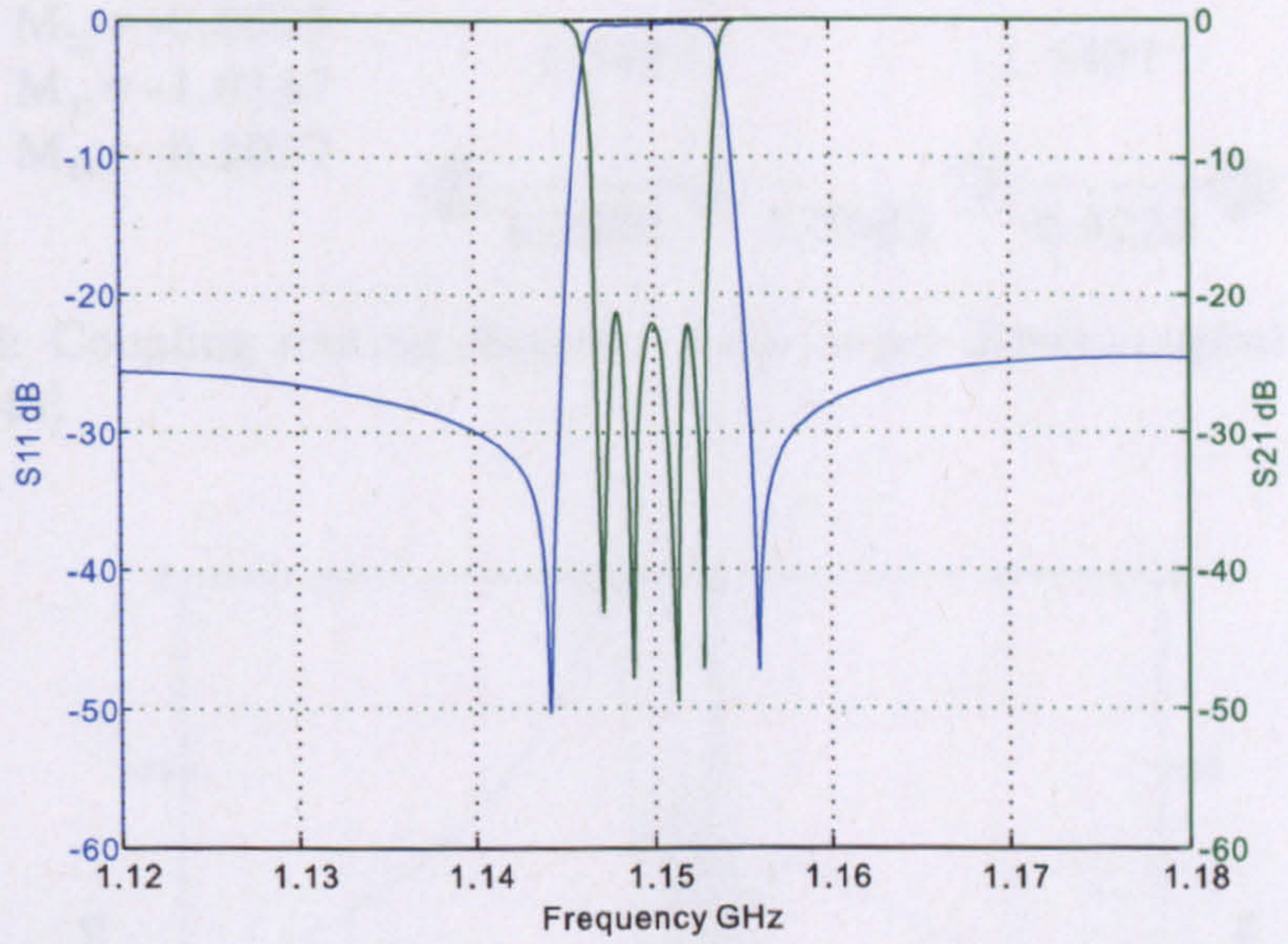

Figure 5.47: Simulated response of optimised direct-coupled HEE_{11} dual-mode bandstop filter

It is interesting to note that the same structure may also be used to realise a cul-de-sac form of the direct-coupled bandstop filter. By considering an example matrix, [48], and associated coupling paths, figure 5.48, the same couplings can be realised in the same structure, described above, for the original direct-coupled form, figure 5.44. This shows the flexibilty of the novel dual-mode bandstop resonator as mono-mode resonators requires an overhaul in their realised resonator coupling structure between the two direct-coupled forms, figures 2.13 and 2.14.

$$M = \begin{bmatrix} 0 & 1.5497 & 0 & 0 & 0 & 1 \\ 1.5497 & 0.5155 & 1.2902 & 0 & 1.28008 & 0 \\ 0 & 1.2902 & -0.0503 & 0 & 0 & 0 \\ 0 & 0 & 0 & -1.0187 & 0.4222 & 0 \\ 0 & 0.9465 & 0 & 0.4222 & -0.2057 & 1.5497 \\ 1 & 0 & 0 & 0 & 1.5497 & 0 \end{bmatrix}$$

It is also clear that the cul-de-sac form brings an advantage for the dual-mode bandstop filter in that no M_{23} cross coupling is required. This means no mode

$M_{11} = 0.5155$
$M_{22} = -0.0503$
$M_{33} = -1.0187$
$M_{44} = -0.2057$

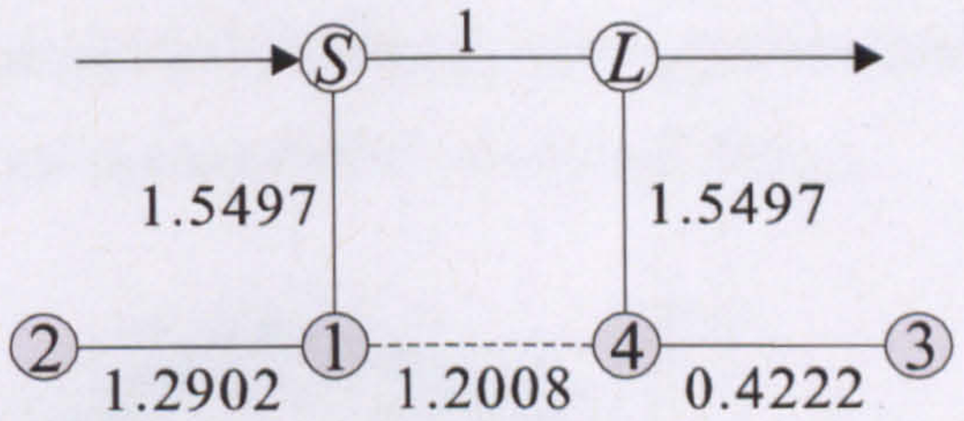

Figure 5.48: Coupling routing diagram of cul-de-sac direct-coupled (4-2) bandstop filter, [48]

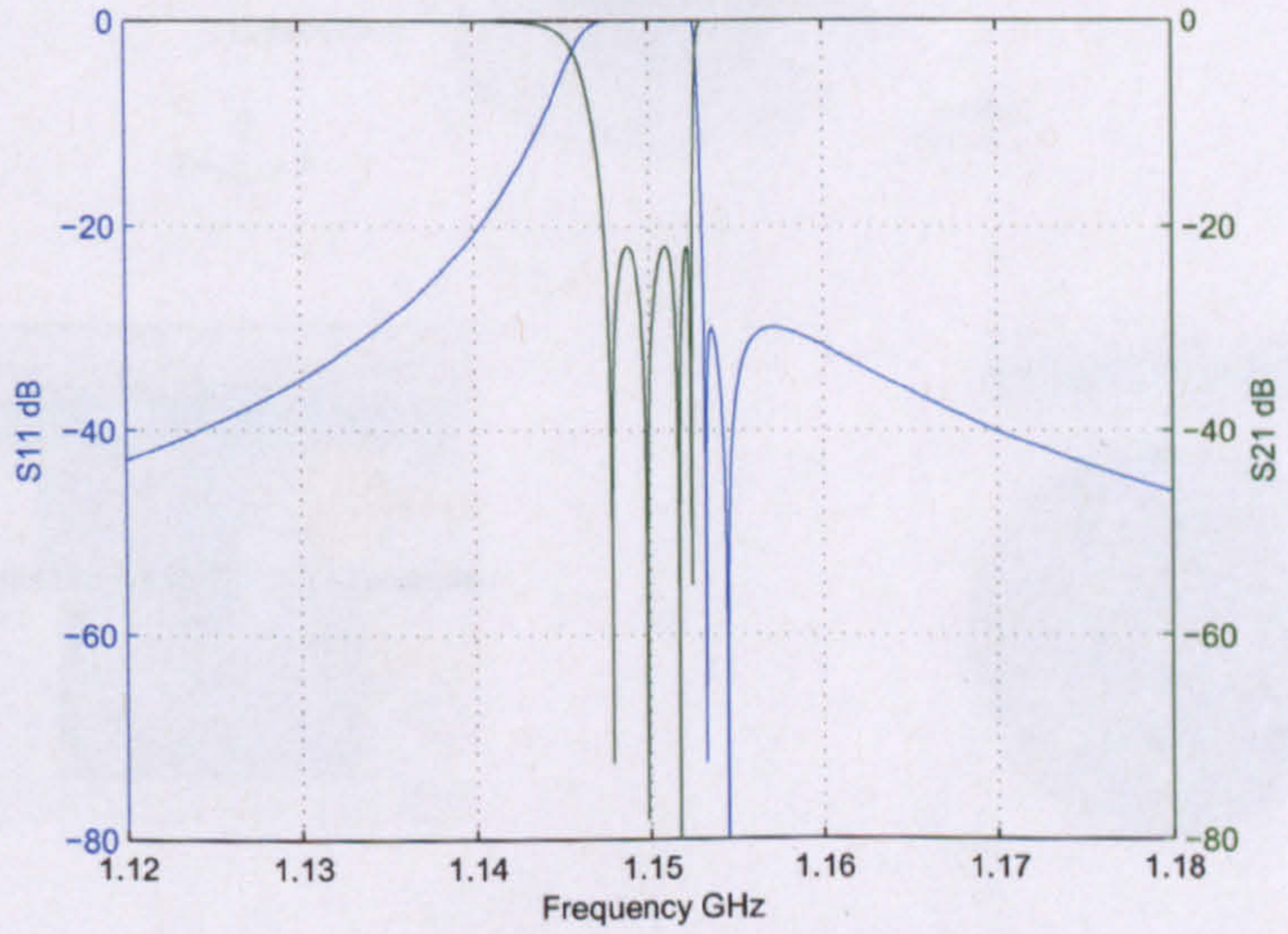

Figure 5.49: Frequency response of cul-de-sac direct-coupled (4-2) bandstop filter

coupling tuning disk is required in the bottom cavity of the filter reducing the complexity of the design. The ideal frequency response of this matrix is shown in figure 5.49 showing an asymmetrical response, with centre frequency of 1.15 GHz and 5 MHz bandwidth, can be acquired and is perfectly realisable in the dual-mode dielectric bandstop resonator filter. Again, performing similar design and optimisation criteria as per the former symmetrical design, the HFSS simulation for the cul-de-sac configuration was performed with the final optimised structure as shown in figure 5.50. Note that for this design, to improve the loss, the cavity height was used to control the centre frequency of the higher resonant mode in each cavity, thus, no tuning disk was required for this degenerate mode and as stated, only one cross-coupling tuning disk in the whole structure was required. The frequency response for the HFSS design, figure 5.51, is comparable to the ideal

response, therefore, the novel dual-mode dielectric resonator bandstop resonator is perfectly suitable to realise an asymmetrical cul-de-sac design.

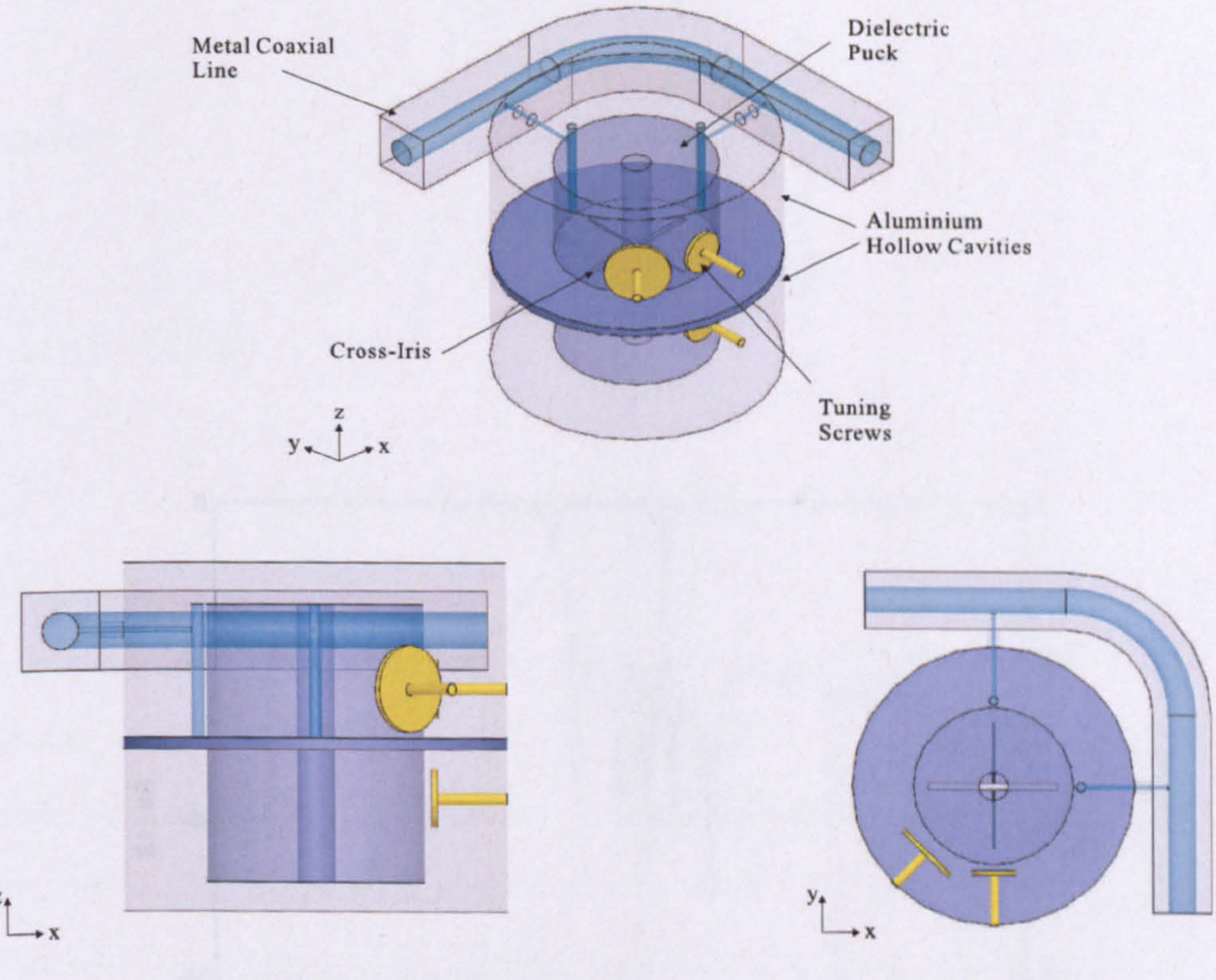

Figure 5.50: HFSS model of optimised cul-de-sac HEE_{11} dual-mode bandstop filter

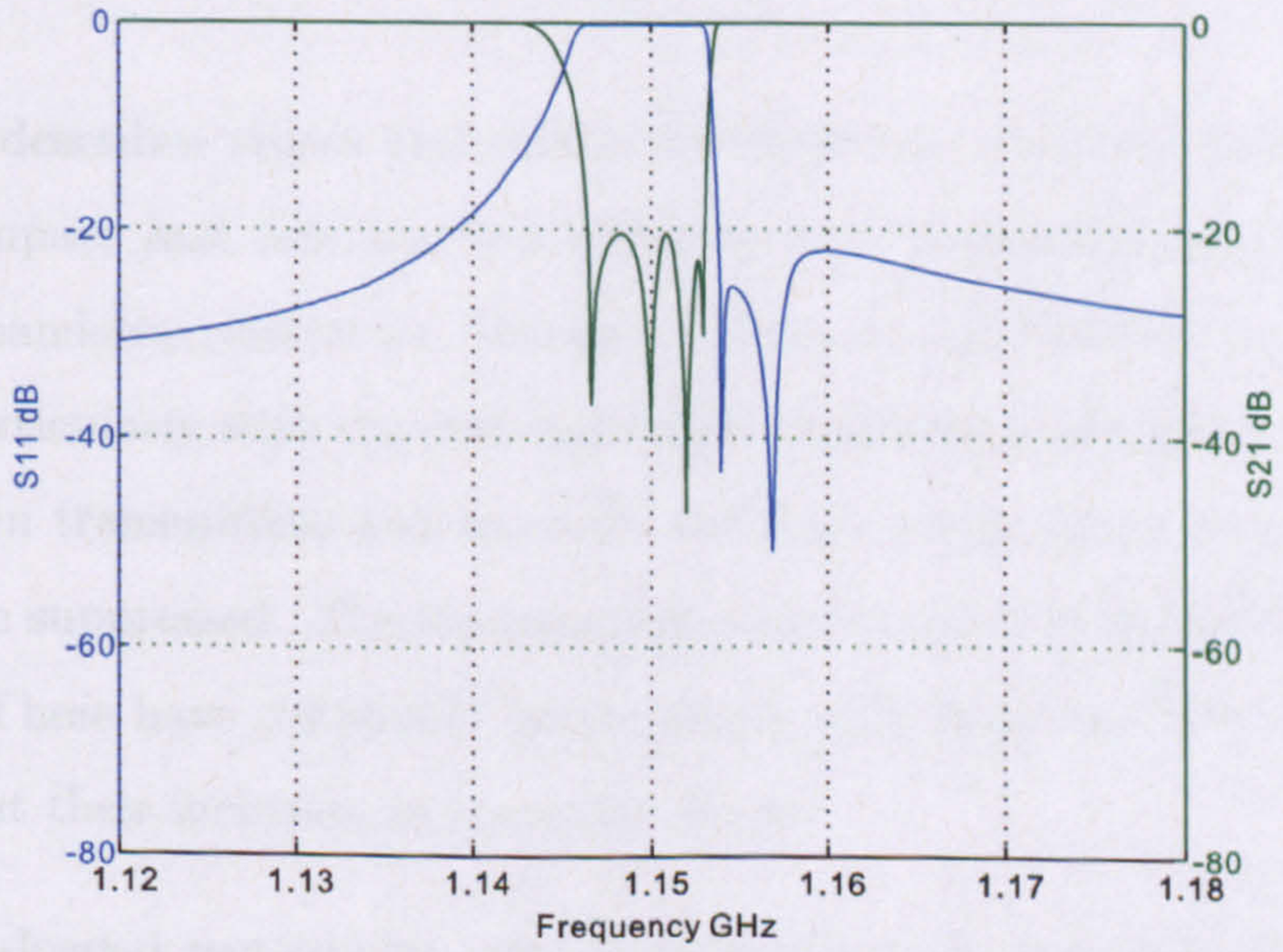

Figure 5.51: Simulated response of optimised cul-de-sac HEE_{11} dual-mode band-stop filter

Chapter 6

Conclusions

This thesis describes mono- and dual-mode dielectric resonator bandstop filters offering compact and miniaturised solutions over convential coaxial cavity or waveguide bandstop resonators. Bandstop filters are necessary in communication systems, particularly with the ever-increasing congested radio spectrum, interference between transmitters and receivers and high power harmonics are harmful and must be suppressed. The fundamental concept revolves around the dielectric resonator. These have commonly been integrated in bandpass filters but little is known about their inclusion in bandstop filters.

A dielectric-loaded rectangular waveguide resonator is developed from classical equations to determine the resonant frequency and unloaded Q for a cavity waveguide resonator. It is apparent through loading the cavity with dielectric, the dimensions of the cavity reduce by a factor of the permittivity of the dielectric material. In addition, the material properties of dielectric allow them to achieve high Qs for comparable performance to cavity resonators, even after miniaturisation. By metallising the four longer faces of a rectangular dielectric resonator, a compact resonator is achieved and observation of the resonant modes indicate $TE_{10\delta}$ is the fundamental mode. To create the bandstop characteristic, the rectangular resonator is coupled to a coaxial transmission line achieving narrow bandwidths. It has been demonstrated that the compact resonator allows $\lambda/4$ transmission line separations avoiding unwanted spurious inter-resonator coupling. An unloaded Q

of 2300 offers performance ideal for less stringent applications where miniaturisation is the key aim. Spurious performance for many dielectric filters are typically poor and require modification to the resonator structure. The technology shown here allowed a spurious free bandwidth of 650 MHz allowing the case of these resonators to be implemented in broadband systems. A 4^{th} degree Chebyshev bandstop filter was designed achieving 1% bandwidth but poor fabrication techniques have incurred losses in the final filter desgin, notably poor metallisation of the dielectric resonator. The drawback of this resonator is the narrowband coupling is unsuitable for applications requiring large bandwidths. This is the compromise for high Q materials where E-fields are mostly concentrated within the dielectric and only magnetic fields are allowed for external coupling. To counter this, a novel coaxial dieletric-loaded resonator was developed. Investigations of this resonator have oberved an unloaded Q of 2670 and 3 dB coupling bandwidths of 200 MHz are achievable, therefore, multi-section designs can provide superior bandwidth designs at higher frequencies.

The second area of contribution is the novel dual-mode dielectric-loaded bandstop filter operating in the HEE_{11} mode. Due to symmetrical geometries, these resonators allow the typically higher order dual degenerate hybrid modes to resonate at the same frequency within the cavity, therefore, only half the number of cavities are required compared to mono-mode resonators. The resonant modes in a cylindrical dielectric puck were observed and for an assumed aspect ratio dielectric puck size, the HEE_{11} was the first spurious mode in a suspended structure. By forcing the puck to the base, the HEE_{11} became the fundamental mode allowing ease of integration in communication systems. The drawback to this is unloaded Q decreases due to metallic contact with one side of the puck but an unloaded Q of 9000 was still achieved. The bandstop response was achieved through magnetic coupling to coupling posts attached to a coaxial transmission line. An experimental cavity was designed highlighting complexities to bend the transmission line to produce the required coupling separations between the transmission line and orthogonal modes of the puck. Simulated and measured responses demonstrated

the principle of the resonator and a 4^{th} degree filter was designed. The response showed 3 dB bandwidth was improved over the single cavity design from 4.3 MHz to 16.3 MHz. The main drawback to this filter was the poor spurious performance, however, it was shown this could be improved by physically removing segments of the DR puck. The measured response gave rise to a rejection zero due to the extra length of transmission line separation between the middle two resonators but it is proposed future designs should reduce the radii of the cavity walls.

The dual-mode dielectric bandstop resonator was perfectly suitable to realise direct-coupled bandstop filters. The benefits of this class of filter are the coupling matrix synthesis technique allows direct coupling between the source and load, bypassing the bandstop resonators. The coupling matrix demonstrated the source-load coupling was unity, implying only a single length of $\lambda/4$ transmission line was required. A full FEM simulation for the novel dual-mode bandstop filter demonstrated the principle producing symmetrical rejection zeros on either side of the stopband for greater selectivity. The coupling matrix synthesized a second cul-de-sac configuration which was realised by the same dual-mode bandstop filter with an improvement in the structure where a cross-coupling element was not required compared to the former design. The principle was demonstrated in a FEM simulation showing the advantage over mono-mode cavity filters where the cavity positions must conform to the correct coupling paths. It has also been shown that using the coupling matrix technique for direct-coupled bandstop filters, advanced filter functions involving prescribed rejection zeros for symmetrical and asymmetrical responses are easily realised by this novel filter.

6.1 Future Work

The work presented in this thesis has proposed and developed the early development of miniaturised mono- and dual-mode bandstop filters employing dielectric resonators. The promising results from these designs should be carried forward to investigate their use in advanced filtering techniques. Foremost, it is imperative

that future work includes the fabrication of the direct-coupled filters to confirm their concepts and compare against simulated reponses to adjust for any repetitive fabrication errors that may occur. Also, it would be interesting to compare results between the direct-coupled bandstop filter and cul-de-sac form for the same specifications to appreciate the difference in performance, for example, when a mode coupling screw is not required in the second cavity of the (4-2) cul-de-sac form. The resonators in direct-coupled filters can consist of mono- dual- or higher order modes to create mixed mode bandstop filters to collectively improve the spurious performance. Lossy filter techniques should also be investigated for the dual-mode bandstop resonator as it allows the realisation of lossy filters with ideal lossless transmission and reflection response. This technique allows further miniaturisation as only low Q dielectric bandstop resonators would be required for ideal responses.

For these 3D structures, FEM simulations can be time consuming, especially during the optimisation process where a huge number of iterations are required to tune the variables to the required response. Computer aided techniques that can readily optimise circuit elements with 3D geometries should be followed such as space-mapping optimization, [83]. Also, a computer program to perform the coupling matrix synthesis technique should be written to readily produce element values for advanced filtering functions involving generalised Chebyshev filter synthesis.

Appendix A

Conferences and Publications

R. Chan, I.C. Hunter, "Dielectric resonator bandstop filters," Filtronic Engineering Symposium, September 2006

References

[1] I. Hunter, L. Billonet, B. Jarry, and P. Guillon, "Microwave filters-applications and technology," *Microwave Theory and Techniques, IEEE Transactions on*, vol. 50, pp. 794–805, Mar 2002.

[2] P. Guillon, S. Mekerta, and Y. Garault, "A dielectric resonator bandstop filter," *Microwave Symposium Digest, MTT-S International*, vol. 81, pp. 170–173, Jun 1981.

[3] J. Plourde and D. Linn, "Microwave dielectric resonator filters utilizing ba2ti9o20 ceramics," *Microwave Symposium Digest, MTT-S International*, vol. 77, pp. 290–293, Jun 1977.

[4] I. C. Hunter, J. D. Rhodes, and V. Dassonville, "Triple mode dielectric resonator hybrid reflection filters," *Microwaves, Antennas and Propagation, IEE Proceedings* -, vol. 145, pp. 337–343, Aug 1998.

[5] K. Kobayashi and C. Inoue, "Bandpass and bandstop filters using dominant tm01 delta; mode dielectric rod resonators," *Microwave Symposium Digest, 1997., IEEE MTT-S International*, vol. 2, pp. 793 –796 vol.2, June 1997.

[6] H. C. Bell, "L-resonator bandstop filters," *Microwave Theory and Techniques, IEEE Transactions on*, vol. 44, pp. 2669–2672, Dec 1996.

[7] C. Nguyen and K. Chang, "On the analysis and design of spurline bandstop filters," *Microwave Theory and Techniques, IEEE Transactions on*, vol. 33, pp. 1416–1421, Dec 1985.

[8] R. D. Richtmyer, "Dielectric resonators," *J. Appl. Phys*, vol. 48, pp. 391–398, June 1939.

[9] A. Okaya, "The rutile microwave resonator," *Proceedings of the IRE*, vol. 48, p. 1921, Nov. 1960.

[10] A. Okaya and L. F. Barash, "The dielectric microwave resonator," *Proceedings of the IRE*, vol. 50, pp. 2081–2092, Oct. 1962.

[11] S. Cohn, "Microwave bandpass filters containing high-q dielectric resonators," *Microwave Theory and Techniques, IEEE Transactions on*, vol. 16, pp. 218–227, Apr 1968.

[12] W. Harrison, "A miniature high-q bandpass filter employing dielectric resonators," *Microwave Theory and Techniques, IEEE Transactions on*, vol. 16, pp. 210–218, Apr 1968.

[13] D. Masse, R. Pucel, D. Readey, E. Maguire, and C. Hartwig, "A new low-loss high-k temperature-compensated dielectric for microwave applications," *Proceedings of the IEEE*, vol. 59, pp. 1628–1629, Nov. 1971.

[14] J. K. Plourde, D. F. Linn, H. M. O'Bryan, and J. Thomson, "$Ba_2Ti_9O_{20}$ as a microwave dielectric resonator," *Journal of the American Ceramic Society*, vol. 58, pp. 418–420, Oct.-Nov. 1975.

[15] K. Wakino, T. Nishikawa, S. Tamura, and Y. Ishikawa, "Microwave bandpass filters containing dielectric resonators with improved temperature stability and spurious response," *Microwave Symposium Digest, MTT-S International*, vol. 75, pp. 63–66, May 1975.

[16] K. Zaki and A. Atia, "Modes in dielectric-loaded waveguides and resonators," *Microwave Theory and Techniques, IEEE Transactions on*, vol. 83, pp. 1039–1045, Dec 1983.

[17] Y. Kobayashi and M. Minegishi, "Precise design of a bandpass filter using high-q dielectric ring resonators," *Microwave Theory and Techniques, IEEE Transactions on*, vol. 35, pp. 1156–1160, Dec 1987.

[18] K. Zaki, C. Chen, and A. Atia, "Canonical and longitudinal dual-mode dielectric resonator filters without iris," *Microwave Theory and Techniques, IEEE Transactions on*, vol. 35, pp. 1130–1135, Dec 1987.

[19] T. Nishikawa, K. Wakino, K. Tsunoda, and Y. Ishikawa, "Dielectric high-power bandpass filter using quarter-cut te01delta image resonator for cellular base stations," *Microwave Symposium Digest, MTT-S International*, vol. 87, pp. 133–136, Jun 1987.

[20] C. Kudsia, R. Cameron, and W.-C. Tang, "Innovations in microwave filters and multiplexing networks for communications satellite systems," *Microwave Theory and Techniques, IEEE Transactions on*, vol. 40, pp. 1133–1149, Jun 1992.

[21] R. Snyder, "Dielectric resonator filters with wide stopbands," *Microwave Theory and Techniques, IEEE Transactions on*, vol. 40, pp. 2100–2103, Nov 1992.

[22] J.-F. Liang, K. Zaki, and A. Atia, "Mixed modes dielectric resonator filters," *Microwave Theory and Techniques, IEEE Transactions on*, vol. 42, pp. 2449–2454, Dec 1994.

[23] C. Wang, H.-W. Yao, K. Zaki, and R. Mansour, "Mixed modes cylindrical planar dielectric resonator filters with rectangular enclosure," *Microwave Theory and Techniques, IEEE Transactions on*, vol. 43, pp. 2817–2823, Dec 1995.

[24] S.-W. Chen and K. Zaki, "Dielectric ring resonators loaded in waveguide and on substrate," *Microwave Theory and Techniques, IEEE Transactions on*, vol. 39, pp. 2069–2076, Dec 1991.

[25] H.-W. Yao, C. Wang, and A. Zaki, "Quarter wavelengtli ceramic combline filters," *Microwave Theory and Techniques, IEEE Transactions on*, vol. 44, pp. 2673–2679, Dec 1996.

[26] D. Kajfez and P. Guillon, *Dielectric Resonators.* Noble Publishing, second ed., 1998.

[27] X.-F. Liang and W. Blair, "High q te01 mode dr cavity filters for wireless base stations," *Microwave Symposium Digest, 1998 IEEE MTT-S International*, vol. 2, pp. 825–828 vol.2, Jun 1998.

[28] S. Fiedziuszko, I. Hunter, T. Itoh, Y. Kobayashi, T. Nishikawa, S. Stitzer, and K. Wakino, "Dielectric materials, devices, and circuits," *Microwave Theory and Techniques, IEEE Transactions on*, vol. 50, pp. 706–720, Mar 2002.

[29] Y. Kobayashi and M. Minegishi, "A bandpass filter using electrically coupled tm01 dielectric rod resonators," *Microwave Symposium Digest, 1988., IEEE MTT-S International*, pp. 507–510 vol.1, May 1988.

[30] S. Fiedziuszko, "Dual-mode dielectric resonator loaded cavity filters," *Microwave Theory and Techniques, IEEE Transactions on*, vol. 82, pp. 1311–1316, Sep 1982.

[31] A. Atia and A. Williams, "Narrow-bandpass waveguide filters," *Microwave Theory and Techniques, IEEE Transactions on*, vol. 20, pp. 258–265, Apr 1972.

[32] Y. Kobayashi and K. Kubo, "Canonical bandpass filters using dual-mode dielectric resonators," *Microwave Symposium Digest, MTT-S International*, vol. 87, pp. 137–140, Jun 1987.

[33] S. Gendraud, S. Verdeyme, P. Guillon, M. Chaubet, J. Sombrin, S. Vigneron, and B. Theron, "Design and realization of a four pole elliptic microwave filter using low dielectric loaded cavities," *Microwave Symposium Digest, 1997., IEEE MTT-S International*, vol. 2, pp. 1091–1094 vol.2, Jun 1997.

[34] I. Hunter, J. Rhodes, and V. Dassonville, "Dual-mode filters with conductor-loaded dielectric resonators," *Microwave Theory and Techniques, IEEE Transactions on*, vol. 47, pp. 2304–2311, Dec 1999.

[35] V. Walker and I. Hunter, "Design of triple mode te01 resonator transmission filters," *Microwave and Wireless Components Letters, IEEE*, vol. 12, pp. 215–217, Jun 2002.

[36] J. Hattori, T. Wada, H. Kubo, and Y. Ishikawa, "2ghz band quadruple mode dielectric resonator filter for cellular base station," *Microwave Symposium Digest, 2003 IEEE MTT-S International*, vol. 2, pp. 933–936 vol.2, June 2003.

[37] C. Wang, K. Zaki, and A. Atia, "Dual mode combined dielectric and conductor loaded cavity filters," *Microwave Symposium Digest, 1997., IEEE MTT-S International*, vol. 2, pp. 1103–1107 vol.2, Jun 1997.

[38] C.-L. Ren, "Waveguide bandstop filter utilizing $Ba_2Ti_9O_{20}$ resonators," *Microwave Symposium Digest, MTT-S International*, vol. 78, pp. 227–229, Jun 1978.

[39] I. Hunter, *Theory and Design of Microwave Filters.* IEE, first ed., 2001.

[40] R. Cameron, "General coupling matrix synthesis methods for chebyshev filtering functions," *Microwave Theory and Techniques, IEEE Transactions on*, vol. 47, pp. 433 –442, Apr. 1999.

[41] J. Rhodes, *Theory of Electrical Filters.* John Wiley and Sons Ltd, first ed., 1976.

[42] A. Atia, A. Williams, and R. Newcomb, "Narrow-band multiple-coupled cavity synthesis," *Circuits and Systems, IEEE Transactions on*, vol. 21, pp. 649 – 655, Sept. 1974.

[43] R. Cameron and J. Rhodes, "Asymmetric realizations for dual-mode band-pass filters," *Microwave Theory and Techniques, IEEE Transactions on*, vol. 29, pp. 51 – 58, Jan. 1981.

[44] R. Cameron, "Advanced coupling matrix synthesis techniques for microwave filters," *Microwave Theory and Techniques, IEEE Transactions on*, vol. 51, pp. 1 – 10, Jan. 2003.

[45] R. J. Cameron, R. Mansour, and K. C. M., *Microwave Filters for Communication Systems: Fundamentals, Design and Applications.* Hoboken, New Jersey: Wiley-Interscience, first ed., 2007.

[46] J. Whitaker, *The Electronics Handbook.* CRC Press, second ed., 2005.

[47] G. Matthaei, L. Young, and E. T. Jones, *Microwave Filters, Imedance Matching Networks and Coupling Structures.* McGraw-Hill, 1964.

[48] R. Cameron, M. Yu, and Y. Wang, "Direct-coupled microwave filters with single and dual stopbands," *Microwave Theory and Techniques, IEEE Transactions on*, vol. 53, pp. 3288 – 3297, nov. 2005.

[49] W. G. Spitzer, R. C. Miller, D. A. Kleinman, and L. E. Howarth, "Far infrared dielectric dispersion in $BaTiO_3$, $SrTiO_3$, and TiO_2," *Phys. Rev.*, vol. 126, pp. 1710–1721, Jun 1962.

[50] Y. Konishi, "Novel dielectric waveguide components-microwave applications of new ceramic materials," *Proceedings of the IEEE*, vol. 79, pp. 726–740, Jun 1991.

[51] B. Hakki and P. Coleman, "A dielectric resonator method of measuring inductive capacities in the millimeter range," *Microwave Theory and Techniques, IRE Transactions on*, vol. 8, pp. 402–410, July 1960.

[52] Y. Kobayashi and M. Katoh, "Microwave measurement of dielectric properties of low-loss materials by the dielectric rod resonator method," *Microwave*

Theory and Techniques, IEEE Transactions on, vol. 33, pp. 586–592, Jul 1985.

[53] R. Bonetti and A. Atia, "Resonant frequency of dielectric resonators in inhomogeneous media," *Microwave Symposium Digest, 1980 MTT-S International*, vol. 80, pp. 218–219, May 1980.

[54] T. Nishikawa, "Microwave ceramic dielectrics and their applications," *European Microwave Conference, 1988. 18th*, pp. 70–80, Oct. 1988.

[55] A. Williams and A. Atia, "Dual-mode canonical waveguide filters," *Microwave Theory and Techniques, IEEE Transactions on*, vol. 25, pp. 1021 – 1026, Dec. 1977.

[56] D. Rebsch, D. Webb, R. Moore, and J. Cowlishaw, "A mode chart for accurate design of cylindrical dielectric resonators (correspondence)," *Microwave Theory and Techniques, IEEE Transactions on*, vol. 13, pp. 468–469, Jul 1965.

[57] W. Courtney, "Analysis and evaluation of a method of measuring the complex permittivity and permeability microwave insulators," *Microwave Theory and Techniques, IEEE Transactions on*, vol. 18, pp. 476–485, Aug 1970.

[58] Y. Kobayashi and S. Tanaka, "Resonant modes of a dielectric rod resonator short-circuited at both ends by parallel conducting plates," *Microwave Theory and Techniques, IEEE Transactions on*, vol. 28, pp. 1077–1085, Oct 1980.

[59] K. Zaki and C. Chen, "New results in dielectric-loaded resonators," *Microwave Theory and Techniques, IEEE Transactions on*, vol. 34, pp. 815–824, Jul 1986.

[60] S. Fiedziuszko and A. Jelenski, "The influence of conducting walls on resonant frequencies of the dielectric microwave resonator (correspondence),"

Microwave Theory and Techniques, IEEE Transactions on, vol. 19, pp. 778–779, Sep 1971.

[61] M. Pospieszalski, "Cylindrical dielectric resonators and their applications in tem line microwave circuits," *Microwave Theory and Techniques, IEEE Transactions on*, vol. 27, pp. 233–238, Mar 1979.

[62] T. Itoh and R. Rudokas, "New method for computing the resonant frequencies of dielectric resonators (short papers)," *Microwave Theory and Techniques, IEEE Transactions on*, vol. 25, pp. 52–54, Jan 1977.

[63] A. Wexler, "Solution of waveguide discontinuities by modal analysis," *Microwave Theory and Techniques, IEEE Transactions on*, vol. 15, pp. 508–517, Sep 1967.

[64] C. Wang and K. Zaki, "Generalized multilayer anisotropic dielectric resonators," *Microwave Theory and Techniques, IEEE Transactions on*, vol. 48, pp. 60–66, Jan 2000.

[65] C. Wang and K. Zaki, "Dielectric resonators and filters," *Microwave Magazine, IEEE*, vol. 8, pp. 115–127, Oct. 2007.

[66] P. P. Silvester and R. L. Ferrari, *Finite Elements for Electrical Engineers*. New York: Cambridge University Press, third ed., 1996.

[67] M. Taheri and D. Mirshekar-Syahkal, "Accurate determination of modes in dielectric-loaded cylindrical cavities using a one-dimensional finite element method," *Microwave Theory and Techniques, IEEE Transactions on*, vol. 37, pp. 1536–1541, Oct 1989.

[68] J.-P. Cousty, S. Verdeyme, M. Aubourg, and P. Guillon, "Finite elements for microwave device simulation: application to microwave dielectric resonator filters," *Microwave Theory and Techniques, IEEE Transactions on*, vol. 40, pp. 925 –932, May 1992.

[69] F. H. Gil and J. Martinez, "Analysis of dielectric resonators with tuning screw and supporting structure," *Microwave Theory and Techniques, IEEE Transactions on*, vol. 33, pp. 1453–1457, Dec 1985.

[70] A. Almeidaa, R. Silva, H. Rocha, H. Fechine, F. Cavalcanti, M. Valente, F. Freire, R. Sohn, and A. Sombra, "Experimental and numerical investigation of a ceramic dielectric resonator (dra): Cacu3ti4o12 (ccto)," *Physica B: Condensed Matter*, vol. 403, no. 4, pp. 586 – 594, 2008.

[71] D. Baillargear, S. Verdeyme, M. Aubourg, and P. Guillon, "Cad applying the finite-element method for dielectric-resonator filters," *Microwave Theory and Techniques, IEEE Transactions on*, vol. 46, pp. 10–17, Jan 1998.

[72] V. Walker and I. Hunter, "Design of cross-coupled dielectric-loaded waveguide filters," *Microwaves, Antennas and Propagation, IEE Proceedings* -, vol. 148, pp. 91 –96, Apr. 2001.

[73] L. Young, G. Matthaei, and E. Jones, "Microwave bandstop filters with narrow stop bands," *PGMTT National Symposium Digest*, vol. 62, pp. 46–51, May 1962.

[74] L. Chen, C. Ong, C. Neo, V. Varadan, and V. Varadan, *Microwave Electronics: Measurement and Materials Characterization.* Jon Wiley and Sons Ltd, first ed., 2004.

[75] D. Pozar, *Microwave Engineering.* John Wiley and Sons, Inc, second ed., 1998.

[76] S. Ramo, J. Whinnery, and T. Van Duzer, *Fields and Waves in Communication Electronics.* John Wiley and Sons, Inc, third ed., 1993.

[77] A. Weily and A. Mohan, "Microwave filters with improved spurious performance based on sandwiched conductor dielectric resonators," *Microwave Theory and Techniques, IEEE Transactions on*, vol. 49, pp. 1501 –1507, Aug. 2001.

[78] J.-S. Hong and M. J. Lancaster, *Microstrip filters for RF/Microwave Applications.* Wiley-Interscience, 2001.

[79] G. Macchiarella, M. Fumagalli, and S. D'Oro, "A new coupling structure for dual mode dielectric resonators," *Microwave and Guided Wave Letters, IEEE*, vol. 10, pp. 523–525, Dec 2000.

[80] J. Krempasky, "Analysis of TEM mode on a curved coaxial transmission line," *Microwave Theory and Techniques, IEEE Transactions on*, vol. 38, pp. 739 –747, June 1990.

[81] R. Mansour, "Dual-mode dielectric resonator filters with improved spurious performance," *Microwave Symposium Digest, 1993., IEEE MTT-S International*, pp. 439–442 vol.1, 1993.

[82] I. Hunter and J. Rhodes, "Electronically tunable microwave bandstop filters," *Microwave Theory and Techniques, IEEE Transactions on*, vol. 82, pp. 1361–1367, Sep 1982.

[83] M. Ismail, D. Smith, A. Panariello, Y. Wang, and M. Yu, "Em based design of large-scale dielectric resonator multiplexers by space mapping," in *Microwave Symposium Digest, 2003 IEEE MTT-S International*, vol. 1, pp. 291 – 294 vol.1, june 2003.